



Ecole Doctorale Sciences de la Matière, du Rayonnement et de l'Environnement (ED-SMRE)

## **Thèse en Codirection**

Pour l'obtention de grade de

### **Docteur de l'Université de Lille**

Discipline : Chimie des Matériaux

Filière : Molécule et Matière Condensée

Par

**Hicham NIMOH**

Thèse soutenue le **26 septembre 2024**

---

# **Valence exotique dans les systèmes métal-phosphate des métaux de transition du 6<sup>e</sup> bloc (Cr, Mo, W)**

---

#### **Thèse dirigée par :**

Dr. Olivier MENTRÉ, Directeur de recherche, CNRS, UCCS, Lille, France.

Prof.Dr. Robert GLAUM, Professeur à l'université Rhénane Frédéric-Guillaume de Bonn,  
Département de Chimie Inorganique, Allemagne.

#### **Co-encadrée par :**

Dr. Angel AREVALO-LOPEZ, Chargé de recherche CNRS, UCCS, Lille, France

#### **Membres du jury :**

##### **Président du jury :**

Dr. Alain PAUTRAT, Directeur de recherche, CNRS, CRISMAT, Caen, France.

##### **Rapportrices :**

Prof. Dr. Angela MÖLLER, Professeure à l'Université Johannes Gutenberg de Mayence,  
Département de Chimie, Allemagne.

Dr. Sophie TENCÉ, Chargée de recherche, HDR, ICMCB, CNRS/Université de Bordeaux, France.

---

**Exotic valence in 6<sup>th</sup> block transition metal-phosphate  
systems (Cr, Mo, W)**

---

## Acknowledgement

I would like to express my deep gratitude to all those who have contributed in any way to the completion of this thesis.

First of all, I would like to thank my thesis supervisors, Olivier Mentré, Robert Glaum, and my co-supervisor Angel Arevalo-Lopez, for all the scientific achievements that would not have been possible without them. I would especially like to thank Olivier Mentré for being the driving force behind this thesis, for his adaptability, especially with a subject as multidisciplinary as this one, bridging physics and chemistry. I would also like to thank Robert Glaum for the warm welcome in his laboratory. The warm atmosphere in his lab made me feel at home. I am grateful for his invaluable advice and for sharing his encyclopedic knowledge of solid-state chemistry. I thank them all for their support throughout this thesis, which has not been an easy task, especially since it was conducted jointly between two countries, at the University of Lille and the University of Bonn, and started during the Covid-19 pandemic.

During this thesis, I had the opportunity to collaborate with two labs and two teams. I would like to start by thanking the team at UCCS, CS axis, where I conducted part of my thesis. I would like to thank Marielle for the TEM analyses, Laurence for the XRD analyses, Frédérique for her help with single-crystal diffraction analysis, Maxence for his EDX analyses and good mood, Myriam for her assistance with TGA analyses and kindness, and Claire for the numerous analyses conducted on the PPMS.

I would also like to thank my PhD colleagues with whom I shared this adventure, especially the members of room 233, both former and current members. I am grateful for the many good moments spent together, which were a great help in overcoming the difficult times that every PhD student encounter during their thesis. I would like to thank Omar, Sandy, Batoul, Ewen, Elias, Hugo C., Hugo D., Raphaël, Mathilde, Soukaina, Ayman, Maxime, Zineb, Fatima, Julien, and more.

I would like to thank Prof. Glaum's team, where I had the great pleasure of conducting the other half of my thesis. From the very first day of my arrival, I felt at home. The supportive atmosphere helped advance my research work and aided in resolving administrative difficulties. I cherish the numerous wonderful moments shared, playing Doppelkopf at lunchtime, our Thursday outings for a Döner at Shatzi, and the help provided to solve my administrative issues. I had the pleasure of working with wonderful people, and I would like to thank them for their legendary good humor, kindness and all their help. Special thanks to Nevena, Mara, Max, Maximilian, Sina, Svenja, Julia, Jonas, Sebastien, Hamza, Lea, Patrick, Henri, Benjamin, Sylvia, and Alexandre. I would like to express my gratitude to the members of my thesis jury for agreeing to evaluate this work. I also wish to express my appreciation to the Hauts-de-France region and the University of Bonn for the funding and resources provided, which made this thesis possible.

Finally, words are insufficient to express my profound gratitude to my parents, my sister Hanane, and my two elder brothers Aziz and Houssein for their unwavering support throughout this thesis. Their love, patience, and unconditional support have been essential for completing this project.

## Résumé

La recherche en chimie des matériaux et en chimie du solide vise à synthétiser de nouvelles substances solides et à caractériser leurs propriétés. La détermination des structures cristallines est essentielle pour explorer les propriétés physiques et chimiques variées des composés étudiés. Les oxo-anions phosphates via leurs effets inductifs stabilisent des états d'oxydation exotiques et l'introduction de grands cations, conduisent à des structures de basse dimensionnalité avec des comportements électroniques et magnétique uniques. Cette recherche se concentre sur les phosphates des métaux de transition du bloc 6 (Cr, Mo, W), caractérisés par une diversité d'états d'oxydation de +II à +VI. Cette thèse explore les nouveaux bronzes tungstènes monophosphates en couches (L-MPTB)  $[\text{Ba}(\text{PO}_4)_2]_m\text{W}_m\text{O}_{3m-3}$  ( $2 \leq m \leq 5$ ), caractérisés par des couche de  $\text{WO}_6$  épaisseur  $m$  séparées par des espaceurs de phosphate de baryum. Les composés présentent des états d'oxydation mixtes du tungstène V/VI, incluant le rare  $\text{W}^{5+}$  pour  $m = 2$ . Les structures cristallines ont été élucidées par diffraction X sur monocristaux et diffraction électronique, et les propriétés physiques étudiées incluent la résistivité, le coefficient de Seebeck et la capacité thermique, appuyées par des calculs DFT. Tous les L-MPTB montrent un comportement métallique jusqu'à 1,8 K sans ordre clair de densité de charge (CDW). Le membre  $m = 2$  se distingue par une expansion thermique négative anisotrope et un coefficient Seebeck négative. Un décentrage significatif du tungstène dans leur coordination octaédrique est identifié, conduisant à une métallicité 2D semblable à la conductivité accrue dans les parois de domaines chargés des ferroélectriques. De plus, nous abordons la découverte des composés phosphates ternaires du tungstène (VI),  $\text{A}(\text{PO}_4)_2(\text{WO}_2)_2$  ( $\text{A} = \text{Ba}, \text{Sr}, \text{Pb}$ ), qui diffèrent structurellement de leurs analogues au molybdène tout en partageant une architecture structural proche en forme de tunnels. Des études computationnelles utilisant des algorithmes évolutifs de cristallographie comme USPEX et des calculs photoniques fournissent des informations sur la stabilité thermo dynamique et dynamique sous-jacentes à ces variations structurelles. En outre, une attention particulière est portée aux phosphates de chrome(II), où l'état d'oxydation rare  $\text{Cr}^{2+}$  est stabilisé par l'effet inductif des groupes phosphate. Celle-ci associé à l'effet Jahn-Teller, donne naissance à une variété de structure cristalline et d'interaction électronique et magnétique. Les phases  $\alpha$ - et  $\beta$ - $\text{Cr}_3(\text{PO}_4)_2$  montrent des structures magnétiques complexes avec des couplage antiferromagnétiques et des arrangements de spins non colinéaires. Les données de diffraction neutronique à basse température identifient des symétries magnétiques uniques et des interactions, offrant des informations sur le comportement magnétique des composés de chrome (II). L'incorporation de grands cations comme Ba dans  $\text{BaCrP}_2\text{O}_7$  induit des structures de basse dimensionnalité avec un comportement antiferromagnétique (AFM) 1D non modulé pour le cas du chrome (II), contrairement aux composés apparentés  $\text{BaM}^{\text{II}}\text{X}_2\text{O}_7$  ( $\text{M} = \text{Co}, \text{Fe}; \text{X} = \text{P}, \text{As}$ ).  $\text{Sr}_2\text{Cr}(\text{PO}_4)_2$  présente une structure magnétique tout à fait unique avec une coordination hautement distordue  $[\text{Cr}(1)\text{O}_{4+1}]$  et  $[\text{Cr}(2)\text{O}_4]$ . L'analyse du champ du ligand montre que la répartition des orbitales d est très différente pour ces deux unités, ce qui contribue à leurs propriétés magnétiques. Les ions Cr(1) et Cr(2) forment des couches distinctes avec des voies d'échange magnétique concurrentes. La susceptibilité magnétique détaillée, la chaleur spécifique, les données de diffraction neutronique sur poudre et les calculs DFT révèlent un fort couplage AFM au sein des couches de Cr(1) et un faible échange entre les couches, conduisant à un ordre magnétique 2D entre 11,5 et 2 K avec des spins de Cr(2) presque inactifs.

## Abstract

Research in materials and solid-state chemistry aims to synthesize new solid substances and characterize their properties. Determining crystal structures is essential to explore the diverse physical and chemical properties of the studied compounds. Phosphate oxo-anions, through their inductive effects, stabilize exotic oxidation states, and the incorporation of large cations frequently leads to low-dimensional structures with unique electronic and magnetic behaviour. This research focuses on phosphates of group VI transition metals (W, Mo, Cr), characterized by an oxidation states ranging from +II to +VI. This thesis explores the new series of layered monophosphate tungsten bronzes (L-MPTB)  $[\text{Ba}(\text{PO}_4)_2]\text{W}_m\text{O}_{3m-3}$  ( $2 \leq m \leq 5$ ), consisting of  $m$ -layer thick slabs of  $\text{WO}_6$  octahedra separated by barium phosphate spacers. These compounds exhibit mixed valent tungsten in oxidation states +5 and +6, including the rarely found pure  $\text{W}^{5+}$  for  $m = 2$ . Crystal structures were solved using single-crystal X-ray and electron diffraction. Physical properties studied include resistivity, Seebeck coefficient, and heat capacity, supported by DFT calculations. All L-MPTB compounds show metallic behaviour down to 1.8 K without clear charge-density wave (CDW) order.  $\text{Ba}(\text{PO}_4)_2\text{W}_2\text{O}_3$  ( $m = 2$ ) displays anisotropic negative thermal expansion and a negative Seebeck coefficient. Significant tungsten off-centring in their octahedral coordination is identified, leading to 2D metallicity similar to enhanced conductivity in charged domain walls of ferroelectrics. Additionally, we discuss the discovery of "fully-oxidized" ternary tungsten(VI) phosphates  $\text{A}(\text{PO}_4)_2(\text{WO}_2)_2$  ( $\text{A} = \text{Ba}, \text{Sr}, \text{Pb}$ ), which differ structurally from their molybdenum analogues while sharing similar tunnel-like architectures. Computational studies using evolutionary crystallographic algorithms like USPEX and phonon calculations provide insights into the thermodynamic and dynamics stability underlying these structural variations. Furthermore, special attention is given to chromium(II) phosphates, where the rare  $\text{Cr}^{2+}$  oxidation state is stabilized by the inductive effect of phosphate groups. This, coupled with the Jahn-Teller effect, gives rise to a variety of crystal structures and electron-magnetic interactions. The modifications  $\alpha$ - and  $\beta$ - $\text{Cr}_3(\text{PO}_4)_2$  phases exhibit complex magnetic structures with antiferromagnetic coupling and non-collinear spin arrangements. Neutron diffraction data at low temperatures identify unique magnetic symmetries and interactions, offering insights into the magnetic behaviour of chromium(II) compounds. Incorporation of large cations (e.g. Ba) as in  $\text{BaCrP}_2\text{O}_7$  induces low-dimensional structures with non-modulated 1D antiferromagnetic behaviour for chromium(II), unlike related  $\text{BaM}^{\text{II}}\text{X}_2\text{O}_7$  ( $\text{M} = \text{Co}, \text{Fe}; \text{X} = \text{P}, \text{As}$ ) compounds.  $\text{Sr}_2\text{Cr}(\text{PO}_4)_2$  displays a very unique magnetic structure with highly distorted  $[\text{Cr}(1)\text{O}_{4+1}]$  five-fold square-pyramidal and  $[\text{Cr}(2)\text{O}_4]$  four-fold square-planar coordination. Ligand field analysis shows significantly different d-orbital splitting for these two units, contributing to their magnetic properties. The Cr(1) and Cr(2) ions form distinct layers with competing magnetic exchange pathways. Detailed magnetic susceptibility, specific heat, neutron powder diffraction data, and DFT calculations reveal strong AFM coupling within the Cr(1)-layers and weak inter-layer exchange, leading to 2D magnetic ordering between 11.5 and 2 K with nearly idle Cr(2) spins.

# Content

ACKNOWLEDGEMENT	2
RESUME	3
ABSTRACT	4
CONTENT	5
LIST OF FIGURES	8
LIST OF TABLES	14
GENERAL INTRODUCTION	16
I. PROSPECTION FOR NOVEL BARIUM TUNGSTEN-PHOSPHATES	20
I.1. STEADY ANTIPOLAR 2D-METALLICITY IN THE NEW L-MPTB, $Ba(PO_4)_2W^{5+,6+}_mO_{3m-3}$	20
I.1.1. Introduction	20
I.1.2. Structural description of the parent the phosphate tungsten bronzes (PTBs) and charge density wave (CDW) phenomenon	21
I.1.2.1 Structural description of the parent phosphate tungsten bronzes (PTBs)	21
I.1.2.2 Charge density waves (CDW) and low-dimensional metals	24
I.1.2.3 Evidence of CDW transitions in MPTBp through physical measurements	30
I.1.3. Experimental	34
I.1.3.1 Materials and methods	34
I.1.3.2 Synthesis of the L-MPTBs $Ba(PO_4)_2W_mO_{3m-3}$ at $2 \leq m \leq 5$	36
I.1.3.3 Attempts to prepare missing members of the series $Ba(PO_4)_2W_mO_{3m-3}$	41
I.1.4. Structure determination and description of the layered monophosphate tungsten bronze (L-MPTB)	42
I.1.4.1 Structural overview and structural analogues to the L-MPTB series	42
I.1.4.2 $Ba(PO_4)_2W_2O_3$ ( $m = 2$ )	44
I.1.4.3 $Ba(PO_4)_2W_3O_6$ ( $m = 3$ )	45
I.1.4.4 $Ba(PO_4)_2W_4O_9$ ( $m = 4$ )	47
I.1.4.5 $Ba(PO_4)_2W_5O_{12}$ ( $m = 5$ )	49
I.1.4.6 Stability of the trigonal symmetry	50
I.1.5. Physical characterisation and DFT calculations	52
I.1.5.1 Steady 2D-metallicity validating the absence of CDW	52
I.1.5.2 Heat capacity	54
I.1.5.3 Fermi Surface Topology and Band Structure Analysis	55
I.1.5.4 Charge distribution	58
I.1.6. $Ba(PO_4)_2W_{m-x}M_xO_{3m-3}$ ( $M = Mo, Fe$ )	62
I.1.6.1 $Ba(PO_4)_2W_{3-x}Mo_xO_6$ ( $m = 3$ )	62
I.1.6.2 $Ba(PO_4)_2W_{4-x}Fe_xO_9$ ( $m = 4$ )	66
I.1.7. Partial conclusion	67
I.2. NEW TUNGSTEN (VI) TERNARY PHOSPHATE $A(PO_4)_2(WO_2)_2$ ( $A = Ba, Sr, Pb$ ) WITH TUNNEL LIKE STRUCTURE	69
I.2.1. Introduction	69
I.2.2. Synthesis	70

1.2.3.	<i>Structure refinement and description</i>	71
1.2.3.1	Crystal structure analysis of $A(PO_4)_2(WO_2)_2$ (A = Ba, Sr, Pb)	71
1.2.3.2	Structure description of $A(PO_4)_2(WO_2)_2$ (A = Ba, Sr, Pb)	74
1.2.4.	<i>Dynamic and thermodynamic stability and its temperature dependence</i>	77
1.2.4.1	USPEX (Universal Structure Predictor: Evolutionary Xtallography) and phonon calculation	77
1.2.4.2	$Ba(PO_4)_2(MO_2)_2$ , M = Mo Vs. W	79
1.2.4.3	$A(PO_4)_2(WO_2)_2$ : Selection between the Ba and Pb Structure Type	81
1.2.5.	<i>Partial conclusion</i>	84

## **II. INSIGHTS INTO THE MAGNETIC BEHAVIOR OF JAHN-TELLER ACTIVE CHROMIUM(II) IONS IN PHOSPHATES** **85**

II.1.	INTRODUCTION	85
II.2.	THE COMPLEX 3D-AFM EXCHANGE PATHWAYS IN A- AND B- $Cr_3(PO_4)_2$	87
II.2.1.	<i>Introduction and survey of the literature</i>	87
II.2.1.1	Synthesis - summary of literature	87
II.2.1.2	Crystal structures	87
II.2.1.3	Magnetic properties	89
II.2.2.	<i>The Magnetic structures of <math>\alpha</math>- and <math>\beta</math>-<math>Cr_3(PO_4)_2</math></i>	90
II.2.2.1.	$\alpha$ -chromium(II) orthophosphate	91
II.2.2.2.	$\beta$ -chromium(II)-orthophosphate	93
II.2.3.	<i>Partial conclusion</i>	95
II.3.	NON-MODULATED AFM IN BARIUM CHROMIUM(II) PYROPHOSPHATE	95
II.3.5.	<i>Introduction</i>	95
II.3.2.	<i>Summary on literature regarding <math>BaCrP_2O_7</math></i>	98
II.3.3.	<i>Synthesis</i>	98
II.3.4.	<i>Crystal structure refinement and description</i>	99
II.3.5.	<i>Magnetic Properties</i>	101
II.3.5.1	Magnetic measurement	101
II.3.5.2	Magnetic structure	104
II.3.6.	<i>Partial conclusion</i>	107
II.4.	TWO-STEP 2D/3D MAGNETIC ORDERING VIA IDLE SPINS AND THE OPTICAL SIGNATURE OF JAHN-TELLER $Cr^{2+}$ IONS IN $Sr_2Cr(PO_4)_2$	109
II.4.1.	<i>Introduction</i>	109
II.4.2.	<i>Experimental</i>	110
II.4.2.2	Synthesis	111
II.4.3.	<i>Crystal structure refinement and description</i>	112
II.4.3.1	Structure refinement	112
II.4.3.2	Crystal Structure description	113
II.4.4.	<i>Magnetic Properties</i>	114
II.4.4.1	DFT+U investigation of magnetic exchanges in competition	114
II.4.4.2	Magnetic Properties and Ordering	116
II.4.4.3	Magnetic Structures refinement	118

II.4.5.	<i>Combined spectroscopic and DFT analysis of ligand fields</i>	122
II.4.6.	<i>Partial conclusion</i>	125
<b>GENERAL CONCLUSION</b>		<b>126</b>
APPENDIX I		129
A.I.1	<i>Crystallographic data</i>	129
A.I.2.	<i>Diffraction experiments</i>	135
A.I.3.	<i>Physical properties and fit functions</i>	135
APPENDIX II		137
A.II.1.	<i>Crystallographic data</i>	137
A.II.2.	<i>DFT Calculations and Magnetic Exchanges</i>	144
A.II.3.	<i>Magnetic structure detail</i>	145
A.II.4.	<i>AOM for <math>Sr_2Cr^{II}(PO_4)_2</math> and selected reference compounds</i>	148
<b>REFERENCES</b>		<b>151</b>

## List of figures

- Figure I-1. Different structural configurations in tungsten phosphate bronzes (PTBs) and their relations are illustrated. Various substitutions in a  $\text{ReO}_3$ -type structure involve replacing one or more  $\text{WO}_6$  octahedra by  $\text{PO}_4$  tetrahedra, leading to monophosphate tungsten bronzes (MPTB). Furthermore, the substitution of two adjacent  $\text{WO}_6$  octahedra, sharing corners for a  $\text{P}_2\text{O}_7$  diphosphate group, results in the formation of diphosphate tungsten bronzes (DPTB). Figure based on [13]. \_\_\_\_\_ 22
- Figure I-2. Illustration of a 1D atomic chain (in blue) and its electron density (in red), along with the electronic spectrum of a 1D electron-dimensional metal in two distinct states: a) the non-modulated normal state, and b) the modulated state, also known as the Charge Density Wave state. Figure based on \_\_\_\_\_ 26
- Figure I-3. Topologies of Fermi surfaces in momentum space and Fermi surface nesting for ideal 3D, 2D, and 1D materials. The regions highlighted in red represent areas prone to nesting. Figure based on [31]. \_\_\_\_\_ 27
- Figure I-4. Fermi surfaces topologies of a) the ideal 2D metal Fermi surface and b) the quasi-2D metal and their nesting vectors. Figure based on [32]. \_\_\_\_\_ 28
- Figure I-5. a) A 3D projection of the purple the quasi 2D conductor molybdenum bronze  $\text{ReO}_3$ -type layer, b) a sketch of the  $t_{2g}$ -block bands of the  $\text{Mo}_4\text{O}_{18}$  displaying a pseudo-1D electrical properties with zig-zag  $\text{Mo}_2\text{O}_{10}$  chains running along c) a, d) b and e) (a + b) directions [29,42]. f-g) Combined Fermi Surface representation for the  $\text{K}_{0.9}\text{Mo}_6\text{O}_{17}$  and its decomposition into three sets of differently oriented 1D Fermi Surfaces. Nesting is achieved through nesting vectors. The ARPES spectral intensity at the Fermi level displayed on the two-dimensional wave vector at h) 140 K and i) 20 K, where these temperatures are situated above and below the transition temperatures,  $T_{c1}$  and  $T_{c2}$  [43]. Permission for reproduction was granted by EPL editorial office. \_\_\_\_\_ 29
- Figure I-6. a) Projection on [001] of the crystal structure for  $\text{WPO}_5$  (MPTB<sub>p</sub> at  $m = 2$ ) and b) Highlights the presence of one-dimensional chains running along the c-axis, as illustrated by the red box [46]. \_\_\_\_\_ 31
- Figure I-7. MPTB<sub>p</sub> resistivity measurements of a)  $m = 2$  [46], b) remeasured  $m = 2$  [31], c)  $m = 4$  [51], d)  $m = 5$  [48], e)  $m = 6$  [48], f)  $m = 7$  [52] g)  $m = 8$  [47], h)  $m = 9$  [47], [31], i)  $m = 10$  [31,53]. \_\_\_\_\_ 32
- Figure I-8. MPTB<sub>p</sub> thermoelectric power vs. temperature for a)  $m = 5$ , with a thermal gradient applied along the b-axis [48] b)  $m = 6$ , with the upper curve is a thermal gradient along the a-axis and the lower one along the b-axis [54], c)  $m = 8$ , with thermal gradient along the a-axis [47]. Permission for reproduction was granted. \_\_\_\_ 33
- Figure I-9. a) Specific heat measurements for  $m = 4$  and  $m = 6$  MPTB<sub>p</sub> crystals, where small vertical arrows indicate the localization of CDW transition temperatures [55], b) Specific heat measurements of three  $m = 6$  MPTB<sub>p</sub> crystals. c) specific heat measurement of  $\text{KMo}_6\text{O}_{17}$  for  $H = 0$  (black circle) and 12 T (red cross) where the small arrow indicate the temperature of the CDW transition [58], d) Plot of  $C_p/T^3$  vs.  $T$  for  $H = 0$  T (black circle) and  $H = 12$  T (red cross), with the dashed line indicating the fit using the modified Debye model [58]. Permission for reproduction was granted. \_\_\_\_\_ 34
- Figure I-10. Experimental (red), calculated (black) and difference patterns after Rietveld refinement of NPD data for  $\text{Ba}(\text{PO}_4)_2\text{W}_2\text{O}_{2.92(5)}$ . \_\_\_\_\_ 38
- Figure I-11. a) Profile matching on lab Xray data for  $m = 2$ . Rietveld refinement on synchrotron powder diffraction data for a)  $m = 3$  b)  $m = 4$  c)  $m = 5$  d) Rietveld refinement on neutron powder diffraction data for  $m = 4$ . e) image of the pellets obtained for different L-MPTB member. \_\_\_\_\_ 39
- Figure I-12. Sketch illustrating the CVT method for crystal growth attempts [69]. \_\_\_\_\_ 40

Figure I-13. a) The obtained  $Ba(PO_4)_2W_3O_6$  ( $m = 3$ ) crystals characterized by a bronze color. b) a zoom-in showcasing a prominent crystal. \_\_\_\_\_ 40

Figure I-14. a) TGA analysis of  $Ba(PO_4)_2W_2O_3$  ( $m = 2$ ) under  $O_2$  with a ramp of  $5^\circ C/min$  till  $850^\circ C$  then a plateau of 3h was applied with a heating and cooling cycle. b) Evolution of the mass gain as a function of time at the plateau temperature of  $850^\circ C$ . \_\_\_\_\_ 40

Figure I-15. Crystal structures principle of the L-MPTB. Projection on [110] of the crystal structures for a)  $Ba(PO_4)_2W_2O_3$  ( $m = 2$ ), b)  $Ba(PO_4)_2W_3O_6$  ( $m = 3$ ), c)  $Ba(PO_4)_2W_4O_9$  ( $m = 4$ ) and d)  $Ba(PO_4)_2W_5O_{12}$  ( $m = 5$ ). \_\_\_\_\_ 42

Figure I-16. Various crystal structures analogous to the L-MPTB family: a)  $KMo_6O_{17}$  [76], b)  $BaFe_2(PO_4)_2$  [74], c)  $CsTi(PO_4)_2$  [70], d)  $\beta$ - $BaZr(PO_4)_2$  [71] and e)  $BaMo(PO_4)_2$  [72]. f) Sketch of the structural passage from MPTB<sub>p</sub> to L-MPTB by slicing/shearing and Ba incorporation. \_\_\_\_\_ 43

Figure I-17. Projection on [110] of the crystal structure for  $Ba(PO_4)_2W_2O_3$  ( $m = 2$  L-MPTB), Projection on a) [110] and b) [001] of the crystal structure for  $Ba(PO_4)_2W_3O_6$  ( $m = 3$  L-MPTB), with details of the W shift and m-octahedra along  $W_mO_{3m-3}$  row. b) the 1D  $W^{5+}$  chains displayed in the  $WOPO_4$  ( $m = 2$  MPTBp) Vs. c) 2D- $W^{5+}$  layers with double-octahedra in  $Ba(PO_4)_2W_2O_3$  ( $m = 2$  L-MPTB). d) HAADF images. The white spots correspond to the heavy Ba and W, while the lighter P and O ones are in the dark areas. The inset shows [010] ED patterns for  $m = 2$  L-MPTB. \_\_\_\_\_ 45

Figure I-18. Projection on [110] a) and b) [001] of the crystal structure for  $Ba(PO_4)_2W_3O_6$  ( $m = 3$  L-MPTB), with details of the W shift and m-octahedra along  $W_mO_{3m-3}$  row. c) HAADF images. The white spots correspond to the heavy Ba and W, while the lighter P and O ones are in the dark areas. The inset shows [010] ED patterns for  $m = 3$  L-MPTB. \_\_\_\_\_ 46

Figure I-19. a) Rietveld refinement of synchrotron powder diffraction data of  $m = 4$ . The refinement shows the peaks corresponding to this modulation (red) b) Rietveld refinement of neutron powder diffraction data. c) 1kl reconstituted precession frame from SC-XRD data at RT with evidence of 2c satellites (yellow). d) oxygen ordering in  $m = 4$ . The two oxygen pairs follow an occupancy crenel-like wave leading to a commensurate modulation. \_\_\_\_\_ 47

Figure I-20. Projection on a) [110] of the crystal structure  $Ba(PO_4)_2W_4O_9$  ( $m = 4$  L-MPTB), with details of the W shift and m-octahedra along  $W_mO_{3m-3}$  row and eclipsed configurations of the coordination polyhedra between two next 2D-units along c, responsible for the c-axis doubling. b) HAADF images. The white spots correspond to the heavy Ba and W, while the lighter P and O ones are in the dark areas. The inset shows [010], [001] and [-110] ED patterns, the latter showing the c-doubling for the  $m = 4$  L-MPTB. \_\_\_\_\_ 48

Figure I-21. Projection on [110] of the crystal structure for  $Ba(PO_4)_2W_5O_{12}$  ( $m = 5$  L-MPTB), with details of the W shift and m-octahedra along  $W_mO_{3m-3}$  row along the perovskite axis (in white). b) HAADF images. The white spots correspond to the heavy Ba and W, while the lighter P and O ones are in the dark areas. The inset shows [010], ED patterns. \_\_\_\_\_ 49

Figure I-22. Projection along the three perovskite pseudo-axes showing the octahedral tilting modes, by analogy with the parent  $WO_3$  the projection (following the Glazer notation), for  $m = 2$ ,  $m = 3$ ,  $m = 4$  and  $m = 5$ . \_\_\_\_\_ 50

Figure I-23.  $Ba(PO_4)_2W_2O_3$  ( $m = 2$ ): a) Smooth thermal evolution of XRPD profile. b) Lattice parameters a and c as a function of temperature. Negative thermal expansion is observed for a. c) Electron-diffraction patterns along the main crystallographic zone axes [001]\* at 297K and 103K.  $Ba(PO_4)_2W_4O_9$  ( $m = 4$ ): a) Smooth thermal evolution of SR-XRD profile b) Thermal evolution of the lattice parameters. c) W-W distances using both SR- and SC-XRD data. \_\_\_\_\_ 51

Figure I-24. a) Physical properties the L-MPTB series  $[Ba(PO_4)_2]W_mO_{3m-3}$ . Resistivity as a function of temperature. b) Seebeck coefficient as a function of temperature with fitted according to [79]. c) Lattice contribution to the

specific heat as a function of temperature (the insert shows the same data at low temperature in a  $C_p/T^3$  vs  $T$  plot, which should be constant according to the universal Debye law). d) Experimental and calculated Sommerfeld coefficient of the electronic contribution to the specific heat obtained for the different members of the series. 53

Figure I-25. Magnetic susceptibility Vs. temperature for the L-MPTB at  $m = 2, 3,$  and  $4$ . \_\_\_\_\_ 53

Figure I-26. a) Electronic band structure calculated for the  $m = 3, 4,$  and  $5$  members of the L-MTPB series  $[\text{Ba}(\text{PO}_4)_2]\text{W}_m\text{O}_{3m-3}$ . The Fermi surface of these systems has a remarkable 2D character. The three different sheets of these Fermi surfaces are associated with the three different bands that cross the Fermi level in the corresponding band plots. These half-filled bands belong to the  $5d$ - $W$  manifold that extend from  $\sim -0.5$  eV to  $\sim +4$  eV. b) Fermi surfaces (FS) of different members of L-MPTB \_\_\_\_\_ 56

Figure I-27. a) Projection of a section ( $\text{ReO}_3$ -type layer bordered by phosphates) of the  $m = 2$  structure along  $[010]$  showing the different orbital overlaps along b)  $[001]$  showing with zigzag chains of  $W$ - $t_{2g}$  and  $O$ - $\pi$  orbitals overlaps. c) intrachain  $t_{2g}$ - $\pi$ - $t_{2g}$  overlap and d) interchain  $t_{2g}$ - $t_{2g}$   $\delta$  overlaps. e) Total (black curves) and  $W$ - $5d$  projected density of states (DOS), with the different  $W$  atoms labelled according to their Wyckoff positions. \_ 57

Figure I-28. a) Height of the different  $\text{WO}_6$  octahedra along the  $c$ -axis as a function of the formal  $W$  valence across the entire L-MPTB series. The arbitrary offset of this plot is fixed with the  $m = 2$  compound. b) Filling of the  $t_{2g}$  manifold per  $W$  atom computed from the total and  $W$ -projected DOS. The  $W$  atoms are labelled as in Figure I-29a-d, so that  $W1$  always corresponds to the outer  $W$  of the  $\text{WO}_3$  slab (i.e. the only ones for  $m = 2$ ). \_\_\_\_\_ 59

Figure I-29. L-MPTB structures showing  $\text{WO}_6$  octahedra with off-centring of  $W$  atoms, leading to anti-polar  $\text{WO}_3$  blocks in a)  $m = 2,$  b)  $m = 3,$  c)  $m = 4$  and d)  $m = 5,$  analogous to charged domain walls in ferroelectric materials. \_\_\_\_\_ 61

Figure I-30. Rietveld refinement on synchrotron powder diffraction data for  $\text{Ba}(\text{PO}_4)_2\text{W}_{3-x}\text{Mo}_x\text{O}_6$  ( $m = 3$ ) for a)  $x = 0.33,$  b)  $x = 1$  and c)  $x = 1.5$ . \_\_\_\_\_ 63

Figure I-31. Variation of unit cell parameters in the  $\text{Ba}(\text{PO}_4)_2\text{W}_{3-x}\text{Mo}_x\text{O}_6$  ( $m = 3$ ) structure as a function of the degree of substitution of  $W$  by  $\text{Mo}$ . \_\_\_\_\_ 64

Figure I-32. Comparing the Rietveld of the SR-PD data considering as a) no substitution of  $W$  by  $\text{Mo}$  in  $m = 3$  b) a substitution of  $W$  by  $\text{Mo}$  and refining the site occupancy. \_\_\_\_\_ 65

Figure I-33. EDS Mapping of  $\text{Ba}(\text{PO}_4)_2\text{Fe}_{0.22}\text{W}_{3.78}\text{O}_9$  crystals with Barium in yellow, tungsten in green, iron in red and phosphorus in blue. \_\_\_\_\_ 67

Figure I-34.  $\text{Ba}(\text{PO}_4)_2(\text{WO}_2)_2$  ED patterns projected along a)  $[001]$  and b)  $[010]$  directions. \_\_\_\_\_ 71

Figure I-35.  $^{31}\text{P}$ -MAS NMR spectra of  $\text{Pb}(\text{PO}_4)_2(\text{WO}_2)_2$  and  $\text{Ba}(\text{PO}_4)_2(\text{WO}_2)_2$  isotropic chemical shift relative to  $\text{H}_3\text{PO}_4$ . \_\_\_\_\_ 72

Figure I-36. Rietveld refinement on synchrotron powder diffraction data for a)  $\text{Ba}(\text{PO}_4)_2(\text{WO}_2)_2$  and b)  $\text{Pb}(\text{PO}_4)_2(\text{WO}_2)_2$ . \_\_\_\_\_ 73

Figure I-37. Comparison between rietveld refinement on synchrotron powder diffraction data of  $\text{Sr}(\text{PO}_4)_2(\text{PO}_4)_2$  for a)  $\text{Sr}(1)$  at  $(0\ 0\ 1/2)$  Vs. b)  $\text{Sr}(1)$  at  $(0\ 0\ 0)$ . \_\_\_\_\_ 74

Figure I-38. a, b) Crystal structures of  $\text{A}(\text{PO}_4)_2(\text{WO}_2)_2$  ( $\text{A} = \text{Ba}, \text{Sr}, \text{Pb}$ ) along different projections.  $\text{WO}_6$  octahedra and  $\text{PO}_4$  tetrahedra form 1D  $[\text{WO}_3\text{O}_3\text{PO}]_\infty$  ribbons interconnected through  $W$ - $O$ - $P$  bridges, creating tunnels that host  $\text{A}(1)$  and  $\text{A}(2)$  cations. c, d) Cross-sections along  $[110]$  show square-lattice ( $\text{Ba}, \text{Sr}$ ) or hexagonal-lattice ( $\text{Pb}$ ) distributions of cations in the channels. (e) Similar structural motifs are observed in related  $\text{AMoO}_2\text{PO}_4$  compounds. Short  $W$ - $O$  distances define the exterior of  $[\text{WO}_4\text{O}_2\text{PO}_4]_3$  rings and channel walls. \_\_\_\_\_ 76

Figure I-39. Topological view of the structure showing the main building units connected by W-O-P bridges in a)  $A(\text{PO}_4)_2(\text{WO}_2)_2$  compared to b)  $A(\text{MoO}_2)_2(\text{PO}_4)_2$  ( $A = \text{Ba}, \text{Sr}, \text{Pb}, (\text{Li}, \text{K})$ ) and c)  $\text{AMo}_2\text{PO}_4$  ( $A = \text{Na}, \text{Ag}, \text{Cs}, \text{K}, \text{M} = \text{Mo}, \text{W}$ ) where  $\text{PO}_4$  groups are in yellow spheres and  $\text{MoO}_6$  octahedra are in grey spheres. \_\_\_\_\_ 77

Figure I-40. Calculation *Ab initio* structural prediction using the USPEX evolutionary algorithm for a)  $\text{Ba}(\text{PO}_4)_2(\text{MoO}_2)_2$  and b)  $\text{Ba}(\text{PO}_4)_2(\text{WO}_2)_2$  showing different generated population (in red) and identified (in green) with their space group number where the monoclinic  $P21/c$  (No. 14) and the trigonal  $P-31m$  (No. 167) are predicted with a certain relative stability. c) Different examples of generated structures with the chemical formula  $\text{Ba}(\text{PO}_4)_2(\text{WO}_2)_2$ . \_\_\_\_\_ 80

Figure I-41. The phonon dispersion from Phonopy associated with VASP of  $\text{Ba}(\text{PO}_4)_2(\text{MoO}_2)_2$  in structure type a) 14-BaMo and b) 162-BaW shows imaginary frequency frequencies. Similarly, for  $\text{Ba}(\text{PO}_4)_2(\text{WO}_2)_2$  in structure type c) 14-BaMo shows imaginary frequency d) 162-BaW. \_\_\_\_\_ 81

Figure I-42. The phonon dispersion and their density-of-states (DOS) curves for a structure type 162-BaW for for a chemical formula a)  $\text{Ba}(\text{PO}_4)_2(\text{O}_2)_2$ , b)  $\text{Pb}(\text{PO}_4)_2(\text{O}_2)_2$  and c)  $\text{Sr}(\text{PO}_4)_2(\text{WO}_2)_2$ . in structure type a) 14-BaMo and b) 162-BaW shows imaginary frequency frequencies. Similarly, for a structure type 162-PbW for for a chemical formula a)  $\text{Ba}(\text{PO}_4)_2(\text{O}_2)_2$ , b)  $\text{Pb}(\text{PO}_4)_2(\text{O}_2)_2$  and c)  $\text{Sr}(\text{PO}_4)_2(\text{O}_2)_2$ . All show no imaginary frequencies \_\_\_\_\_ 82

Figure I-43. Summary of the results obtained using various techniques to investigate the stability and predictability of these structures. \_\_\_\_\_ 84

Figure II-1. a) Projection of the crystal structure of  $\alpha\text{-Cr}_3(\text{PO}_4)_2$  on the  $ac$  plane. The crystal structure consists of close-packed tubes parallel to the  $b$ -axis, with Cr atoms on the inner surface and  $[\text{PO}_4]$  groups on the outer surface and tube centres. Adjacent tubes are related by pseudo  $3_1$  screw axes. b) Projection on the  $bc$  plane of the atomic arrangement in proximity to a pseudo  $3_1$  screw-axis. Crystal structure  $\beta\text{-Cr}_3(\text{PO}_4)_2$  projected on the c)  $bc$  plane d)  $ab$  plane and e)  $ac$  plane. \_\_\_\_\_ 88

Figure II-2. sketch of the plausible direct bonding between Cr(4) and Cr(5). \_\_\_\_\_ 89

Figure II-3. a) Magnetic susceptibility measurement (insert)  $\chi_M$  and its inverse  $1/\chi_M$  for  $\alpha\text{-Cr}_3(\text{PO}_4)_2$  (in blue) (remeasured) and for  $\beta\text{-Cr}_3(\text{PO}_4)_2$  (in green) as measured by HAMMER [20,145]. b) Magnetization  $M$  versus field  $H$  at different temperature for  $\alpha\text{-Cr}_3(\text{PO}_4)_2$ . \_\_\_\_\_ 90

Figure II-4. Neutron powder diffraction refinement of magnetic and nuclear structures for a)  $\alpha\text{-Cr}_3(\text{PO}_4)_2$  at 1.5 K and b)  $\beta\text{-Cr}_3(\text{PO}_4)_2$  at 2 K. Neutron powder diffraction refinement of the magnetic structures only for c)  $\alpha\text{-Cr}_3(\text{PO}_4)_2$  from 1.2-40 K data and d)  $\beta\text{-Cr}_3(\text{PO}_4)_2$  from 2-50 K data. \_\_\_\_\_ 90

Figure II-5. a) Projection of  $\alpha\text{-Cr}_3(\text{PO}_4)_2$  magnetic structure on (100). b) Same figure showing the magnetic moments orientations of its six independent  $\text{Cr}^{2+}$  ions (in different colours) in their respective coordination. c) Magnetic moment presentation of the various  $\text{Cr}^{2+}$  ions without their surroundings, illustrating a complex AFM arrangement with different moment orientations. d) An example of the arrangement within the structure highlighting the multitude and complexity of magnetic exchange pathways among different  $\text{Cr}^{2+}$  ions with a sketch of the plausible direct bonding between Cr(4) and Cr(5). \_\_\_\_\_ 93

Figure II-6.  $\beta\text{-Cr}_3(\text{PO}_4)_2$  a) Projection on [001] of the magnetic structure showing the orientation of the magnetic moments of its two independent  $\text{Cr}^{2+}$  ions (in red and green) in their coordination. b) Projection of magnetic structure on (100). c) Projection on (010) of the magnetic structure, consisting of layers interconnected through the  $[\text{PO}_4]$  groups in an AFM configuration. b) Illustration of a layer showing the two magnetically inequivalent sub-unites. \_\_\_\_\_ 95

Figure II-7. a) Average  $\text{BaMX}_2\text{O}_7$  ( $M = \text{Co}, \text{Fe}; X = \text{P}, \text{As}$ ) crystal structure projection on (100) [157]. b)  $7 \times 1 \times 3$  supercell [157]. c) evolution of  $M_B\text{-}M_C$ ,  $M_A\text{-}M_B$ ,  $\text{Fe}_B\text{-}O_3$ ,  $\text{Co}_B\text{-}O_3$  distances along the real space  $t$ -axis ( $t = x_4\text{-}q^- \cdot r^-$ ,  $q^-$  is the modulation vector and  $r^-$  an average position in physical space) [155]. d) Magnetic Structures: Collinear \_\_\_\_\_ 95

and modulated spin arrangement where  $BaCoX_2O_7$  ( $X = P, As$ ) are type II multiferroics with incommensurate shifts and AFM Ising-spins and  $BaFeP_2O_7$  has strong spin-lattice coupling and a modulated AFM structure [155]. Permission for reproduction was granted. \_\_\_\_\_ 97

Figure II-8.  $BaCrP_2O_7$  Le-Bail fit of the polycrystalline sample (IP-Guinier technique;  $CuK\alpha_1$ ,  $\lambda = 1.54051 \text{ \AA}$ , quartz monochromator, ambient temperature). \_\_\_\_\_ 98

Figure II-9.  $BaCrP_2O_7$ . a) Single crystal reconstructed  $hk0$  frames at ambient conditions and the overlaid calculated positions. Crystal structure projection on b) (100) and c) on (001). \_\_\_\_\_ 99

Figure II-10.  $BaCrP_2O_7$ . a) Magnetic susceptibility measurement  $\chi_M$  (in blue) and its inverse  $1/\chi_M$  (in black) and b) magnetization  $M$  versus field  $H$  at different temperature. \_\_\_\_\_ 102

Figure II-11.  $BaCrP_2O_7$ . a) Specific heat measured at  $H = 0$ , from 300 K to 2 K. b) Specific heat measured from 25 K to 2 K under different fields from 0 to 9 T. \_\_\_\_\_ 103

Figure II-12. Schematic of spin-flop transition in a uniaxial antiferromagnet with two sublattices. At a critical magnetic field, the sublattice magnetizations rotate perpendicular to the easy axis ( $z$ ) and applied field ( $b$ ), indicating a spin-flop transition, followed by continuous rotation as  $H$  increases [166]. \_\_\_\_\_ 104

Figure II-13.  $BaCrP_2O_7$  a) NPD pattern of magnetic satellite show their appearance and evolution of magnetic at low  $T$ . b) NPD refinement at 1.5K of magnetic and nuclear structures. c) Magnetization Vs  $T$ . d) refined magnetic moment from NPD at 1.5 K. \_\_\_\_\_ 105

Figure II-14.  $BaCrP_2O_7$ . Projection on (001) of the magnetic structure showing the magnetic moments orientations within the  $Cr^{2+}$  ions coordination. \_\_\_\_\_ 106

Figure II-15. a) Spin-interaction scheme for Chromium in  $BaCrP_2O_7$ . b) comparison of the filling of the  $d$ -orbital configuration in the pyramid square based coordination of  $Cu^{2+}$  ( $d^9$ ,  $S = 1/2$ ) and  $Cr^{2+}$  ( $d^4$ ,  $S = 2$ ). c) Comparison of Different  $[M_2O_8]$  Dimers ( $M: Fe, Cu, Cr$ ) geometry and the  $d$ -orbitals Involved in the magnetic interactions for  $Cu^{2+}$  ( $d^9$ ,  $S = 1/2$ ) and  $Cr^{2+}$  ( $d^4$ ,  $S = 2$ ). \_\_\_\_\_ 107

Figure II-16. Different  $BaM^II P_2O_7$  ( $M = Co, Fe, Cr$ ) structural and magnetic properties. \_\_\_\_\_ 108

Figure II-17.  $Sr_2Cr(PO_4)_2$ . a) Le-Bail fit of the polycrystalline sample (Guinier recordings;  $Cu K\alpha_1$ ,  $\lambda = 1.54051 \text{ \AA}$ , quartz monochromator). b) Micro-photograph of an as-grown crystal. \_\_\_\_\_ 112

Figure II-18. Reconstructed  $hk0$  frames for  $Sr_2Cr(PO_4)_2$  single crystal at ambient conditions and the over layered calculated positions in the three domains rotated by  $120^\circ$ . \_\_\_\_\_ 113

Figure II-19. a) Projections of the crystal structure of  $Sr_2Cr(PO_4)_2$  onto the  $ac$  plane. b-c) Individual  $Cr(1)$  and  $Cr(2)$  layers. d-f) Scheme of the main magnetic exchanges considered in the layers. g) Visualisation of the magnetic frustration within the  $Cr(2)$ -layers induced by the two neighbouring  $Cr(1)$ -layers. \_\_\_\_\_ 114

Figure II-20. a) Magnetic susceptibility ( $\chi$ ) and its inverse vs. temperature with zoom of the low-temperature shift for the later in the top inset and derivative  $d\chi/dT(T)$  in the bottom inset. b) the deconvolution of  $\chi(T)$  in a paramagnetic ( $Cr(2)$ -like) and gapped ( $Cr(1)$ -like) contributions. c) fit of the  $\chi(Cr(1))$  contribution obtained through Monte-Carlo simulation. d) field dependence of the Magnetization at 2K (before (black) and after (blue) removal of the AFM contribution (red)). \_\_\_\_\_ 116

Figure II-21. a) Specific heat Measurement and the magnification at low  $T$  showing two sharp  $\lambda$ -type peaks. b)  $C_{magn}/T(T)$  plot and its integration. c)  $C_p/T(T)$  plot under different magnetic field. \_\_\_\_\_ 118

Figure II-22. a) NPD patterns on cooling. b) Refinement of the magnetic peaks at 1.5K using two Irreps and c) using the magnetic space group approach. d) Refinement of the full pattern at 1.5 K using the magnetic space group approach. e) Thermal evolution of the refined magnetic moments and f) cell parameters. \_\_\_\_\_ 121

Figure II-23. Overlay of the nuclear structure and the magnetic structure at a) 5K and b) 1.5K with the various magnetic couplings and symmetries involved. \_\_\_\_\_ 121

Figure II-24.  $Sr_2Cr(PO_4)_2$ . a) Diffuse reflectance spectrum (DRS, greyish-green) and polarized single-crystal absorption spectra (incident light beam // crystallographic c-axis, hpol and vpol polarisation directions approximately bisecting the crystallographic a- and b-axis). b) d-orbital splitting for chromophores  $[Cr(1)O_{4+1}]$  and  $[Cr(2)O_4]$  from AOM (see A.II.4 in the appendix section). c) Total and Cr d-resolved density of states of  $Sr_2Cr(PO_4)_2$ . \_\_\_\_\_ 123

Figure A I-1. Evolution of a) (0 0 3) and b) (4 -2 0) peaks for different temperatures ..... 135

Figure A I-2.  $C_p/T$  as a function of  $T^2$  lower temperature a)  $m = 2$ , b)  $m = 3$ , c)  $m = 4$  and d)  $m = 5$ . ..... 135

Figure A II-1. Different spin configurations of Cr onto a classical Heisenberg model, spin up (white) spin down (black) for the DFT. .... 144

Figure A II-2.  $Sr_2Cr(PO_4)_2$  NPD refinement at 5K of a) the magnetic structure only and b) magnetic and nuclear structures at 5K, NPD refinement of the magnetic structure at c)3K and d) 2K. NPD refinement of the magnetic structure at 5 K with: e) the magnetic component refined only along the x-axis and f) refined along both the x and y axes. NPD refinement of the magnetic structure at 1.5 K with the magnetic component refined for Cr(1): g) using only the  $mGM3-$  Irrep, compared to h) using  $mGM3- \oplus mGM1+$  Irreps and Cr(2) both refinement have  $mGM1+$  only as Irreps ..... 147

Figure A II-3. Comparison of observed optical spectra and energy levels from AOM for the  $[Cr^{II}O_n]$  chromophores in  $Sr_2Cr^{II}(PO_4)_2$ ,  $SrCr^{II}P_2O_7$ , and  $\alpha-Ba_2Cr^{II}(PO_4)_2$ . Single-crystal (SXTAL) spectra for all compounds, diffuse powder reflectance spectrum (DRS) at ambient temperature is given for  $Sr_2Cr^{II}(PO_4)_2$ . Quintet levels from AOM are given as red ticks at the bottom of each spectrum. .... 150

## List of tables

Table I-1. Summary of structural distortions observed for tungsten atomic positions in the L-MPTB. _____	58
Table I-2. $A(\text{PO}_4)_2(\text{WO}_2)_2$ ( $A = \text{Ba}, \text{Pb}, \text{Sr}$ ) compounds described in different structure types and the $\Delta E$ relative to the most stable structure (the lowest energy) from DFT calculations. _____	83
Table II-1. Summary of divalent chromium and alkali/alkali earth-transition metal (II)-phosphates _____	86
Table II-2. alkali earth-transition metal(II)-phosphate-compounds with similar structural formula to $\text{Sr}_2\text{Cr}(\text{PO}_4)_2$ _____	109
Table II-3. $J$ values from DFT+U calculations, Cr-Cr distances and Cr-O-O-Cr torsion angles. _____	115
Table II-4. $\text{Sr}_2\text{Cr}^{\text{II}}(\text{PO}_4)_2$ . Assignment of optical spectra. _____	123
Table A I-1. Data collection and refinement details. ....	129
Table A I-2. Interatomic distances ( $\text{\AA}$ ). ....	130
Table A I-3. Atomic coordinates and isotropic displacement parameters.....	131
Table A I-4. Data collection and refinement details for $\text{Ba}(\text{PO}_4)_2\text{Fe}_{0.22}\text{W}_{3.78}\text{O}_9$ ( $m = 4$ ). ....	132
Table A I-5. Interatomic distances ( $\text{\AA}$ ) for $\text{Ba}(\text{PO}_4)_2\text{Fe}_{0.22}\text{W}_{3.78}\text{O}_9$ ( $m = 4$ ). ....	133
Table A I-6. Data collection and refinement details for $A(\text{PO}_4)_2(\text{WO}_2)_2$ ( $A = \text{Ba}, \text{Pb}$ ). ....	133
Table A I-7. Interatomic distances ( $\text{\AA}$ ) for $A(\text{PO}_4)_2(\text{WO}_2)_2$ ( $A = \text{Ba}, \text{Pb}$ ). ....	134
Table A I-8. Atomic coordinates and isotropic displacement parameters Interatomic distances ( $\text{\AA}$ ) for $A(\text{PO}_4)_2(\text{WO}_2)_2$ ( $A = \text{Ba}, \text{Pb}$ ). ....	134
Table A I-9. Fit functions coefficients for $C_p$ and Seebeck measurements. ....	136
Table A II-1. Data collection and refinement details for $\text{BaCrP}_2\text{O}_7$ . ....	137
Table A II-2. $\text{BaCrP}_2\text{O}_7$ atomic coordinates and isotropic displacement parameters ( $P-1, Z = 2, a = 5.359(2)\text{\AA}, b = 7.259(3)\text{\AA}, c = 7.568(3)\text{\AA}, \alpha = 103.156(13)^\circ, \beta = 90.004(14)^\circ, \gamma = 93.527(14)^\circ$ ) ....	138
Table A II-3. ADP harmonic parameters $U_{ij}$ ( $\text{\AA}^2$ ) for $\text{BaCrP}_2\text{O}_7$ . ....	138
Table A II-4. Selected interatomic distances ( $\text{\AA}$ ), bond valences and valence sums for $\text{BaCrP}_2\text{O}_7$ . ....	139
Table A II-5. Data collection and refinement details for $\text{Sr}_2\text{Cr}(\text{PO}_4)_2$ . ....	140
Table A II-6. Atomic coordinates and isotropic displacement parameters ( $Pbca, Z = 4, a = 10.7064(18), b = 9.2730(14)\text{\AA}, c = 21.272(3)\text{\AA}$ ). ....	141
Table A II-7. $\text{Sr}_2\text{Cr}(\text{PO}_4)_2$ . Selected interatomic distances ( $\text{\AA}$ ), bond valences and valence sums.....	142
Table A II-8. ADP harmonic parameters $U_{ij}$ ( $\text{\AA}^2$ ) for $\text{Sr}_2\text{Cr}(\text{PO}_4)_2$ . ....	143
Table A II-9. Energy value for different configuration from DFT+U calculations.....	144

<i>Table A II-10. Magnetic Space Group (MSG) description of the commensurate magnetic structure of Sr<sub>2</sub>Cr(PO<sub>4</sub>)<sub>2</sub> at 5K.</i> .....	145
<i>Table A II-11. Magnetic Space Group (MSG) description of the commensurate magnetic structure of Sr<sub>2</sub>Cr(PO<sub>4</sub>)<sub>2</sub> at 1.5K.</i> .....	146
<i>Table A II-12. Chromophores and observed transition energies as well as AOM parameters derived thereof for Sr<sub>2</sub>Cr<sup>II</sup>(PO<sub>4</sub>)<sub>2</sub>, SrCr<sup>II</sup>P<sub>2</sub>O<sub>7</sub>, SrCr<sup>II</sup>Si<sub>4</sub>O<sub>10</sub>, and α-Ba<sub>2</sub>Cr<sup>II</sup>(PO<sub>4</sub>)<sub>2</sub>.</i> .....	149

## General introduction

The ultimate goals of materials research and solid-state chemistry are synthesis and characterization of new solid substances. These quests are driven on one hand by the desire of the synthetic chemist to provide -by ingenious experiments- access to solids that do not form in nature. Obviously, such research serves the purpose to extend the chemists toolbox of synthesis techniques. Furthermore, new compounds can be expected to show properties which were previously unknown. The desire for characterization (measurement), understanding and, eventually, technical exploitation of these properties creates the second driving force for solid state research. Establishing the arrangement of the atoms in a solid (crystal structure determination) is frequently the prerequisite and therefore first step for further studies. These might comprise measurement of colour, magnetic behaviour and transport properties (like thermal and electric conductivity). Elucidating the relations between chemical composition, crystal structure and both chemical and physical properties of a solid ("structure-property-relationship") not only allows validation of our theoretical understanding of electronic structure and chemical bonding in solids but also helps in optimizing these properties for technical applications. The latter cover a huge range of compounds and properties relevant for development of new materials for energy conversion (e.g. solar cells, thermoelectric materials, battery electrodes, and fuel cell) [1–3], information storage (e.g. magnetic storage media, and phase-change memory materials) [4], building and construction materials (e. g. high-performance concrete, insulation materials, and smart glass) [5,6], catalyst materials (e. g. zeolites, supported metal catalysts, perovskite catalysts and nanoparticle catalysts) [7].

Historically the quest for new solids was based on known chemical principles and past discoveries. It started frequently from the investigation of naturally occurring minerals, which allowed to predict and synthesize new materials. Once a new compound is discovered, the focus shifts to a detailed characterization of its structure to determine the accurate arrangement of atoms within the material and to understand its properties. This research is intrinsically linked to understanding how elements, their valence states, and their organization within a crystalline structure give rise to unique properties. This knowledge eventually is used to establish predictive models based on the relationships between the structures and

properties and of course rely on the relative energies (stabilities) of the systems in competition. The aim is to lay the foundations for a better understanding of how new materials can be designed with specific properties for potential applications in technology, industry and various scientific fields [8]. All these aspects are now fully included in the automated search for new compounds, based on various “AI” algorithms [9].

The research in this PhD thesis is focused on phosphates of specific transition metals. First, dealing with the choice for phosphate oxo-anions, one can state that it is a common “building unit” of inorganic solid materials, intensively studied at the University of Bonn and at the UCCS/Lille. Indeed, it is at the origin of the collaboration between these two labs, and of this PhD thesis. Chemically, solid phosphates possess numerous applications that can be classified into two main categories. Solid phosphates can either be traditional products of low added value but high tonnage, such as fertilizers, detergents, flame retardants, and phosphates utilized in nutrition and pharmaceutical industries, or they can be materials with high added value and low tonnage that are still under development at various stages of industrial/technical applications. The second group includes applications in optics (phosphors, lasers, frequency doublers), electronics (dielectrics), electrochemistry and energy storage (LiFePO<sub>4</sub> as a cathode material, cobalt phosphate "CoP<sub>i</sub>" as a water oxidation catalyst), catalysis (zeolites, (VO)<sub>2</sub>P<sub>2</sub>O<sub>7</sub> for selective oxidation of short chain hydrocarbons), biomaterials, and storage of radioactive or heavy elements. This thesis concentrates on the second category establishing the academic/scientific foundations for such applications.

Dealing with d-block elements, we have selected the 6<sup>th</sup>-block transition metals (Cr, Mo, W) that are known to cover a wide range of oxidation numbers from +II to +VI in anhydrous solid phosphates (Cr<sup>2,3+</sup>, Mo<sup>3,4,5,6+</sup>, W<sup>4,5,6+</sup>). Phosphate anions are particularly suited to stabilize transition metals in low oxidation states through their inductive effect on M → O → P bonds. Related to this effect is also the peculiar stability of phosphate anions towards any kind of redox reaction on one hand and the strong oxide acceptor behaviour of P<sub>2</sub>O<sub>5</sub> on the other. Frequently, in anhydrous phosphates the coexistence of mixed oxidation states of a given transition metal is observed (e.g. Ti<sup>3+,4+</sup>[10], V<sup>3+,4+</sup> [11], Cr<sup>2+,3+</sup>[12], W<sup>5+,6+</sup>[13]). The stabilization of mixed-valency, which is still a quite exotic valence behaviour, is the basis for electronic properties of solids ranging from localized (“ionic”) to fully delocalized (“metallic”). By using a combination of [PO<sub>4</sub>]<sup>3-</sup> or [P<sub>2</sub>O<sub>7</sub>]<sup>4-</sup> oxo-anions and large cations (e.g. Ba<sup>2+</sup>, K<sup>+</sup>, Rb<sup>+</sup>, Cs<sup>+</sup>...), a

variety of compounds can be formed which show low-dimensional structural features and, consequently, physical properties.

Chapter I of this thesis reports on exploration of the quasi-ternary system BaO/WO<sub>x</sub>/P<sub>2</sub>O<sub>5</sub> and the discovery of a new series of compounds falling within the phosphate tungsten bronzes (PTB), a family of mixed-valent tungsten V/VI phosphates. The new compounds exhibit low-D metal character, like the classic PTB, but in addition several exotic properties which are quite distinct from the “parent” family. For this newly identified series of compounds the name layered monophosphate tungsten bronze (L-MPTB) was chosen to emphasize its enhanced two-dimensional (2D) nature compared to other MPTB’s further considered as quasi-2D, or at least more “3D”. The new series obeys the general formula [Ba(PO<sub>4</sub>)<sub>2</sub>]<sub>m</sub>W<sub>m</sub>O<sub>3m-3</sub>, with 2 ≤ m ≤ 5. A detailed study of this family will be the focus of the sections I.1 of chapter I. In an attempt to achieve mixed-metal substitution in this new L-MPTB family, similar to what has been accomplished for mm-MPTBs, W<sup>V</sup> was substituted with (M<sup>IV</sup><sub>1/2</sub>W<sup>VI</sup><sub>1/2</sub>), (M<sup>III</sup><sub>1/3</sub>W<sup>VI</sup><sub>2/3</sub>), or (M<sup>II</sup><sub>1/4</sub>W<sup>VI</sup><sub>3/4</sub>) pairs [14,15]. For the L-MPTB series, the attempt of substitution of W<sup>V</sup> by (Ni<sup>II</sup><sub>1/4</sub>W<sup>VI</sup><sub>3/4</sub>) led to the discovery of the new “fully-oxidized” tungsten phosphates A(PO<sub>4</sub>)<sub>2</sub>(W<sup>VI</sup>O<sub>2</sub>)<sub>2</sub> (A = Ba, Sr, Pb). Surprisingly, their crystal structures show a different symmetry compared to their molybdenum-analogues A(MoO<sub>2</sub>)<sub>2</sub>(PO<sub>4</sub>)<sub>2</sub> (A = Ba, Pb, (Li,K)) [16]. However, they share similar tunnel-like structures. To understand these structural differences, various calculations have been conducted using evolutionary crystallographic algorithms with USPEX, alongside phonon calculations, to comprehend the dynamic or thermodynamic driving forces behind their existence. This first “endeavour” into predictive chemistry, in closed relation with artificial intelligence (AI) and exploitation of “big data” (as contained in crystallographic databases), led to the identification of the important thermodynamic and dynamical features, interacting in these crystal structures and dictating the stability of the various polymorphs. This will be the focus of the following sections I.2 in chapter I.

As for Chapter II, it will be dedicated to the study of Cr<sup>2+</sup> phosphates. The understanding of the chromium(II) compound is still limited, leaving much to explore. Therefore, choosing phosphates, which are good at stabilizing Cr<sup>2+</sup> thanks to their inductive effect is a natural choice. In fact, the solid monoxide “Cr<sup>II</sup>O” has not yet been observed experimentally due to its instability with respect to disproportionation to Cr<sub>2</sub>O<sub>3</sub> and elemental chromium [17]. Anhydrous chromium(II) oxo-compounds (phosphates, silicates, borates) on the other hand

reveal unique properties such as metal-metal bonding and strong interactions between lattice dynamics, magnetic effects, and electronic instability due to the Jahn-Teller effect [18]. Additionally, the strongly covalent nature of the  $[\text{PO}_4]^{3-}$  polyanion, along with its geometry and high charge, offers unique opportunities for tailoring low-dimensional (Low-D) crystal structures when paired with large ionic-covalent cations (e.g.  $\text{Ba}^{2+}$ ,  $\text{K}^+$ ,  $\text{Rb}^+$ ,  $\text{Cs}^+$ ). However, among all chromium(II) oxo-compounds synthesized and crystallographically characterized up to now only for  $\alpha\text{-Cr}_2\text{P}_2\text{O}_7$  the magnetic behaviour is fully understood [19]. This part of the thesis builds in particular upon the work of E. Hammer [20], who discovered and studied several  $\text{Cr}^{2+}$  compounds. The aim to understand these peculiarities by studying structural dynamics and magnetic ordering of selected compounds ( $\text{Cr}_3(\text{PO}_4)_2$ ,  $\text{Sr}_2\text{Cr}(\text{PO}_4)_2$ ,  $\text{BaCrP}_2\text{O}_7$ ) will be the scope of chapter II.

## I. Prospection for novel barium tungsten-phosphates

### I.1. Steady antipolar 2D-Metallicity in the new L-MPTB, $\text{Ba}(\text{PO}_4)_2\text{W}^{5+,6+}_m\text{O}_{3m-3}$

#### I.1.1. Introduction

Chronologically, the first tungsten bronzes,  $\text{A}_x\text{WO}_3$  (A: Na, K;  $0 < x < 1$ ), were discovered by Wöhler in 1825. The term "bronze" was chosen for these compounds due to their metallic lustre, reminiscent of the Cu-Sn alloys with the same name [21]. Their structures range from  $\text{ReO}_3$ -related to a distorted perovskite, achieved by the insertion of A-cations into the cuboctahedra cavities, resulting in mixed valency tungsten (V, VI). Subsequently, the term "bronze" has been used to encompass a broad range of ternary oxides with the general formula  $\text{A}_x\text{M}_y\text{O}_z$ , where A is mostly a monovalent (often alkali) cation or other elements (e.g. Ge, Sb, In, Pr...) [22]. This compound exhibits various distinctive characteristics, including high electrical conductivity (either metallic or semi-conducting), vibrant colour with a metallic lustre in its crystalline form, chemical inertness and displays various crystal structures as x varies [22]. The family as a whole is highly versatile, with variations in composition and structure leading to significant changes in physico-chemical properties and colours. Notably, certain compounds, such as  $\text{Rb}_{0.33}\text{WO}_3$  display metallic conductivity and even superconductivity at low temperatures ( $T_c \approx 5.5$  K) [23].

An unsuccessful attempt to synthesize  $\text{Rb}_x\text{WO}_3$  in 1978 led to the discovery by Raveau and co-workers of the phosphate bronze family, where phosphorus appeared as an impurity from the silica ampoule [13,24]. The new compound  $\text{Rb}_{0.8}\text{P}_4\text{W}_{16}\text{O}_{56}$  [25], identified as the first Diphosphate tungsten bronze (DPTB), was discovered. This family follows the general formula  $\text{A}_x(\text{P}_2\text{O}_4)_2(\text{WO}_3)_{2m}$ . In 1981, the same research group discovered the first Monophosphate Tungsten Bronze (MPTB)  $\text{P}_4\text{W}_8\text{O}_{32}$  [26] with the general formula  $\text{A}_x(\text{WO}_3)_{2m}(\text{PO}_2)_4$ , (A = Na, K, Pb...), where x can be equal to 0 [13].

The interest for the monophosphate tungsten bronze (MPTB) family intensified following the pioneering study by Greenblatt and co-workers in 1989. Their investigation, focussing on the quasi-2D metal monophosphate tungsten bronze  $\text{P}_4\text{W}_{12}\text{O}_{44}$  ( $m = 6$ ), provided evidence of electronic instabilities associated with the "Charge Density Wave (CDW)" state at low temperatures [8]. This property is shared with the molybdenum bronze family, first discovered in  $\text{A}_{0.33}\text{MoO}_3$ , known as the "blue bronze" [28]. In the 1990s, the concept of Fermi Surface

"hidden nesting" emerged, explaining the occurrence of the charge density wave (CDW) state in these low-dimensional (low-D) metallic compounds [29]. Currently, MPTBs are the subject of extensive investigation, with some members exhibiting successive CDW transitions [13], and others showing superconductivity at low temperatures [30].

During the work of this thesis, we discovered a new series of compounds falling within the phosphate bronze (PTB) family. Specifically they are related to the monophosphate tungsten bronzes (MPTB). This new series of compounds exhibits exotic properties distinct to its "parent" family. The newly identified series of compounds were named layered monophosphate tungsten bronzes (L-MPTB) to emphasize its enhanced two-dimensional (2D) nature compared to other MPTB's further considered as quasi 2D, or at least more "3D". The new series obeys the general formula  $[\text{Ba}(\text{PO}_4)_2]_m\text{W}_m\text{O}_{3m-3}$ , with  $2 \leq m \leq 5$ . This discovery of genuine 2-D MPTB-related compounds created renewed interest offering rich perspectives and new paradigms, with respect to their 3D counterpart. Here we present the structural and electronic properties of our original series of L-MPTB family, meeting such 2D-criteria. They are discussed under the scope of their sizeable structural perspectives, transport and thermodynamic properties and preliminary electronic structures, in strong echo with the quasi 2D-bronzes.

Before discussing this family, it's beneficial to first introduce the phosphate tungsten bronze (PTBs), specifically focusing on the monophosphate tungsten bronzes (MPTBs) to which our new compounds are related. Secondly, it's essential to briefly introduce the concept of CDW states inherent to such low-dimension metals.

### 1.1.2. Structural description of the parent the phosphate tungsten bronzes (PTBs) and charge density wave (CDW) phenomenon

The information in this section is primarily based on the review authored by P. Roussel et al. [13]. Also the PhD thesis of E. Duverger-Nédellec [31], the PhD thesis of A. Minelli [32] as well as insights from the book physics and chemistry of low-dimensional inorganic conductors [30]. All were valuable sources of information.

#### 1.1.2.1 Structural description of the parent phosphate tungsten bronzes (PTBs)

**The monophosphate tungsten bronzes (MPTB)** comprise of two distinct subfamilies: monophosphate tungsten bronzes with **pentagonal** tunnels (MPTBp), characterized by the



tetrahedra, forming monolayers within the crystallographic *ab* plane. In  $\text{MPTB}_p$ , at the interface between two  $\text{ReO}_3$ -type layers,  $\text{WO}_6$  octahedra and  $\text{PO}_4$  tetrahedra again share vertices but in these cases creating a pentagonal tunnel. Conversely, in  $\text{MPTB}_h$ , these octahedra and tetrahedra form hexagonal tunnels, accommodating A cations.

The two forms of MPTB differ in the way how they connect two slabs through the chain of  $\text{WO}_6$  octahedra sharing corners with the  $\text{PO}_4$  tetrahedra along the [110] perovskite axis:

- In  $\text{MPTB}_p$ , the blocks are linked by rotation around 2-fold axes. This gives them characteristic zigzag patterns, see Figure I-1.
- In the  $\text{MPTB}_h$ , the blocks are linked to each other by translation, leading to stripe-like patterns, see Figure I-1.

The index  $m$  defines the specific member and indicates the number of  $\text{WO}_6$  octahedra along the longest chain connected at the ends by adjacent  $\text{PO}_4$  tetrahedra. Note that for that the even-numbered terms of  $\text{MPTB}_p$  have orthorhombic symmetry, while the odd-numbered terms are monoclinic. As for the  $\text{MPTB}_h$ , the basic arrangement is monoclinic, as founded for five members out of seven, the last two being triclinic ( $m = 7$ :  $\text{Pb}_{0.66}\text{P}_4\text{W}_{14}\text{O}_{50}$  and  $\text{Na}_{1.7}\text{P}_4\text{W}_{14}\text{O}_{50}$ ).

The  $\text{MPTB}_p$  exhibit a framework structure similar to  $\gamma\text{-Mo}_4\text{O}_{11}$  [33,34], this latter particularly resembling the  $m = 4$  member. This molybdenum (V, VI) molybdate is formed by the stacking of layers built of  $\text{MoO}_6$  octahedra and  $\text{MoO}_4$  tetrahedra, with the latter replacing the  $\text{PO}_4$  tetrahedra in the MPTBs.

**The diphosphate tungsten bronzes (DPTB)** represent the second sub-family of the phosphate bronzes (PTB). Chronologically they were discovered first, as mentioned in the introduction. Unlike monophosphate tungsten bronzes (MPTBs), DPTBs have received relatively little attention in terms of both physical properties and structural investigations. Similar to MPTB, DPTB can be further divided into two sub-families: diphosphate tungsten bronze with pentagonal tunnels ( $\text{DPTB}_p$ ) and hexagonal tunnels ( $\text{DPTB}_h$ ).  $\text{DPTB}_h$  are more commonly encountered and easily synthesized, while  $\text{DPTB}_p$  have never been successfully synthesized as a pure phase.  $\text{DPTB}_h$  obey the chemical formula  $\text{A}_x(\text{P}_2\text{O}_4)_2(\text{WO}_3)_{2m}$ , where  $4 \leq m \leq 10$ , and A = K, Rb, Ba, and Tl, occupying the hexagonal tunnels. The fundamental building blocks of the

crystal structure remain largely consistent with the MPTBs. The  $\text{ReO}_3$ -type slabs exhibit variable thickness along the (102) perovskite axes, depending on their  $m$  index. These slabs are connected by  $\text{P}_2\text{O}_7$  groups.  $\text{P}_2\text{O}_7$  groups in conjunction with  $\text{WO}_6$  octahedra form hexagonal tunnels. These compounds frequently crystallize in monoclinic space groups, with the lattice parameter  $b \approx 7.5 \text{ \AA}$  preserved across the whole series. While  $a$  is dependent on the thickness of  $\text{ReO}_3$ -type slabs in the even  $m$ ,  $b$ ,  $c$ , and  $\beta$  remain almost constant. Dealing with the  $\text{DPTB}_p$ , mainly HRTEM images [35] provided structural information. This fourth family could crystallize with orthorhombic symmetry showing  $\text{ReO}_3$ -type domains of varying thickness separated from each other by  $\text{P}_2\text{O}_7$  groups (see Figure I-1).

Structural relationships between  $\text{WO}_3$ ,  $\text{ReO}_3$ -type, perovskite and various family of phosphate tungsten bronzes (PTBs) are summarized in Figure I-1.

#### *1.1.2.2 Charge density waves (CDW) and low-dimensional metals*

The layered crystal structures of MPTBs, comprising of conducting  $\text{ReO}_3$ -type layers with mixed-valence composition  $[\text{W}^{\text{V,VI}}\text{O}_3]_{2m}^{4+}$  and variable thickness, and their separation by the insulating  $\text{PO}_4$  tetrahedral units, determine their two-dimensional properties. In reality, this family exhibits only quasi-2D metallic behaviour, wherein the resistivity along the  $c$  direction (= across the  $\text{PO}_4$  “pseudo-layers”, see Figure I-1) was measured approximately one order of magnitude higher than in other crystallographic directions. As quasi-2D inorganic metals, the MPTBs display highly anomalous conducting properties that tend to stabilize charge density waves (CDW) or a superconducting ground state, as in the case of the  $\text{P}_4\text{W}_{14}\text{O}_{50}$  ( $m = 7$ ) [30]. This behaviour was also observed, for instance, in layered metal dichalcogenides (TMLD), Mo bronzes like the purple bronzes  $\text{AMo}_6\text{O}_{17}$  ( $A = \text{Na}$  or  $\text{K}$ ),  $\text{Mo}_4\text{O}_{11}$  [30], and almost all of the compounds of the layered cuprate family. The observation of CDW state above  $T_c$  rises questions about the role of the CDW in high  $T_c$  superconductors [36]. Experimentally, proof for such CDW-phenomena and the associated electronic transitions are given by diffuse X-ray scattering experiments, as well as by large anomalies in transport phenomena, heat capacity and/or seebeck measurements. Among the transport measurements, DC resistivity on single crystals is the most frequently reported method for almost all  $\text{MPTB}_p$  members [31]. In the literature, MPTBs are described as a “textbook” model for studying the impact of the thickness of the conducting layers (the ' $m$ ' parameter) on properties, while maintaining a constant

electron count, in agreement with the general formula  $(\text{PO}_2)_4(\text{WO}_3)_{2m}$ , which correspond to  $(\text{PO}_2)_4\text{W}^{d1}_2\text{W}^{d0}_{2m-2}\text{O}_{6m}$  ( $\text{W}^{d1} = \text{W}^{5+}$ ,  $\text{W}^{d0} = \text{W}^{6+}$ ) within the Brillouin zone.

Charge density waves are observed in many compounds, especially in low-dimensional metals that they tend to stabilize. The original model was first predicted in the 1930s by R. Peierls, who concluded that CDWs would exist in an ideal one-dimensional (1D) chain. While charge-density waves also occur in materials with two- or three-dimensional band structures, they are predominantly a one-dimensional phenomenon. The first discovery of the charge density wave (CDW) phenomenon in related-bronzes is assigned to W. Frogle and J.H. Perlstien in 1972 in  $\text{K}_{0.3}\text{MoO}_3$ , also known as the blue molybdenum bronze [37]. The theoretical description of CDW was first proposed by W.L. McMillan for quasi-2D layered metal dichalcogenides (TMLD) [38]. CDWs have been extensively studied during the 1980's. Here also, the coexistence of various density waves ( $C_{\text{charge DW}}$  and/or  $S_{\text{spin DW}}$ ) in certain materials, such as  $\text{NbSe}_2$ , and their relationship with superconductivity [39], has raised several questions. In the case of high- $T_c$  superconducting cuprates, this point remains not fully explained till today.

**Peierls transition and CDW.** A crystal is composed of a repeating pattern of atoms in space. In a metal, the atoms can be described as an assembly of ions with fixed positions, surrounded by valence electrons weakly bound to the nucleus, which can spread throughout the entire crystal (following the free electron gas model). In a perfect metal, the electron density distribution, noted as  $\rho_0(r)$ , is considered to share the same symmetry as the crystal structure [31].

Considering, a one-dimensional metal with electron states filled up to the Fermi level ( $E_F$ ) and the periodic lattice parameter ' $a$ ' (see Figure I-2). The presence of electron-phonon interaction leads to a sinusoidal modulation of the electron density with a period longer than the one of the crystal lattices. Modulating the electron density will alter the potential perceived by the atoms in the chain, causing them to be shifted to new equilibrium positions with the same periodicity (as shown in Figure I-2). This establishes long-period order, with most often incommensurate modulations towards the original crystal lattice [31].

The modulation of the electronic density and the distortion of the crystal lattice are interdependent and occur concurrently. This results in the opening of an energy gap in the

electronic states dispersion spectrum at the Fermi level. Consequently and ideally, the gap divides the  $E_F$  energy band into a full conduction band and an empty valence band, thereby altering the material's behaviour, shifting it towards a metal-semiconductor or metal-insulator transition (see Figure I-2). This transition occurs at sufficiently low temperatures, robust to thermal excitation, which would cancel the gain in the kinetic energy. It is such that the gain in electronic energy becomes greater than the elastic cost induced by the lattice deformation. In comparison to weak electron-phonon coupling, strong coupling is characterized by larger anionic displacements and energy gaps, with the CDW being generally commensurate relative to the lattice.

Speaking for weak electron-phonon coupling, the CDW state formation is primarily influenced by electronic entropy. In contrast, strong electron-phonon coupling, is driven by lattice entropy. In the former, the CDW state completely disappears above the transition temperature, while in the latter, short-range order is maintained which vanishes eventually at higher temperatures, restoring a non-distorted state. It is suggested that an order-disorder type transition may underlie the CDW formation [40].

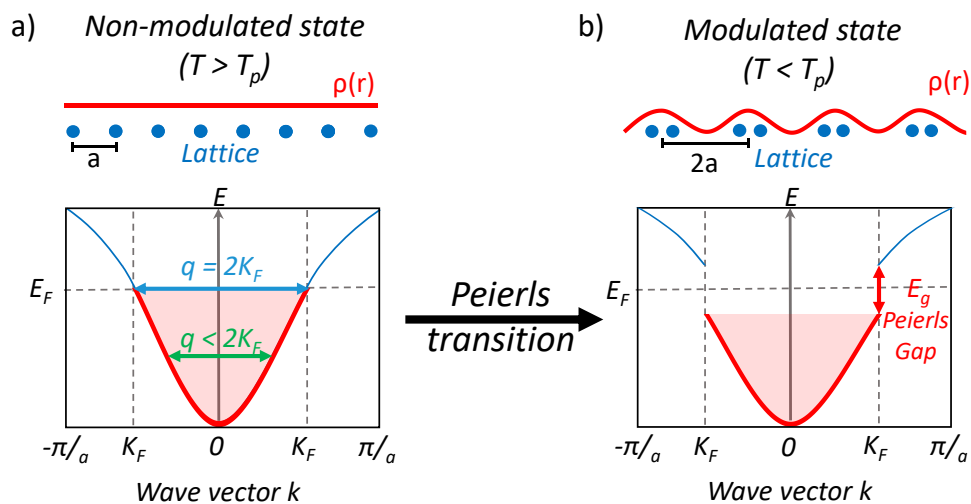


Figure I-2. Illustration of a 1D atomic chain (in blue) and its electron density (in red), along with the electronic spectrum of a 1D electron-dimensional metal in two distinct states: a) the non-modulated normal state, and b) the modulated state, also known as the Charge Density Wave state. Figure based on [41].

**Fermi Surface (FS) and CDW.** The search for an understanding of the mechanism of CDW formation in the low-dimensional systems related to the W-bronze series has led to the

concept of fermi surface nesting and its key role in the Peierls-like transition towards CDW states at low temperatures.

The Fermi surface can be described, in a perfectly 3D metal, as the envelope/surface of the filled electronic states sphere in a crystal momentum space, also called the K space (see Figure I-3). Electrons occupy energy states from the lowest to the highest to minimize total energy, following Pauli's exclusion principle. The lowest energy state is at the centre of the sphere, known as the "zero momentum" state. Occupied states are distributed around the "zero momentum" state, and the volume of the sphere represents the occupied states for a given k. The highest energy level, called the Fermi level, lies on the surface of this sphere, forming the "Fermi surface" (FS).

The search for an understanding of the mechanism of Charge Density Wave (CDW) formation in low-D bronzes has led to the concept of Fermi surface nesting and its pivotal role in the formation of CDWs at low temperatures. Here the FS is no longer a sphere, but ideally consist of sheet and cylindrical surfaces, 1D and 2D topologies respectively (refer to Figure I-3). This means that knowledge of the shape of the Fermi surface, and of the energy dispersion in its immediate vicinity, are of paramount importance in order to understand the properties of a metal.

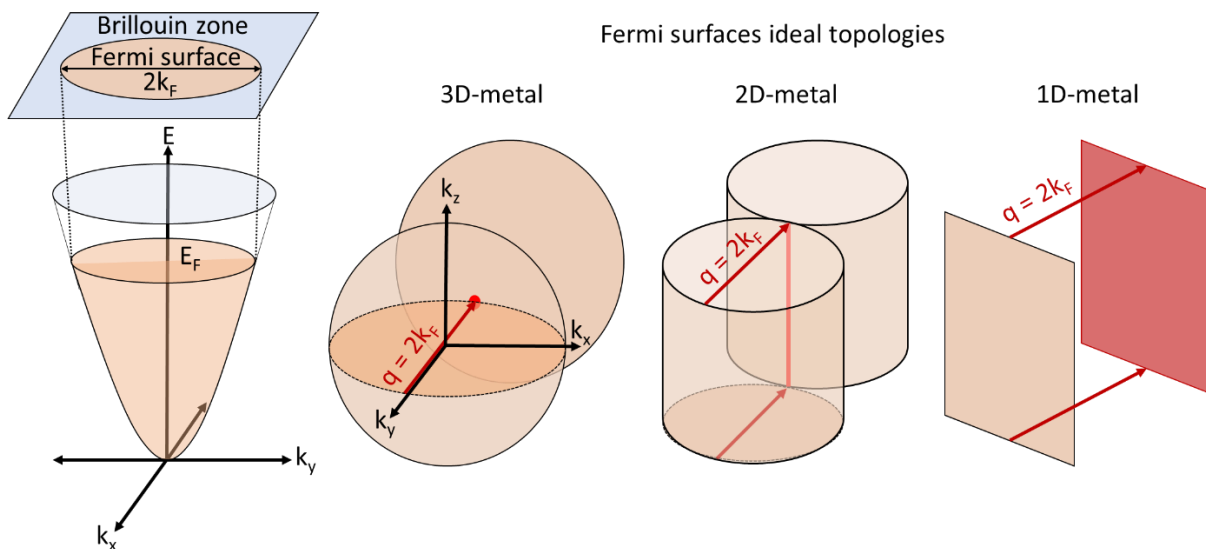


Figure I-3. Topologies of Fermi surfaces in momentum space and Fermi surface nesting for ideal 3D, 2D, and 1D materials. The regions highlighted in red represent areas prone to nesting. Figure based on [31].

At the Charge Density Wave (CDW) state, an energy gap opens for all zones of the Fermi surface that can be nested at the wavevector  $k_F = \pm 2\pi/a$  (refer to Figure I-3) by a single nesting

vector of  $q = 2k_F$ . Fermi surface nesting implies the possibility of superposing one part of it onto another part through translation by the  $q$ -vector, included in the low-dimension of the system. This has the advantage of lowering the energy of electrons near the Fermi level ( $E_F$ ). However, this is not the case for a wavevector connecting two states deep in the Fermi sea, as opening a gap will increase the energy of electrons above the gap by an amount equal to the decrease in energy of electrons below the gap.

**Hidden nesting.** In the 1D case, perfect nesting is achieved since the entire Fermi surface, consisting of parallel sheets, can be linked by translation with a single nesting vector of  $q = 2k_F$ . These nested areas of the Fermi surface are destroyed in favour of the gap opening, resulting in a metal  $\rightarrow$  insulator transition. For a quasi-1D system (i.e., chains coupled to each other), these nested areas are reduced to finite  $q$  nesting vectors.

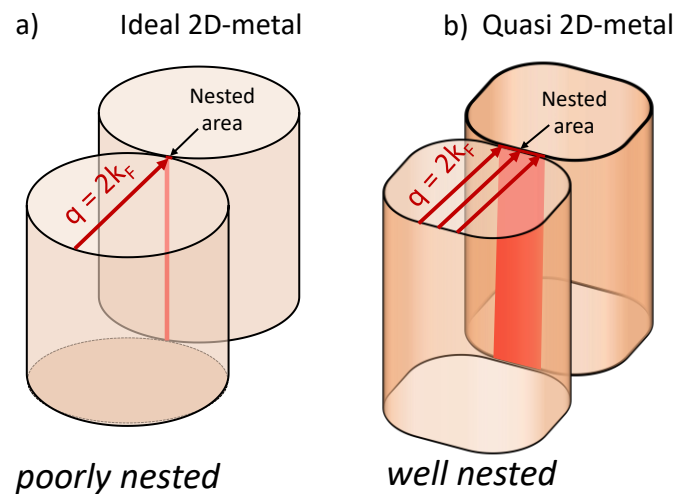


Figure I-4. Fermi surfaces topologies of a) the ideal 2D metal Fermi surface and b) the quasi-2D metal and their nesting vectors. Figure based on [32].

In a perfect 2D and 3D systems the Fermi surface allows nesting only on one line for 2D system and on a single point in 3D one, which leads to poor nesting (see Figure I-3). However, in reality its 2D and 3D systems, the Fermi surface is not perfectly cylindrical and spherical, and is subject to deformation following the crystal symmetry. The quasi 2D-system can then be described as a cylinder with undulations that contains larger parallel flat areas that will allow partial nesting (see Figure I-4). these areas are not perfectly parallel which lead to a residual pocket of electrons and holes that provides free charge carriers at CDW transition. This explains why these materials do not become insulating but still display a metallic character.

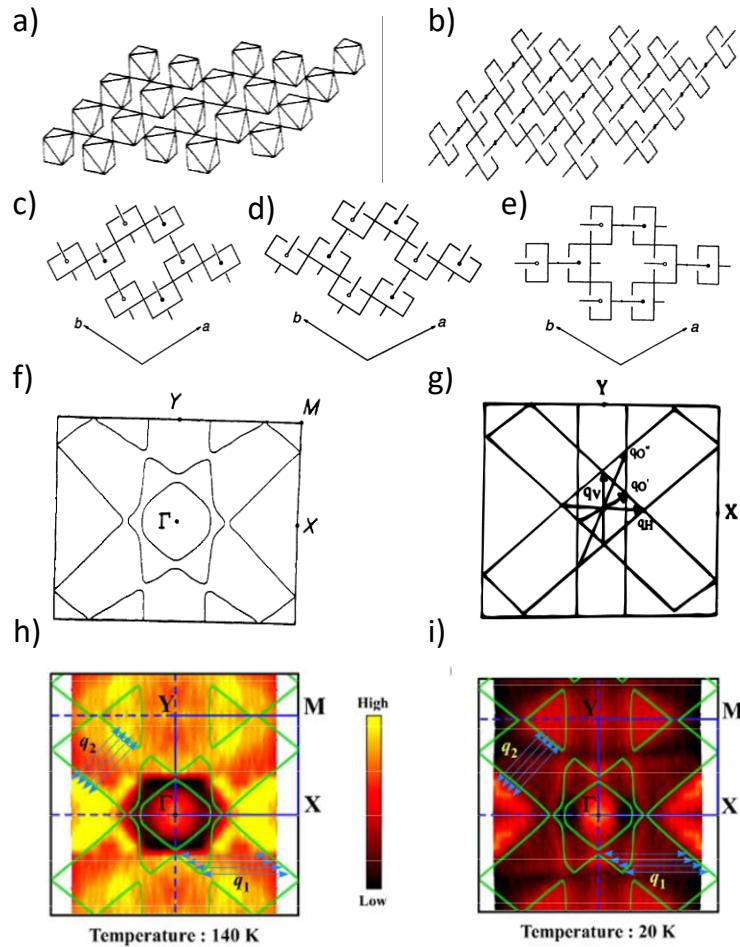


Figure I-5. a) A 3D projection of the purple the quasi 2D conductor molybdenum bronze  $\text{ReO}_3$ -type layer, b) a sketch of the  $t_{2g}$ -block bands of the  $\text{Mo}_4\text{O}_{18}$  displaying a pseudo-1D electrical properties with zig-zag  $\text{Mo}_2\text{O}_{10}$  chains running along c) a, d) b and e) (a + b) directions [29,42]. f-g) Combined Fermi Surface representation for the  $\text{K}_{0.9}\text{Mo}_6\text{O}_{17}$  and its decomposition into three sets of differently oriented 1D Fermi Surfaces. Nesting is achieved through nesting vectors. The ARPES spectral intensity at the Fermi level displayed on the two-dimensional wave vector at h) 140 K and i) 20 K, where these temperatures are situated above and below the transition temperatures,  $T_{c1}$  and  $T_{c2}$  [43]. Permission for reproduction was granted by EPL editorial office.

These pockets of carriers will then be nested together according to a nesting vector  $q$ , accordingly to an "hidden nesting" mechanism. This concept was developed by M. -H. Whangbo et E. Canadell in more detail the forming mechanism of CDW in the quasi 2D system like for the MPTBs and purple molybdenum bronze [29,44]. The quasi-2D  $\text{K}_{0.9}\text{Mo}_6\text{O}_{17}$  exhibits a Fermi surface shaped by "hidden nesting," a concept introduced by E. Canadell and M. -H. Whangbo [29,44]. This involves three sets of quasi-1D nested surfaces forming parallel lines (see Figure I-5a, b), which better explain the experimental CDW nesting vectors than a simple 2D-FS [29,44]. Specific directions within the vertex-shared  $\text{MoO}_6$  octahedra layers display significant  $d-t_{2g}$  orbital overlap, forming weakly coupled conductive zigzag chains in the ab

plane along the a, b, and (a + b) directions, sharing "axial" oxygen atoms (see Figure I-5 c, d, e). The electronic structure includes intrachain  $t_{2g}-\pi-t_{2g}$  and interchain  $t_{2g}-t_{2g}$   $\delta$  overlaps, enabling quasi-1D conductivity (see Figure I-5 c, d, e) [29,42]. This led to a Fermi surface (FS) is built from a superposition of 3 sets of nested quasi-1D surfaces which form parallel lines (Figure I-5f, g). This is what is called the 'hidden' Fermi surface nesting and the correlated Charge Density Wave (CDW) instability. This concept was later experimentally validated through Angle-Resolved Photoemission Spectroscopy (ARPES) measurements, enabling the direct observation of the Fermi Surface topology (See Figure I-5h, i) [43,45]. The identified nesting vectors align with the modulation vectors determined via X-ray diffraction.

### *1.1.2.3 Evidence of CDW transitions in MPTBp through physical measurements*

**Resistivity measurements.** The MPTBp exhibit highly anisotropic conductivity, with significantly higher conductivity along the two directions with percolative connectivity of  $WO_6$  octahedra, compared to directions crossing the insulating  $PO_4$  layers. In this latter, the conductivity was measured one order of magnitude lower (for instance see Figure I-7c). So, they are generally considered as pseudo-2D metals. Hereafter we show how measurements on single crystals or polycrystalline samples systematically evidence CDW-like transitions with drastic effects. By anticipation, these results are fundamental to emphasize the steady metallic states measured in our new series.

In the MPTBs, the Peierls transition, inducing the opening of a gap within nested Fermi surfaces, induces alterations in the number of charge carriers within the conduction band. This alteration manifests as an anomaly in the temperature dependence of transport and phonon-based properties. It is evidenced in parameters like resistivity and Seebeck versus temperature, while the structural transition also manifests by discrepancies in the heat capacity. This anomaly is marked by a metal  $\rightarrow$  metal or metal  $\rightarrow$  semiconductor transition. Simultaneously, a shift in the slope of magnetic susceptibility may occur at the transition temperature, aligning with changes in the systems charge carrier mobility and a reduction in the density of states at the Fermi level. Among the PTBs, the sub-family of MPTB<sub>p</sub> with  $(PO_2)_4(WO_3)_{2m}$  ( $2 \leq m \leq 12$ ) are the most studied and virtually all the members in this family have been measured for resistivity.

$W^{5+}PO_5$  the member at  $m = 2$  is distinct by different in comparison to the rest of the family. Its crystal structure displays single chains of corner-sharing  $WO_6$  octahedra separated by  $PO_4$  tetrahedra (see Figure I-6), suggesting quasi-1D behaviour (see Figure I-7a). It was first reported to be semi-conductor [46], but more recent studies suggest bad metallic conductivity [31]. However, in this particular compound, the CDW transition being observed at 290 K by resistivity measurement, is not really highlighted in the 400-2K range (see Figure I-7b) investigated by the authors [31].

For  $m$  values ranging from 4 to 6, a resistive anomaly at the “Peierls” transition is observed, characterized by increased resistivity at TP followed by a return to the metallic state. These terms demonstrate a metal  $\rightarrow$  metal transition (see Figure I-7c-e).

However, from  $m = 7, 8,$  and  $9,$  following the monotone decrease of carrier concentration the reported data display distinctly different resistivity behaviour differing from one another [47] and being quite different from those of  $m = 4, 5,$  and  $6$  [48], [49]. Notably,  $m = 7,$  aside from two transitions with a wide hysteresis in the second transition, revealed a superconducting state at very low temperatures [50]. For the  $MPTB_p$  at higher  $m$  limited or preliminary observations of the transition have been feasible due to the high temperatures required for measurement [31].

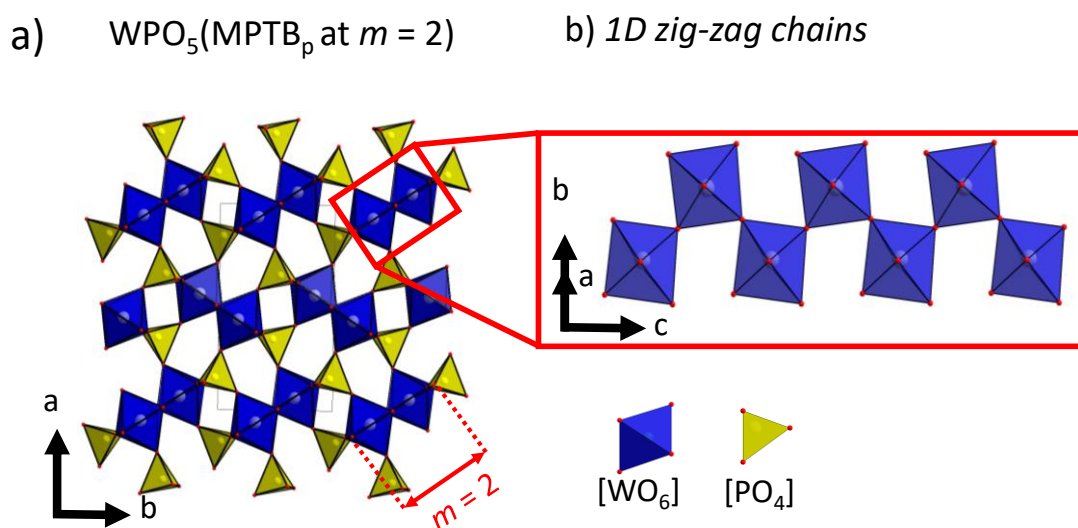


Figure I-6. a) Projection on  $[001]$  of the crystal structure for  $WPO_5$  ( $MPTB_p$  at  $m = 2$ ) and b) Highlights the presence of one-dimensional chains running along the  $c$ -axis, as illustrated by the red box [46].

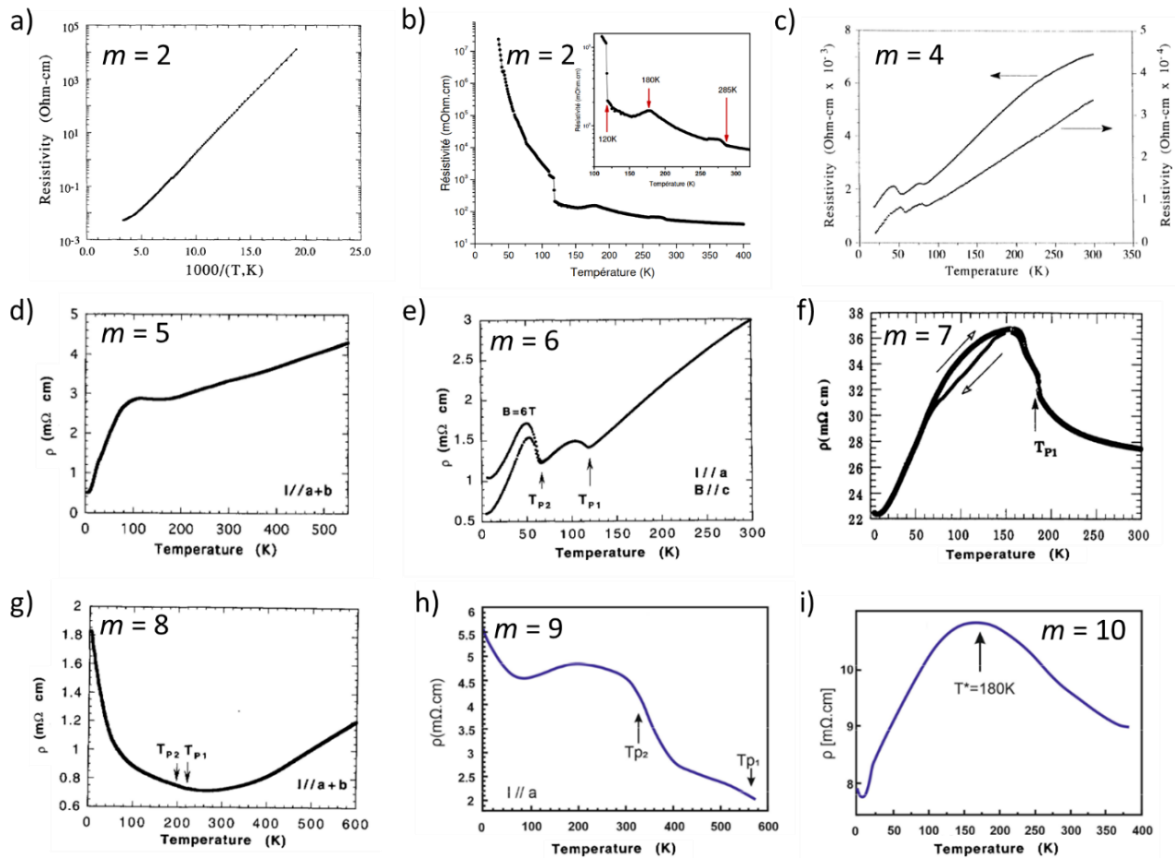


Figure I-7. MPTBp resistivity measurements of a)  $m = 2$  [46], b) remeasured  $m = 2$  [31], c)  $m = 4$  [51], d)  $m = 5$  [48], e)  $m = 6$  [48], f)  $m = 7$  [52] g)  $m = 8$  [47], h)  $m = 9$  [47], [31], i)  $m = 10$  [31,53].

Overall, it has been observed that as  $m$  increases, the compounds turn to poorer metallic conductors on the basis of their absolute conductivity values. This is in line with the decrease of the carrier concentration (i.e. electrons per tungsten count) as  $m$  increases.

**Thermoelectric power measurements of  $(\text{PO}_2)_4(\text{WO}_3)_{2m}$  ( $m = 5, 6, 7$ ).** The transition to the CDW state also affects the thermopower as expressed by the Seebeck coefficient  $S$ , providing information about the nature of the charge carriers. In Figure I-8, three examples are illustrated. For  $m = 5$ , two transitions manifest distinctly as peaks in the curve. These peaks correspond to the CDW gap openings and indicate a change in the sign of the dominant carriers at each transition. Although  $S$  remains negative, the change in slope below  $T_{p1}$  suggests a prevalence of hole pockets at this temperature, followed by the dominance of electron pockets below  $T_{p2}$  (see Figure I-8a). Regarding  $m = 6$ , below  $T_{p2}$ , the Seebeck coefficient  $S$  shows a clear p-type behaviour along the  $a$ -axis and n-type along  $b$ . This implies that the CDW pockets induced by the  $T_p$  transition are mainly electrons along  $b$  and holes along  $a$ . The p-type behaviour along  $a$  suggests that it is driven by carriers remaining from the

Fermi sheet corresponding to the lower band (first Brillouin zone), exhibiting a negative curvature along this direction (Figure I-8b). Subsequently, below  $T_{p2}$ , the  $T_{EP}$  indicates the emergence of hole-type pockets due to this second gap opening. For  $m = 8$ , the anomaly observed in resistivity  $\rho(T)$  curve is also evident in the Seebeck measurement, both associated with the CDW state transition. In conclusion, both the resistivity and the Seebeck measurements offer strong evidence for the occurrence of CDW phenomena.

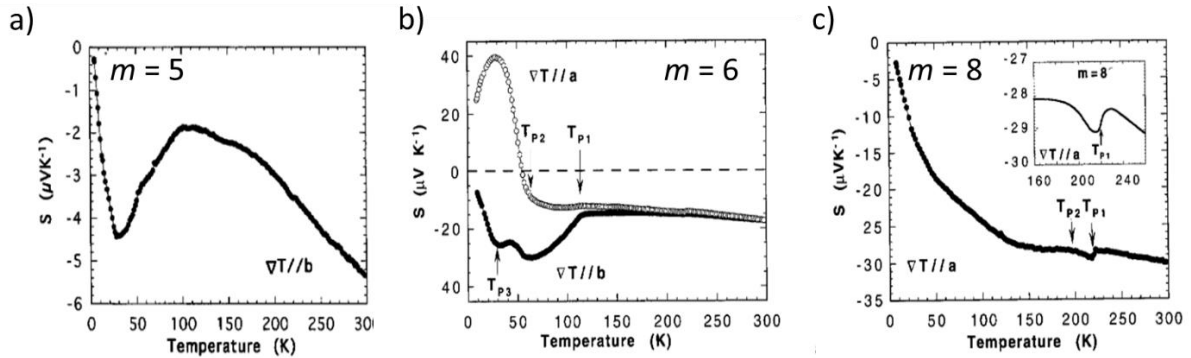


Figure I-8. MPTBp thermoelectric power vs. temperature for a)  $m = 5$ , with a thermal gradient applied along the  $b$ -axis [48] b)  $m = 6$ , with the upper curve is a thermal gradient along the  $a$ -axis and the lower one along the  $b$ -axis [54], c)  $m = 8$ , with thermal gradient along the  $a$ -axis [47]. Permission for reproduction was granted.

**Heat capacity measurements.** Only few reports of the heat capacity of MPTBs across the CDWs are available. Chung et al. [55] looked at the heat capacity of the MPTBs  $P_4W_8O_{32}$  ( $m = 4$ ) and  $P_4W_{12}O_{44}$  ( $m = 6$ ), as shown in Figure I-9. While no significant changes were revealed during the CDW transitions for  $m = 4$  (see Figure I-9a), significant anomalies were measured during the upper CDW transition of  $P_4W_{12}O_{44}$  ( $m = 6$ ), as seen in Figure I-9b. Another study on the specific heat of  $K_xP_4W_8O_{32}$  ( $0.75 < x < 2$ ), an MPTB<sub>h</sub>, identified thermal changes at the CDW transition temperature and concluded that these changes are primarily caused by the structural transition that systematically occurs alongside these transitions [56].

A particular signature characterizing compounds with a charge density wave states (CDW) is the presence of a bump in the plot of  $C_p/T^3$  against  $T$ , known as the Boson peak (BP). This bump has been observed in several compounds exhibiting a CDW state, such as  $TaS_3$ ,  $(TaSe_4)_2I$  and  $K_{0.3}MoO_3$  [57]. For example, in the quasi-2D conductor  $KMo_6O_{17}$ , this bump was seen between 4 and 48 K, with a centre around 12.5 to 15 K (see Figure I-9d). This bump seems to be linked to phason excitations, which add to the total specific heat. Phasons, like phonons, involve atomic motion but are specifically associated with atomic rearrangements. This bump

occurs due to disorder. In CDW compounds, particularly in incommensurate systems, the lack of translational symmetry results in slight disorder in the lattice position. In such cases, phasons represent fluctuations in the periodic modulation of the charge density waves. This specific feature will be discussed in the frame of my work.

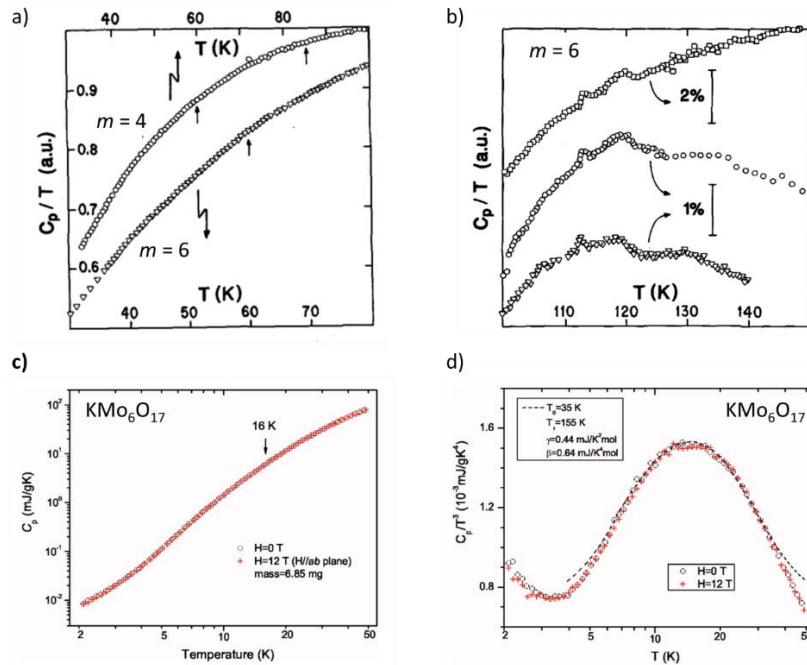


Figure I-9. a) Specific heat measurements for  $m = 4$  and  $m = 6$  MPTBp crystals, where small vertical arrows indicate the localization of CDW transition temperatures [55], b) Specific heat measurements of three  $m = 6$  MPTBp crystals. c) specific heat measurement of  $KMo_6O_{17}$  for  $H = 0$  (black circle) and 12 T (red cross) where the small arrow indicate the temperature of the CDW transition [58], d) Plot of  $C_p/T^3$  vs.  $T$  for  $H = 0$  T (black circle) and  $H = 12$  T (red cross), with the dashed line indicating the fit using the modified Debye model [58]. Permission for reproduction was granted.

### I.1.3. Experimental

#### I.1.3.1 Materials and methods

**XRD.** Routine X-ray powder diffraction (XRPD) for sample purity verification was performed on a Bruker D8 Advance diffractometer with a Bragg-Brentano geometry using monochromated  $CuK\alpha$  radiation in the range  $2\theta = (5-80)^\circ$  with  $0.02^\circ$  steps and 0.5 seconds per step.

Synchrotron powder X-ray diffraction (SPXRD) was performed at the Alba-synchrotron source (MSPD diffractometer) with  $\lambda = 0.41 \text{ \AA}$ , at RT for  $m = 3$  to 5 and between 110 and 440 K for  $m = 4$ . The temperature-dependent tracking of diffractograms of  $m = 2$  from 19 to 299K was carried out on the Rigaku SmartLabXE using monochromated  $CuK\alpha_1$  radiation in the range  $2\theta = (5-90)^\circ$  with  $0.02^\circ$  steps and  $10^\circ$  per minute.

Single crystal X-ray diffraction (SCXRD) was performed on a Bruker diffractometer, as detailed in Table A 0-1. After reduction of the data using SAINT [59], the crystal structures were solved using the charge flipping method (Superflip) [60] and refined with Jana 2006 [61].

**NPD.** Neutron Powder Diffraction (NPD) was performed on the D20 diffractometer ( $\lambda = 1.540 \text{ \AA}$ ) at the Institute Laue-Langevin (Grenoble, France) for  $m = 4$  at 200, 260 and 300 K. For  $m = 2$ , neutron powder diffraction data were collected at 293K using the high-resolution D2B diffractometer at the Institute Laue-Langevin. The incident wavelength was  $\lambda = 1.594 \text{ \AA}$  with a Ge(335) monochromator, covering an angular range of  $0^\circ < 2\theta < 155^\circ$ . A 2 g loose powder sample was placed in a vanadium sample can.

**TGA.** Thermogravimetric analysis (TGA) were carried out on a thermoanalyser TGA-DSC3+ Mettler Toledo device under air using a ramp of  $5^\circ\text{C}/\text{min}$  from room temperature up to  $850^\circ\text{C}$  on a grinded polycrystalline sample of  $\text{Ba}(\text{PO}_4)_2\text{W}_2\text{O}_3$  ( $m = 2$ ).

**HAADF (High-angle annular dark-field imaging).** The powder was crushed and dropped in the form of alcohol suspension on carbon supported copper grids followed by evaporation under ambient condition. TEM measurements were conducted on the TEM FEI TITAN Themis 300. It is equipped with a probe corrector for resolution of  $0.7\text{\AA}$  in STEM mode.

**Resistivity** was measured between 400 and 1.8K using a Physical Properties Measurement System (PPMS) from Quantum Design, with the 4-point probes method on a dense parallelepiped pellet.

**The Seebeck coefficient (S) and heat capacity** were measured on a Physical Properties Measurement System (PPMS) from Quantum Design using a dense pellet.

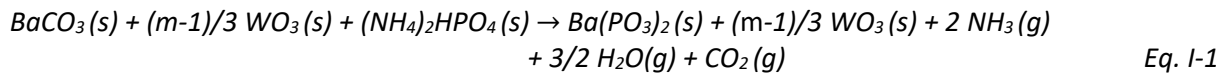
**The density functional calculations (DFT)** were carried out in collaboration with Andres Cano from the NÉEL Institute (Grenoble). DFT calculations were performed with the Quantum ESPRESSO package [62] using the norm-conserving pseudopotentials from the Pseudo Dojo library [63]. We used the Perdew-Burke-Ernzerhof form of the generalized gradient approximation [64]. We considered the crystal structures determined experimentally. However, for the  $m = 4$  member of the series, we simplified the actual structure by assuming no doubling of the unit cell along the  $c$  axis and shifting the atomic positions accordingly. The calculations were converged with a Monkhorst-Pack mesh of  $10 \times 10 \times 10$   $k$ -points and a 100 Ry cut-off for the wavefunctions with a 0.01 Ry smearing. A denser  $30 \times 30 \times 30$   $k$ -mesh was

used to compute the density of states. The  $k$ -points in the band plots are labelled according to reference [65].

### ***1.1.3.2 Synthesis of the L-MPTBs $Ba(PO_4)_2W_mO_{3m-3}$ at $2 \leq m \leq 5$***

The strategy behind the synthesis was to grow blocks of  $WO_3$  with  $ReO_3$ -like structure in between thick  $[Ba(PO_4)_2]^{4-}$  spacer layers. These latter are known to be excellent separators and confine quasi 2D magnetic properties in structural layers as for instance in the  $BaM_2(XO_4)_2$  series ( $X = P, V, As$ ) [66], which includes the Ising 2D-ferromagnetic  $BaFe_2(PO_4)_2$  phase discovered and studied earlier in the UCCS laboratory [67]. Polycrystalline samples of the new series  $Ba(PO_4)_2W_mO_{3m-3}$  with  $m = 2$  to  $m = 5$  were prepared by a solid state route in two steps. The synthesis includes thermal decomposition of the Barium and phosphate precursors with liberation of volatile reaction products and eventually reduction of  $W^{6+}$  to  $W^{5+}$ . Therefore, a multistep synthesis was developed for the preparation.

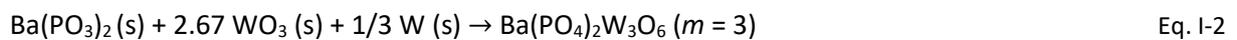
**First step:** For the reactions described subsequently, stoichiometric mixtures 2:1:( $m-1$ )/3 of  $(NH_4)_2HPO_4$  (ACROS organics,  $\geq 99\%$ ),  $BaCO_3$  (Alfa Aesar,  $\geq 99\%$ ) and  $WO_3$  (Fulka Analytical, 99.9%) were milled in an agate mortar, placed in corundum crucibles and heated in air at 873 K for 12h. This process aimed to decompose and eliminate the volatile species ( $CO_2$ ,  $H_2O$ ,  $NH_3$ ) according to the following equation:

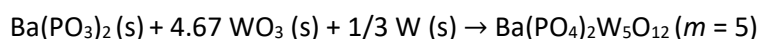


X-ray diffraction (XRD) analyses were conducted, revealing the formation of  $Ba(PO_3)_2$  alongside with  $WO_3$  as intermediates.

#### **Second step:**

**Stoichiometric cases for  $Ba(PO_4)_2W_mO_{3m-3}$  at  $3 \leq m \leq 5$ .** These were all obtained following a stoichiometric mixture of resultant products from the preliminary step with a suitable amount of metallic tungsten ( $1/3 W$  per formula unit) according to the following case-by-case equations:





Eq. I-4

The mixtures were pelletized and placed in silica tubes sealed under vacuum and heated at 1273K for 2 days. It should be noted that the sealed tube must be placed in an area where the temperature is homogeneous and there is no temperature gradient. Otherwise,  $\text{WO}_{3-x}$  could be easily transported, resulting in a depletion of tungsten detrimental to the desired stoichiometry. Thus, we successfully synthesized single phase compounds at  $m = 3$  and 4 (See Figure I-11b and c). The  $m = 5$  member presents 10.1 w% of  $\text{Ba}(\text{P}_2\text{O}_4)_2(\text{WO}_3)_{16}$  (the  $m = 8$  DTPB<sub>h</sub> member) (See Figure I-11d). These two phases have a similar Ba/P ratio and close W valence ( $\text{W}^{5.6+}$  for the  $m = 8$  DTPB<sub>h</sub> and  $\text{W}^{5.60+}$  for the  $m = 5$  L-MPTB), which may explain the co-formation of this by-phase. Neutron powder diffraction (NPD) which was carried out on the phase at  $m = 4$ , which will be discussed later, validates its stoichiometric oxygen content (see Figure I-19b). Images of pellets of the L-MPTB are shown in Figure I-11e, where we can see that there is a difference in colour which is following the change of main tungsten valence.

**Oxygen sub-stoichiometry for  $\text{Ba}(\text{PO}_4)_2\text{W}_2\text{O}_3 (m = 2)$ .** The synthesis of the new  $m = 2$  member of the L-MPTB series was achieved by adapting the solid-state reaction procedure described in the stoichiometric case. This procedure consists of two steps. First,  $\text{BaCO}_3$ ,  $(\text{NH}_4)_2\text{HPO}_4$  and  $\text{WO}_3$  were reacted in the ratio 1:1:( $m-1/3$ ) at 873 K in air. This reaction product is then reduced at 1273 K by freshly reduced W metal (1/3). However, this well-established reaction route with stoichiometric ratio of the reactants failed to yield the targeted  $m = 2$  compound, resulting in various mixtures in which the  $m = 3$  member of the L-MPTB series was predominant instead. This problem was overcome by producing in two-step reaction the targeted  $\text{Ba}(\text{PO}_4)_2\text{W}_2\text{O}_{3-x}$  phase with a number of oxygen vacancies ( $0.1 \leq x \leq 0.2$ ). This procedure allows the preparation of single-phase material, which is in particular free of other L-MPTB phases with higher  $m$  (see Figure I-11a).

Considering our specific synthesis method, we checked that the refinement of the single free O(1) site (*i.e.* not part of a  $\text{PO}_4$  group) occupancy converged to 1.00(4), although our polycrystalline sample may have some degree of oxygen deficiency. The Rietveld refinement of a polycrystalline sample using NPD data collected at room temperature (Institut Laue Langevin, D2b diffractometer,  $\lambda = 1.59\text{\AA}$ ,  $R_{\text{Bragg}} = 3.28\%$ ) is shown on the Figure I-10. After several tests, only the refinement of the O(1) site occupancy at the centre of the perovskite

slabs, led to a slight deviation from the ideal stoichiometry leading to the composition  $\text{Ba}(\text{PO}_4)_2\text{W}_2\text{O}_{2.92(5)}$  formula.

Also, the stability of the fully stoichiometric phase was confirmed by single crystal XRD from grown crystal at the external surface of a pellet.

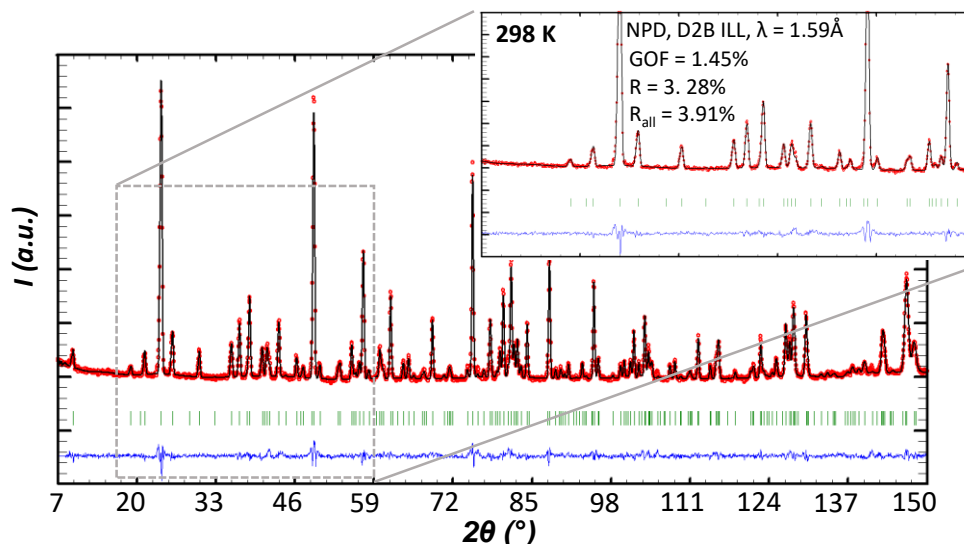
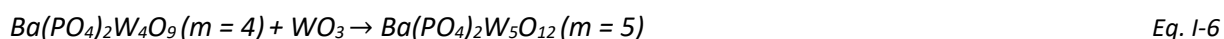
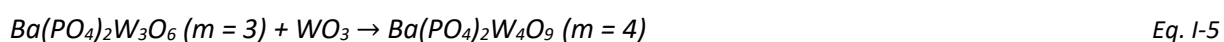


Figure I-10. Experimental (red), calculated (black) and difference patterns after Rietveld refinement of NPD data for  $\text{Ba}(\text{PO}_4)_2\text{W}_2\text{O}_{2.92(5)}$ .

**Alternative synthesis route for  $\text{Ba}(\text{PO}_4)_2\text{W}_m\text{O}_{3m-3}$  at  $2 \leq m \leq 5$ .** It was also possible to obtain the L-MPTB at  $m = 5$  starting from  $m = 4$  or  $m = 3$  compounds respectively, with extra  $\text{WO}_3$ , as described in the following reaction equations:



**Crystal growth attempts.** For all compounds, at some point, we used small single crystals (100  $\mu\text{m}$  max dimension) for crystal structure determination or verification. These were manually extracted from the surface of the as-prepared pellets. Nevertheless, several attempts were made to obtain sufficiently large crystals, primarily for physical measurements, for instance for measurement of their anisotropic transport properties. For this purpose, a chemical vapor transport (CVT) experiment was conducted by placing a pellet composed of a mixture of  $m = 5$  and  $m = 4$  into a sealed tube positioned in the targeted zone, in the presence of  $\text{NH}_4\text{Cl}$  (5 mg). A temperature gradient was applied, as described in Figure I-12, for 12 days. This procedure resulted in the formation of crystals of  $\text{W}_{18}\text{O}_{49}$  [68] and  $\text{W}_3\text{PO}_{11}$  at the ampoules

sink end leaving  $m = 4$  at the source. The low solubility of barium in the gas phase makes crystal growth of the L-MPTB phases by CVT impossible. Therefore, a crystallization attempt was made by isothermal heating of  $m = 3$  at 1000 °C for 31 days, leading to crystals growing on the surface of the pellet with some crystals that reached a max. dimension of  $l \approx 200 \mu\text{m}$  (see Figure I-13a-b). However, the crystal size remained too small to allow physical measurements on them; hence, alternative methods need to be explored.

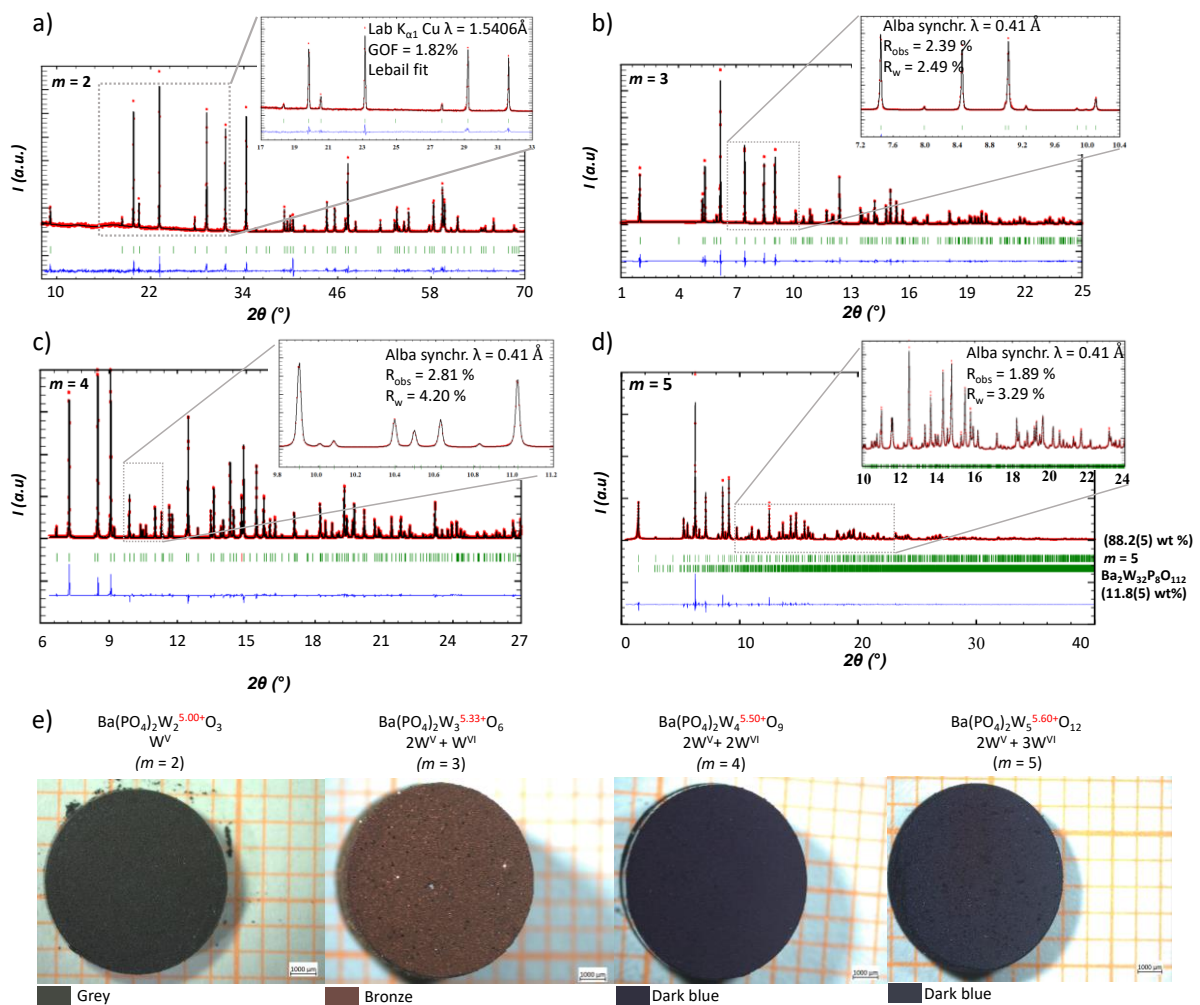


Figure I-11. a) Profile matching on lab Xray data for  $m = 2$ . Rietveld refinement on synchrotron powder diffraction data for a)  $m = 3$  b)  $m = 4$  c)  $m = 5$  d) Rietveld refinement on neutron powder diffraction data for  $m = 4$ . e) image of the pellets obtained for different L-MPTB member.

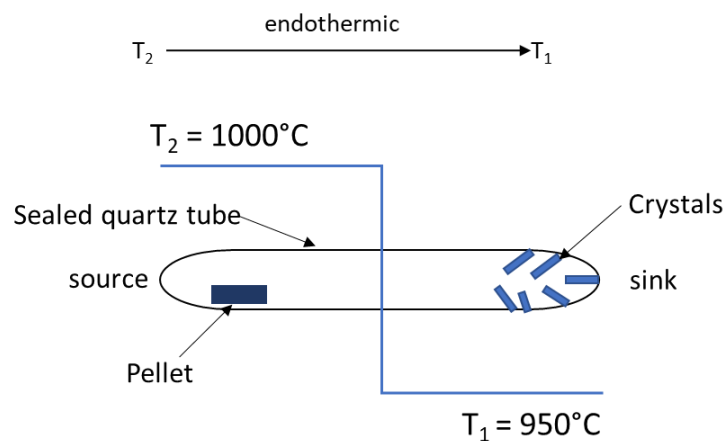


Figure I-12. Sketch illustrating the CVT method for crystal growth attempts [69].

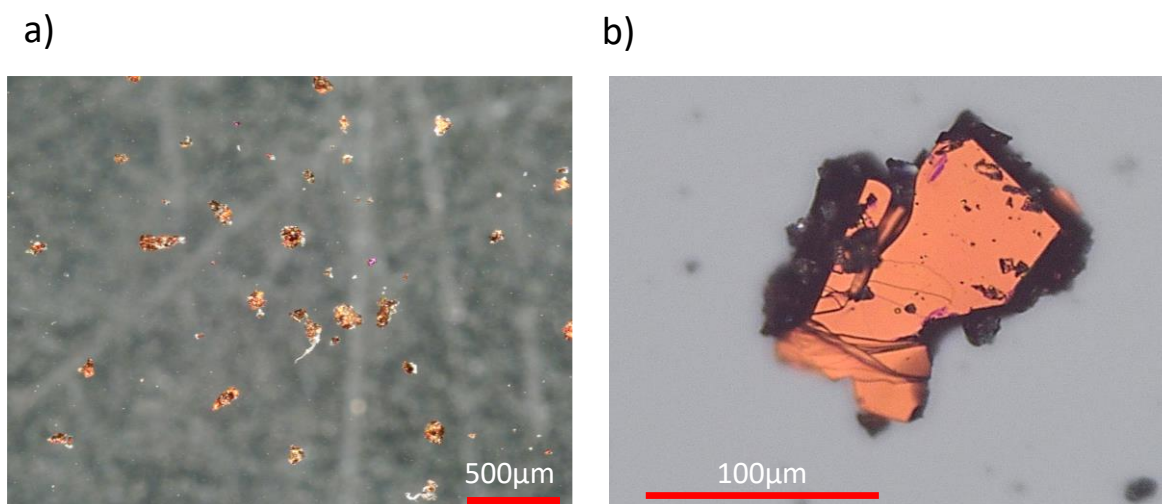


Figure I-13. a) The obtained  $\text{Ba}(\text{PO}_4)_2\text{W}_3\text{O}_6$  ( $m = 3$ ) crystals characterized by a bronze color. b) a zoom-in showcasing a prominent crystal.

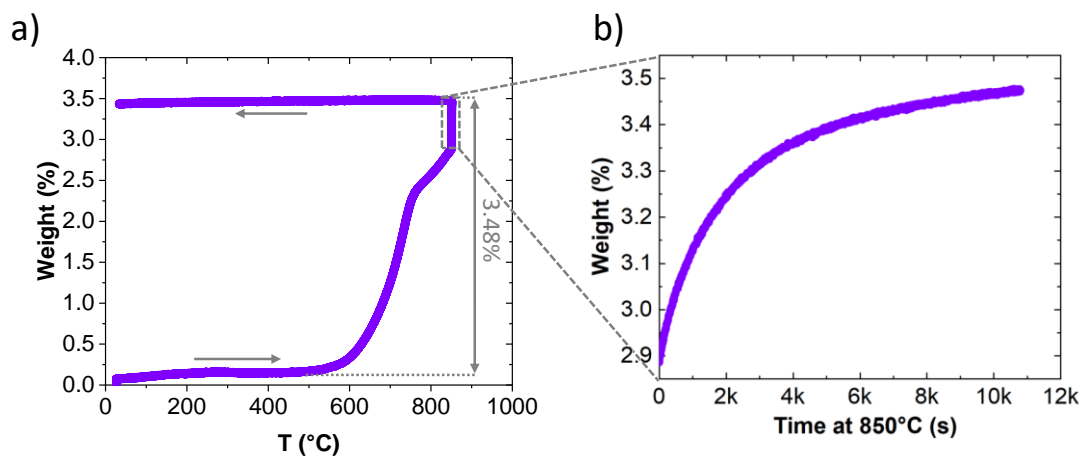


Figure I-14. a) TGA analysis of  $\text{Ba}(\text{PO}_4)_2\text{W}_2\text{O}_3$  ( $m = 2$ ) under  $\text{O}_2$  with a ramp of  $5^\circ\text{C}/\text{min}$  till  $850^\circ\text{C}$  then a plateau of 3h was applied with a heating and cooling cycle. b) Evolution of the mass gain as a function of time at the plateau temperature of  $850^\circ\text{C}$ .

**Stability.** The obtained compounds are stable in air. The XRPD analysis of powder samples, two and a half year after their syntheses did not show any changes.

Furthermore, heating  $m = 2$  up to 1200°C for a day in a sealed tube showed stability with no decomposition. The TGA conducted on  $m = 2$  under air showed an oxidation above 500°C (mass gain) with an accelerated reaction above 850°C (see Figure I-14a, b).

### ***1.1.3.3 Attempts to prepare missing members of the series $\text{Ba}(\text{PO}_4)_2\text{W}_m\text{O}_{3m-3}$***

**“ $\text{BaW}(\text{PO}_4)_2$  ( $m = 1$ )”.** To extend our series we attempted to synthesize “ $\text{BaW}^{4+}(\text{PO}_4)_2$  ( $m = 1$ )”. Stability of this compound is suggested by the existence of structural analogues such as  $\text{CsTa}(\text{PO}_4)_2$  [70] and  $\beta\text{-BaZr}(\text{PO}_4)_2$  (high-temperature phase) [71]. This structural analogy will be discussed later (see section 1.1.4.1). Additionally,  $\text{BaMo}(\text{PO}_4)_2$  corresponding to the  $\alpha\text{-BaZr}(\text{PO}_4)_2$  structural type also exists [72]. Owing to their similar crystal chemistry and very close ionic radii ( $\text{W}^{\text{IV}} = 0.66\text{\AA}$ ,  $\text{Mo}^{\text{IV}} = 0.65\text{\AA}$  [73]), the existence of the  $m = 1$  member appeared highly likely. Yet, all attempts following a stoichiometric reaction pathway failed. Instead, they led to the formation of nearly pure  $m = 2$  instead of the targeted  $m = 1$ , with weak reflections belonging to an unidentified phase. Interestingly, it was through this approach that the existence of  $m = 2$  was discovered.

Synthesizing “ $\text{Ba}(\text{PO}_4)_2\text{W}$ ” with a lower oxidation state ( $\text{W}^{(4-x)+}$ ) similar to the  $m = 2$  case while maintaining the ideal cationic stoichiometry is unfeasible since all the oxygen are part of the phosphate groups for  $m = 1$ . Tests tuning the reaction temperature were conducted. At 800°C, a multitude of unidentified reflections was observed in the XRPD. At 900°C, the  $m = 2$  is formed up and it remained stable up to 1200°C.

**“ $\text{Ba}(\text{PO}_4)_2\text{W}_6\text{O}_{15}$ ” ( $m = 6$ ) and “ $\text{Ba}(\text{PO}_4)_2\text{W}_7\text{O}_{18}$ ” ( $m = 7$ )”.** Due to time constraints, only two synthetic routes were pursued. The first followed the same two-step synthetic pathway employed previously. The initial step involved the reaction of  $\text{WO}_3$  with  $(\text{NH}_4)_2\text{HPO}_4$  and  $\text{Ba}(\text{CO}_3)_2$  to remove volatile species (at 600°C for 2 days), followed by adding the stoichiometric amount of W. The precursor and W were ground, pelletized, and placed under vacuum in a sealed tube, heated at 900°C and 1000°C for 2 days each. For  $m = 6$  at both temperatures mixtures of the L-MPTB at  $m = 3$  and  $\text{Ba}(\text{P}_2\text{O}_4)_2(\text{WO}_3)_{16}$  were obtained as products. For  $m = 7$ , a mixture of  $m = 4$  and  $\text{Ba}(\text{P}_2\text{O}_4)_2(\text{WO}_3)_{16}$  (the DTPB<sub>h</sub> at  $m = 8$ ) was obtained. Another method was attempted by starting from  $m = 3$  and reacting it with the

stoichiometric proportion of  $\text{WO}_3$ , assuming that starting from an L-MPTB structure, it would have less tendency to form the impurity  $\text{Ba}(\text{P}_2\text{O}_4)_2(\text{WO}_3)_{16}$ , thereby accessing higher terms. This later way was also led to the same result obtained previously.

#### I.1.4. Structure determination and description of the layered monoposphate tungsten bronze (L-MPTB)

##### I.1.4.1 Structural overview and structural analogues to the L-MPTB series

The figure below illustrates a summary of the crystalline structure of the various members of the L-MPTB series. This structure family is characterized by layered arrangements, featuring  $[\text{ReO}_3]$ -type slabs of varying thickness ( $m$  octahedra thick) determined by the number of  $\text{WO}_6$  octahedra comprising each layer. They are separated by the  $[\text{Ba}(\text{PO}_4)_2]^{4-}$  spacers sharing common  $\text{PO}_4$  corners (see Figure I-15).

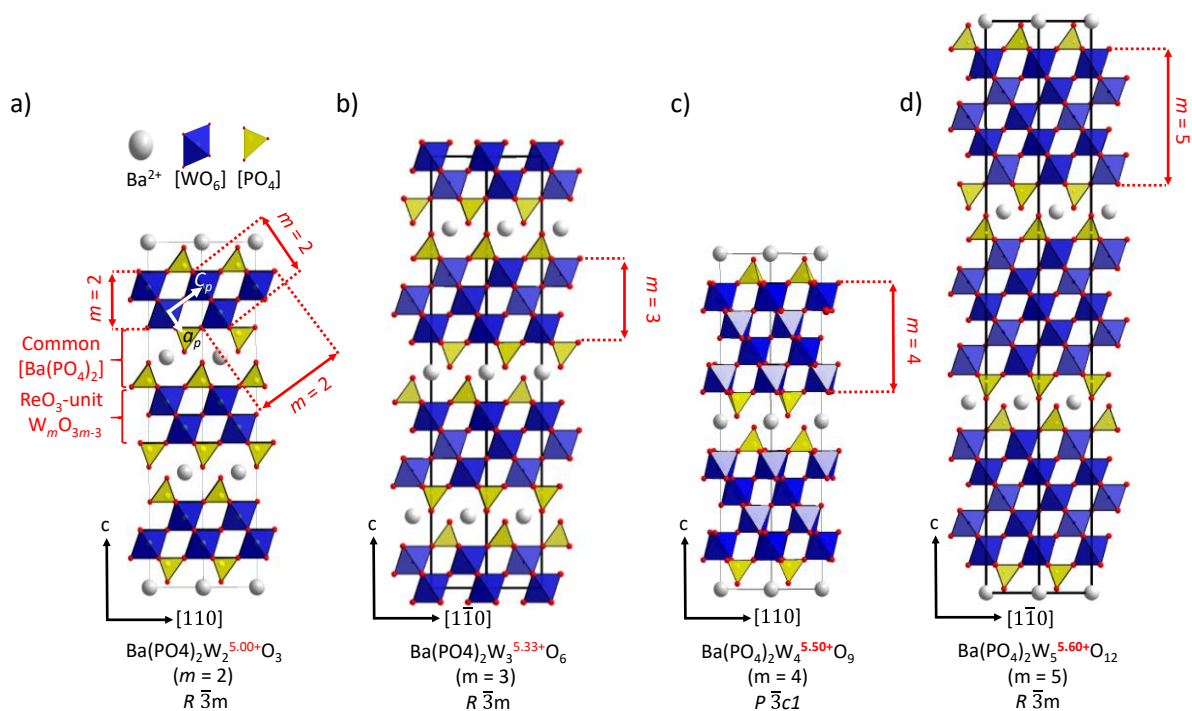


Figure I-15. Crystal structures principle of the L-MPTB. Projection on  $[110]$  of the crystal structures for a)  $\text{Ba}(\text{PO}_4)_2\text{W}_2\text{O}_3$  ( $m = 2$ ), b)  $\text{Ba}(\text{PO}_4)_2\text{W}_3\text{O}_6$  ( $m = 3$ ), c)  $\text{Ba}(\text{PO}_4)_2\text{W}_4\text{O}_9$  ( $m = 4$ ) and d)  $\text{Ba}(\text{PO}_4)_2\text{W}_5\text{O}_{12}$  ( $m = 5$ ).

Starting from the crystal structures of MPTBs, the L-MPTB series can be seen as the result of separating  $\text{ReO}_3$ -type through  $\text{PO}_4$  groups and the insertion of  $\text{Ba}^{2+}$  cations in between. This forms a  $[\text{Ba}(\text{PO}_4)_2]^{4-}$  spacer, leading to a distinct separation of the  $\text{ReO}_3$ -type slabs (see Figure I-16a). This spacer layer, in particular, tends to enforce a trigonal symmetry to the system as

exemplified in the aforementioned quasi-2D magnets  $[\text{Ba}(\text{PO}_4)_2]M_2$  ( $M = \text{Co}, \text{Ni}, \text{Fe}$ ) [66,74,75] (see Figure I-16c). The layer thickness  $d \approx 5 \text{ \AA}$  and iono-covalent character emphasizes a “genuine” 2D-behavior, disrupting electronic interactions between the  $\text{ReO}_3$ -like layers. Eventually, this high trigonal symmetry contrasts from those of the MPTBs which are monoclinic or orthorhombic. Another difference stems from the  $m$  index which refers in previous MPTBs to the maximal diagonal thickness of the crenelated perovskite slabs.

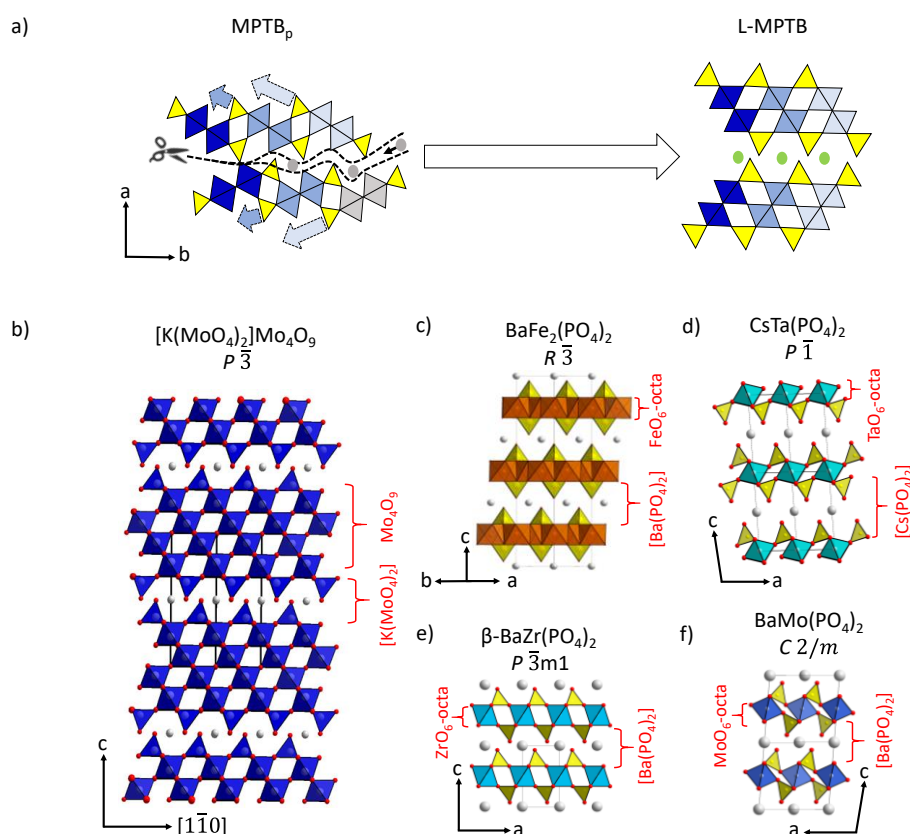


Figure I-16. Various crystal structures analogous to the L-MPTB family: a)  $\text{KMo}_6\text{O}_{17}$  [76], b)  $\text{BaFe}_2(\text{PO}_4)_2$  [74], c)  $\text{CsTa}(\text{PO}_4)_2$  [70], d)  $\beta\text{-BaZr}(\text{PO}_4)_2$  [71] and e)  $\text{BaMo}(\text{PO}_4)_2$  [72]. f) Sketch of the structural passage from MPTB<sub>p</sub> to L-MPTB by slicing/shearing and Ba incorporation.

In our L-MPTBs, the  $m$  index corresponds to the number of stacked octahedra along both the trigonal  $c$ -axis and the pseudo perovskite-axis  $c_p$ , simplifying their structural interpretation (see Figure I-15).

The L-MPTBs have various structural analogues in the literature, with the closest being the violet bronze  $\text{AMo}_6\text{O}_{17}$  ( $A = \text{Na}$  or  $\text{K}$ ) [76,77] (see Figure I-16b). This structure corresponds to the  $m = 4$  term of our L-MPTB and is formed by the stacking of layers composed of  $\text{Mo}^{3.5+}\text{O}_6$

octahedra and  $\text{Mo}^{6+}\text{O}_4$  tetrahedra, with the latter replacing the  $\text{PO}_4$  groups. By analogy, this corresponds to the formula  $[\text{K}(\text{MoO}_4)_2]\text{Mo}_4\text{O}_9$ . The structural resemblance suggests a possible extension of our L-MPTB series to a more general series with the generic formula  $[\text{A}(\text{XO}_4)_2]\text{M}_m\text{O}_{3m-3}$ . We already mentioned that the “*so-far*” virtual  $m = 1$  member for the L-MPTB corresponds to the  $\beta$ - $[\text{Ba}(\text{PO}_4)_2]\text{Zr}$  [71] structural prototype (see Figure I-16c), or a more distorted version such as  $[\text{Cs}(\text{PO}_4)_2]\text{Ta}$  (see Figure I-16d) [70] and  $[\text{Ba}(\text{PO}_4)_2]\text{Mo}$  (see Figure I-16f) [72].

#### I.1.4.2 $\text{Ba}(\text{PO}_4)_2\text{W}_2\text{O}_3$ ( $m = 2$ )

The phosphate  $[\text{Ba}(\text{PO}_4)_2][\text{W}^{5+}_2\text{O}_3]$  corresponds to the  $m = 2$  member and currently serves as the initial member in the L-MPTB series. It crystallizes in the trigonal space group  $R\bar{3}m$  with the unit cell parameters  $a = 5.2308(2)$  Å,  $c = 29.024(1)$  Å, and  $V = 687.73(5)$  Å<sup>3</sup>. The structure model could be refined to  $R = 1.92\%$  (SC-XRD). The lab XRPD pattern is shown in Figure I-11a. Further details on the crystallographic data, measurements, and structure refinements are summarized in Table A 0-1-4 in the appendix. According to our specific synthesis method, we checked that the refinement of the O(1) occupancy converged to 1.00(4), although our polycrystalline sample may have some degree of oxygen deficiency refined from NPD data to 3.28 %, see section I.1.3.2.

The crystal structure can be described by layers of a thick  $[\text{Ba}(\text{PO}_4)_2]^{4-}$  spacer, sandwiching  $[\text{ReO}_3]$ -type slabs. These slabs of vertex sharing  $\text{WO}_3$  is characteristic of previous bronzes, but much more regularly aligned along the three pseudo-cubic (perovskite) axis shown in red in the L-MPTB see Figure I-17a. They are built from a single independent  $\text{W}(1)$  with the formal  $\text{W}^{5+}$  valence.

The  $m = 2$  phase exhibits a single W-W distance of  $3.6919(3)$  Å along the linear W-O-W bonds with an angle of  $180^\circ$ . Which is ideal for efficient  $\text{W}_d\text{-O}_p$   $\sigma$ -overlap, as discussed later. Similarly, to all the L-MPTB members to be discussed later, W is slightly off-centred along on trigonal axis in its octahedra, opposite to the three P-O-W bonds (see Table A 0-2). This displacement, magnified in Figure I-17a, is commonly observed in previous MPTB and is related to participation of the external oxide anions at the interface between  $\text{ReO}_3$ -type layers and phosphate groups in strongly covalent P-O bonds. This led to an anti-parallel displacement of these atoms perpendicular to the barium-phosphate spacers. As a result, the  $\text{WO}_6$  octahedra display long and short W-O bonds with distances  $3 \times 2.031(4)$  Å and  $3 \times 1.8459(2)$  Å for  $m = 2$ .

We notice that this type of anti-polar displacements is in fact characteristic of the entire L-MPTB series.

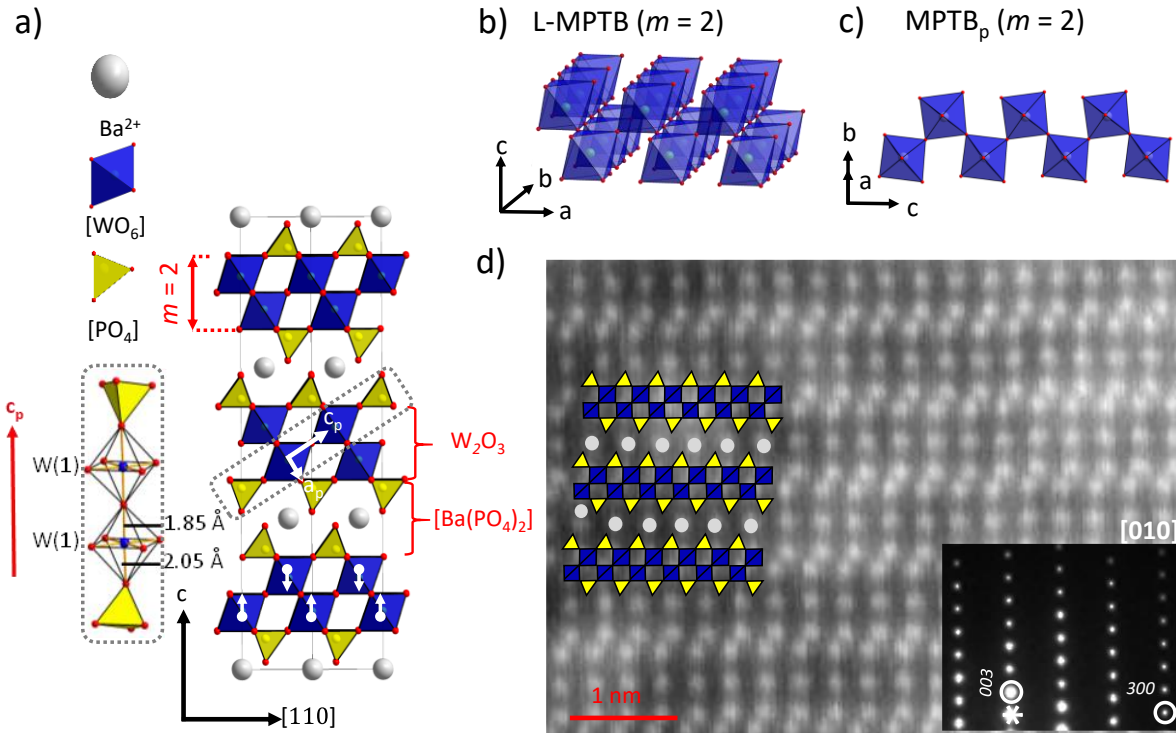


Figure I-17. Projection on  $[110]$  of the crystal structure for  $Ba(PO_4)_2W_2O_3$  ( $m = 2$  L-MPTB), Projection on a)  $[110]$  and b)  $[001]$  of the crystal structure for  $Ba(PO_4)_2W_3O_6$  ( $m = 3$  L-MPTB), with details of the W shift and  $m$ -octahedra along  $W_mO_{3m-3}$  row. b) the 1D  $W^{5+}$  chains displayed in the  $WOPO_4$  ( $m = 2$  MPTBp) Vs. c) 2D- $W^{5+}$  layers with double-octahedra in  $Ba(PO_4)_2W_2O_3$  ( $m = 2$  L-MPTB). d) HAADF images. The white spots correspond to the heavy Ba and W, while the lighter P and O ones are in the dark areas. The inset shows  $[010]$  ED patterns for  $m = 2$  L-MPTB.

The  $m = 2$  case is critical, leading either to i) 1D zigzag chains of  $W^{5+}O_6$  octahedra for MPTB<sub>p</sub> (see Figure I-17c) or ii) double-octahedral layers for L-MPTB (see Figure I-17b). The Figure I-17d shows a high angle annular dark-field scanning transmission electron microscopy (HAADF-STEM) image of this structure projected on the  $(101)$  plane, with a strong contrast between the bright W atoms and Ba to darkest spacers. As we see, the obtained intergrowth of the  $WO_3$  blocks between the phosphate spacers is regular with neither defects nor diffuse lines (in ED).

#### 1.1.4.3 $Ba(PO_4)_2W_3O_6$ ( $m = 3$ )

$[Ba(PO_4)_2][W^{5+}_{3.333}O_6]$  ( $m = 3$ ) crystallizes in the trigonal space group  $R\bar{3}m$  with  $a = 5.2380(2)$  Å,  $c = 35.464(3)$  Å, and  $V = 842.65(9)$  Å<sup>3</sup>. The crystal structure was solved from single-crystal X-ray diffraction (SC-XRPD) data, and the model could be refined to  $R = 2.39\%$ . Additionally, a

Rietveld refinement was conducted on synchrotron powder X-ray diffraction data (SR-XRD) (see Figure I-11b). Information on crystal structure refinement is provided in Table A 0-1-4 in the appendix.

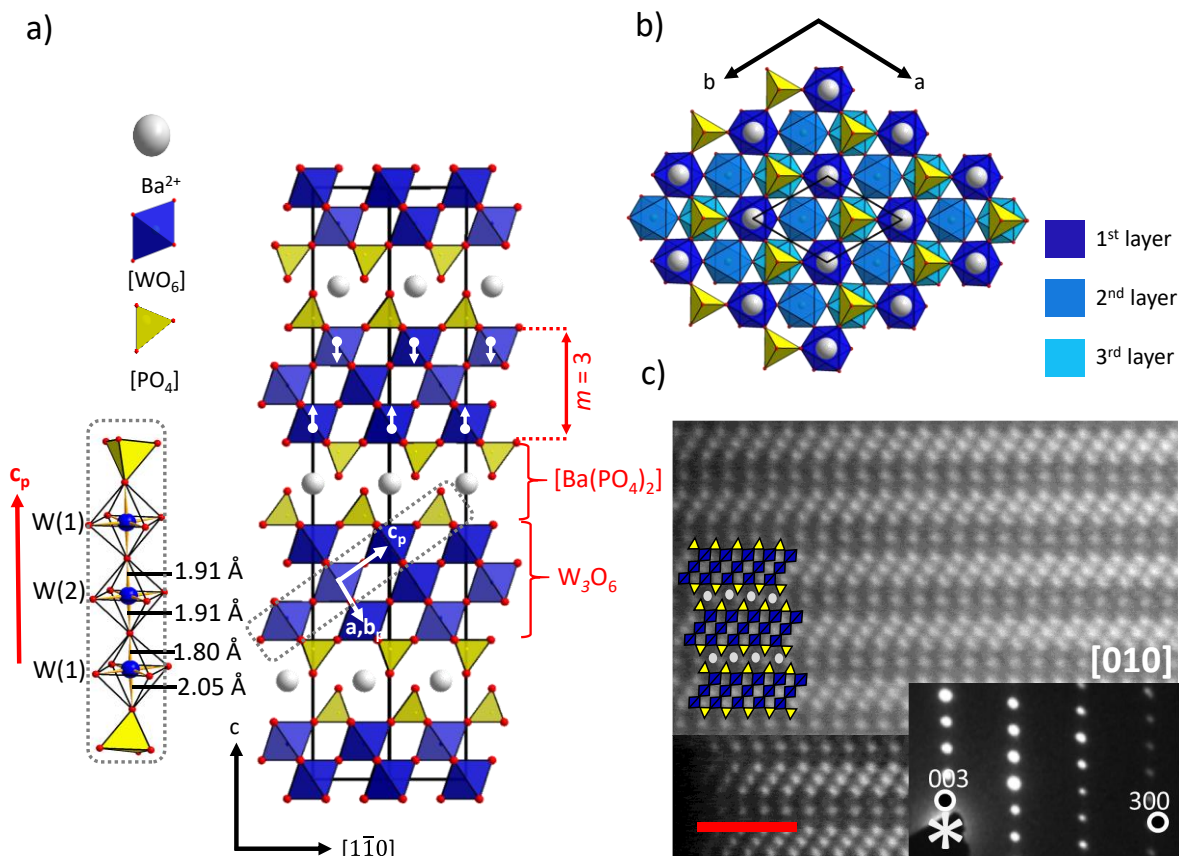


Figure I-18. Projection on  $[1\bar{1}0]$  a) and b)  $[001]$  of the crystal structure for  $\text{Ba}(\text{PO}_4)_2\text{W}_3\text{O}_6$  ( $m = 3$  L-MPTB), with details of the W shift and  $m$ -octahedra along  $W_m\text{O}_{3m-3}$  row. c) HAADF images. The white spots correspond to the heavy Ba and W, while the lighter P and O ones are in the dark areas. The inset shows  $[010]$  ED patterns for  $m = 3$  L-MPTB.

The crystal structure can be described similarly to the  $m = 2$  case, featuring a layered structure consisting of a thick  $[\text{Ba}(\text{PO}_4)_2]_4$ -spacer, sandwiching the  $[\text{ReO}_3]$ -type infinite layer. A projection along the  $c$ -axis is shown in Figure I-18a. The  $\text{ReO}_3$ -type layer consists of two independent tungsten sites W(1) and W(2) (Figure I-18a).

Similarly to the case of  $m = 2$ , and for the same reasons, the W(1) atoms are shifted along the crystallographic  $c$ -axis towards the centre of the  $\text{ReO}_3$ -like slabs. This displacement is magnified in Figure I-18a. The  $\text{ReO}_3$ -type layer show  $\approx 3$  Å thick, W-O-W distances of 3.7073(8) Å with nearly linear W-O-W angle ( $175.8^\circ$ ), optimal for 5d electron  $\sigma$ -type overlap (see Figure I-18a).

Electron diffraction (ED) patterns and high-angle annular dark-field scanning transmission electron microscopy (HAADF-STEM) confirm the absence of stacking faults, with strong contrast between the bright W atoms and darkest spacers, as shown in Figure I-18c.

#### I.1.4.4 $Ba(PO_4)_2W_4O_9$ ( $m = 4$ )

$[Ba(PO_4)_2][W^{+5.5}_4O_9]$  ( $m = 4$ ) displays a more complex structure, which was initially determined from powder data due to the lack of suitable crystals. The initial structure model showed a unit cell with  $a = 5.2099(2)$  Å,  $c = 14.0868(1)$  Å and space group  $P-3$ . This model could be refined against single-crystal data (SC-XRD) to  $R = 4.28\%$  and allowed the assignment of all reflections, except for a few weak ones that were not associated with any impurity. Doubling the  $c$  parameter allowed the indexing of these reflections (see Figure I-19a). This  $2 \times c$  supercell with  $a = 5.2092(2)$  Å,  $c = 2 \times 14.0812(1)$  Å,  $V = 661.83(5)$  Å<sup>3</sup> and space group  $P-3c1$  could be refined in down to supercell approach  $R_F = 2.41\%$  (SC-XRD).

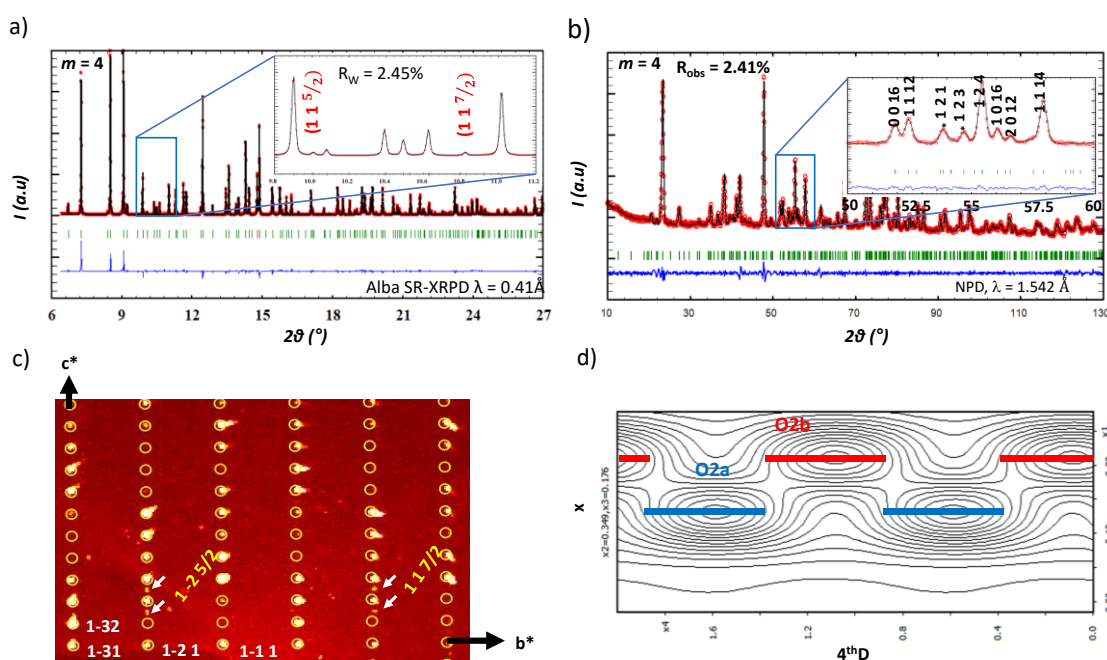


Figure I-19. a) Rietveld refinement of synchrotron powder diffraction data of  $m = 4$ . The refinement shows the peaks corresponding to this modulation (red) b) Rietveld refinement of neutron powder diffraction data. c)  $1kl$  reconstituted precession frame from SC-XRD data at RT with evidence of  $2c$  satellites (yellow). d) oxygen ordering in  $m = 4$ . The two oxygen pairs follow an occupancy crenel-like wave leading to a commensurate modulation.

**4D approach (modulated structure).** In a first refinement stage, we used a four-dimension (4D) commensurately modulated approach, with a commensurate modulation vector  $\vec{q}(0, 0, \frac{1}{2})$  (super space group  $P-3(0, 0, \frac{1}{2})$  which exacerbates the atomic origins of the modulation peaks. It follows that only the oxygen positions of the metallic-blocks require to be split and

assigned to occupancy crenel-like waves, see Figure I-19d. The SR-XRPD was combined with neutron powder diffraction data for more accurate oxygen positions using Fullprof software [78] (see Figure I-19d). The subsequent finding of crystals enabled the crystal structure to be resolved using SC-XRD data, confirming the results obtained on powder. It is the structural data from data SC-XRD that are listed in the Table AI-2a-b in the appendix. It results in the alternation along the  $c$ -axis of two-slight modifications of  $m = 4$  octahedra thick blocks, with eclipsed oxygen coordination between one-block to the next one, by  $\approx 20^\circ$ , see Figure I-20a. Additionally, the  $\text{ReO}_3$ -type slabs display an anti-parallel displacement of W atoms along the crystallographic  $c$ -axis towards the centre, as magnified in Figure I-20a.

**3D approach (superstructure).** The structure was also adequately reproduced by the standard 3D-approach in space group  $P-3c1$  using SR-XRPD and NPD data. In essence, the main ingredient of this structural distortion is the tilting of each oxygen layers out-of-phase from each other in the layers and transmitted across the  $[\text{Ba}(\text{PO}_4)_2]^{4-}$  spacer, likely transmitted by coulombic forces.

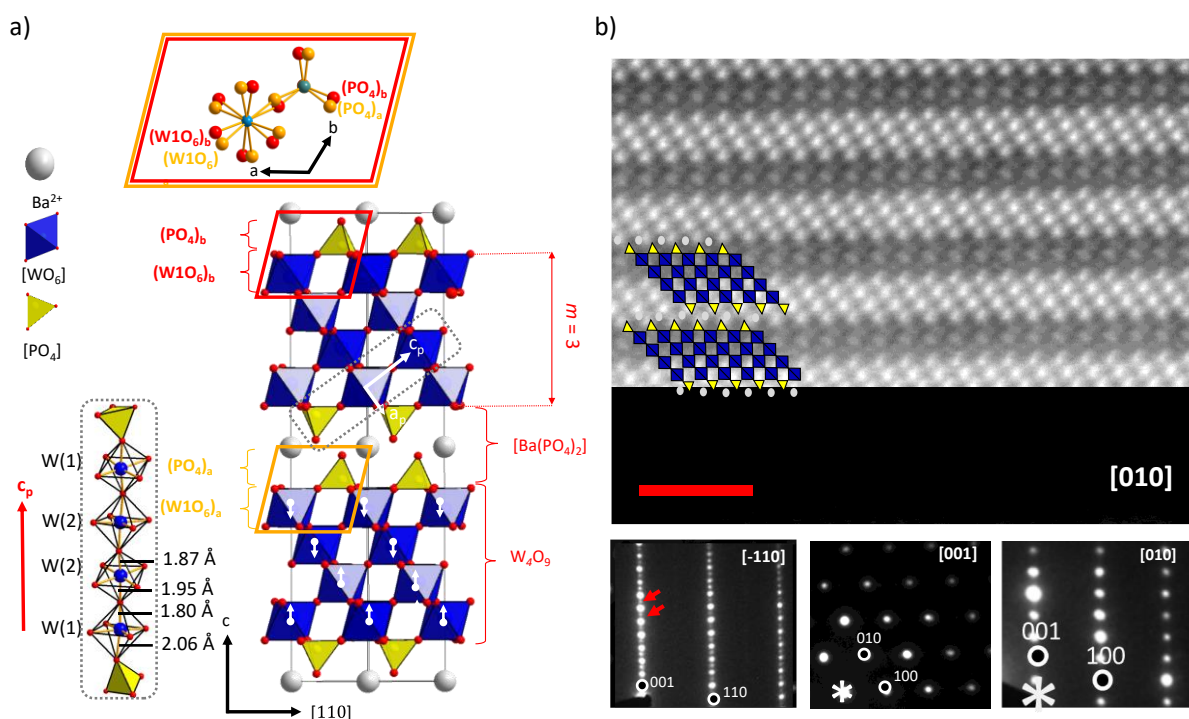


Figure I-20. Projection on a)  $[110]$  of the crystal structure  $\text{Ba}(\text{PO}_4)_2\text{W}_4\text{O}_9$  ( $m = 4$  L-MPTB), with details of the W shift and  $m$ -octahedra along  $W_m\text{O}_{3m-3}$  row and eclipsed configurations of the coordination polyhedra between two next 2D-units along  $c$ , responsible for the  $c$ -axis doubling. b) HAADF images. The white spots correspond to the heavy Ba and W, while the lighter P and O ones are in the dark areas. The inset shows  $[010]$ ,  $[001]$  and  $[-110]$  ED patterns, the latter showing the  $c$ -doubling for the  $m = 4$  L-MPTB.

HAADF images reveal again neither chemical defects nor stacking faults. However, the  $[-110]$  ED pattern allows for a clear observation of the supercell oxygen ordering, Figure I-20b. The  $m = 4$  member, as said before, of the new L-MTPB series represents the tungsten counterpart of the reference molybdenum bronze  $[\text{K}(\text{MoO}_4)_2]\text{Mo}_4\text{O}_9$ .

#### 1.1.4.5 $\text{Ba}(\text{PO}_4)_2\text{W}_5\text{O}_{12}$ ( $m = 5$ )

$[\text{Ba}(\text{PO}_4)_2]\text{W}^{5.6+}_5\text{O}_{12}$  ( $m = 5$ ) crystallizes in the space group  $R\bar{3}m$  ( $a = 5.2292(6)$  Å,  $c = 48.740(6)$  Å,  $R_F = 5.29\%$ ), see Figure I-21a. Selected crystallographic information is provided in Table A 0-1-4. The anti-parallel displacement of W atoms along the crystallographic  $c$ -axis towards the centre of the  $\text{ReO}_3$ -like slabs is magnified in Figure I-21a.

The ED patterns on selected areas confirmed the existence of regions with fully ordered  $m = 5$  L-MPTB. However, we observed the intergrowth of multiple  $m$  L-MPTB\*s in the thin part of crystals in the HAADF images. This suggests a relative chemical instability of this “high”  $m$  member but also the possibility to extend the series up to  $m = 7$ .

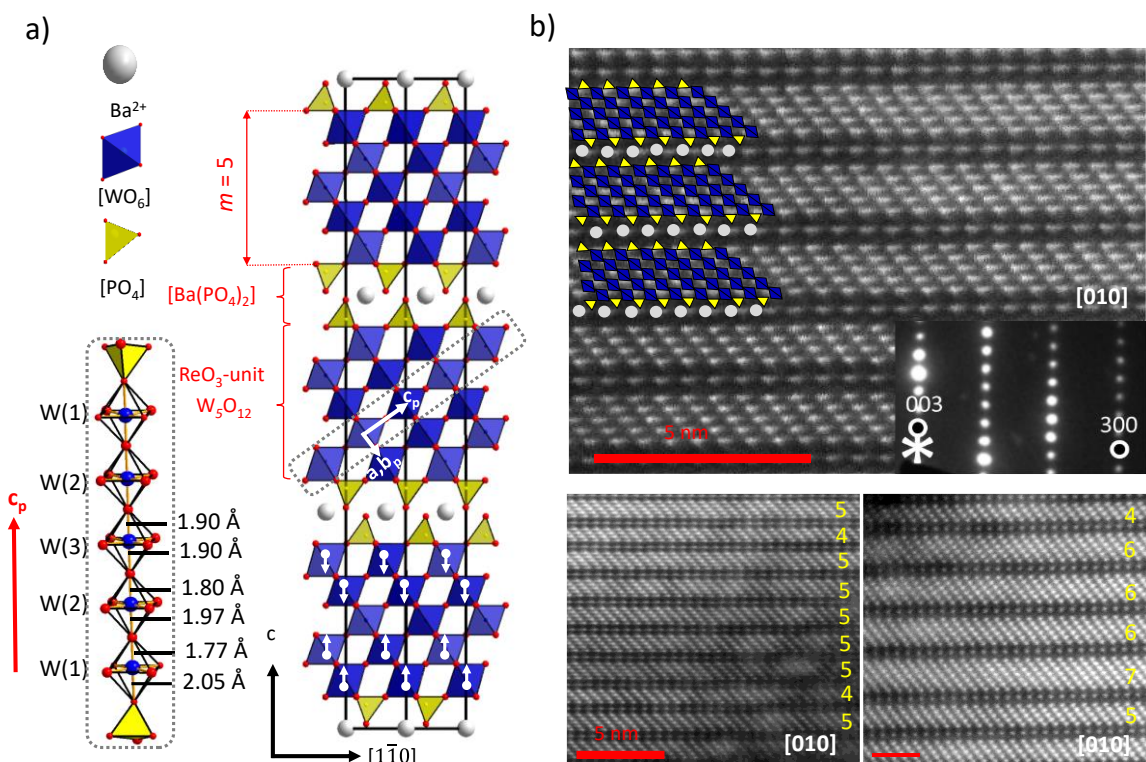


Figure I-21. Projection on  $[1\bar{1}0]$  of the crystal structure for  $\text{Ba}(\text{PO}_4)_2\text{W}_5\text{O}_{12}$  ( $m = 5$  L-MPTB), with details of the W shift and  $m$ -octahedra along  $W_m\text{O}_{3m-3}$  row along the perovskite axis (in white). b) HAADF images. The white spots correspond to the heavy Ba and W, while the lighter P and O ones are in the dark areas. The inset shows  $[010]$ , ED patterns.

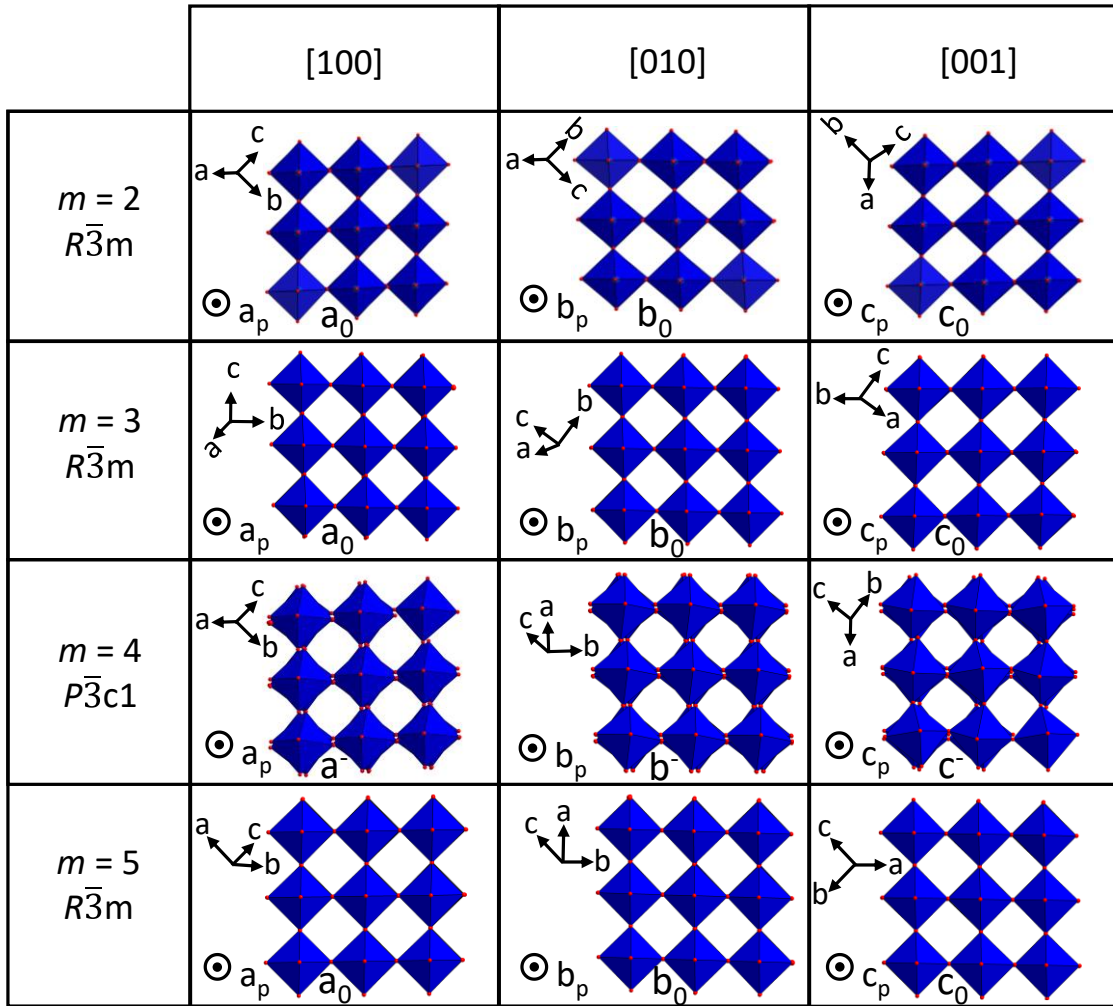


Figure I-22. Projection along the three perovskite pseudo-axes showing the octahedral tilting modes, by analogy with the parent  $WO_3$  the projection (following the Glazer notation), for  $m = 2$ ,  $m = 3$ ,  $m = 4$  and  $m = 5$ .

The octahedral tilting modes in L-MPTBs, by analogy with the parent  $WO_3$  structure which is well known to exhibit a variety of transitions with temperature [13], reveals an undistorted  $ReO_3$ -like slab for  $m = 2, 3$ , and  $5$  along the perovskites pseudocubic axes (*i.e.*  $a^0b^0c^0$  in the Glazer notation) (see Figure I-22), while  $m = 4$  shows a tilt ( $a-b-c$  in Glazer notation) due to oxygen tilting modulation (see Figure I-22).

#### 1.1.4.6 Stability of the trigonal symmetry

We have intensively studied the L-MPTBs for clues on any structural effect mediating CDW phenomena discussed in the introduction (see section 1.1.2.2).

**[Ba(PO<sub>4</sub>)<sub>2</sub>]W<sub>m</sub>O<sub>3m-3</sub> ( $2 \leq m \leq 5$ ).** The members of the L-MPTB series show no evidence of CDW structural distortions.

**Ba(PO<sub>4</sub>)<sub>2</sub>W<sub>2</sub>O<sub>3</sub> (*m* = 2).** Its crystal structure remains trigonal within the measured temperature range of  $19 \leq T \leq 300$  K, using high-resolution low-temperature XRPD (Cu-K<sub>α1</sub> radiation) and electron-diffraction. The "smooth" evolution of lattice parameters upon cooling, along with the absence of supercell reflections or diffuse scattering in reciprocal space, confirmed a locked trigonality. Furthermore, the *m* = 2 compound exhibits negative thermal expansion ( $\alpha = 5.6 \times 10^{-6} \text{ K}^{-1}$ ) within the ab plane, contrasting with observations for the *m* = 4 compound, as depicted in Figure I-23d-f. This behaviour is illustrated by the opposite thermal evolution of the (0 0 3) and (4 -2 0) reflections peaks (see Figure A 0-1 in Appendix I) and (see Figure I-23b) will be discussed in section I.1.5.4.

**Ba(PO<sub>4</sub>)<sub>2</sub>W<sub>4</sub>O<sub>9</sub> (*m* = 4).** In a broad thermal domain, the *m* = 4 compound did not reveal any evidence of characteristics associated with charge density waves (CDWs), such as diffuse-scattering streaks or (in)commensurate modulation satellites related to the Peierls-like transition. This was confirmed through electron diffraction (77 K to RT), single crystal XRD (130-380 K), and synchrotron powder diffraction (120-440 K) screenings. The c-doubling is preserved between 110 and 440 K, while the lattice parameters and W-W distances evolve gradually with temperature [13], as shown in Figure I-23a-c.

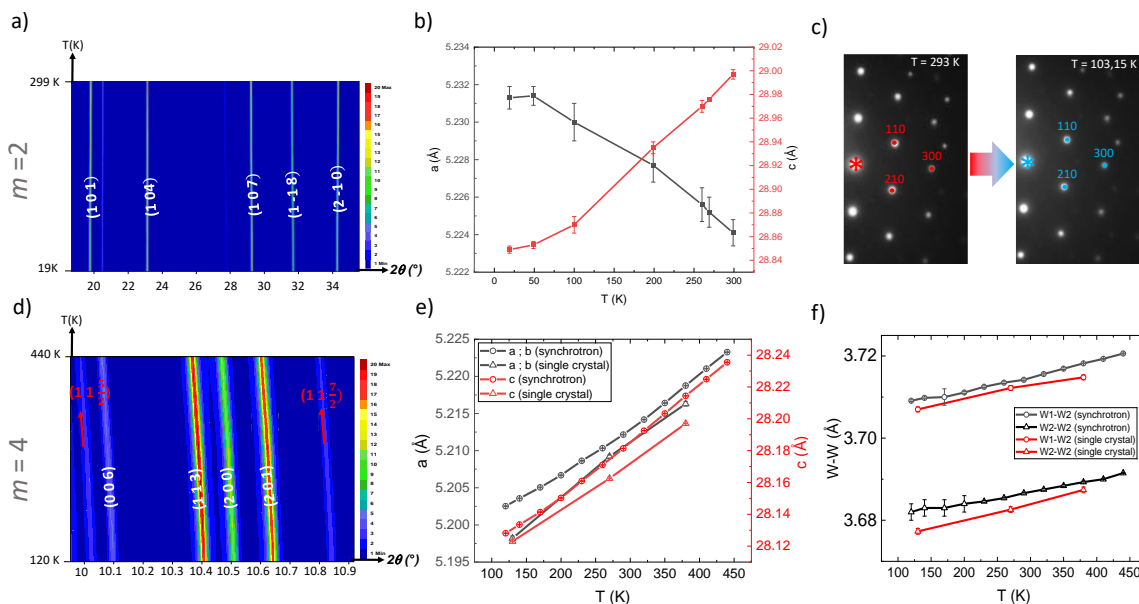


Figure I-23. *Ba(PO<sub>4</sub>)<sub>2</sub>W<sub>2</sub>O<sub>3</sub> (*m* = 2):* a) Smooth thermal evolution of XRPD profile. b) Lattice parameters *a* and *c* as a function of temperature. Negative thermal expansion is observed for *a*. c) Electron-diffraction patterns along the main crystallographic zone axes [001]\* at 297K and 103K. *Ba(PO<sub>4</sub>)<sub>2</sub>W<sub>4</sub>O<sub>9</sub> (*m* = 4):* a) Smooth thermal evolution of SR-XRD profile b) Thermal evolution of the lattice parameters. c) W-W distances using both SR- and SC-XRD data.

Finally, at this point, the L-MPTB members exhibit robust structural stability in contrast to commonly observed (in)commensurate modulations associated with CDW-instabilities in their parent monophosphate tungsten bronzes, where upon cooling W-shifts are observed for the monoclinic and orthorhombic structures. Such in-plane atomic displacements are inhibited by the trigonal symmetry, which is stabilized by the rigid  $[\text{Ba}(\text{PO}_4)_2]^{4-}$  interfacial spacers. This is supported by the relatively large in-plane lattice parameter ( $a \approx 5.2 \text{ \AA}$ ) compared to other inorganic materials built on the same  $[\text{Ba}(\text{PO}_4)_2]$  slab, such as  $\text{BaFe}_2(\text{PO}_4)_2$  ( $a \approx 4.9 \text{ \AA}$ ), which undergoes a trigonal  $\rightarrow$  triclinic Jahn-Teller distortion around 140 K [67]. It is assumed that this longer in-plane lattice parameter compared to  $\text{BaFe}_2(\text{PO}_4)_2$ , could better accommodate lattice parameter variations, thereby preventing distortion and phase transition.

### I.1.5. Physical characterisation and DFT calculations

#### I.1.5.1 *Steady 2D-metallicity validating the absence of CDW*

**Transport properties.** As detailed in section I.1.2.3 dedicated to the parent monophosphate tungsten bronze (MPTBs), they are well-known as quasi-2D metal prototypes for the development of Peierls-like charge instability. It results in systematic CDWs across one or multiple phase transitions at different critical temperatures  $T_{c1,2,3\dots}$  which govern almost entirely the various structural series including molybdenum bronzes. The strong anomalies reported in the thermal dependence of the electronic properties are associated with incommensurate or incommensurate periodic lattice distortions. Generally, the transition temperatures increase significantly with  $m$  (from 50 K to 700 K for  $m = 2$  to 14 MPTBp) [13].

The L-MTPB series contrasts significantly with this behaviour, since no structural distortion/modulation nor electronic instability was detected on the  $m = 2$  to 5 members down to 1.8 K. The electronic transport shows that they all behave as steady, true-2D metals (see Figure I-24a). However, for  $m = 4$  we observe a slight upturn in the very-low temperature regime that we ascribe to sample quality.

As expected, susceptibility measurements reveal a nearly temperature independent Pauli paramagnetic behaviour with a weak Curie-Weiss paramagnetic term emphasized at low-T, assigned to intrinsic impurities (Figure I-25).

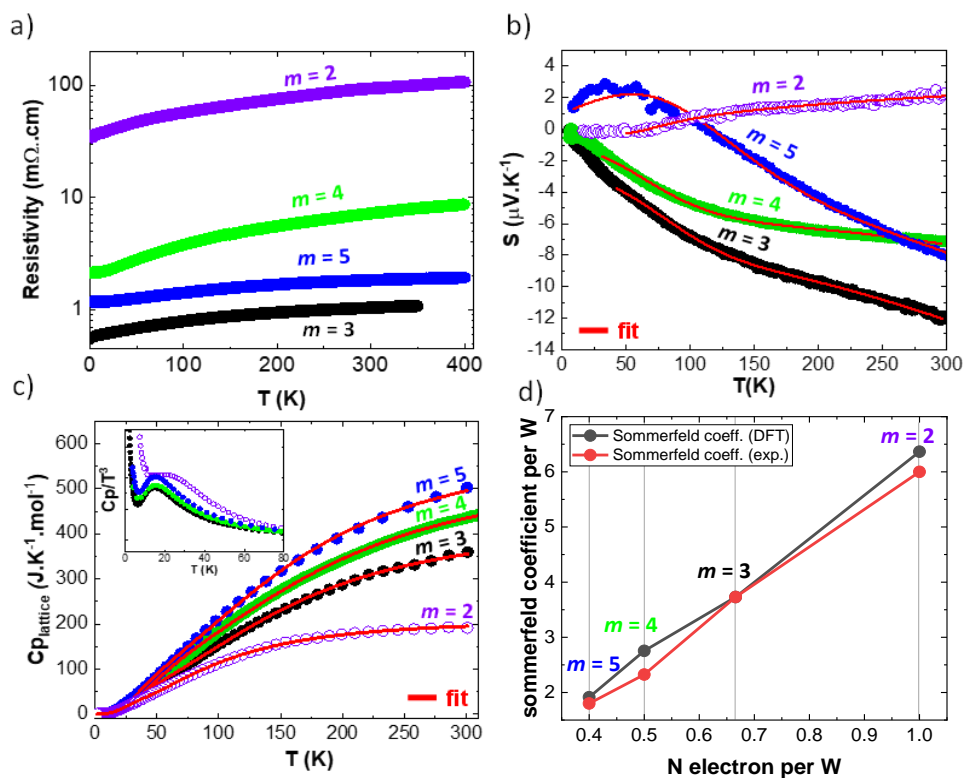


Figure I-24. a) Physical properties the L-MPTB series  $[Ba(PO_4)_2]W_mO_{3m-3}$ . Resistivity as a function of temperature. b) Seebeck coefficient as a function of temperature with fitted according to [79]. c) Lattice contribution to the specific heat as a function of temperature (the insert shows the same data at low temperature in a  $Cp/T^3$  vs  $T$  plot, which should be constant according to the universal Debye law). d) Experimental and calculated Sommerfeld coefficient of the electronic contribution to the specific heat obtained for the different members of the series.

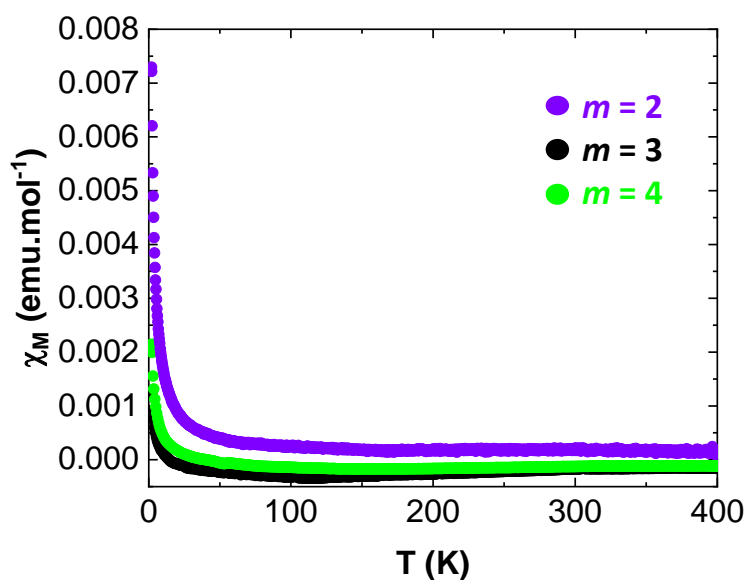


Figure I-25. Magnetic susceptibility Vs. temperature for the L-MPTB at  $m=2, 3$ , and  $4$ .

**Thermopower.** Similarly our thermopower measurements show rather continuous behaviours fitted as follows. In general, the Seebeck coefficient is the sum of two parts, the carrier thermodiffusion part  $S_{diff}$  and the phonon drag  $S_{Ph}$  which allows for description of the Seebeck coefficient over a wide temperature range. The  $S_{diff}$  contribution due to the thermodiffusion of the charge carriers corresponds to  $F_{diff}T/\Theta_D$ . While the low-temperature part is dominated by  $S_{diff}$  and carrier information about the carrier type and concentration, the high temperature is dominated by phonon-phonon umklapp scattering and obeys a Debye model in connection with the phonon specific heat. The intermediate temperature combines electron-phonon and phonon-phonon interactions such that the extended thermal range can be fitted using [79,80].

$$S = S_{diff} + S_{ph} = F_{diff} \frac{T}{\theta_D} + \frac{F_{Ph} \left(\frac{T}{\theta_D}\right)^3 \int_0^{\frac{\theta_D}{T}} \frac{x^4 \exp(x)}{(\exp(x)-1)^2} dx}{1 + F_{\tau} T \exp\left(-\frac{\theta_D}{T}\right)} \quad \text{Eq. I-7}$$

The total S coefficient contribution is a sum of  $S_{diff}$  (electron-phonon) and the  $S_{Ph}$  (phonon-phonon) interactions.  $\theta_D$  represents the Debye temperature. Results are given in Table A 0-9 in Appendix I, which validates electronic carriers (negative sign of  $F_{diff}$ ). The special case of the  $m = 2$  compound, with mainly positive  $S(T)$  values will be discussed in section 1.1.5.4. Thermopower measurements don't show any anomalies over the entire temperature range (1.8 K-300 K) contrast to what is observed for MPTBs (see Figure I-24b). In fact, the data can be nicely fitted using a negative-charge carrier thermodiffusion term (which dominates the high-temperature behaviour), which means that over the whole temperature range electrons are the charge carriers, plus a phonon-drag contribution (Table A 0-9 in the appendix section), except for the  $m = 2$ . The case of  $m = 2$  is distinguished from other members of the series by its positive sign for  $F_{diff}$ . At this stage, we have established that the electronic nature of the charge carriers persists across the whole L-MPTBs series, although the metallicity is provided by different W atoms, according to their Wyckoff positions. We can assume that this Seebeck coefficient measurement of the L-MPTB members is the result of multiple, and in the case of  $m = 2$  suggests a more direct effect of the spacer on the relevant electron-phonon interaction.

### 1.1.5.2 Heat capacity

*The specific heat of  $m = 3, 4,$  and  $5$  was analysed by using the expression  $C = \gamma T + AT^{-3}$ , in which the first and second terms represent the electronic and lattice contributions respectively.*

It is generally accepted that the validity of the Debye  $T^3$  approximation requires temperatures lower than  $\theta_D/50$  (see Figure A 0-2 in the appendix section). The results are given in Table A 0-9 in Appendix I. After removal of the contribution of the “low-T approximate”  $\gamma T$ , the relevant high temperature lattice contribution was fitted up to 300 K using two Debye contributions leading to  $C_i$  and  $\theta_i$  listed in Table A 0-9 in Appendix I, using the following formula:

$$C_{latt} = 9R \sum_{i=1}^2 C_i (T/\theta_{Di})^3 \int_0^{x_{Di}} \frac{x^4 e^x}{(e^x - 1)^2} dx \quad \text{Eq. I-8}$$

After subtraction of the lattice contributions, the deduced Sommerfeld coefficient associated with the electronic contribution is plotted in Figure I-24d as a function of  $m$  and summarized in Table A 0-9 in Appendix I. As a result, the concentration of charge carriers (predominantly  $e^-$ ) decreases as  $m$  increases, logically being inversely related to the formal oxidation state of tungsten which is given by  $(4+(m-1)*6)/m$ , e.g.  $1e^-/W$  for  $W^{5.00+}$  at  $m = 2$ ,  $0.67e^-/W$  for  $W^{5.33+}$  at  $m = 3$ , and eventually  $0.40e^-/W$  for  $W^{5.60+}$  at  $m = 5$ . The remaining specific heat due to the lattice is shown in Figure I-24c as a function of temperature. A closer look at the low-temperature specific heat data reveals a quasi-linear-in-T behaviour together with a broad peak in the  $C_p(T)/T^3$  plots (see inset in Figure I-24c). These features appear systematically across the entire series, including the  $m = 2$  compound. In the latter case, the bump is a little bit broader and shifted towards higher temperatures. These bumps are generally associated with phason excitations (*i.e.* structural excitations) that emerge in the presence of aperiodic modulations as in the case of charge-density-wave ordering (see *e.g.* [58,81]). The observation of these features in the L-MPTB systems, however, is surprising because their crystal and electronic structure both remain exceptionally stable (in particular, with no evidence of CDW order). All together these features suggest exotic electronic states at the frontier between emergent ordering and unstable 2D-metals.

### I.1.5.3 Fermi Surface Topology and Band Structure Analysis

Figure I-26a shows the calculated band structures for all members of the L-MPTB series. We find three bands crossing the Fermi level, which is in accordance with the measured metallic character of these systems. The corresponding Fermi surface is illustrated in Figure I-26b. It shows a similar Fermi surface shape as it was found for the quasi-2D  $K_{0.9}Mo_6O_{17}$  [42]. This Fermi

surface (FS) can be regarded as the result of three sets of parallel planes of the Fermi surfaces (FS) forming quasi-1D nested surfaces, a concept that was introduced by Canadell and Whangbo [29], where the 2D-FS cannot explain the experimental CDW nesting vectors. Instead, they can be understood as a superposition of 3 sets of nested quasi-1D surfaces which form parallel lines. In real space, the crystal structure of the L-MPTBs display corner-sharing  $\text{WO}_6$  octahedra within the  $ab$  plane (see Figure I-27a and b for the  $m = 2$  as an example).

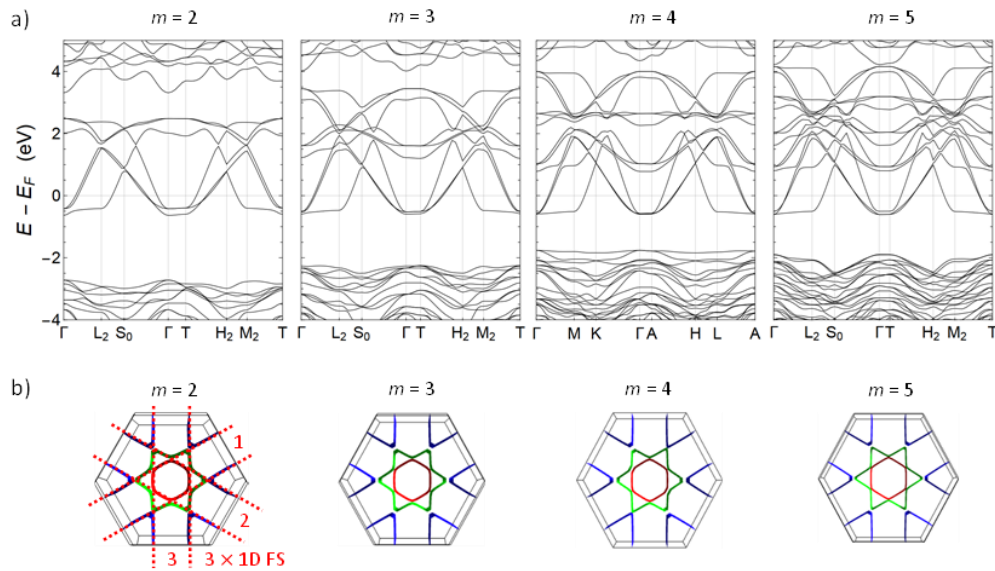


Figure I-26. a) Electronic band structure calculated for the  $m = 3, 4,$  and  $5$  members of the L-MTPB series  $[\text{Ba}(\text{PO}_4)_2]_m\text{W}_m\text{O}_{3m-3}$ . The Fermi surface of these systems has a remarkable 2D character. The three different sheets of these Fermi surfaces are associated with the three different bands that cross the Fermi level in the corresponding band plots. These half-filled bands belong to the  $5d$ - $W$  manifold that extend from  $\sim -0.5$  eV to  $\sim +4$  eV. b) Fermi surfaces (FS) of different members of L-MPTB

Consequently, the corresponding electronic structure features weakly coupled conductive zigzag chains running along that  $a$ ,  $b$ , or  $(a + b)$  (respectively red, blue and yellow in Figure I-27b) directions by sharing their “axial” O atoms involving  $W$ - $t_{2g}$ , contained in the in planes chains, and O- $\pi$  orbitals overlaps. Thus the orbitals are intrachain of  $t_{2g}$ - $\pi$ - $t_{2g}$  (Figure I-27c) and interchain  $t_{2g}$ - $t_{2g}$   $\delta$  overlaps (Figure I-27d) [29]. That should yield six bands (three bands for each  $W$  atom in the unit cell from the aforementioned atomic-orbital overlaps). These bands belong to a well-separated manifold of  $W$ - $t_{2g}$  derived states composed of a total of  $3m$  bands dispersing along  $a$ ,  $b$ , and the  $(a + b)$  direction along the trigonal axis, thereby exhibiting a 1D character [29,43] (Figure I-26b). For  $m = 2$ , these states are formally occupied by 2 electrons so that the nominal filling of these bands is  $1/3$  each. These features of suggests a “latent” tendency towards charge-density-wave order. Again, this tendency, however, is avoided in

the L-MPTB systems most likely because of the rigidity provided by the phosphate spacer  $[\text{Ba}(\text{PO}_4)_2]^{4-}$ .

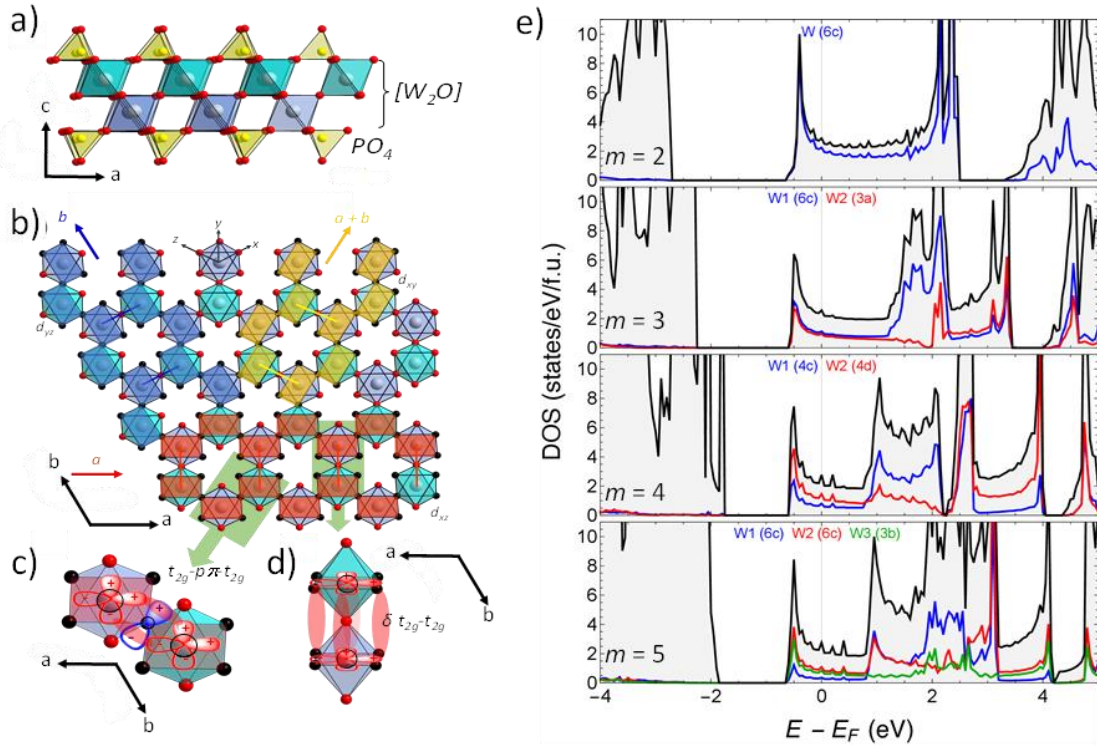


Figure I-27. a) Projection of a section ( $\text{ReO}_3$ -type layer bordered by phosphates) of the  $m = 2$  structure along  $[010]$  showing the different orbital overlaps along b)  $[001]$  showing with zigzag chains of  $\text{W}-t_{2g}$  and  $\text{O}-\pi$  orbitals overlaps. c) intrachain  $t_{2g}-\pi-t_{2g}$  overlap and d) interchain  $t_{2g}-t_{2g}$   $\delta$  overlaps. e) Total (black curves) and  $\text{W}-5d$  projected density of states (DOS), with the different  $\text{W}$  atoms labelled according to their Wyckoff positions.

The calculated Fermi surface is associated with the well-separated  $\text{W}-t_{2g}$  manifold of derived states composed of a total of  $3m$  bands, split into doubly-degenerate  $1e$ , and singlet  $1a$  levels in an ideal case of a regular  $\text{WO}_3$  octahedra, these three bands would be degenerate at the  $\Gamma$  point. However, as we pointed out before, there is an off-centring of the  $\text{W}$  atoms resulting in two different  $\text{W}-\text{O}$  distances, which lowers the local symmetry of the  $[\text{WO}_6]$  to  $3m$  ( $\text{Q}^3$ ). For the  $\text{Q}^6$   $[\text{WO}_6]$  octahedra within the  $\text{ReO}_3$ -type layers this effect decreases with increasing  $m$ . As a result, there is partial splitting of the  $\text{W}-t_{2g}$  derived bands at  $\Gamma$ . Interestingly, a closer look at this splitting across the L-MPTB series reveals a progressive inversion of the relative energies of the single  $1a$  and double degenerate  $1e$  bands (see Figure I-26a). In addition to the off-centring of the  $\text{W}$  atoms, the L-MPTB series also shows significant differences in the distortions of the  $[\text{WO}_6]$  octahedra for each  $m$  member. These distortions are distinct for each individual  $\text{WO}_6$ , as depicted in Table I-1. When  $m$  is even, one regular  $\text{WO}_6$  is present, the

distortion pattern varies notably. This variation in the local environment of the W atoms contributes significantly to the changes in the electronic band structure.

*Table I-1. Summary of structural distortions observed for tungsten atomic positions in the L-MPTB.*

$m$	Space group	W-sites	Site symmetry	Geometric distortion
2	$R\bar{3}m$	6c	3m	(6c) strongly disordered, but less so than W(1) and W(2) in $m = 5$ , and W(1) in $m = 3$
3	$R\bar{3}m$	6c, 3a	3m, $\bar{3}m$	(3a) close to ideal, (6c) strongly distorted
4	$P\bar{3}c1$	4c, 4d	3m, $\bar{3}m$	(4c) distorted, (4d) distorted
5	$R\bar{3}m$	6c, 6c, 3b	3m, 3m, $\bar{3}m$	(6c) strongly distorted, (6c) strongly distorted, (3b) close to ideal

Figure I-27e compares the total density of states (DOS) and the DOS contribution from the different W atoms computed for the L-MPTB series. The corresponding Sommerfeld coefficient is compared with its experimental value in Figure I-24c. The calculation captures the experimental trend with a quantitative agreement also. Further, from the corresponding bands occupancies (see Figure I-27c), we find that the metallicity of these systems is mainly associated with the most central W atoms within the  $WO_3$  slab. This aspect is discussed below, in particular in relation to the oxidation state of the W atoms and their anti-polar displacement.

#### *1.1.5.4 Charge distribution*

**W valence.** We first discuss the uncommon pentavalent tungsten state in  $[Ba(PO_4)_2]W_2O_3$  and the evolution of the metal valence across the L-MPTB series. To this purpose, we start by plotting the height along the c-axis of the different  $WO_6$  octahedra and their average as a function of the nominal W valence for each compound including the  $d^0$  case of the cubic  $WO_3$  ( $m \rightarrow \infty$ ) variant stabilized by doping. [82] The average height (see Figure I-28a and Table A 0-2 in appendix) decreases nearly linearly in agreement with the increase of the tungsten ionic radius (IR) upon reduction (IR ( $W^{6+}$ ) = 0.60 Å and IR ( $W^{5+}$ ) = 0.62Å [73]). For all members of the L-MPTB series, the distribution of octahedral sizes appears rather homogeneous. However, the close similarity in ionic radii between  $W^{6+}$  and  $W^{5+}$  (only 0.02 Å difference) does not allow one to definitively exclude the possibility of such charge ordering.

In order to clarify this point, we inspect the filling of the  $W-t_{2g}$  derived bands from the computed electronic structure of these systems. Figure I-28b shows this quantity per W atoms

as a function of the nominal number of electrons per W across the L-MPTB series. For  $m = 2$ , the filling obtained from the total DOS is in tune with the nominal  $W^{5+}-d^1$  configuration expected in this case. However, when filling is calculated from the W-derived states only, it turns out to be noticeably below its nominal value. The difference is due to the hybridization with O- $p$  derived states. This difference decreases as  $m$  increases, which suggests that the W-O hybridization is higher in the proximity of the spacer (where, in addition, the W off-centring is more pronounced). In any case, the computed filling reveals a trend from the  $W^{5+}-d^1$  configuration for  $m = 2$  towards the  $W^{6+}-d^0$  one of the  $WO_3$  perovskite-type layers as  $m$  increases (see Figure I-28b).

Further, for  $m > 2$ , we find that the filling of the states associated with the outer tungsten atoms (W(1)) is always below the average filling while filling of the central tungsten atoms (W(2) and W(3)) is significantly above that average (see Figure I-28b). As  $m$  increases, the outer W atoms (W(1) and then W(2) also) contribute less and less to the metallic behaviour which is eventually dominated by the tungsten atoms at the centre of the  $WO_3$  slab (i.e. W(3) for  $m = 5$ ). Therefore, the metallicity of these systems remains remarkably 2D even if the crystal structure tends to the bulk  $WO_3$  on increasing  $m$ .

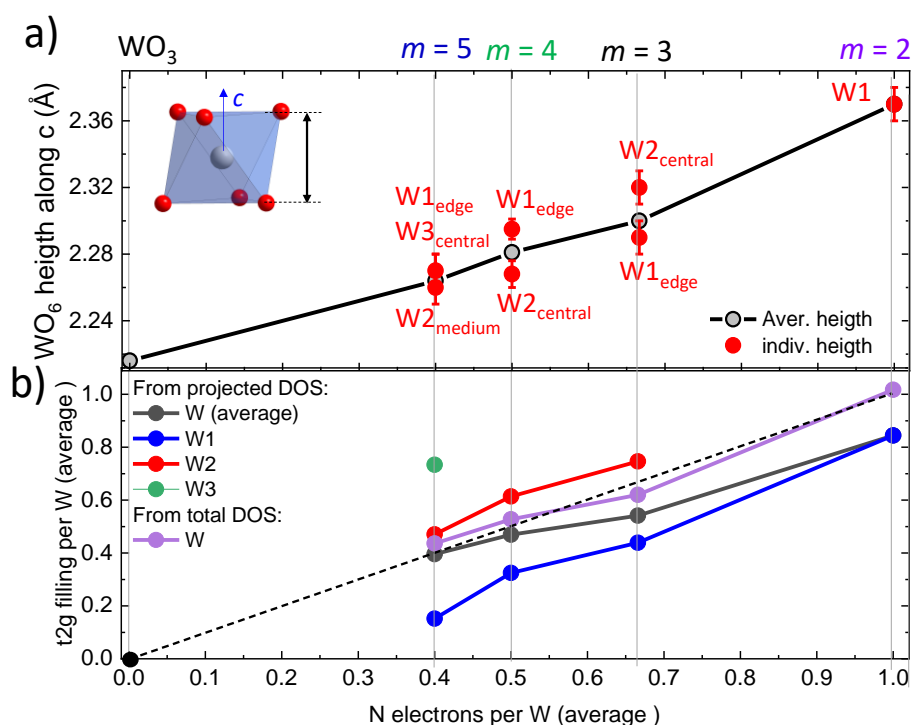


Figure I-28. a) Height of the different  $WO_6$  octahedra along the  $c$ -axis as a function of the formal W valence across the entire L-MPTB series. The arbitrary offset of this plot is fixed with the  $m = 2$  compound. b) Filling of the  $t_{2g}$  manifold per W atom computed from the total and W-projected DOS. The W atoms are labelled as in Figure I-29a-d, so that W1 always corresponds to the outer W of the  $WO_3$  slab (i.e. the only ones for  $m = 2$ ).

**Role of the spacer.** Next, we discuss the relative importance of the phosphate spacer in the L-MPTB series  $[\text{Ba}(\text{PO}_4)_2]_m\text{W}_m\text{O}_{3m-3}$  from the following observations. The member at  $m = 2$  displays negative thermal expansion within the trigonal  $ab$  plane (see Figure I-17a in section I.1.4.2), which changes to positive across the series for  $m = 5$  (see [83]). While the layered structure of the L-MPTBs explains their anisotropic thermal behaviour, the distinct expansion properties of the  $m = 2$  phase could be related to that observed in other layered perovskites such as  $\text{Sr}_2\text{IrO}_4$ . [84] In that case, it has been associated with equatorial rotations of the  $\text{IrO}_6$  octahedra in this tetragonal example. However, such a rotation is not allowed in the trigonal structure of the L-MPTBs. The behaviour of  $m = 2$  can then be regarded as reminiscent of the negative-thermal-expansion behaviour of the prototype  $\text{ReO}_3$  material [85]. In this case, the electron-phonon coupling is believed to play the key role, which can be expected to be different at the W-O-P bridges. The Seebeck coefficient provides a direct measure of the electron-phonon coupling. This coefficient is positive for  $m = 2$  and negative for the rest of the members of the L-MPTB series. However, the calculations show that the charge carriers have electron character in all these systems and are always related to the central tungsten atoms of the  $\text{W}_m\text{O}_{3m-3}$  blocks irrespective of  $m$ . Accordingly, we can assume that this Seebeck coefficient is the result of multiple couplings, and in the case of  $m = 2$ , it suggests a more direct effect of the spacer on the relevant electron-phonon interaction. The increased influence of the  $[\text{Ba}(\text{PO}_4)_2]^{4-}$  spacer can also be deduced from the crystal-field splitting of the W- $t_{2g}$  states across the series, as it was indicated above. In particular, we have shown that the band structure of the L-MPTB systems displays a progressive inversion of this splitting at the bottom of the W- $t_{2g}$  manifold, suggesting a transition from the  $(1e, 1a)$  configuration to the more exotic  $(1a, 1e)$  one as  $m$  decreases. This *virtual* trigonal compression like effect is assigned to the influence of the  $\text{PO}_4$  ligand effect in the vicinity of the W ions, on the crystal field.

**Anti-polar metallicity.** The electronic disproportionation of the W atoms observed in the DFT calculations is the manifestation of the extraordinary effect that, even when the thickness of  $\text{WO}_3$  slab increases, the metallicity is preserved in the L-MPTB series. This is rather counterintuitive since, as  $m$  increases, the nominal oxidation state of the W atom tends to  $6+$  and therefore should correspond to the  $d^0$  configuration of bulk  $\text{WO}_3$ . Furthermore, the calculations reveal that such a metallicity has a 2D character since the conduction is due to the central W atoms of the  $\text{WO}_3$  slab. The different participation of the different W atoms in

the overall conduction is, in part, certainly caused by the inductive effect of the  $\text{PO}_4$  groups, as they polarize the electronic clouds along the W-O-P bridges. However, on closer inspection, we identify another superimposed mechanism that is crucial for the 2D character of the observed metallicity.

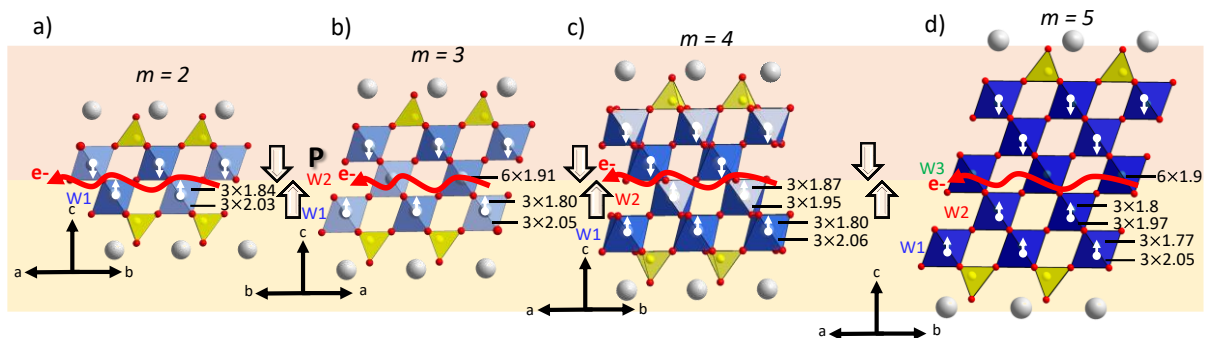


Figure I-29. L-MPTB structures showing  $\text{WO}_6$  octahedra with off-centring of W atoms, leading to anti-polar  $\text{WO}_3$  blocks in a)  $m = 2$ , b)  $m = 3$ , c)  $m = 4$  and d)  $m = 5$ , analogous to charged domain walls in ferroelectric materials.

Specifically, we notice that the off centring of the W atoms within the  $\text{WO}_6$  octahedra is such that the  $\text{W}_m\text{O}_{3m-3}$  slab is composed of two polar sub-slabs arranged in an anti-parallel fashion so that it contains a domain wall at the middle as illustrated in Figure I-29a-d. In fact, the hypothetical cubic phase of  $\text{WO}_3$  is inherently soft with respect to polar displacements of this type [86,87] (although they are eventually allowed by structural distortions that increase the size of the unit cell in that case).

In the L-MPTB systems, the presence of covalent P-O bonds naturally induces displacements of the W atoms, consistent with the previously proposed bond valence (BV) model (see Table A 0-2). These displacements cooperatively take place towards the centre of the  $\text{W}_m\text{O}_{3m-3}$  slabs. In a purely ionic picture, the resulting anti-polar distortion of the  $\text{WO}_3$  slab generate bound charges at the domain wall (see Figure I-29a). In reality, additional screening arises due to distortions in the electronic clouds, which enhance the carrier concentration at the centre of the perovskite blocks. This is confirmed by our density of states (DOS) calculations, which show that the central tungsten atoms mainly contribute to the metallicity. Thus, the central part of  $\text{WO}_3$  block in the L-MPTB systems becomes analogous to the charged domain walls with enhanced conductivity, similar to those observed in some ferroelectrics (see *e.g.* [88]).

### 1.1.6. $Ba(PO_4)_2W_{m-x}M_xO_{3m-3}$ ( $M = Mo, Fe$ )

All the substitutions discussed below were attempted for  $Ba(PO_4)_2W_3O_6$  ( $m = 3$ ) or  $Ba(PO_4)_2W_4O_9$  ( $m = 4$ ) since they were obtained in a pure form on multiple occasions, unlike  $Ba(PO_4)_2W_5O_{12}$  ( $m = 5$ ).  $Ba(PO_4)_2W_2O_3$  ( $m = 2$ ), was obtained at a later stage of this thesis, therefore no trials were conducted. It is important to mention that beyond the results presented below, which indicate to some extent the possibility of substitution, numerous attempts have been made, especially attempts to substitute the Ba by lanthanide. These attempts could be summarized by the general formula  $Ba_{1-x}A_x(PO_4)_2W_3O_6$  ( $A = Sr, Pb, Bi, La, Sm, Eu, Sm$ ). However, none of these attempts were successful, further confirming the rigid framework of this series and the reduced ability for substitution.

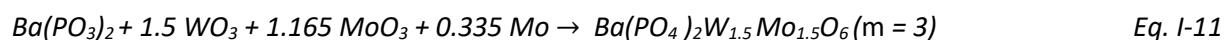
#### 1.1.6.1 $Ba(PO_4)_2W_{3-x}Mo_xO_6$ ( $m = 3$ )

Substitution of W by Mo was conducted to expand the family of L-MPTB, as previously mentioned, owing to the structural resemblance to the reference molybdenum bronze,  $KMo_6O_{17}$  [76], which could lead to a broader family of materials with the generic formula  $[A(XO_4)_2]M_mO_{3m-3}$ .

Synthesis was carried out for the preparation of  $Ba(PO_4)_2[W_{3-x}Mo_x]O_6$  with L-MPTB structure where tungsten is partially or fully replaced by molybdenum through isomorphic substitution in the L-MPTB.

To determine the maximum tolerable ratio within the L-MPTB structures, several experiments were carried out with varying Mo:W ratios: 0, 0.33, 1, and 1.5. We limited ourselves to these fractions because heating these compounds at 1173K results in a melt, due to the low melting point of Mo compare to W. This melt coats the entire surface of the ampoule, making it impossible to remove. Heating below this temperature leads to the formation of multiple undefined product phases.

The synthesis follows the usual two-step process. Initially, a stoichiometric mixture of  $BaCO_3$  (Alfa Aesar,  $\geq 99\%$ ),  $(NH_4)_2HPO_4$  (ACROS organics,  $\geq 99\%$ ),  $WO_3$  (Fulka Analytical, 99.9%) and  $MoO_3$  Alfa Aesar,  $\geq 99\%$ ), when it is used, was heated in air at 873 K for 12h. this process aimed to decompose and eliminate the volatile species ( $CO_2, H_2O, NH_3$ ). Then resultant products were mixed and milled with a suitable amount of metallic tungsten and molybdenum according to following equations:



The mixture has been pelletized and placed in silica tubes sealed under vacuum and heated at 1173K for 2 days.

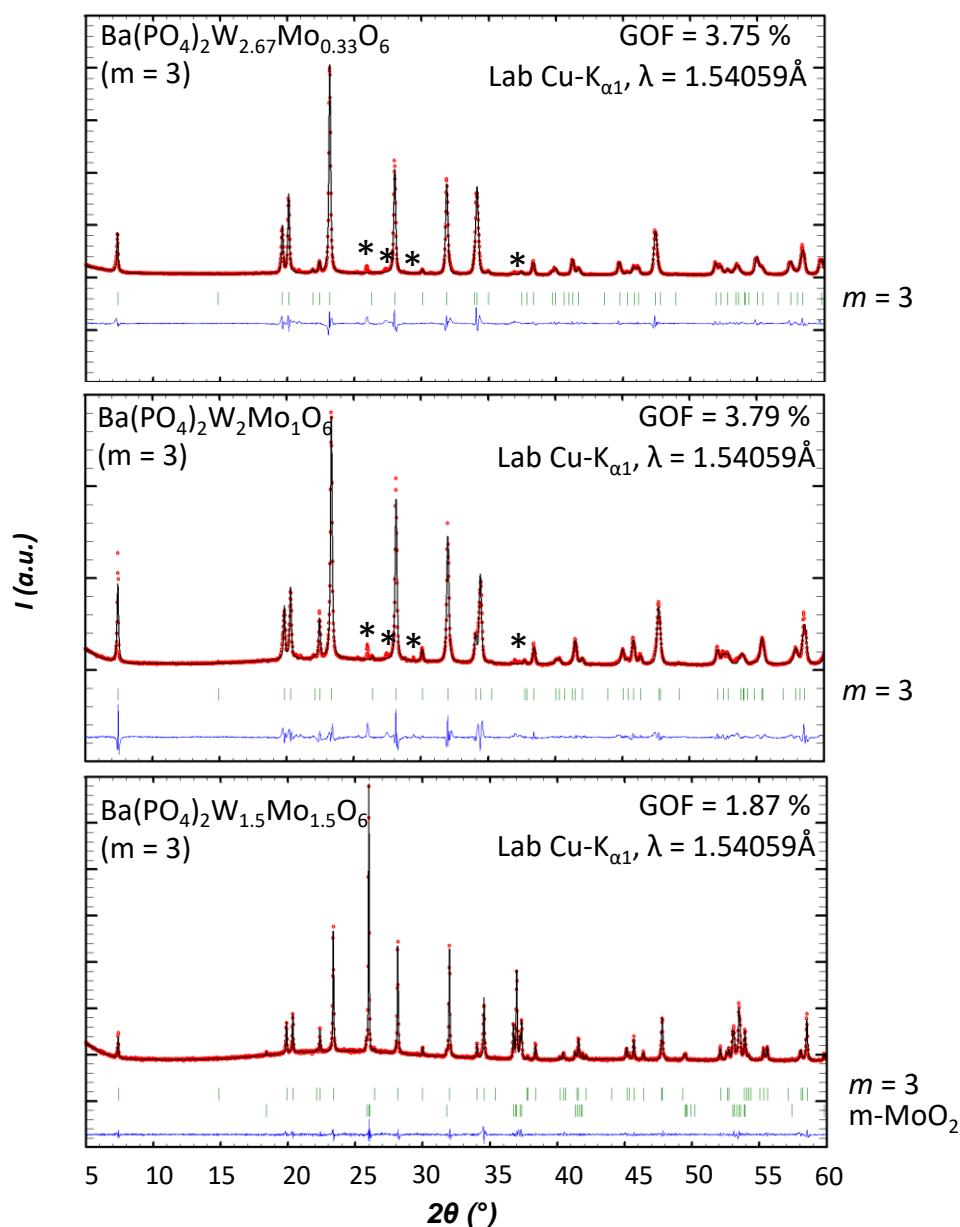


Figure I-30. Rietveld refinement on synchrotron powder diffraction data for  $\text{Ba}(\text{PO}_4)_2\text{W}_{3-x}\text{Mo}_x\text{O}_6$  ( $m = 3$ ) for a)  $x = 0.33$ , b)  $x = 1$  and c)  $x = 1.5$ .

Lebail fit is carried out for each compound to accurately determine lattice parameters and track the evolution of these parameters with respect to the Mo:W ratio (see Figure I-30).

These diffractograms show nearly pure compounds with some unidentified reflections (see Figure I-30), except for the sample containing m-MoO<sub>2</sub> as an impurity (see Figure I-30). This result show that isomorphic substitution between W and Mo is possible, as anticipated considering their respective ionic radii and coordination. The Shannon ionic radius for 6-coordinated Mo<sup>6+</sup> and W<sup>6+</sup> is 0.59 Å and 0.60 Å [73], respectively, while for W<sup>5+</sup> and Mo<sup>5+</sup> it's 0.61 Å and 0.61 Å [73].

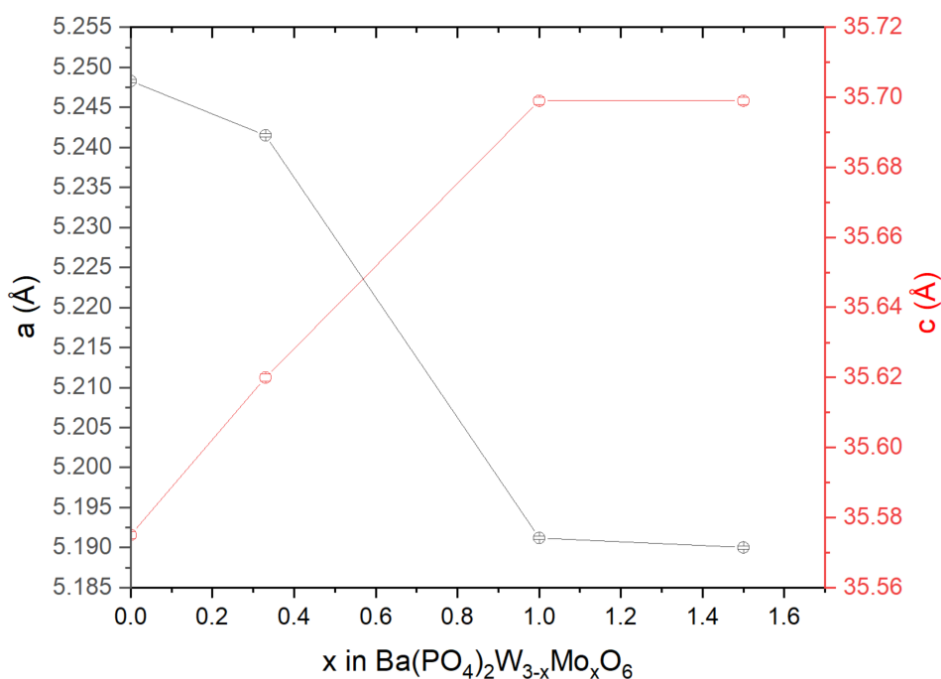


Figure I-31. Variation of unit cell parameters in the Ba(PO<sub>4</sub>)<sub>2</sub>W<sub>3-x</sub>Mo<sub>x</sub>O<sub>6</sub> (m = 3) structure as a function of the degree of substitution of W by Mo.

The close proximity in size supports the complete replacement of W by Mo. Consequently, due to molybdenum's slightly smaller ionic radius, lattice parameters undergo changes with increasing Mo content, specifically, a decrease in the a-axes to a minimum value of 5.1859(2) Å the theoretical composition: Ba(PO<sub>4</sub>)<sub>2</sub>W<sub>2</sub>Mo<sub>1</sub>O<sub>6</sub> (Figure I-31) and increase in the c-axis and, which increases to a maximum of 35.698(1) Å. This trend corresponds to what has been observed for the isomorphic substitution of molybdenum by tungsten in tetragonal tungsten bronzes [89]. Then a plateau is reached, which suggests that we have reached the limit of the solid solution, peaking for the aforementioned composition. (Superposition of the different XRD patterns will be added.) Besides tracking the evolution of the lattice parameters, an EDS measurements was performed on the three samples, revealing that the measured Mo content for the Ba(PO<sub>4</sub>)<sub>2</sub>W<sub>2</sub>Mo<sub>1</sub>O<sub>6</sub> and Ba(PO<sub>4</sub>)<sub>2</sub>W<sub>2.67</sub>Mo<sub>0.33</sub>O<sub>6</sub> samples are close to the expected values

with respectively . However, for the compound  $\text{Ba}(\text{PO}_4)_2\text{W}_{1.5}\text{Mo}_{1.5}\text{O}_6$ , it exhibits a multi-phase nature with a phase that doesn't contain W and can be attributed to  $m\text{-MoO}_2$ , which corresponds to the XRPD result (see Figure I-30).

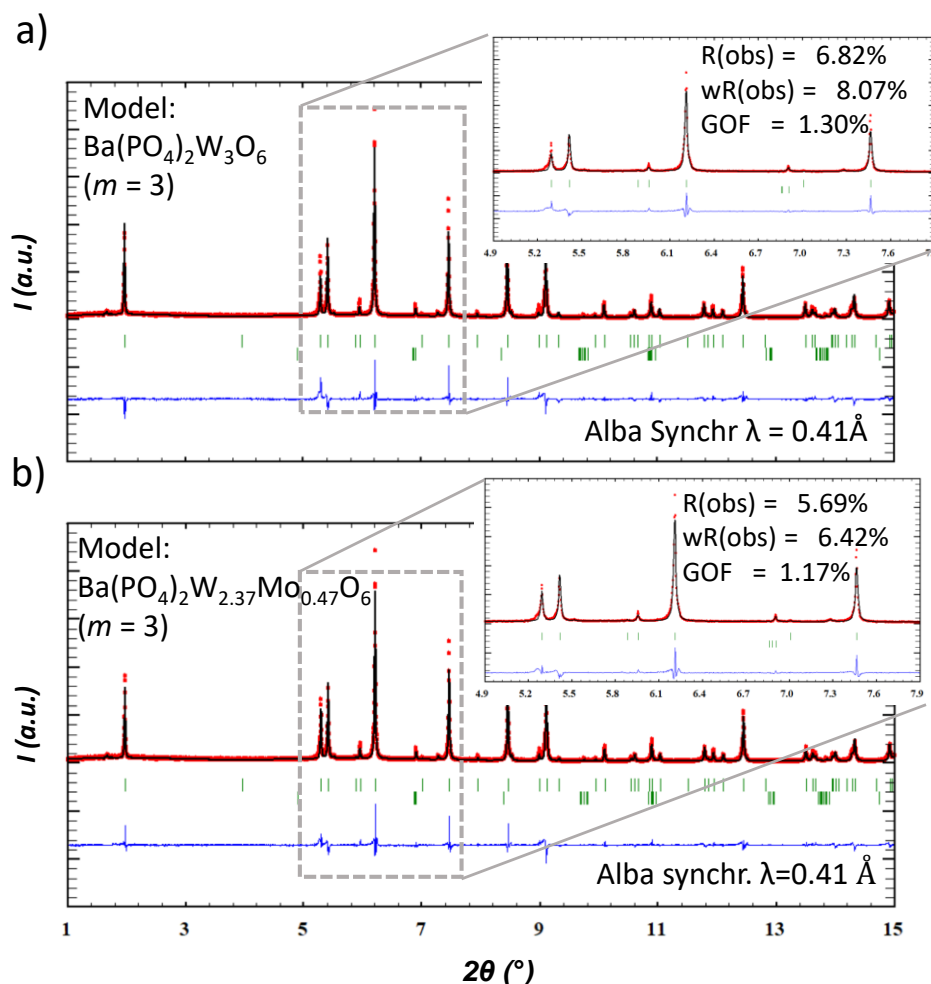


Figure I-32. Comparing the Rietveld of the SR-PD data considering as a) no substitution of W by Mo in  $m = 3$  b) a substitution of W by Mo and refining the site occupancy.

Rietveld refinements were conducted on synchrotron powder diffraction (SR-PD) (Alba synchrotron,  $\lambda = 0.41288 \text{ \AA}$ ) data for the  $\text{Ba}(\text{PO}_4)_2\text{W}_{2.67}\text{Mo}_{0.33}\text{O}_6$  sample, considering a substitution of W by Mo and refining the site occupancy. In the alternative scenario without W substitution, Rietveld refinement was performed. Comparing the two cases, the hypothesis of substitution resulted in better refinement for a composition of  $\text{Ba}(\text{PO}_4)_2\text{W}_{2.37}\text{Mo}_{0.47}\text{O}_6$ , which closely aligns with the targeted composition of  $\text{Ba}(\text{PO}_4)_2\text{W}_{2.67}\text{Mo}_{0.33}\text{O}_6$  (see Figure I-32).

### 1.1.6.2 $Ba(PO_4)_2W_{4-x}Fe_xO_9$ ( $m = 4$ )

Given the resemblance between  $BaFe_2(PO_4)_2$  [67] and L-MPTB, sharing the same  $[Ba(PO_4)_2]^{4-}$  spacer, conferring it with a 2D-Ising FM character and 2D-metal, attempts were made to explore the possibility of combining these properties. One approach involved sandwiching  $BaFe_2(PO_4)_2$  (2D FM Ising) between conductive layers of  $ReO_3$ -type, as depicted in the Figure I-16c in section 1.1.5.1, where the conductive and FM 2D-ising layers would be separated by the  $[Ba(PO_4)_2]$  spacer, potentially yielding a multifunctional FM-metal compound. Attempts were conducted via hydrothermal synthesis, at suitable conditions for  $BaFe_2(PO_4)_2$ , but these experiments proved unsuccessful. Subsequently, efforts were made to substitute W for Fe in  $Ba(PO_4)_2W_4O_9$  ( $m = 4$ ). In the literature it was shown that  $WO_3$  can accommodate a weak ratio of  $Fe^{2+}$  due to its large ionic radius, either in the square tunnels associated with the cubic bronzes or in the pentagonal tunnels associated with tetragonal bronzes [90].

The syntheses were conducted under the same conditions as those employed for the synthesis of L-MPTBs in two steps. Initially, a stoichiometric mixture of  $BaCO_3$  (Alfa Aesar,  $\geq 99\%$ ),  $(NH_4)_2HPO_4$  (ACROS organics,  $\geq 99\%$ ),  $WO_3$  (Fulka Analytical, 99.9%), and  $Fe_2O_3$  (Fulka Analytical, 99%) was heated in air at 873 K for 12h. this process aimed to decompose and eliminate the volatile species ( $CO_2$ ,  $H_2O$ ,  $NH_3$ ). Then resultant products were mixed and milled with a suitable amount of metallic tungsten and iron according to following equation targeting  $m = 4$  stoichiometry:



The mixture has been pelletized and placed in silica tubes sealed under vacuum and heated at 1273K for 2 days.

For  $x = 0.20$ , a mixture was obtained of phase  $m = 4$ ,  $m = 5$  and reflections belonging to an unidentified phase. At  $x > 2$ , experiments led to the products  $BaO_{18}P_2W_4$  and  $W_{18}P_2O_{59}$ , along with several other unidentified reflections. The parameters derived from the Rietveld refinement do not show significant variation in the lattice parameters, which does not indicate any substitution.

Several crystals were found at the surface of the pellet prepared with the formulation  $Ba(PO_4)_2W_{3.8}Fe_{0.2}O_9$  ( $m = 4$ ). EDS analyses were conducted on those crystals, giving a ratio of very close to the desired composition which corresponds to the term  $m = 4$  (See Figure I-33). Then, the crystal structure was solved and refined by single crystal X-ray diffraction (SC-XRD).

The crystal selected corresponds to the compound  $\text{Ba}(\text{PO}_4)_2\text{Fe}_{0.2}\text{W}_{3.8}\text{O}_9$  ( $m = 4$ ) and it displays the same  $2 \times c$  supercell discussed above. The following cell parameters were determined:  $a = 5.2049(5) \text{ \AA}$ ,  $c = 14.0870(1) \times 2 \text{ \AA}$  with  $V = 661.00(13) \text{ \AA}^3$  in *space group*  $P\bar{3}c1$  (see Table A 0-4-5) in the appendix section for more details). The shift of the lattice parameters from the starting  $x = 0$  phase ( $a = 5.2099 \text{ \AA}$ ,  $c = 14.0868 \text{ \AA}$ ) are minor. The structural model could be refined to  $R_f = 3.91\%$  (SC-XRD). Refining the occupancies of the two individual W/Fe sites converge to 3.78(13) and 0.22(3) which show a uniform distribution of Fe in all octahedra layers, this leads to the following chemical formula  $\text{Ba}(\text{PO}_4)_2\text{Fe}^{3+}_{0.22}\text{W}^{5.65+}_{3.78}\text{O}_9$  (see Table A 0-5).

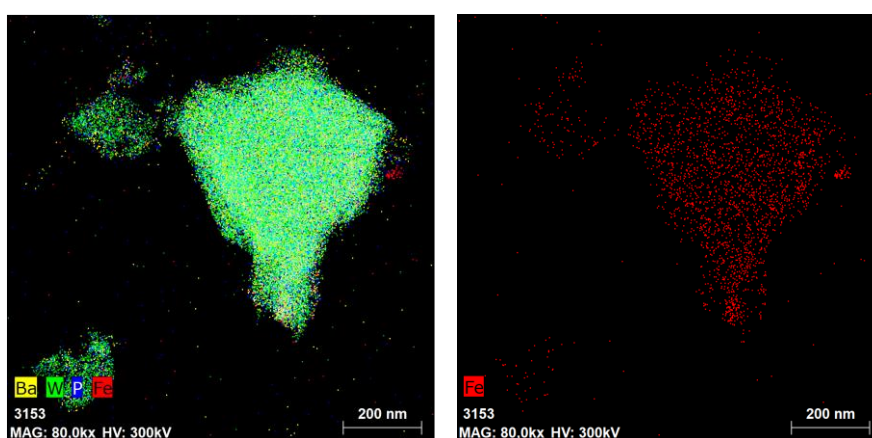


Figure I-33. EDS Mapping of  $\text{Ba}(\text{PO}_4)_2\text{Fe}_{0.22}\text{W}_{3.78}\text{O}_9$  crystals with Barium in yellow, tungsten in green, iron in red and phosphorus in blue.

### I.1.7. Partial conclusion

In summary, we have synthesized a completely new series of monophosphate tungsten bronzes, which exhibit both similarities and significant differences compared to their parent phosphate tungsten bronzes (PTB series). The main innovation of this series stems from the  $[\text{Ba}(\text{PO}_4)_2]^{4-}$  spacer, which separates regular  $\text{WO}_3$ -like layers, thereby imposing an overall trigonal symmetry and an anticipated enhanced 2D metallicity. This is confirmed by DFT calculations, which demonstrate that the electronic structure of the new bronzes displays a distinct 2D character with concealed Fermi surface nesting. Despite these characteristics, the anticipated CDW-like instabilities that occur in low-dimensional conductive compounds, including PTBs, are absent in the L-MPTBs. Indeed, the crystal structures of these systems remain unchanged with temperature variations, and they maintain their metallic properties without exhibiting any CDW signatures in terms of structure, resistivity, or thermopower. In

contrast, the systematic CDWs observed in previous bronzes are attributed to electronic localizations along specific nesting vectors, often interpreted as Peierls-like transitions permissible in orthorhombic/monoclinic symmetries but not in trigonal symmetry. The influence of the rigid  $[\text{Ba}(\text{PO}_4)_2]^{4-}$  spacer layer likely contributes to maintaining the crystal system at various temperatures, as in-plane atomic displacements are restricted by trigonal symmetry and possibly constrained by the rigid  $[\text{Ba}(\text{PO}_4)_2]^{4-}$  interfacial spacers. Altogether, structural studies physical properties measurements and DFT calculations unravel this counterintuitive behaviour and show that besides the influence of the phosphate spacers, the antipolar displacement of the tungsten atoms along with their concomitant induced polarity achieve the equivalent to charged domain walls in ferroelectrics. This effect genuinely increases the carrier concentration towards the centre of the  $\text{WO}_3$  blocks and thus, preserves the 2D metallic character across the whole series. This sets the path for a novel design scheme to induce 2D metallic behaviour in layered oxides and related compounds.

Attempts to isomorphic substitution of tungsten by molybdenum suggest an expansion of the L-MPTB family to  $\text{Ba}(\text{PO}_4)_2\text{W}_{m-x}\text{Mo}_x\text{O}_{3m-3}$  with  $x \leq 1$ . Additionally, attempts to substitute Fe for W in  $\text{Ba}(\text{PO}_4)_2\text{W}_{4-x}\text{Fe}_x\text{O}_9$  ( $m = 4$ ) have been possible up to  $x = 0.22$ . Single crystal X-ray diffraction (SC-XRD) confirmed the presence of Fe in the octahedral layers, with a refined structure model showing uniform distribution over the two metal sites. This substitution did not significantly alter the lattice parameters, indicating minimal structural distortion. All these findings, along with numerous unsuccessful attempts to substitute Ba, further confirm the rigid framework of this series conferred by their spacers, which reduces the possibility of substitution.

## 1.2. New tungsten (VI) ternary phosphate $A(\text{PO}_4)_2(\text{WO}_2)_2$ ( $A = \text{Ba}, \text{Sr}, \text{Pb}$ ) with tunnel like structure

### 1.2.1. Introduction

In the previous chapter, we highlighted the extent to which already largely studied systems, such as tungsten phosphates, can still reveal original compounds because of the sizeable compositional and structural variety that can be reached. The tungsten phosphate of divalent or monovalent cations, are mainly known as monophosphate tungsten bronze with hexagonal tunnels (MPTB<sub>h</sub>), as it was presented in the section 1.1.2. We have seen how their metallic properties, black color, weak magnetism, etc., are induced by tungsten mixed valence. However, considering the phosphates of the fully oxidized tungsten (VI), only a few compounds have been reported:  $A_2\text{MoO}_2\text{P}_2\text{O}_7$  ( $A = \text{K}, \text{Rb}, \text{or } \text{NH}_4; M = \text{W}, \text{Mo}$ ) [91–93],  $\text{AMo}_2\text{PO}_4$  ( $A = \text{Na}$  and  $\text{Ag}, \text{Cs}, \text{Tl}$  and  $\text{K}$  only with  $\text{Mo}$ ;  $M = \text{Mo}, \text{W}$ ) [94–97],  $\text{Cs}_3\text{W}_3\text{PO}_{13}$  [98], and a large number of polyoxometalate salts, such as Keggin type  $\text{A}_3\text{PM}_{12}\text{O}_{40}$  ( $A = \text{K}, \text{Cs},$  and  $\text{Rb}$  only for  $\text{Mo}$ ;  $M = \text{Mo}, \text{W}$ ) [99–101]. Notably, some molybdenum and tungsten phosphates exhibit distinct compositions, which is somewhat surprising given their close crystallochemistry. The analysis of this aspect will be central in this chapter.

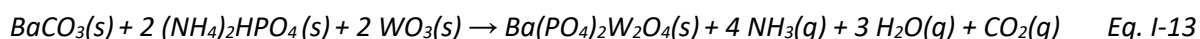
The attempt to achieve mixed-metal substitution of  $\text{W}^{\text{V}}$  by  $(\text{Ni}^{\text{II}}_{1/4}\text{W}^{\text{VI}}_{3/4})$  in the L-MPTB family, similar to that achieved for mm-MPTBs [14,15], led to the discovery of the new "fully-oxidized" tungsten phosphate  $\text{Ba}(\text{PO}_4)_2(\text{W}^{\text{VI}}\text{O}_2)_2$  within the L-MPTB family. Surprisingly, its crystal structure shows a different symmetry compared to that observed in the isoformular molybdenum phosphates  $\text{A}(\text{MoO}_2)_2(\text{PO}_4)_2$  ( $A = \text{Ba}, \text{Pb}, (\text{Li}, \text{K})$ ) [16,102]. In this chapter, we will investigate the origin of these differences. In the frame of this work, due to time limits we have not been able to measure properties in addition to the structural characterization. We will investigate the structural characteristics, focusing on both the differences and common motifs, while also highlighting structural features shared with related phases, such as  $\text{NaWO}_2\text{PO}_4$ , which exhibits yellow photoluminescence (PL) at room temperature [103], unlike its molybdenum phosphate analogue, which lacks any PL effect.

Despite the close crystal chemistry with almost identical ionic radii in octahedral coordination ( $\text{IR}(\text{W}^{\text{VI}}) = 0.60 \text{ \AA}$  and  $\text{IR}(\text{Mo}^{\text{VI}}) = 0.59 \text{ \AA}$  [73],  $\text{W}^{\text{VI}}$  and  $\text{Mo}^{\text{VI}}$  show some distinction. From a chemical point of view  $\text{WO}_3$  exhibits higher optical basicity than  $\text{MoO}_3$ , which is reflected in their oxoacidity, with  $\text{MoO}_3$  being more acidic [104]. As a result,  $\text{MoO}_3$  forms stronger metal-

oxygen bonds compared to  $WO_3$  [105]. Spectroscopic studies on mixed oxide thin films, such as  $(MoO_3)_{1-x}(WO_3)_x$ , show how oxoacidity influences the vibrational modes and structural properties of these materials [106]. From a crystallographic point of view, the most stable  $m-WO_3$  [107] and  $o-MoO_3$  compounds [108] exhibit different crystal structures which emphasize some distinctions. In the  $PO_{2.5}-MO_3$  ( $M = W$  or  $Mo$ ) systems, the tungsten(VI) display ortho [109] and diphosphate [110] structures, while for the Molybdenum(VI) only the diphosphate structure exists [111]. Even more, the Molybdenum(VI), unlike the tungsten(VI) and the Chromium(VI), displays a number of different coordination geometries and various structures and bonding situations, indicating its more adaptable bonding character [112].

### 1.2.2. Synthesis

Polycrystalline samples of  $Ba(PO_4)_2(WO_2)_2$ ,  $Sr(PO_4)_2(WO_2)_2$ , and  $Pb(PO_4)_2(WO_2)_2$  were synthesized using the conventional solid-state route. The first synthesized was  $Ba(PO_4)_2(WO_2)_2$ , but generally we used the same process, starting from a stoichiometric mixture of  $BaCO_3$  (Alfa aesar, 99%),  $SrCO_3$  (Alfa aesar, 99%) and  $PbO$  (Alfa aesar, 99,9 %) respectively with  $(NH_4)_2HPO_4$  (ACROS organics, 99%) and  $WO_3$  (Fulka Analytical, 99.9%) according to the following chemical equations:



Mixtures of the starting materials were ground in an agate mortar, placed in a corundum crucibles and heated in air at 1073 K for 2 days and then cooled to room temperature. The reaction products generally show  $WO_3$  as side phase. Unfortunately, although much effort by tuning the  $AO-PO_{2.5}-WO_3$  system ( $A = Ba, Pb, Sr$ ), the surplus of  $WO_3$  systematically remained in our samples, even after targeting sub  $W$ -stoichiometry, *e.g.* of  $Ba(PO_4)_2(WO_2)_{1.8}$ .

Routine X-ray powder diffraction (XRPD) for sample purity verification was performed on a Bruker D8 Advance diffractometer with a Bragg-Brentano geometry using monochromated  $Cu-K\alpha_1$  radiation in the range  $2\theta = (5-80)^\circ$  with  $0.02^\circ$  steps and 0.5 seconds per step.

Synchrotron powder diffraction (SR-PD) was performed at the Alba-synchrotron source (MSPD diffractometer) with  $\lambda = 0.41 \text{ \AA}$ , at room temperature (RT) for the three samples (A = Ba, Sr, Pb).

### 1.2.3. Structure refinement and description

#### 1.2.3.1 Crystal structure analysis of $A(\text{PO}_4)_2\text{WO}_2$ (A = Ba, Sr, Pb)

For  $\text{Ba}(\text{PO}_4)_2\text{WO}_4$ , the trigonal unit cell ( $a = 11.5083(9) \text{ \AA}$ ,  $c = 6.3411(5) \text{ \AA}$ ) was determined using Dicvol [113] with standard laboratory XRPD data. For A = Pb and Sr a similar cell allow for indexation of the pattern,  $\text{Pb}(\text{PO}_4)_2\text{WO}_4$ :  $a = 11.3540(4) \text{ \AA}$ ,  $c = 6.3159(2) \text{ \AA}$ ;  $\gamma = 120^\circ$  and  $\text{Sr}(\text{PO}_4)_2\text{WO}_4$ :  $a = 11.3506(6) \text{ \AA}$ ,  $c = 6.3187(4) \text{ \AA}$ ;  $\gamma = 120^\circ$ . For the Ba compound the structure was resolved using synchrotron X-ray diffraction data collected at room temperature (RT) at the Alba synchrotron source (MSPD diffractometer) with  $\lambda = 0.41 \text{ \AA}$ . We used a direct-space approach through the program FOX (Free Object for Crystallography) [114] for this task.

FOX (Free Object for Crystallography) is an open-source program that allows structure resolution in direct space using the reverse Monte Carlo algorithm for global optimization. The structure can be described using any combination of isolated atoms, molecules, or polyhedra (e.g.  $[\text{PO}_4]$ ). The structure can be determined without any information about the connections between these building blocks. Knowing certain information (a priori information), such as lattice parameters, atomic ratios, the number of sites and the connectivity of certain groups of atoms, such as the phosphates, the use of rigid-body molecules allowed for obtaining a faster solution [114]. The FOX program refines the structure by minimizing the R- value.

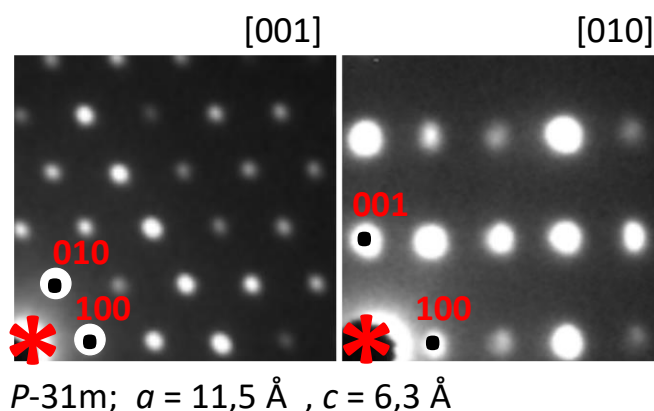


Figure I-34.  $\text{Ba}(\text{PO}_4)_2\text{WO}_2$  ED patterns projected along a)  $[001]$  and b)  $[010]$  directions.

The lattice parameters were obtained from the iterative DICVOL [113] routine and confirmed by Transmission Electron Microscopy (TEM) (see Figure I-34) (see Figure I-34), as well as the Ba:W:P ratio of 1:2:2 determined by TEM and coupled with EDS chemical analysis. Additionally, we employed solid state  $^{31}\text{P}$  MAS-NMR (Magic-Angle Spinning Nuclear Magnetic Resonance) analysis that were conducted at 161.9 MHz on a 9.4 T in AVANCE II, Bruker spectrometer. This analysis indicated a single phosphorus site, as the NMR spectrum showed a single well-defined peak, see Figure I-35. All of this information was used as “a priori information” to obtain a preliminary crystal structure model using the FOX program. After the FOX stage, the crystal structure was refined against the SC-PD data using JANA2006 [61].

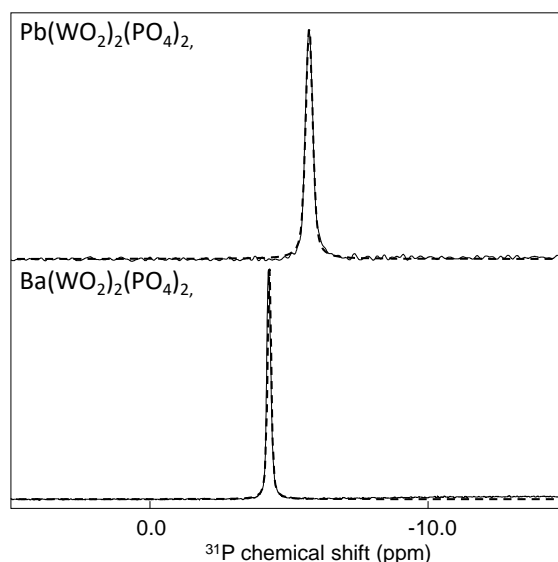


Figure I-35.  $^{31}\text{P}$ -MAS NMR spectra of  $\text{Pb}(\text{PO}_4)_2(\text{WO}_2)_2$  and  $\text{Ba}(\text{PO}_4)_2(\text{WO}_2)_2$  isotropic chemical shift relative to  $\text{H}_3\text{PO}_4$ .

**$\text{Ba}(\text{PO}_4)_2(\text{WO}_2)_2$**  crystallizes in the trigonal space group  $P\bar{3}1m$  (No. 162) with the following cell parameters:  $a = 11.5083(9)$  Å,  $c = 6.3411(5)$  Å. The crystal structure was solved from synchrotron powder diffraction (SR-PD) data (see Table A 0-6-8 in the appendix section for more details), and refined to  $R = 1.74\%$  (see Figure I-36a). The crystal structure features two independent Ba sites, one W, one P, and four O. tungsten(VI) is in an octahedral coordination with two short ( $1.782(7)$  Å), one medium ( $1.823(6)$  Å) and three long distances ( $2.177(5)$  Å and  $2 \times 2.155(5)$ ) (see Table A 0-7).

**Pb(PO<sub>4</sub>)<sub>2</sub>(WO<sub>2</sub>)<sub>2</sub>** crystallizes in the trigonal space group *P*-31m (No. 162) with the following cell parameters: *a* = 11.5083(9) Å, *c* = 6.3411(5) Å. Our Rietveld refinement of the Synchrotron data (see Figure I-36b) could only be achieved when Pb(1) was positioned at coordinates (0 0 0) instead of (0 0 1/2) in the case of Ba(1) in Ba(PO<sub>4</sub>)<sub>2</sub>(WO<sub>2</sub>)<sub>2</sub>. Meanwhile, Pb(2) (1/3 2/3 1/2) retains identical coordinates to Ba(2).

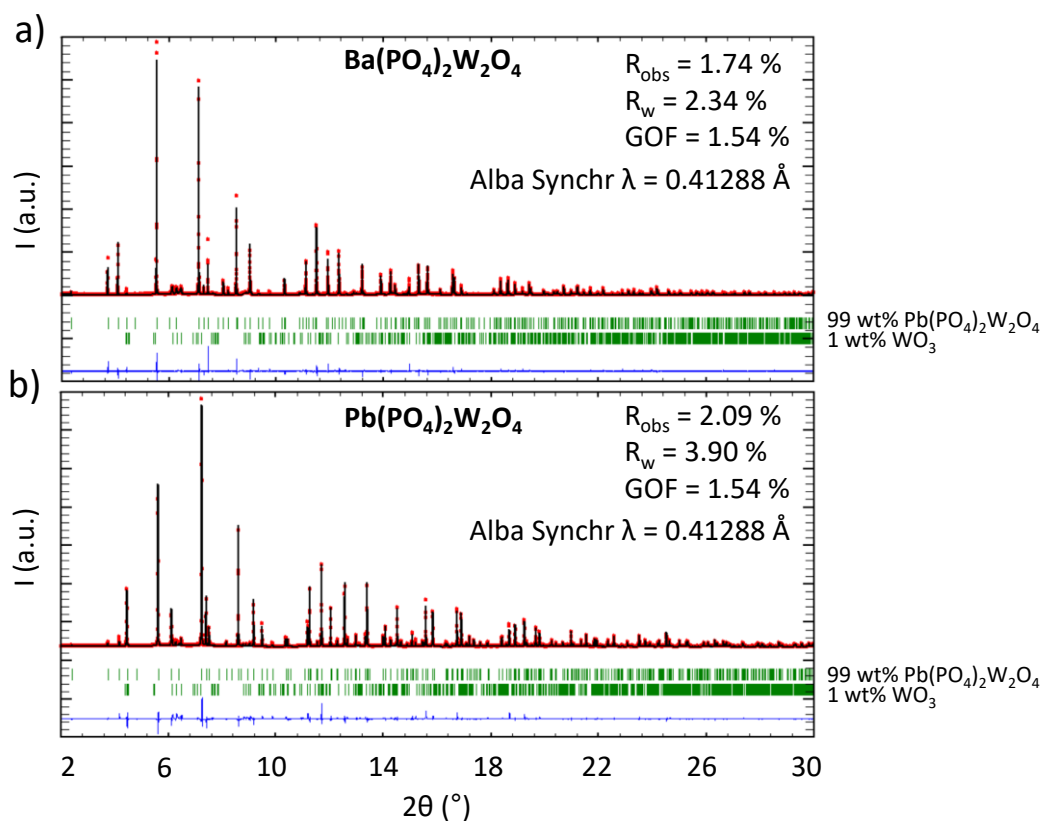


Figure I-36. Rietveld refinement on synchrotron powder diffraction data for a) Ba(PO<sub>4</sub>)<sub>2</sub>(WO<sub>2</sub>)<sub>2</sub> and b) Pb(PO<sub>4</sub>)<sub>2</sub>(WO<sub>2</sub>)<sub>2</sub>.

**Sr(PO<sub>4</sub>)<sub>2</sub>(WO<sub>2</sub>)<sub>2</sub>** is isotypic to Ba(PO<sub>4</sub>)<sub>2</sub>(WO<sub>2</sub>)<sub>2</sub> with the cell parameters: *a* = 11.3506(6) Å, *c* = 6.3187(4) Å;  $\gamma = 120^\circ$ . Refinement was impossible due to unidentified impurities. Instead, we just refined the scale factor on the SR-XRPD data based on two models derived from Ba and Pb. The best fit came from adjusting the scale factor in the Ba model, although the R = 3.76 % was not very decisive, some reflections in particular (0 0 1) and (1 0 1), showed clear enhancements of the fitting of the peak shape (see Figure I-37a, b).

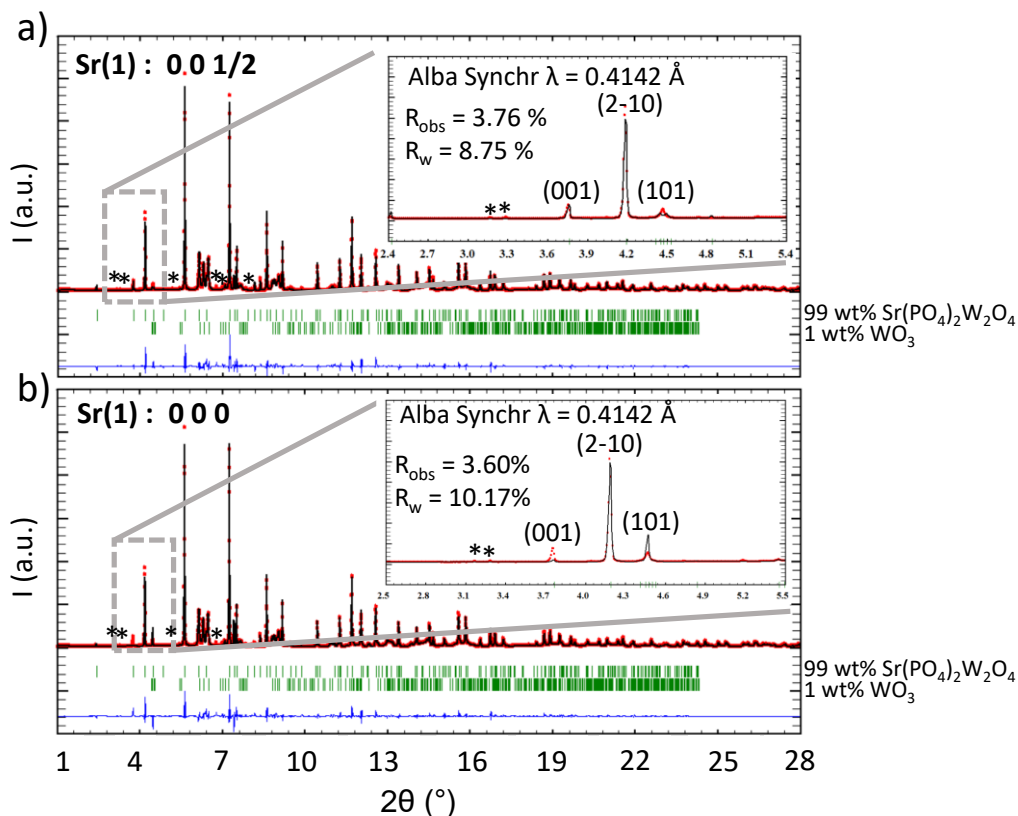


Figure I-37. Comparison between rietveld refinement on synchrotron powder diffraction data of  $\text{Sr}(\text{PO}_4)_2(\text{PO}_4)_2$  for a)  $\text{Sr}(1)$  at  $(0\ 0\ 1/2)$  Vs. b)  $\text{Sr}(1)$  at  $(0\ 0\ 0)$ .

### I.2.3.2 Structure description of $\text{A}(\text{PO}_4)_2(\text{WO}_2)_2$ ( $\text{A} = \text{Ba}, \text{Sr}, \text{Pb}$ )

**Tunnel-like structure and cation distribution.** The basic building units consist of  $\text{WO}_6$  octahedra connected to each other through  $\text{PO}_4$  tetrahedra. Each  $\text{WO}_6$  octahedron shares four of its corners with  $\text{PO}_4$  groups, leaving two free corners with short W-O bonds of  $1.7826(1)$  Å. These short distances point to the exterior of  $[\text{WO}_2\text{O}_4\text{PO}_4]_3$  rings (see structure Figure I-38a, b). These rings form tunnels where the independent divalent cations  $\text{A}(1)$  reside. In addition to the previously described tunnels, another type of tunnel is present at their junctions. These junctions form 1D channels, which are occupied by the independent divalent cations  $\text{A}(2)$ . These tunnels can also be viewed as constructed from three  $[\text{WO}_3\text{O}_3\text{PO}]_\infty$  ribbons connected together through W-O-P bridges (Figure I-38a, b). Such  $[\text{MO}_3\text{O}_3\text{PO}]_\infty$  ribbons are building blocks found in several compounds, such as  $\text{Mo}(\text{OH})_3(\text{PO}_4)$  [19] (see Figure I-38a, b),  $\text{MoO}_2\text{PO}_3\text{OH}\cdot\text{H}_2\text{O}$  [20], and  $\beta\text{-LiMoPO}_6$  [21], and also in  $\text{A}(\text{MoO}_2)_2(\text{PO}_4)_2$  ( $\text{A} = \text{Ba}, \text{Pb}, (\text{Li}, \text{K})$ ) [10] (Figure I-38e). The positioning of  $\text{A}(1)$  differs between  $\text{Ba}(\text{WO}_2)_2(\text{PO}_4)_2$  and  $\text{Pb}(\text{WO}_2)_2(\text{PO}_4)_2$ , while  $\text{A}(2)$  remain with the same coordinates at  $(1/3, 2/3, 1/2)$  in the two compound.  $\text{Ba}(1)$  is found at  $(0, 0, 1/2)$  while  $\text{Pb}(1)$  is also at  $(0, 0, 1/2)$ . The cross-section of the tunnels and

channels projected along the [110] direction, shown in Figure I-38c, highlights the distribution of the Ba(1) and Ba(2) ions in a square lattice with empty sites at  $z = 0$ . In contrast, Pb(1) and Pb(2) are organized in a hexagonal lattice with empty sites at  $z = 1/2$  for Pb(1) and  $z = 0$  for Pb(2) (Figure I-38d). The two barium and lead sites have different coordination. Ba(1) and Pb(1) have hexagonal-prismatic 12-fold coordination ( $12 \times d(\text{Ba}(1)\text{-O}(4)) = 3.079(7) \text{ \AA}$ ,  $12 \times d(\text{Pb}(1)\text{-O}(4)) = 3.006(1) \text{ \AA}$ ). The 12 involved corners are two by two, the edges of six  $\text{PO}_4$  groups. Ba(2) and Pb(2) are at the centre of a regular  $\text{AO}_6$  ( $A = \text{Ba, Pb}$ ) octahedron ( $6 \times d(\text{Ba}(2)\text{-O}(2)) = 2.514(6) \text{ \AA}$ ,  $6 \times d(\text{Pb}(2)\text{-O}(2)) = 2.078(6) \text{ \AA}$ ), which is a relatively rare coordination for alkaline-earth elements.

**Topological Comparison.** The crystal structure of the isoformular  $\text{A}(\text{MoO}_2)_2(\text{PO}_4)_2$  ( $A = \text{Ba, Sr, Pb, (Li,K)}$ ) [16,102] is shown on the Figure I-38e). Surprisingly, besides obvious similarities, notably the existence of channels built from an arrangement of ribbons of  $[\text{MoO}_3\text{O}_3\text{PO}]_\infty$  ribbons that host A cations ( $A = \text{Ba, Pb, (Li,K)}$ ), the two families are polymorphic (Figure I-38e). Indeed, in the  $\text{Ba}(\text{MoO}_2)_2(\text{PO}_4)_2$  the monoclinic symmetry is such that the short Mo-O distances (two in cis positions per  $\text{MoO}_6$  octahedra) are distributed in a complex manner both inside and outside the channels. Then the bridging phosphates Mo-O-P oxygen via longer Mo-O bonds lock a 3D framework with 1D chain. It can be finely visualized by the scheme of the P-W chains, shown in the Figure I-38b with same black, in-plane and red-out of plane colour code. Their 3D assembly is shown in the Figure I-39b Concerning the Ba distribution is similar to the  $\text{Ba}(\text{WO}_2)_2(\text{PO}_4)_2$ , leaving unoccupied rows of possible positions at  $z = 0$ . In comparison, the crystal structure the alkali/silver-based  $\text{AMoO}_2\text{PO}_4$  ( $A = \text{Na and Ag, Cs and K only with Mo; M = Mo, W}$ ) [94–97] (see Figure I-38f) share the same 3D-framework tunnels like structure than  $\text{A}(\text{MoO}_2)_2(\text{PO}_4)_2$  ( $A = \text{Ba, Sr, Pb, (Li,K)}$ ), although more distorted see Figure I-39c. The hosting of monovalent cations naturally doubles the channel occupancy such that both the  $z = 0$  and  $z = 1/2$  positions are occupied by the  $\text{A}^+$  cations (see Figure I-38f). In a topological view, since two terminal oxygen atoms of  $\text{MoO}_6$  are not involved in the formation of the 3D topological structure,  $\text{MoO}_6$  and  $\text{PO}_4$  groups can be seen as 4-connected nodes.

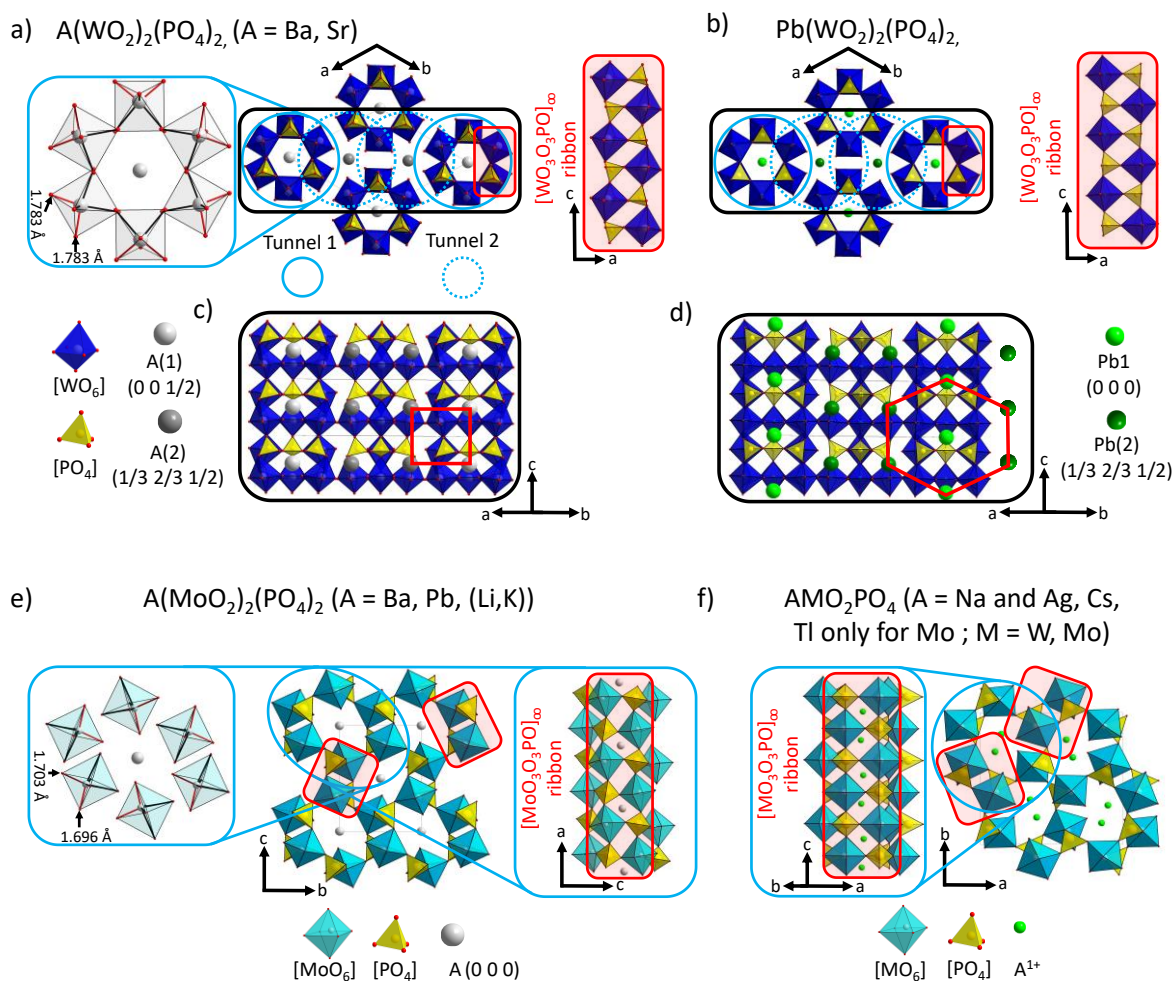


Figure I-38. a, b) Crystal structures of  $A(\text{PO}_4)_2(\text{WO}_2)_2$  ( $A = \text{Ba}, \text{Sr}, \text{Pb}$ ) along different projections.  $\text{WO}_6$  octahedra and  $\text{PO}_4$  tetrahedra form 1D  $[\text{WO}_3\text{O}_3\text{PO}]_\infty$  ribbons interconnected through W-O-P bridges, creating tunnels that host A(1) and A(2) cations. c, d) Cross-sections along  $[110]$  show square-lattice (Ba, Sr) or hexagonal-lattice (Pb) distributions of cations in the channels. (e) Similar structural motifs are observed in related  $\text{AMoO}_2\text{PO}_4$  compounds. Short W-O distances define the exterior of  $[\text{WO}_4\text{O}_2\text{PO}_4]_3$  rings and channel walls.

The crystal structures of  $A(\text{MoO}_2)_2(\text{PO}_4)_2$  ( $A = \text{Ba}, \text{Sr}, \text{Pb}, (\text{Li}, \text{K})$ ) and  $A(\text{MO}_2)(\text{PO}_4)$  (with  $A = \text{Na}, \text{Ag}, \text{Cs}, \text{K}$ , and  $M = \text{Mo}, \text{W}$ ) share similarities, featuring tunnels formed by zig-zag chains along the c-axis for the  $A(\text{MoO}_2)_2(\text{PO}_4)_2$  and along the b-axis for the  $A(\text{MO}_2)(\text{PO}_2)$  ( $A = \text{Na}$  and  $\text{Ag}, \text{Cs}$  and  $\text{K}$  only with  $\text{Mo}$ ;  $M = \text{Mo}, \text{W}$ ) connected by W-O-P-O-W bridges, which house monovalent or divalent cations and form a 3D-framework tunnels. In contrast,  $\text{Ba}(\text{PO}_4)_2(\text{WO}_2)_2$  has distinct tunnels made of  $[\text{WO}_2\text{O}_4\text{PO}_4]_3$  rings connected by P-O-W connections (black in plane) running along threefold roto-inversion and connected also through W-O-P bridges (red out-of-plane). This construction leads to distinct and disconnected 1D-tunnels (see Figure I-39c).

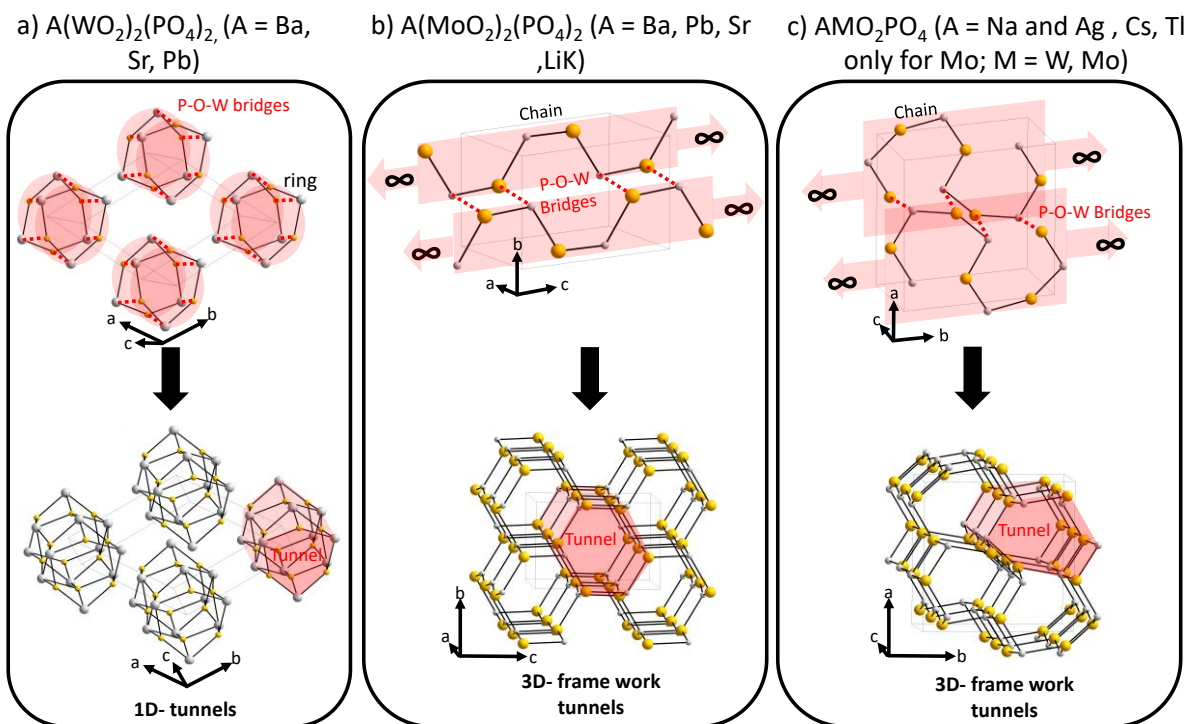


Figure I-39. Topological view of the structure showing the main building units connected by W-O-P bridges in a)  $A(PO_4)_2(WO_2)_2$  compared to b)  $A(MoO_2)_2(PO_4)_2$  (A = Ba, Sr, Pb, (Li, K)) and c)  $AMo_2PO_4$  (A = Na, Ag, Cs, K, M = Mo, W) where  $PO_4$  groups are in yellow spheres and  $MoO_6$  octahedra are in grey spheres.

Finally we end up with three models in competition labelled for our study:

- 14-BaW stands for the structure type of the  $Ba(PO_4)_2(MoO_2)_2$  with the space group  $P2_1/c$  (No. 14).
- 162-BaW stand for the structure type of the  $Ba(PO_4)_2(MoO_2)_2$  with the space group  $\bar{P}31m$  (No. 162) and Ba(1) at (0 0 1/2).
- 162-PbW stand for the structure type of the  $Pb(PO_4)_2(MoO_2)_2$  with the space group  $\bar{P}31m$  (No. 162) and Pb(1) at (0 0 1/2).

## I.2.4. Dynamic and thermodynamic stability and its temperature dependence

### I.2.4.1 USPEX (Universal Structure Predictor: Evolutionary Xtallography) and phonon calculation

To understand their relative stabilities, when assorted with M = Mo and W respectively, we have used the USPEX (Universal Structure Predictor: Evolutionary Xtallography) [115], a computational software used to predict crystal structures. We have also used Phonopy [116] for phonon calculation to predict the dynamic stability of these structures.

This work was performed in collaboration with A. Sayede and N. Harrati from the UCCS (Unité de catalyse et de chimie du solide). It uses a method developed by the Oganov laboratory since 2004 [8]. According to their website, predicting crystal structures is an old and major problem in theoretical crystal chemistry [117,118]. In 1988 John Maddox wrote that:

*"One of the continuing scandals in the physical sciences is that it remains in general impossible to predict the structure of even the simplest crystalline solids from a knowledge of their chemical composition. Solids such as crystalline water (ice) are still thought to lie beyond mortals' ken".*

USPEX code solves this problem as it has proven to be a very efficient and reliable method, leading to a number of important findings [117,118]. USPEX can predict the stable and metastable crystal structures of a material starting only from its chemical composition. This is particularly useful for designing new materials "in silico" and understanding the structures of existing ones, thus making it a complementary tool to empirical research.

The Evolutionary Algorithm (EA) implemented in USPEX (Universal Structure Predictor: Evolutionary Xtallography) simulates the process of natural selection to predict stable crystal structures [8,115]. The algorithm starts with a population of randomly generated structures, which are then locally optimized and ranked according to their fitness, typically measured by their Density Functional Theory (DFT) calculated free energy. The EA then selects the most promising structures to "breed" the next generation through various genetic operations, including inheritance (combining structural fragments from parent structures), mutation (random changes in lattice parameters or atomic positions), and occasionally specialized moves such as coordinate flipping or cell splitting. Each new generation undergoes local optimization and fitness evaluation, and this iterative process continues for a predefined number of generations or until certain convergence criteria are met. This evolutionary strategy enables USPEX to efficiently navigate the complex energy landscape of possible crystal structures, often identifying the global minimum (most stable structure) and several competing metastable structures. Dynamical stability is verified through phonon calculations. USPEX, when combined with ab initio calculations, requires considerable computing resources, which is why it is essential to have access to high-performance computing resources.

A structure that appears stable based on its energy alone may actually be dynamically unstable [119]. Phonon calculations elucidate the vibrational properties of a crystal, and the presence of imaginary (negative) frequencies in the phonon spectrum signals instability for certain atomic displacements. Phonon calculations are therefore an essential validation step to ensure that predicted structures are not only energetically favourable but also dynamically stable. This verification is crucial for the potential experimental realization and practical applications of the predicted structures, ensuring their viability under real-world conditions.

In our study, we used this feature starting with the chemical formula of the three polymorphs, namely: In our study, we used these features, starting with the chemical formula of three polymorphs, namely, to determine which structure is predicted to be thermodynamically stable for a given chemical formula.

to determine which structure is predicted to be thermodynamically stable for a given chemical formula.

#### *1.2.4.2 Ba(PO<sub>4</sub>)<sub>2</sub>(MO<sub>2</sub>)<sub>2</sub>, M = Mo Vs. W*

The results obtained from applying the USPEX algorithm is shown in Figure I-40a based on the based on the simple Ba(PO<sub>4</sub>)<sub>2</sub>(MO<sub>2</sub>)<sub>2</sub> formula with the only constraint being the geometry of the PO<sub>4</sub> group (prior knowledge). This graphic shows the variation in free enthalpy for several generated polymorphs (red dots) and identified ones (green dots), The number next to the lines refers to the space group number.

We observe the recurrence of two polymorphs over the number of structures generated, indicating their thermodynamic stability. The most stable is described in the 14-BaMo structure type, corresponding to its experimental structure, and the 162-BaW structure type, which comes in second place ( $\Delta E = 0.408$  eV/unit). This outcome validates its use.

The same process was also applied to the chemical formulas Ba(PO<sub>4</sub>)<sub>2</sub>(WO<sub>2</sub>)<sub>2</sub> the results are shown in Figure I-40b. The 14-BaMo structure was predicted to be the most thermodynamically stable, followed by the 162-BaW ( $\Delta E = 0.290$  eV/unit). Several generated identified instable polymorphs (green dots) are shown in Figure I-40c.

The experimental preference was not respected. USPEX predicts that the three compounds are thermodynamically stable in the 14-BaW type structure.

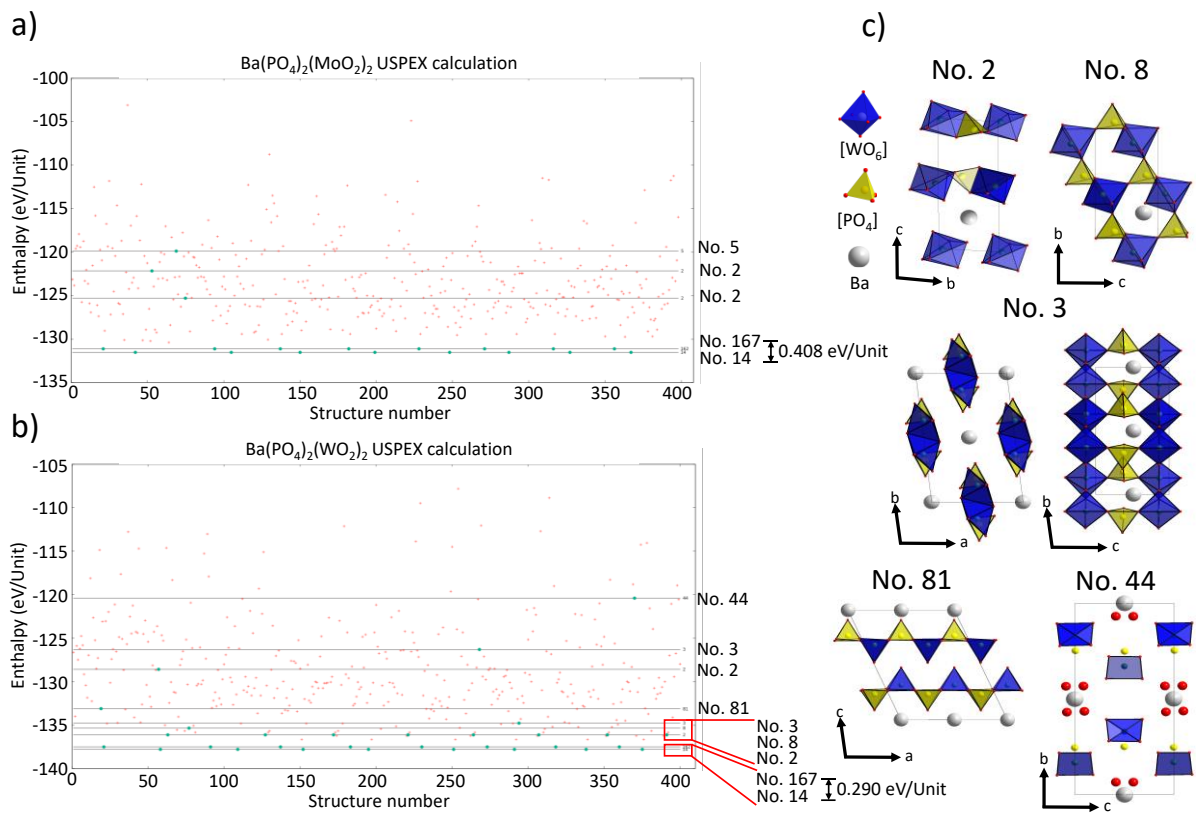


Figure I-40. Calculation *Ab initio* structural prediction using the USPEX evolutionary algorithm for a)  $Ba(PO_4)_2(MoO_2)_2$  and b)  $Ba(PO_4)_2(WO_2)_2$  showing different generated population (in red) and identified (in green) with their space group number where the monoclinic  $P21/c$  (No. 14) and the trigonal  $P-31m$  (No. 167) are predicted with a certain relative stability. c) Different examples of generated structures with the chemical formula  $Ba(PO_4)_2(WO_2)_2$ .

To unravel this problem, we calculate the phonon modes for  $A(PO_4)_2(MO_2)_2$  ( $A = Ba, Pb$ ;  $M = Mo, W$ ) to determine the dynamic stability of these compounds in different polymorphs (see Figure I-41a-d).

The  $A(PO_4)_2(MoO_2)_2$  described in its experimentally observed structure, 14-BaW, doesn't exhibit negative frequencies, implying dynamic stability (Figure I-41a)., when described in a structure type 162-BaW, it exhibits forbidden imaginary phonon modes leading to negative frequencies (Figure I-41a).

For  $Ba(PO_4)_2(WO_2)_2$ , phonon calculations show dynamic instability in the 14-BaMo structure (see Figure I-41c) for the same reasons mentioned earlier. While it shows dynamic stability in its experimental structure 162-BaW (see Figure I-41d). The presence of imaginary harmonic modes in the spectrum indicates that a structure is not a local minimum on the structural

potential-energy surface and is instead a saddle point or a hilltop [120]. We did not go in deeper exploration of what modes were concerned, at this level.

In fact, as gathered in the Table I-1, the monoclinic Mo-polytype was obtained as the most stable for all tested tungstate (A = Ba, Pb and Sr) and we assume that their inexistence in this crystallographic form is due to dynamic instability.

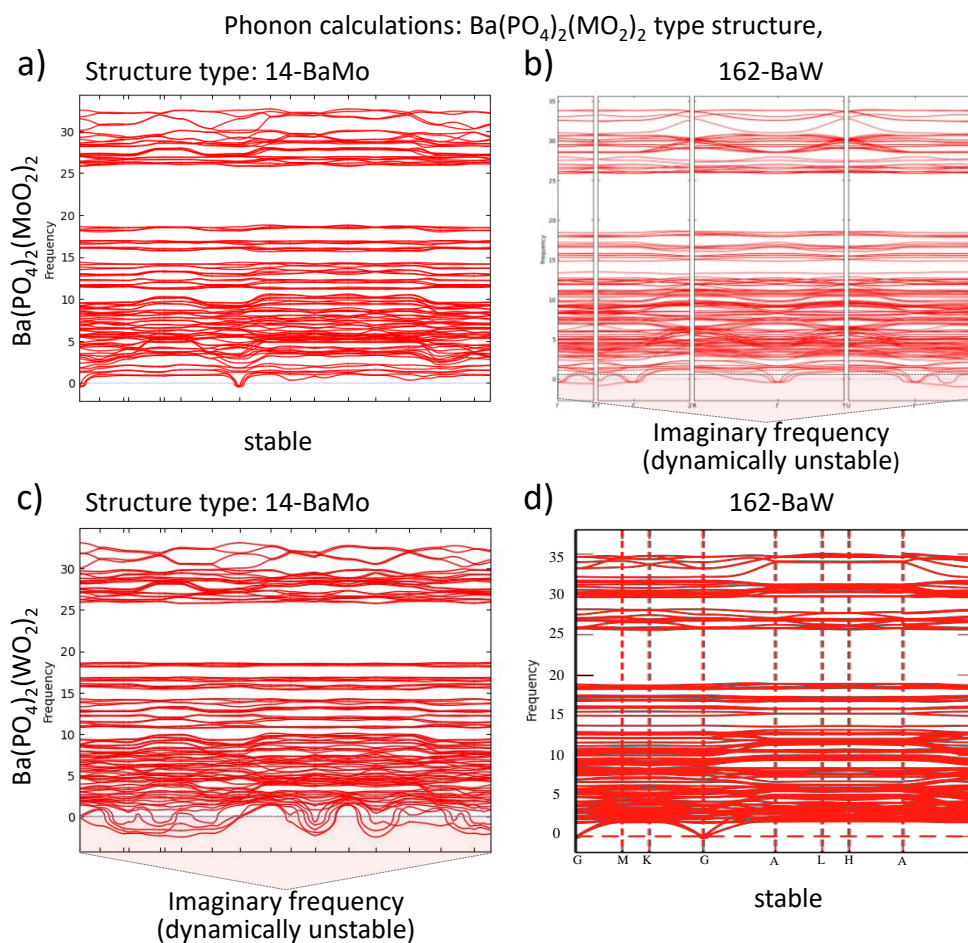
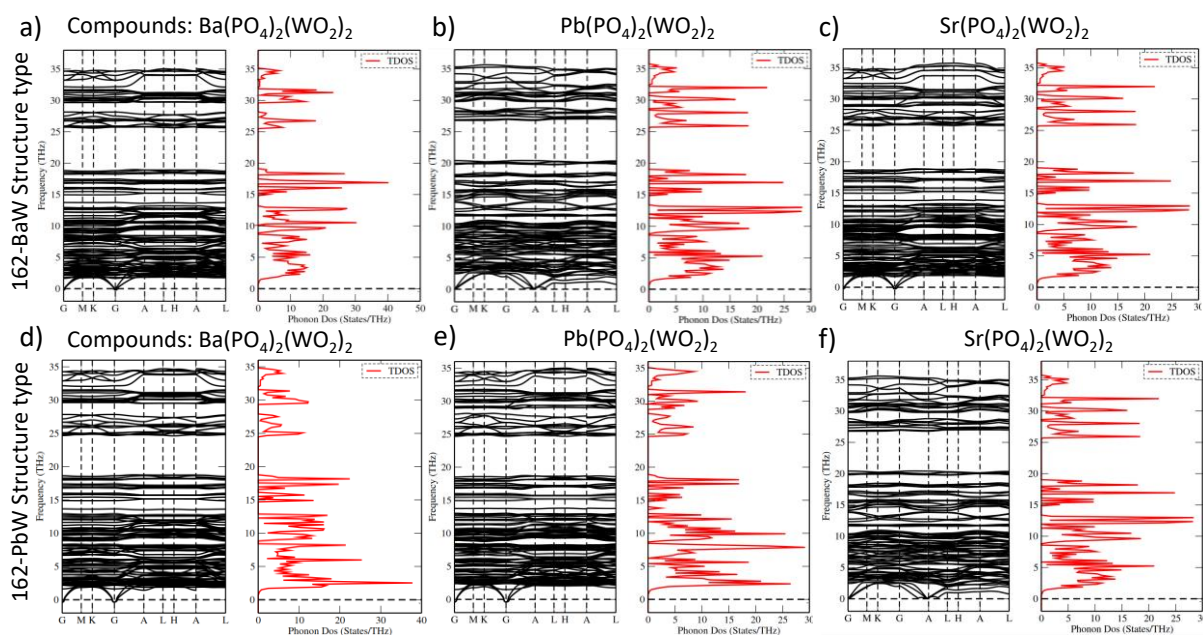


Figure I-41. The phonon dispersion from Phonopy associated with VASP of  $\text{Ba}(\text{PO}_4)_2(\text{MoO}_2)_2$  in structure type a) 14-BaMo and b) 162-BaW shows imaginary frequency frequencies. Similarly, for  $\text{Ba}(\text{PO}_4)_2(\text{WO}_2)_2$  in structure type c) 14-BaMo shows imaginary frequency d) 162-BaW.

#### 1.2.4.3 $\text{A}(\text{PO}_4)_2(\text{WO}_2)_2$ : Selection between the Ba and Pb Structure Type

To go in deeper investigation we have also investigated the trigonal 162-BaW type structure with A(1) at (Z = 1/2) against the 162-PbW type structure, with A(1) (at z = 0) for

$A(\text{PO}_4)_2(\text{WO}_2)_2$  ( $A = \text{Ba}, \text{Pb}, \text{Sr}$ ) and  $\text{Ba}(\text{PO}_4)_2(\text{MoO}_2)_2$ .



*Figure I-42. The phonon dispersion and their density-of-states (DOS) curves for a structure type 162-BaW for a chemical formula a)  $\text{Ba}(\text{PO}_4)_2(\text{O}_2)_2$ , b)  $\text{Pb}(\text{PO}_4)_2(\text{O}_2)_2$  and c)  $\text{Sr}(\text{PO}_4)_2(\text{WO}_2)_2$ . in structure type a) 14-BaMo and b) 162-BaW shows imaginary frequency frequencies. Similarly, for a structure type 162-PbW for a chemical formula a)  $\text{Ba}(\text{PO}_4)_2(\text{O}_2)_2$ , b)  $\text{Pb}(\text{PO}_4)_2(\text{O}_2)_2$  and c)  $\text{Sr}(\text{PO}_4)_2(\text{O}_2)_2$ . All show no imaginary frequencies*

USPEX calculation shows that all the models appear dynamically stable (Figure I-42), and refute the systematic monoclinic “most-stable” USPEX solutions. Since USPEX calculations require significant computation resources and time, we also used accurate DFT calculations to determine the energy of  $\text{Ba}(\text{PO}_4)_2(\text{WO}_2)_2$ ,  $\text{Sr}(\text{PO}_4)_2(\text{WO}_2)_2$  and  $\text{Pb}(\text{PO}_4)_2(\text{WO}_2)_2$  in two polymorph forms 162-BaW and 162-PbW.

The accurate DFT relaxation (with electronic convergence criteria:  $1 \cdot 10^{-09}$  eV (VASP), ionic convergence criteria:  $-3 \cdot 10^{-03}$  eV (VASP)) are consistent with those from USPEX which showed that all these compounds are predicted to be stable in the 14-BaMo structure (see Table I-1). However, the second most stable structure depends on whether energy is calculated per formula unit or per volumetric unit. In terms of energy per formula unit,  $\Delta E = 0.01$  to  $0.06$  eV/FU indicates that the best model is the most stable one for 162-PbW though it is very close to BaW model. However, it seems that the compacity of the structural model intervenes, because the energy per volume unit is systematically in favour of the experimental cell, see Table I-1.

Table I-2.  $A(PO_4)_2(WO_2)_2$  ( $A = Ba, Pb, Sr$ ) compounds described in different structure types and the  $\Delta E$  relative to the most stable structure (the lowest energy) from DFT calculations.

Compound	Type Structure	USPEX prediction	$\Delta E$ (eV/UF)	$\Delta E$ (eV/Å <sup>3</sup> )	Cell parameters
Ba(PO <sub>4</sub> ) <sub>2</sub> W <sub>2</sub> O <sub>2</sub>	14-BaMo	Stable	0.000000	0.0000000000	a = 6.44208 Å b = 7.30863 Å c = 10.19270 Å β = 94.7300° V = 478.266402 Å <sup>3</sup>
	162-BaW Exp. Struct.	Metastable	0.300145	<u>0.0005448896</u>	a = 11.86467 Å b = 11.86467 Å c = 6.48473 Å V = 790.558187 Å <sup>3</sup>
	162-PbW	Metastable	<u>0.290375</u>	0.0005648790	a = 11.88764 Å b = 11.88764 Å c = 6.48498 Å V = 793.653456 Å <sup>3</sup>
Pb(PO <sub>4</sub> ) <sub>2</sub> W <sub>2</sub> O <sub>2</sub>	14-BaMo	Stable	0.000000	0.0000000000	a = 6.43117 Å, b = 7.14273 Å c = 10.20022 Å, β = 92.9464° V = 467.939231 Å <sup>3</sup>
	162-BaW	Metastable	0.202840	0.0003930981	a = 11.58914 Å b = 11.58914 Å c = 6.46647 Å V = 752.143175 Å <sup>3</sup>
	162-BaW Exp. Struct.	Metastable	<u>0.177520</u>	<u>0.0003718299</u>	a = 11.56324 Å b = 11.56324 Å c = 6.47108 Å V = 749.317717 Å <sup>3</sup>
Sr(PO <sub>4</sub> ) <sub>2</sub> W <sub>2</sub> O <sub>2</sub>	14-BaMo	Stable	0.000000	0.0000000000	a = 6.43339 Å b = 7.08438 Å c = 10.19915 Å β = 92.9609° V = 464.221850 Å <sup>3</sup>
	162-BaW Exp. Struct.	Metastable	0.296975	<u>0.0004303925</u>	a = 11.56662 Å b = 11.56662 Å c = 6.46690 Å V = 749.272840 Å <sup>3</sup>
	162-PbW	Metastable	<u>0.232725</u>	0.0004458004	a = 11.57726 Å b = 11.57726 Å c = 6.47621 Å V = 751.732459 Å <sup>3</sup>

### I.2.5. Partial conclusion

In summary, polycrystalline samples of  $\text{Ba}(\text{PO}_4)_2(\text{WO}_2)_2$ ,  $\text{Sr}(\text{PO}_4)_2(\text{WO}_2)_2$ , and  $\text{Pb}(\text{PO}_4)_2(\text{WO}_2)_2$  were synthesized and their crystal structures determined via Synchrotron XRPD, all crystallizing in trigonal space group  $P\bar{3}1m$ .  $\text{Ba}(\text{PO}_4)_2(\text{WO}_2)_2$  and  $\text{Pb}(\text{PO}_4)_2(\text{WO}_2)_2$ , sharing  $P\bar{3}1m$  symmetry, exhibit differing A(1) cation positions: Ba(1) at (0, 0, 1/2) and Pb(1) at (0, 0, 0), resulting in two polymorphs. These compounds feature  $[\text{WO}_6]$  octahedra and  $[\text{PO}_4]$  tetrahedra forming tunnels housing A cations, distinct from  $\text{Ba}(\text{PO}_4)_2(\text{MoO}_2)_2$  that shows lower symmetry ( $P2_1/c$ ) with 3D-framework tunnels, contrasting  $\text{Ba}(\text{PO}_4)_2(\text{WO}_2)_2$ 's higher symmetry ( $P\bar{3}1m$ ) and disconnected 1D tunnels. USPEX and phonon calculations provide insights into thermodynamic and dynamic stabilities.  $\text{Ba}(\text{PO}_4)_2(\text{MoO}_2)_2$  is stable both thermodynamically and dynamically, while  $\text{A}(\text{PO}_4)_2(\text{WO}_2)_2$  (A = Ba, Sr, Pb) favours the monoclinic-type structure (14-BaMo). Detailed DFT calculations confirm structural compactness as crucial, favouring the experimental cell energetically. Additionally, phonon calculations confirm  $\text{A}(\text{PO}_4)_2(\text{WO}_2)_2$  (A = Ba, Sr, Pb) stability in experimental structures, irrespective of 162-BaW or 162-PbW polymorphs, but instability in the 14-BaMo structure. All these results are summarized in Figure I-43. This highlights dynamic stability's importance, emphasizing the need for combined USPEX and phonon calculations to ensure predicted structures are both energetically and dynamically stable. USPEX, a tool for structural prediction, represents a promising addition to the future chemist's toolbox.

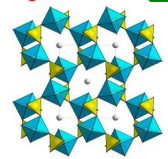
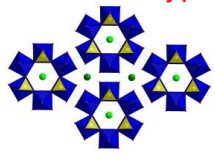
	$\text{Ba}(\text{PO}_4)_2(\text{MoO}_2)_2$	$\text{Ba}(\text{PO}_4)_2(\text{WO}_2)_2$ $\text{Sr}(\text{PO}_4)_2(\text{WO}_2)_2$	$\text{Pb}(\text{PO}_4)_2(\text{WO}_2)_2$
Experimental structure	1 $P2_1/c(14)$ ✓ 	2 $P\bar{3}1m(162)$ - Ba type ✓ 	3 $P\bar{3}1m(162)$ - Pb type ✓ 
USPEX calculation	Structure 1 ✓	Structure 1 ✗	Structure 1 ✗
Phonon calculation	Structure 1 ✓	Structure <del>1</del> 2 3 ?	Structure <del>1</del> 2 3 ?
Accurate DFT relaxation		Structure 2 ✓	Structure 3 ✓

Figure I-43. Summary of the results obtained using various techniques to investigate the stability and predictability of these structures.

## II. Insights into the magnetic behavior of Jahn-Teller active chromium(II) ions in phosphates

### II.1. Introduction

The strongly reducing hexaaqua-chromium(II) complex is readily oxidized in air and, in contrast to the other 3d metals, no monoxide “Cr<sup>II</sup>O”<sup>a)</sup> is known in the solid state. Earlier reports on “Cr<sup>II</sup>O” described red powders with rock-salt type XRPD pattern ( $a = 4.12 \text{ \AA}$ ) which decomposed upon heating into Cr<sub>2</sub>O<sub>3</sub> and mixtures of various chromium carbides [121–124]. Thus, it appears likely that actually some chromium(III) oxide-carbide “Cr<sup>III</sup>(O<sub>0.5</sub>C<sub>0.5</sub>)”, similar to the well-established Sc<sup>III</sup>(O<sub>0.5</sub>C<sub>0.5</sub>) [125] had been obtained. Only recently, results of *ab initio* calculations summarized in the *Materials Project* [17] suggested for “Cr<sup>II</sup>O” several unique crystal structures (*mp*-1283577, *mp*-1302566) besides those related to PdO/CuO (e.g. *mp*-755073 [126]). Yet, according to these calculations, these phases are all metastable with respect to decomposition into Cr(s) and Cr<sub>2</sub>O<sub>3</sub>(s) [126]. This outcome is in line with estimates on the thermodynamic instability of solid “Cr<sup>II</sup>O” based on the stability of Cr<sup>II</sup>O(g) [127], the heats of sublimation for MnO and FeO [127] and eventually the thermodynamic data for Cr(s) and Cr<sub>2</sub>O<sub>3</sub>(s) [127]. Therefore, chromium(II) oxo-compounds were regarded for a long time as non-existent. Nevertheless, during the last decades stabilization of “Cr<sup>II</sup>O” was achieved in some boracite type borate-halogenides (Cr<sup>II</sup><sub>3</sub>B<sub>7</sub>O<sub>13</sub>X with X = Cl [128] [129], Br [130], I [131]), silicates (Cr<sup>II</sup><sub>2</sub>SiO<sub>4</sub> [132], [133]ACr<sup>II</sup>Si<sub>4</sub>O<sub>10</sub> with A = Ca, Sr, Ba [134], [135], Cr<sup>II</sup><sub>4</sub>(Si<sub>2</sub>O<sub>7</sub>)X<sub>2</sub> with X = Cl, Br [136], Cr<sup>II</sup><sub>3</sub>Si<sub>2</sub>O<sub>7</sub> · 1/4AX with AX = NaCl, NaBr, KCl, KBr [137]) and in a large number of (multinary) phosphates, which are summarized in Table II-1 [13-28]. The stabilization of this unusual oxidation state of chromium by a phosphate (silicate, borate) environment is favoured by an inductive effect on the M < O < P(Si, B) bonds. It is related to the peculiar stability of the phosphate and silicate anions towards any kind of redox reaction on one hand and to the strong oxide acceptor behaviour of P<sub>2</sub>O<sub>5</sub> and SiO<sub>2</sub> on the other, therefore stabilizing the low oxidation state. Cr<sup>II</sup><sub>2</sub>P<sub>2</sub>O<sub>7</sub> [138] is a prominent example for this behavior which enabled for the first time deeper insight into the peculiar crystal chemistry of the Jahn-Teller (*JT*) active Cr<sup>2+</sup> ions (*d*<sup>4</sup> electron configuration) in oxo-compounds. Thus, Cr<sup>2+</sup> in oxo-compounds shows almost no crystal-chemical similarity to Cu<sup>2+</sup>, the best-known divalent *JT* active cation. At the same time hints on metal-metal bonding in solid Cr<sup>2+</sup> oxo-compounds (e. g. Cr<sub>2</sub>SiO<sub>4</sub> [132,133], α-Cr<sub>3</sub>(PO<sub>4</sub>)<sub>2</sub> [19,139,140]), similarity to presumably much bigger, electronically

isotropic cations like  $\text{Ca}^{2+}$  or  $\text{Cd}^{2+}$  ( $\text{LiCr}_4(\text{PO}_4)_3$  [141] is isotypic to  $\text{NaCd}_4(\text{PO}_4)_3$  [142] and  $\text{Ca}_5(\text{PO}_4)_2(\text{SiO}_4)$  [143]), and a strong interplay between lattice dynamics, cooperative magnetic effects and the electronic instability caused by the JT effect appear to be characteristic for  $\text{Cr}^{2+}$  ions [138,144]. In addition, the redox behaviour, the geometry and high charge of the  $\text{PO}_4^{3-}$  group offers unique features for tailoring low-dimensional (Low-D) crystal structures, when combined with large ionic-covalent cations.

Table II-1. Summary of divalent chromium and alkali/alkali earth-transition metal (II)-phosphates

Compound	Space group	Cell parameters ( $\text{\AA}$ , $^\circ$ ); Z	Dimensionality <sup>b)</sup>	Reference
$\alpha\text{-Cr}_3(\text{PO}_4)_2$	$P2_12_12_1$ (19)	$a = 8.4849(10)$ , $b = 10.3317(10)$ , $c = 14.206(2)$ ; 8	3D framework	[19,139,140]
$\beta\text{-Cr}_3(\text{PO}_4)_2$	$P2_1/n$ (14)	$a = 4.9653(3)$ , $b = 9.4951(8)$ $c = 6.4839(4)$ ; $\beta = 91.382(4)^\circ$ ; 2	3D framework with M-O-M paths way	[20,145]
$\text{Cr}_2\text{P}_2\text{O}_7$	$C2/m$ ( $\sigma_1 0 \sigma_3$ ) $\bar{1}s$ [(-0.361 (1), 0, 0.471 (1))] ( $T > 285$ K)	$a = 7.0192(5)$ , $b = 8.4063(6)$ , $c = 4.6264(3)$ ; $\beta = 108.6111(64)^\circ$ ; 2	2D layer with M-O-M paths way	[19,138]
$\text{LiCr}_4(\text{PO}_4)_3$	$Pnma$ (62)	$a = 6.1745(12)$ , $b = 14.316(3)$ $c = 10.277(2)$ ; 4	1D chains of M-O-M dimers	[141]
$\text{Mg}_3\text{Cr}_3(\text{PO}_4)_4$	$P2_1/n$ (14)	$a = 4.863(2)$ , $b = 9.507(4)$ , $c = 6.439(2)$ ; $\beta = 91.13(6)^\circ$ ; 1	3D framework with 1D M-O-M chains	[146]
$\text{Mg}_{3.74}\text{Cr}_{2.25}$ ( $\text{PO}_4$ ) <sub>4</sub>	$P2_1/a$ (14)	$a = 6.427(2)$ , $b = 9.363(2)$ , $c = 10.051(3)$ ; $\beta = 106.16(3)^\circ$ ; 2	1D ribbons arranged in layers	[146]
$\text{Ca}_3\text{Cr}_3(\text{PO}_4)_4$	$P-1$ (2)	$a = 8.961(1)$ , $b = 8.994(1)$ , $c =$ $9.881(1)$ , $\alpha = 104.96(2)^\circ$ ; $\beta = 106.03(2)^\circ$ ; $\gamma = 110.19(2)^\circ$ ; 2	1D ribbons arranged in layers	[146]
$\text{Ca}_2\text{Cr}_4(\text{PO}_4)_4$	$C2/c$ (15)	$a = 17.511(2)$ , $b = 4.9933(6)$ , $c = 16.825(2)$ ; $\beta = 117.951(13)^\circ$ ; 4	3D framework with edge sharing trimers	[146]
$\text{CaCrP}_2\text{O}_7$	$P-1$ (2)	$a = 6.312(2)$ , $b = 6.499(2)$ , $c = 6.916(2)$ ; $\alpha = 83.12(3)^\circ$ , $\beta = 88.37(3)^\circ$ , $\gamma = 67.72(3)^\circ$ ; 2	3D framework with M-P-M connections	[147]
$\text{SrCrP}_2\text{O}_7$	$P2_1/n$ (14)	$a = 5.422(2)$ , $b = 8.3254(19)$ , $c = 12.542(4)$ ; $\beta = 90.39(3)^\circ$ ; 4	3D framework with M-P-M connections	[147,148]
$\text{BaCrP}_2\text{O}_7$	$P-1$ (2)	$a = 5.382(8)$ , $b = 7.271(8)$ , $c = 7.589(4)$ , $\alpha = 103.33(7)^\circ$ ; $\beta = 89.91(9)^\circ$ , $\gamma = 93.62(11)^\circ$ ; 2	1D chains of M-O-M dimers	[147]

a) "CrO" is not yet an established compound.

b) Dimensionality refers to the arrangement of magnetoactive cations (superexchange M–O–M pathways) or the induced low-D due to the presence of non-magnetically active cations.

## II.2. The complex 3D-AFM exchange pathways in $\alpha$ - and $\beta$ -Cr<sub>3</sub>(PO<sub>4</sub>)<sub>2</sub>

### II.2.1. Introduction and survey of the literature

#### II.2.1.1 *Synthesis - summary of literature*

The  $\alpha$ -modification of chromium(II) orthophosphate was first synthesized by SCHMIDT [139] reducing CrPO<sub>4</sub> by elemental chromium. An ampoule containing stoichiometric amounts of elemental chromium and CrPO<sub>4</sub>, along with elemental Iodine, was prepared. The resulting internal pressure at 1200°C prevents the collapse of the ampoules. Iodine acted as a mineralizer for crystallization in a tube. To counteract the oxidative effects of I<sub>2</sub>, Cr was added in stoichiometric amounts to form CrI<sub>2</sub>. Temperatures below 1150 °C lead to disproportionation into CrP, Cr<sub>2</sub>O<sub>3</sub>, and Cr<sub>2</sub>P<sub>2</sub>O<sub>7</sub>.  $\alpha$ -Cr<sub>3</sub>(PO<sub>4</sub>)<sub>2</sub> is a high-temperature phase and it's obtained at a temperature between 1150°C and 1250°C. The high-temperature modification,  $\beta$ -Cr<sub>3</sub>(PO<sub>4</sub>)<sub>2</sub>, was discovered by E. Hammer [20,145]. The stability range for  $\beta$ -Cr<sub>3</sub>(PO<sub>4</sub>)<sub>2</sub> extends from 1250 to 1350°C (melting point). The resulting crystals of  $\alpha$ - and  $\beta$ -Cr<sub>3</sub>(PO<sub>4</sub>)<sub>2</sub> displayed distinct optical characteristics, with  $\alpha$ -Cr<sub>3</sub>(PO<sub>4</sub>)<sub>2</sub> exhibiting a dark-blue colour and  $\beta$ -Cr<sub>3</sub>(PO<sub>4</sub>)<sub>2</sub> presenting light-blue with a turquoise hue. Both forms demonstrated notable stability against oxidation and resistance to acids.

#### II.2.1.2 *Crystal structures*

The  $\alpha$ -form of Cr<sub>3</sub>(PO<sub>4</sub>)<sub>2</sub> (*P*2<sub>1</sub>2<sub>1</sub>2<sub>1</sub>; *Z* = 8; *a* = 8.4849(10) Å, *b* = 10.3317(10) Å, *c* = 14.206(2) Å) exhibits a complex structure that consists of six crystallographically independent Cr<sup>2+</sup> ions per unit cell. Four of them have a distorted square-planar coordination [Cr<sup>II</sup>O<sub>4</sub>] with four oxygen atoms at distances 1.96 Å ≤ *d*(Cr-O) ≤ 2.15 Å, while Cr(5) and Cr(6) exhibit square pyramid coordination [Cr<sup>II</sup>O<sub>5</sub>] with strong radial distortion (coordination sphere up to 2.40 Å) (see Figure II-1b). These coordination polyhedra share vertices and/or edges together and with PO<sub>4</sub> groups into a dense low-symmetry packing. The complex crystal structure can be described as closely packed tubes along the *b*-axis, with Cr on the inner and PO<sub>4</sub> groups on the outer surfaces and in the centres, aligned by pseudo 3<sub>1</sub>-screw axes (see Figure II-1a, b).

The crystal structure of the  $\beta$ -Cr<sub>3</sub>(PO<sub>4</sub>)<sub>2</sub> is closely related to that of Mg<sub>3</sub>(PO<sub>4</sub>)<sub>2</sub> (Farringtonite structure type [149]; *P*2<sub>1</sub>/*n*; *Z* = 2; *a* = 4.9641(5) Å, *b* = 9.492(1), *c* = 6.4849(5) Å,  $\beta$  = 91.412(8)°). The crystal structure can be described as an arrangement of phosphate groups in a hexagonal

close packing with slightly undulating layers parallel to the crystallographic  $ab$  plane. Between these layers, half of the octahedral voids are occupied by Cr(2) cations in centrosymmetric coordination with six oxygen atoms from six phosphate groups, while Cr(1) cations fill trigonal-bipyramidal voids in the dense packing of phosphate groups (see Figure II-1c-e). If one extends the Cr(1)O<sub>5+1</sub> coordination to 2.74 Å, it involves six oxygen atoms from five phosphate groups, which means that one PO<sub>4</sub> (i.e. P(1)) shares an edge with Cr(1). The two crystal structures will be shown later, together with their magnetic structures.

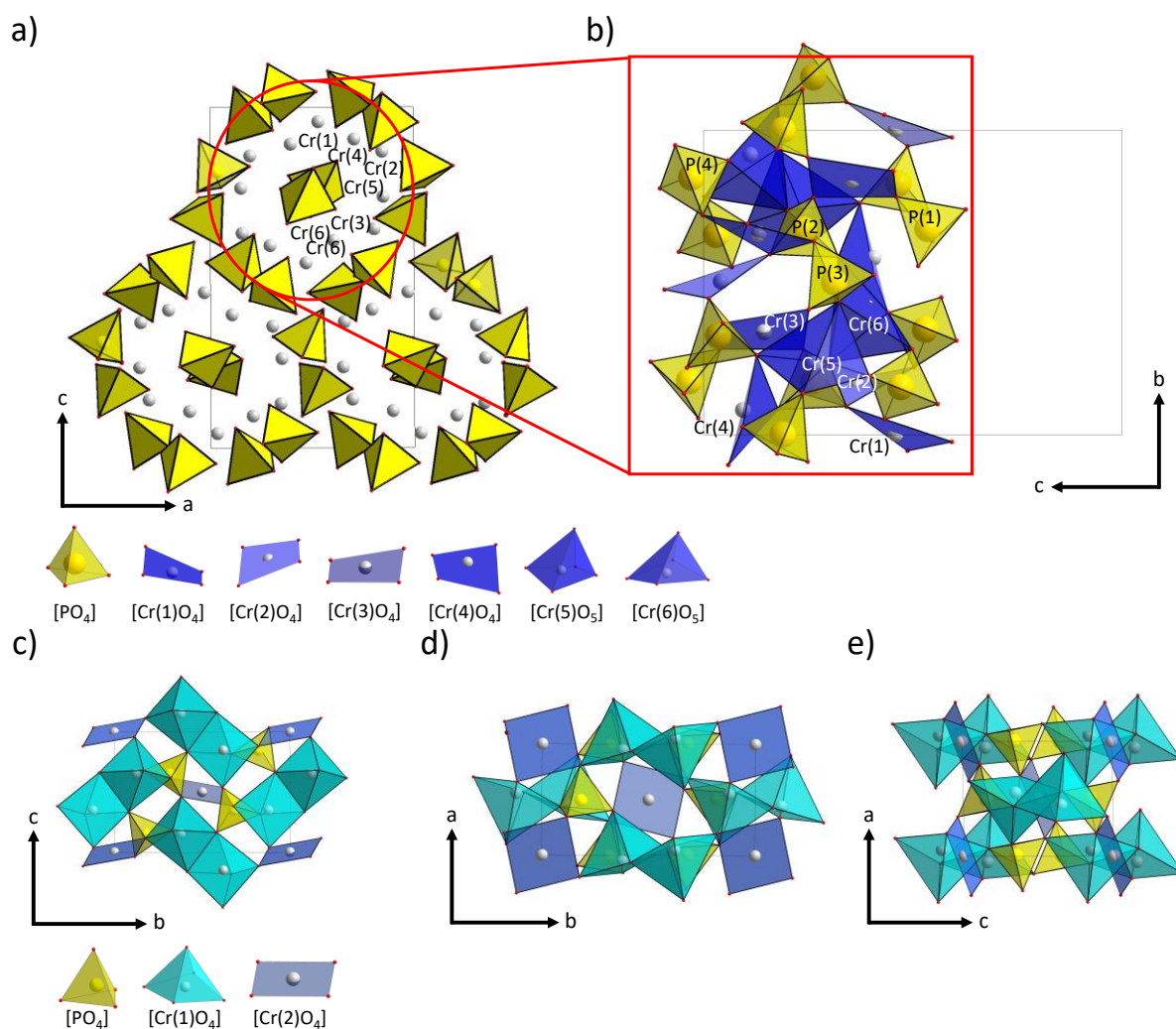


Figure II-1. a) Projection of the crystal structure of  $\alpha$ -Cr<sub>3</sub>(PO<sub>4</sub>)<sub>2</sub> on the  $ac$  plane. The crystal structure consists of close-packed tubes parallel to the  $b$ -axis, with Cr atoms on the inner surface and [PO<sub>4</sub>] groups on the outer surface and tube centres. Adjacent tubes are related by pseudo  $3_1$  screw axes. b) Projection on the  $bc$  plane of the atomic arrangement in proximity to a pseudo  $3_1$  screw-axis. Crystal structure  $\beta$ -Cr<sub>3</sub>(PO<sub>4</sub>)<sub>2</sub> projected on the c)  $bc$  plane d)  $ab$  plane and e)  $ac$  plane.

### II.2.1.3 Magnetic properties

New samples of  $\alpha$ - $\text{Cr}_3(\text{PO}_4)_2$  were prepared and remeasured during this thesis. Three-dimensional magnetic order was identified at  $T \leq 28$  K, wide hump below (see Fig. II-3a), which suggests some free components of the spins after the overall ordering. At very low temperature we observed a small hysteresis in  $M(H)$  which may be a sign for the existence of a weak ferromagnetic component in this complex system (see Fig. II-3b). In its paramagnetic domain,  $\alpha$ - $\text{Cr}_3(\text{PO}_4)_2$  shows an effective moment of  $\mu_{\text{eff}} = 4.30 \mu_{\text{B}}/\text{Cr}^{2+}$  and a Curie-Weiss (CW) temperature  $\Theta_{\text{p}} = -69.9$  K.  $\mu_{\text{eff}}$  is significantly below the spin-only value of  $4.92 \mu_{\text{B}}$ . The most plausible explanation relies on the previous study by A. N. Vasiliev et al. [150] have concluded that this reduced value of the effective magnetic moment of  $\mu_{\text{eff}} = 4.30 \mu_{\text{B}}$  per  $\text{Cr}^{2+}$  ion in the paramagnetic state is hardly attributable to the presence of an spin-orbit coupling and a possible explanation is  $d_{z^2}$  orbital overlap in the adjacent  $\text{Cr}(4)\text{O}_4$  and the  $\text{Cr}(5)\text{O}_5$  units, that exhibit a short distance  $d_{\text{Cr-Cr}} = 3.08 \text{ \AA}$  suggesting direct Cr—Cr chemical bonding (see

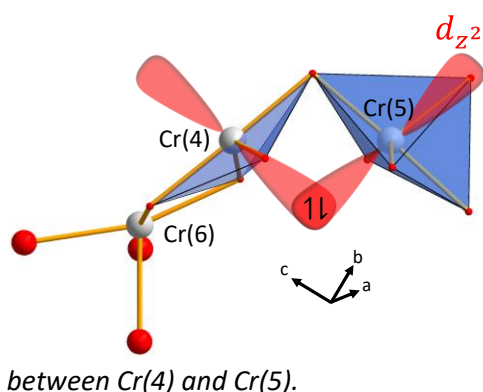


Figure II-2) as it was seen for  $\text{Cr}_2\text{SiO}_4$  [132]. This lead to three unpaired electrons per  $\text{Cr}(4)$  and  $\text{Cr}(5)$  ions. The system is containing four  $\text{Cr}^{2+}$  ions ( $S = 2$ ) and two with  $S = 3/2$ . Which will match an average moment of  $4.30 \mu_{\text{B}}$  per  $\text{Cr}^{2+}$ .

Figure II-2. sketch of the plausible direct bonding between  $\text{Cr}(4)$  and  $\text{Cr}(5)$ .

Magnetic measurements on  $\beta$ - $\text{Cr}_3(\text{PO}_4)_2$  have been performed on selected ground crystal in the GLAUM research team [20,145] prior to this study. Results of the measurements are shown on Figure II-3. They yield in the paramagnetic domain (RT to 125 K) an effective moment ( $\mu_{\text{eff}}$  of  $4.89 \mu_{\text{B}}/\text{Cr}^{2+}$ , in line with the spin-only value of  $4.92 \mu_{\text{B}}$ . The negative Curie-Weiss temperature  $\Theta_{\text{p}} = -190$  K suggests AFM exchange with a large number of  $\text{Cr}^{2+}$  neighbours around each individual one. Between 125 and 50 K, the smooth hump pictures the setting of low-dimensional antiferromagnetic couplings. It was associated with dimers  $[\text{Cr}_2\text{O}_{10}]$ , which finally order with the square-planar  $\text{Cr}(2)$ . These comprehensive findings are the result of collaborative efforts, of HAMMER [20,145] contributing to the  $\beta$ -form and SCHMIDT [139] to the  $\alpha$ -form of  $\text{Cr}_3(\text{PO}_4)_2$ . The study in this thesis aims to solve/refine their magnetic structures

using neutron data collected on the D2b beamline ( $\lambda = 2.52 \text{ \AA}$ ) from previous experiments. It would allow to gain insights into the magnetic structure of these two intriguing phases.

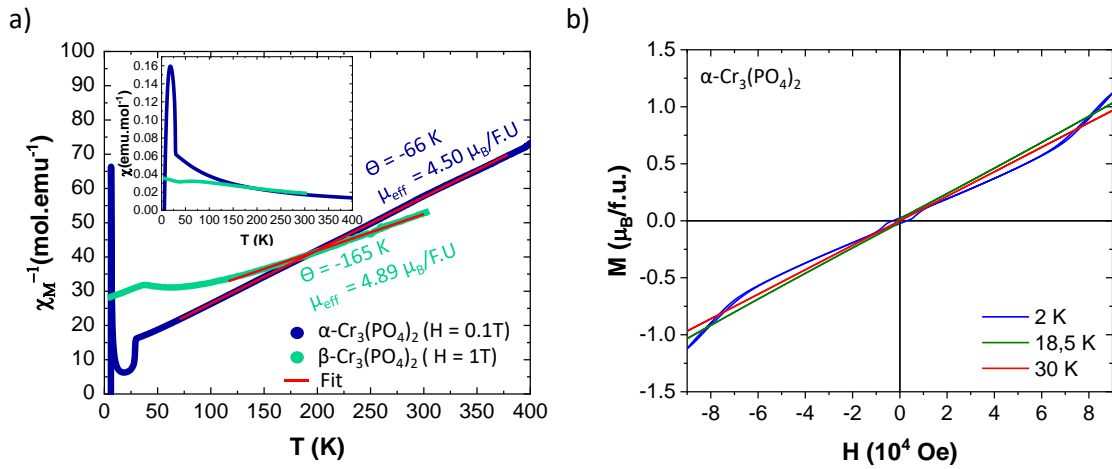


Figure II-3. a) Magnetic susceptibility measurement (insert)  $\chi_M$  and its inverse  $1/\chi_M$  for  $\alpha\text{-Cr}_3(\text{PO}_4)_2$  (in blue) (remeasured) and for  $\beta\text{-Cr}_3(\text{PO}_4)_2$  (in green) as measured by HAMMER [20,145]. b) Magnetization M versus field H at different temperature for  $\alpha\text{-Cr}_3(\text{PO}_4)_2$ .

## II.2.2. The Magnetic structures of $\alpha$ - and $\beta\text{-Cr}_3(\text{PO}_4)_2$

The magnetic structures were determined using data collected at the D2b beamline ( $\lambda = 1.59 \text{ \AA}$ ) at the ILL (Institute Laue Langevin, Grenoble, France).

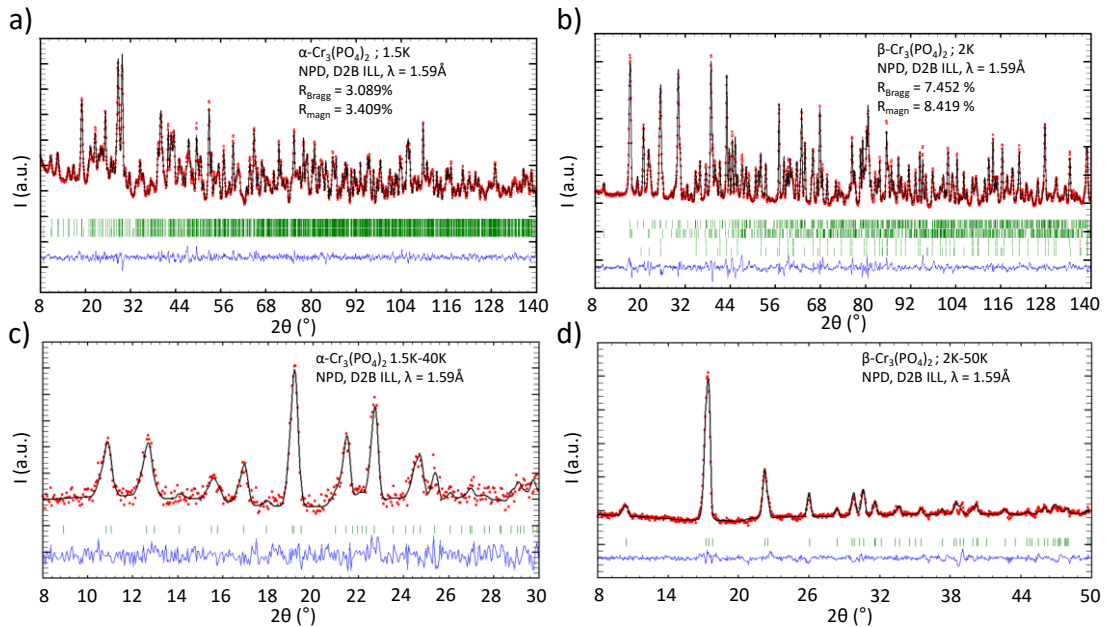


Figure II-4. Neutron powder diffraction refinement of magnetic and nuclear structures for a)  $\alpha\text{-Cr}_3(\text{PO}_4)_2$  at 1.5 K and b)  $\beta\text{-Cr}_3(\text{PO}_4)_2$  at 2 K. Neutron powder diffraction refinement of the magnetic structures only for c)  $\alpha\text{-Cr}_3(\text{PO}_4)_2$  from 1.2-40 K data and d)  $\beta\text{-Cr}_3(\text{PO}_4)_2$  from 2-50 K data.

### II.2.2.1. $\alpha$ -chromium(II) orthophosphate

The magnetic structure was investigated using data collected at 40 K (paramagnetic) and at 1.5 K (see Figure II-4a, c). The magnetic propagation vector is  $k = [0\ 0\ 0]$ . The structure involves six independent magnetic ions  $\text{Cr}^{2+}$ , making the solution complex. Initially, refining the atoms without any constraints proved to be very unstable with six independent  $\text{Cr}^{2+}$ , each at the general Wyckoff positions (4a):  $(x, y, z)$ ,  $(-x+1/2, y+1/2, -z+1/2)$ ,  $(-x, -y, -z)$ ,  $(x+1/2, -y+1/2, z+1/2)$ . It was first refined using the “1.5K–40 K” (see Figure II-4c) difference pattern and in a second step refining simultaneously the magnetic and nuclear structures (Figure II-4a).

The magnetic symmetry analysis indicates that the magnetic representation  $\Gamma$  can be decomposed into four irreducible representations of dimension 1, each in  $\Gamma$ :  $3\Gamma_1 + 3\Gamma_2 + 3\Gamma_3 + 3\Gamma_4$ . Only the  $\Gamma_3$  leads to calculated magnetic intensities consistent with experimental data, where  $S_i^d$  is the spin component of  $\text{Cr}_i$  atom along the three crystallographic axes ( $d = a, b, c$ ) leading to the description of each single magnetic site by magnetic moment components  $M_x, M_y, M_z$ . The same representation  $\Gamma_3$  is active for the six independent  $\text{Cr}^{2+}$  ions.

$$\Gamma_3 = \begin{pmatrix} S_1^x & + & S_2^x & + & S_3^x & + & S_4^x \\ S_1^y & + & S_2^y & - & S_3^y & - & S_4^y \\ S_1^z & - & S_2^z & + & S_3^z & - & S_4^z \end{pmatrix} \quad \text{Eq. II-1}$$

This led to the magnetic space group  $P2_1'2_1'2_1$  (No. 19.27). Using a most “universal” labelling, the decomposition of the magnetic representation for all the six independent Cr is given on the Bilbao crystallographic server by:  $\Gamma_{\text{mag,Cr}} = 3 \times \text{mGm}_1 \oplus 3 \times \text{mGm}_2 \oplus 3 \times \text{mGm}_3 \oplus 3 \times \text{mGm}_4$  in which the  $\Gamma_3$  Irrep used above corresponded to the  $\text{mGm}_3$  using the Bilbao standard description.

To address this refinement, certain constraints were imposed to limit the number of free parameters on the basis of the spins found nearly parallel with close values (we note that despite the hypothesis of direct Cr(4)-Cr(5) metal bonding discussed above, the directions of their spins was not restrained together):

- Cr(2)-Cr(5) share an edge (green and orange, see Fig. II-5d), set equal and are antiferromagnetic (AFM) in dimers ( $M = 3.33(6) \mu_B$ ) parallel to the b-axis.

- Cr(4)-Cr(6) share an edge (purple and turquoise, see Fig. II-5d), set equal and are AFM in dimers ( $M = 3.13(6) \mu_B$ ) parallel to the b-axis.
- Cr(1) (red, see Fig. II-5d) and Cr(6) (turquoise, see Fig. II-5d) are vertex-sharing and set equal in a  $[\text{Cr}(6)\text{O}_{5+1}]$  coordination, with AFM coupling in close connection ( $M = 2.90(2) \mu_B$ ). However, components along the three directions ( $M_x = 0.81(3) \mu_B$ ,  $M_y = 2.50(1) \mu_B$ ,  $M_z = 1.23(3) \mu_B$ ).

The best refinement was obtained with  $R_{\text{magn}} = 3.409\%$  and  $R_{\text{Bragg}} = 3.089\%$  at 1.5 K (see Figure II-4a). The refined magnetic structure at 1.5 K is illustrated in Figure II-5a, b, c. The magnetic structure arises from various interactions, with each Cr linked to others through multiple exchange paths. Figure II-5d also demonstrates the interplay between the spin-exchanges, where, for instance, Cr(6) is simultaneously connected to one Cr(5) by one shared corner and to another one Cr(5) through super-super exchanges Cr(5)-O...O-Cr(6). This is just one example among many, highlighting the complexity of exchanges contributing to the resolved magnetic structure.

In this case, the orientations of the moments do not show any systematic orientations towards their basal square-plane. It suggests that they are not strongly dependent on the local overlap of the oxygen ligands in their respective crystal fields, but the set of magnetic interactions dictate the “overall” magnetic structure. It is not a collinear structure, even though 4 out of 6 spins align along the crystallographic b-axis. We note that the spins Cr(4) and Cr(5) related by their mixed  $d_{z^2}$  orbital are antiparallel, as expected from direct exchanges, see Figure II-5d. As a result, the Heisenberg behaviour is more pronounced for Cr(2) / Cr(5) ( $M_y = 3.33(6) \mu_B$ ) and Cr(4) / Cr(6) ( $M_y = 3.13(6) \mu_B$ ), Cr(1) ( $M_x = 0.81(3) \mu_B$ ,  $M_y = 2.50(1) \mu_B$ ,  $M_z = 1.23(3) \mu_B$ ,  $M_{\text{tot}} = 2.90(3) \mu_B$ ), Cr(3) ( $M_x = 0.81(3) \mu_B$ ,  $M_y = 2.50(1) \mu_B$ ,  $M_z = 1.23(3) \mu_B$ ,  $M_{\text{tot}} = 2.90(3) \mu_B$ ) (in line with their weaker refined moments, as discussed above for the  $S = 2$  case). It's rather challenging to explain the magnetic structure due to the multitude of interactions in this highly complex system.

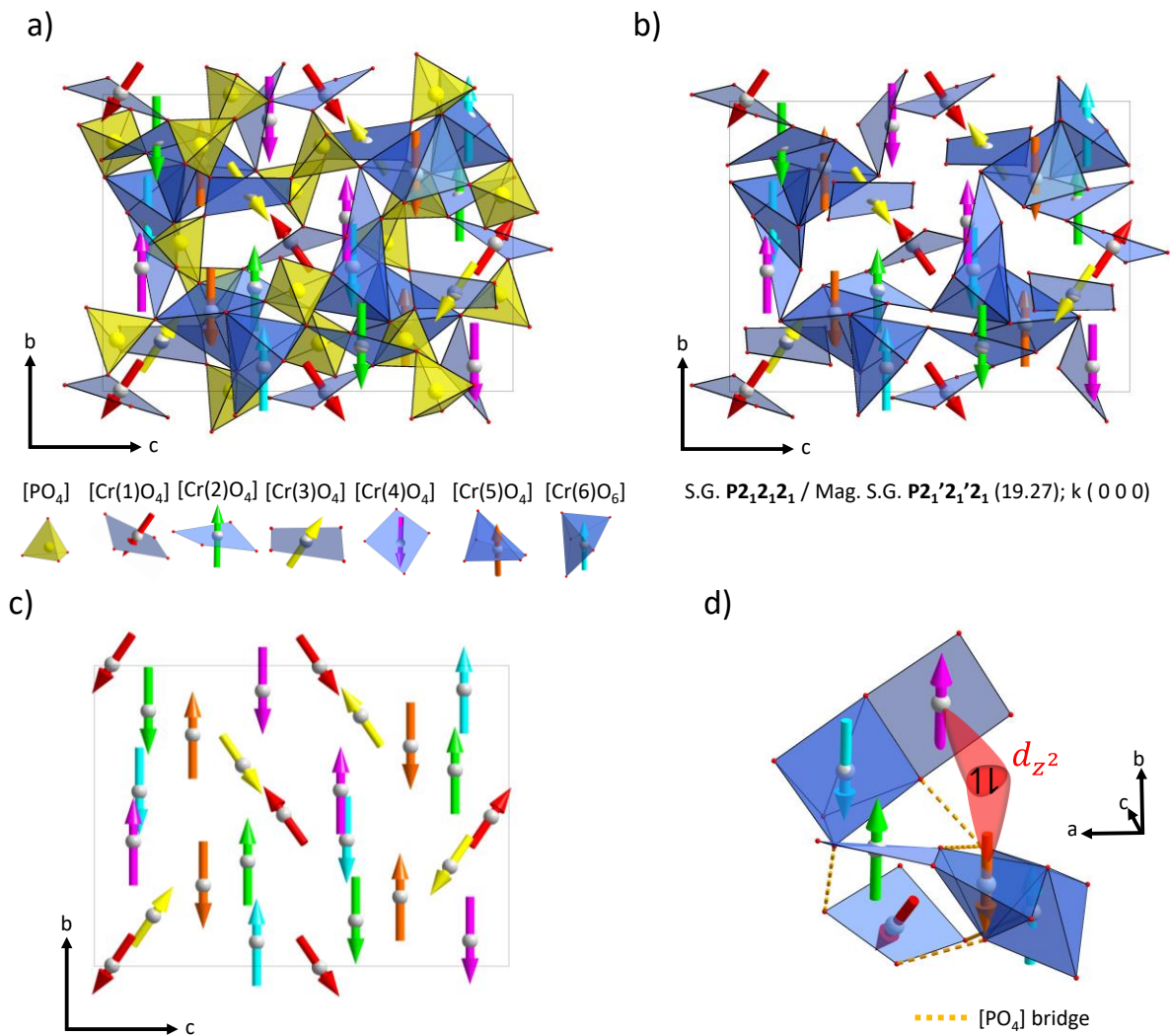


Figure II-5. a) Projection of  $\alpha\text{-Cr}_3(\text{PO}_4)_2$  magnetic structure on (100). b) Same figure showing the magnetic moments orientations of its six independent  $\text{Cr}^{2+}$  ions (in different colours) in their respective coordination. c) Magnetic moment presentation of the various  $\text{Cr}^{2+}$  ions without their surroundings, illustrating a complex AFM arrangement with different moment orientations. d) An example of the arrangement within the structure highlighting the multitude and complexity of magnetic exchange pathways among different  $\text{Cr}^{2+}$  ions with a sketch of the plausible direct bonding between Cr(4) and Cr(5).

#### II.2.2.2. $\beta$ -chromium(II)-orthophosphate

The magnetic structure of  $\beta\text{-Cr}_3(\text{PO}_4)_2$  was refined at  $T = 2\text{ K}$ . With the help of the ksearch tool in the FullProf software [151], magnetic satellites were indexed with a propagation vector  $k = [1/2\ 1/2\ 0]$ . There are only two magnetic ions, Cr(1) and Cr(2), on the Wyckoff sites 4e and 2a respectively, in the  $P2_1/n$  unit cell, which can be decomposed into positions for Cr(1):  $(x, y, z)$ ,  $(1/2-x, -1/2+y, 3/2-z)$ ,  $(1-x, 1-y, 1-z)$ ,  $(1/2+x, 3/2-y, -1/2+z)$ . For Cr(2):  $(x, y, z)$ ,  $(1/2-x, 1/2+y, 1/2-z)$ . A symmetry analysis was performed using Basireps). For Cr(1), the magnetic representation

can be decomposed into 4 irreducible representations of dimension 1, each in  $\Gamma$ :  $3\Gamma_1 + 3\Gamma_2 + 3\Gamma_3 + 3\Gamma_4$ , with some of them containing imaginary components. This latter involves “in theory” a possible dephasing of some spins in equivalent positions. However, in this case it did not occur. For Cr(2), there are 2 irreducible representations of dimension 1:  $3\Gamma_1 + 3\Gamma_3$  also with imaginary terms. After testing multiple possibilities, we used for a combination of  $\Gamma_3$  for Cr(1) (real Irrep.) and  $\Gamma_1$  for Cr(2) (imaginary terms as indicated below) but without any dephasing.

$$\Gamma 1 = \begin{matrix} S_1^x & + & S_{2im}^x \\ S_1^y & - & S_{2im}^y \\ S_1^z & + & S_{2im}^z \end{matrix} \quad \text{Eq. II-2}$$

$$\Gamma 3 = \begin{matrix} S_1^x & + & S_2^x & + & S_3^x & - & S_4^x \\ S_1^y & + & S_2^y & + & S_3^y & + & S_4^y \\ S_1^z & - & S_2^z & + & S_3^z & - & S_4^z \end{matrix} \quad \text{Eq. II-3}$$

Eventually, the refined magnetic structure consists of AFM dimers formed by two edge-sharing Cr(1)O<sub>5</sub> polyhedra and square planar AFM Cr1O<sub>4</sub> (see Figure II-6a, b). Spins are arranged in a non-collinear manner in planes connected only by super exchange, such that the predominant components of the Cr(1) ( $M_x = 2.87(3) \mu_B$ ,  $M_y = 0.98(2) \mu_B$ ,  $M_z = 0.92(2) \mu_B$ ) and Cr(2) ( $M_x = 2.53(2) \mu_B$ ,  $M_y = 1.08(5) \mu_B$ ,  $M_z = 1.65(3) \mu_B$ ) moments is the  $M_x$  one, leading to barely collinear structure (see Figure II-6a, b). The combination of the  $k = \frac{1}{2}, \frac{1}{2}, 0$  and of the  $\Gamma_1$  indeed creates specific magnetic symmetry “lowering”. As seen on the Figure II-6d, two crystallographically equivalent sub-units become magnetically inequivalent with either four nearly-parallel Cr(1) spins around (orange in Figure II-6d) either antiparallel by two Cr(1) spins (blue in Figure II-6d). The moments of the square planar Cr(2) inside show then, two possible neighbouring magnetic configurations. This suggests a magnetic symmetry lowering, which was not studied in detail in the frame of my thesis, due to time limit. However, a rapid look of the output in the mcif file using the isodistort suite [152] indicates the triclinic magnetic space group  $P-1.1'$ .

The AFM character obeys the  $k = 1/2, 1/2, 0$  propagation vector, such that all the [110] direction, one can imagine the stacking of some planes, two next planes being magnetically by Cr+O –(P)–O–Cr super-super exchanges only, via the PO<sub>4</sub> bridges and are AFM with respect to the shortest inter-plane Cr---Cr distances, see Figure II-6c.

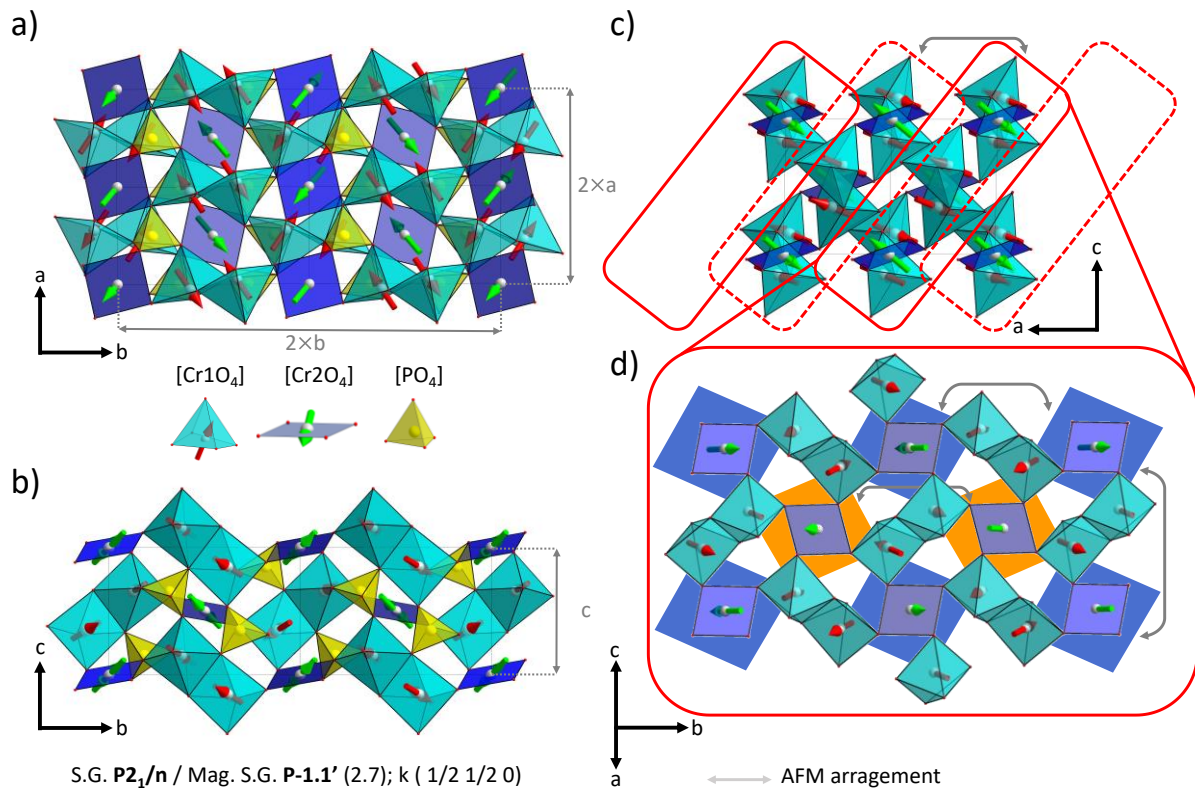


Figure II-6.  $\beta\text{-Cr}_3(\text{PO}_4)_2$  a) Projection on [001] of the magnetic structure showing the orientation of the magnetic moments of its two independent  $\text{Cr}^{2+}$  ions (in red and green) in their coordination. b) Projection of magnetic structure on (100). c) Projection on (010) of the magnetic structure, consisting of layers interconnected through the  $[\text{PO}_4]$  groups in an AFM configuration. b) Illustration of a layer showing the two *magnetically inequivalent* sub-unites.

### II.2.3. Partial conclusion

As a partial conclusion, we have shown here the complexity of the two magnetic structures. It arises due to the strong competition between a multitude of exchanges, and the JT  $\text{Cr}^{2+}$  certainly drives their amplitude. We will now shift to crystal structures with magnetic structures of lower dimensionality where the dimensionality will have a stronger control on the final spin arrangements.

## II.3. Non-modulated AFM in barium chromium(II) pyrophosphate

### II.3.5. Introduction

The pursuit of new compounds exhibiting low-dimensional magnetic properties and unveiling of the underlying quantum effect have garnered increasing interest. As system dimensions decrease, quantum mechanical effects become more prominent, giving rise to quantum cooperative phenomena with magnetoactive ions organized into zero-dimensional (0D), one-dimensional (1D), or two-dimensional (2D) topologies. It may favour strong magnetic

anisotropy in magnetic clusters, chains, or layers and the emergence of exotic magnetic properties, such as the recently discovered antiferromagnetic excitonic insulator state [153]. These emergent phenomena are supposed to revolutionize advanced technologies. Consequently, the search for compounds with exotic electronic and magnetic ground states continues, providing renewed inspiration for researchers in their quest to comprehend the quantum ground states of matter.

In this context, the exploration of  $A_2O/A'O-MO-X_2O_5$  systems ( $A = K\dots$ ;  $A' = Ba, Pb, Sr$ ;  $M = Co, Fe, Ni, Mn, Cu$ ;  $X = P, As, \text{ or } V$ ) led to the discovery of several compounds with low-dimensional magnetic properties. Structurally, the combination of large counter-ions ( $Ba^{2+}$  for instance) and  $XO_4$  groups, non-magnetoactive ions, provide confinement of the magnetoactive ions ( $Fe^{2+}, Co^{2+}, Ni^{2+}, Cu^{2+}\dots$ ) in chains, layers, or blocks that are separated by the combination of these non-magnetic structure units. For instance, phosphate and or arsenate  $BaM_2(XO_4)_2$  display isolated  $M^{2+}$  honeycomb layers with quasi-2D magnetic behaviour [66], including 2D Ising ferromagnetic (FM) properties in the  $BaFe_2(PO_4)_2$  case [67,154]. In this chapter, we report the results of the study on the pyrophosphate  $BaCrP_2O_7$  which belongs to rather extended a broad family of compounds  $BaMX_2O_7$  ( $A = Ba$ ;  $M = Co, Fe, Ni, Cu$ ;  $X = As, P$ ) [155–157], crystallizing into two polymorphic: ( $\alpha, \beta$ ), with space groups  $P2_1/n$  and  $P-1$ , respectively. Their first identification dates back to 1988, when Riou et al. [158] determined the structures of  $BaCoP_2O_7$  and  $BaNiP_2O_7$ , initiating further exploration within this series. Magnetically,  $BaMP_2O_7$  ( $M = Cu, Ni, Co$ ) were investigated in detail and show 1D-Heisenberg AFM/FM chain properties for  $M = Cu$ , and a large distribution of short range correlations above their magnetic ordering temperatures  $T_N$  for  $M = Co$  and  $Ni$  [156]. While it was not explicitly included in the magnetic analysis, the reported structural modulations, which exist for  $M = Co$  and  $Ni$ , influence the bulk magnetism. This aspect has been previously studied in Lille for the modulated compounds  $BaMX_2O_7$  ( $M = Co, Fe$ ;  $X = P, As$ ); PhD thesis by R. David [159] and B. Lecercq [160]. The polymorphous  $\alpha$ - $BaCoX_2O_7$  ( $X = P, As$ ), display similar behaviour as the change between  $As^{5+}$  and  $P^{5+}$  does not significantly alter the structural and magnetic properties. Their crystal structures consist of isolated infinite chains aligned along the  $a$ -axis, built from  $Co_2O_8$  edge-sharing dimers of square pyramids connected by  $XO_4$  groups (see Figure II-7a, b). These chains are magnetically all most isolated, which should result in quasi 1D-antiferromagnetic chains (see Fig. II-7c). However, the compounds are characterized by

incommensurate structural modulations with substantial atomic displacements (see Figure II-7d). In real, the chains are undulated in the  $(ac)$ -plane, creating a modulated distribution of strong and weak magnetic exchange pathways between next chains. Metamagnetic transitions stem from this uncommon topology. In the  $\text{Co}^{2+}$  case with strong uniaxial anisotropy (unaffected by the structural modulations) it was shown that, the structural modulation induces multiferroic behaviour and magneto-electric (ME) exchange below  $T_N = 10$  K. this behaviour is assigned to a unique combination of the modulated magnetoactive ions, collinear magnetic structure, and magnetic dipole–dipole interactions [155]. These unusual properties are accompanied by an abrupt spin-flip transition under magnetic field, in line with the  $\text{Co}^{2+}$  single-ion anisotropy. In contrast, in  $\text{BaFeP}_2\text{O}_7$  [160], although isostructural to  $\text{BaCoX}_2\text{O}_7$  and similarly structurally modulated, the Heisenberg nature of the  $\text{Fe}^{2+}$  ions, make them more sensitive to the main lattice. this feature promotes a non-collinear modulated AFM ordering, but with the absence of experimental magnetolectric (ME) response. Here the metamagnetic spin-alignment is more progressive (spin-flop like transition) in line with the more isotropic features of  $\text{Fe}^{2+}$ .

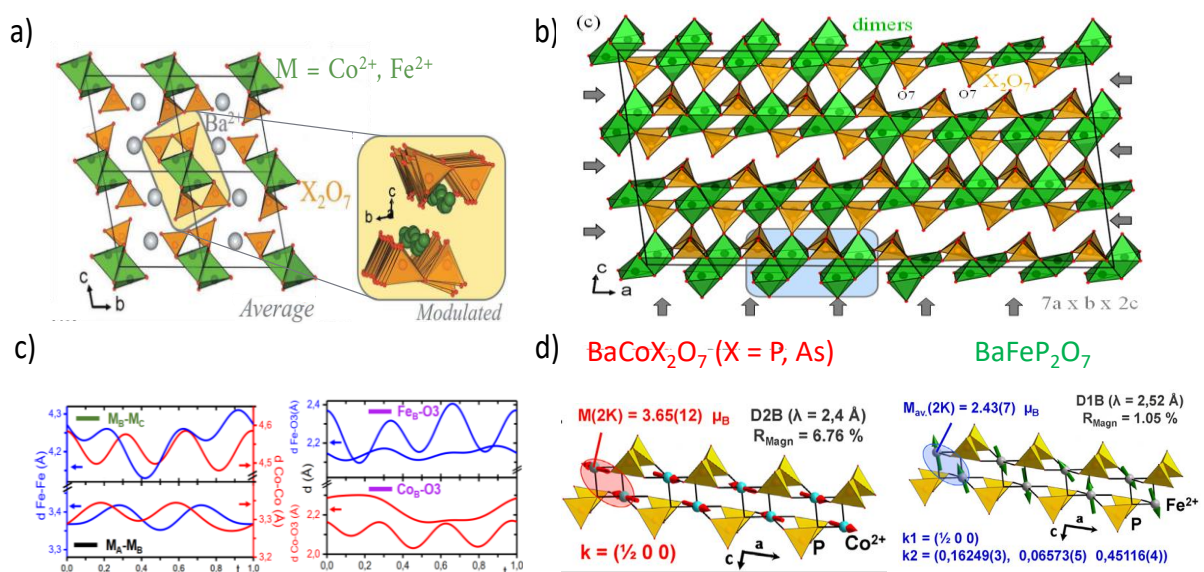


Figure II-7. a) Average  $\text{BaMX}_2\text{O}_7$  ( $M = \text{Co, Fe}$ ;  $X = \text{P, As}$ ) crystal structure projection on  $(100)$  [157]. b)  $7 \times 1 \times 3$  supercell [157]. c) evolution of  $M_B-M_C$ ,  $M_A-M_B$ ,  $\text{Fe}_B-\text{O}_3$ ,  $\text{Co}_B-\text{O}_3$  distances along the real space  $t$ -axis ( $t = x_4 - q \cdot r$ ,  $q$  is the modulation vector and  $r$  an average position in physical space) [155]. d) Magnetic Structures: Collinear and modulated spin arrangement where  $\text{BaCoX}_2\text{O}_7$  ( $X = \text{P, As}$ ) are type II multiferroics with incommensurate shifts and AFM Ising-spins and  $\text{BaFeP}_2\text{O}_7$  has strong spin-lattice coupling and a modulated AFM structure [155]. Permission for reproduction was granted.

### II.3.2. Summary on literature regarding BaCrP<sub>2</sub>O<sub>7</sub>

Exploration of the quasi-binary systems A<sub>2</sub>P<sub>2</sub>O<sub>7</sub>/Cr<sub>2</sub>P<sub>2</sub>O<sub>7</sub> (A = Mg, Ca, Sr, Ba) by Maaß et al. [147] led to the discovery of BaCrP<sub>2</sub>O<sub>7</sub>, which is isostructural to α-BaCoX<sub>2</sub>O<sub>7</sub> (X = As, P). K. Maaß et al. [160] reported details on the crystal structure, UV/VIS spectroscopic results, magnetic measurements, and IR spectra on BaCrP<sub>2</sub>O<sub>7</sub>. The Cr<sup>2+</sup> coordination in the BaCrP<sub>2</sub>O<sub>7</sub> exhibits a strong Cr<sup>2+</sup> Jahn-Teller (JT) effect with a rigid Cr<sup>2+</sup>O<sub>4</sub> square-planar configuration. In this thesis the crystal structure of the BaCrP<sub>2</sub>O<sub>7</sub> was revised due to the literature modest R<sub>all</sub> = 9.63% [147] and to elucidate the magnetic structure. To rationalize its magnetic structure in comparison to those of the reported parent compounds (especially the signature of Cr<sup>2+</sup>), a low-temperature neutron diffraction experiment using the D1b beamline (λ = 2.52 Å) at the ILL (Institute Laue Langevin, Grenoble, France) was carried out.

### II.3.3. Synthesis

BaCrP<sub>2</sub>O<sub>7</sub> was synthesized for neutron diffraction analysis to determine its magnetic structure and to obtain crystals for improved crystal structure refinement.

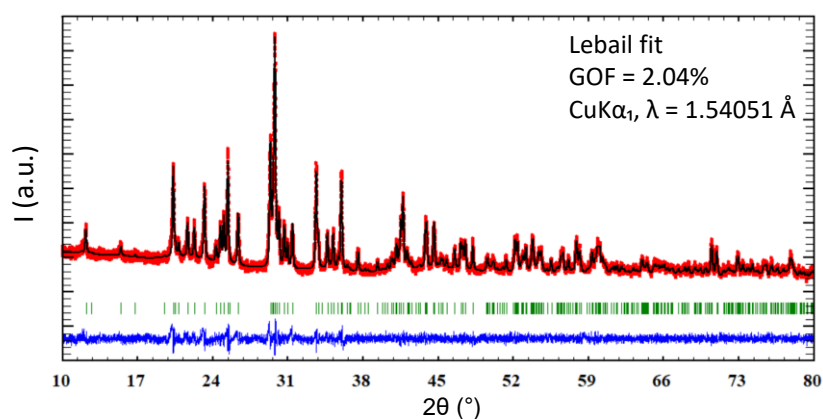


Figure II-8. BaCrP<sub>2</sub>O<sub>7</sub> Le-Bail fit of the polycrystalline sample (IP-Guinier technique; CuKα<sub>1</sub>, λ = 1.54051 Å, quartz monochromator, ambient temperature).

First, Ba<sub>2</sub>P<sub>2</sub>O<sub>7</sub> was prepared from a stoichiometric mixture of BaCO<sub>3</sub> (Alfa Aesar, ≥ 99 %) and (NH<sub>4</sub>)<sub>2</sub>HPO<sub>4</sub> (ACROS organics, ≥ 99 %), which was ground and then heated at 900 °C for 2 days. Then, α-Cr<sub>2</sub>P<sub>2</sub>O<sub>7</sub> [138] was obtained from a stoichiometric mixture of CrPO<sub>4</sub> [161] and CrP [162] as described by the following equation:



This mixture was pressed into pellets, placed in a sealed tube, and heated at 1000 °C for 4 days.  $\alpha$ - $\text{Cr}_2\text{P}_2\text{O}_7$  [138] and  $\text{Ba}_2\text{P}_2\text{O}_7$  [163] were then combined in stoichiometric proportions according to the following reaction equation:



The compounds were mixed, ground, pressed into pellets, and placed in an evacuated quartz glass ampoule. The ampoule was also filled with 10 mg of CrP and 130 mg of  $\text{I}_2$ . The mixture was reacted at 950 °C for 7 days. An excess of CrP was used to trap residual oxygen and moisture. Iodine serves to promote crystallization. A pure phase (XRPD) of approximately 500 mg was obtained. This product showed a turquoise color. The phase purity of the obtained products was checked by Guinier photographs ( $\text{CuK}\alpha_1$ ,  $\lambda = 1.54051 \text{ \AA}$ , quartz monochromator), see Figure II-8. Turquoise crystals of  $\text{BaCrP}_2\text{O}_7$  were found on the surface of reaction pellets. Some of these crystals were collected for single crystal XRD measurements.

#### II.3.4. Crystal structure refinement and description

Maaß et al. [147] observed that the structure refinement of  $\text{BaCrP}_2\text{O}_7$  with reliability factors  $R = 8.51\%$ ,  $R_{\text{all}} = 9.63\%$  was not particularly satisfying. Therefore, the initial step of this study was to improve the structure refinement. and check for the presence or absence of a structure modulation.

Our refined model agrees to the one reported by Maaß et al. [147]. Yet in our refinement, slightly better residuals  $R = 5,16 \%$ ,  $R_{\text{all}} = 6.58\%$  instead of  $R_{\text{all}} = 9.63\%$  were achieved. In fact, all crystals under consideration were systematically twinned, with twin domains related by a  $180^\circ$  rotation about the a-axis, as seen in Figure II-9a. The twin ratio was refined to 50(1)% and generates significant overlap of specific reflections, corrected in the refinement process.

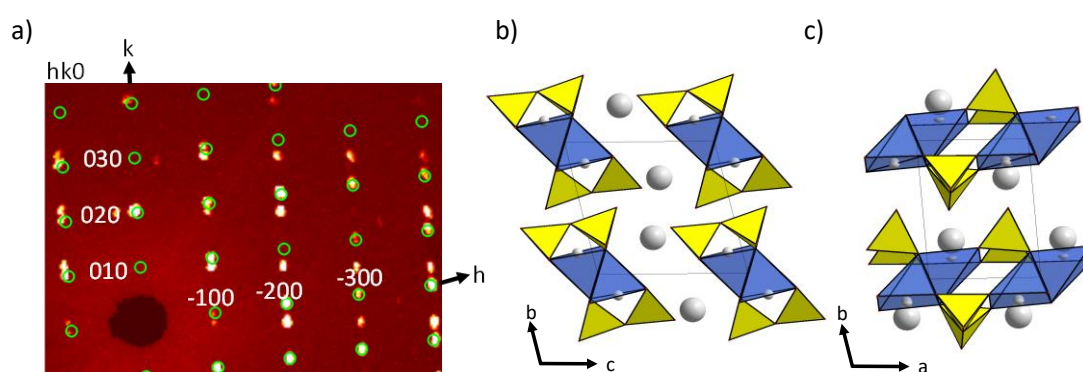


Figure II-9.  $\text{BaCrP}_2\text{O}_7$ . a) Single crystal reconstructed  $hk0$  frames at ambient conditions and the overlaid calculated positions. Crystal structure projection on b)  $(100)$  and c) on  $(001)$ .

The crystal structure of BaCrP<sub>2</sub>O<sub>7</sub> is isotypic to that of other BaMX<sub>2</sub>O<sub>7</sub> compounds (M = Co, Fe; X = P, As), and adopts the triclinic space group *P*-1 with the lattice parameters  $a = 5.352(2)$  Å,  $b = 7.239(3)$  Å,  $c = 7.558(3)$  Å,  $\alpha = 103.226(13)^\circ$ ,  $\beta = 90.006(14)^\circ$ ,  $\gamma = 93.702(14)^\circ$ , and  $V = 284.43(20)$  Å<sup>3</sup>. The crystallographic details along with the data related to single-crystal collection are presented in Table A 0-10-4. Besides the extra-peaks due to twinning, the structure does not exhibit any modulation, contrary to what is observed in the series BaMX<sub>2</sub>O<sub>7</sub> with M = Co, Fe; X = P, As described above. To understand this feature, one should recall that the local effect of the modulation on the metal-oxygen polyhedra results in a transition from MO<sub>5+1</sub> to MO<sub>6</sub> coordination with modulated distances. Indeed, it was shown that by applying pressure eventually the atoms locked into a non-modulated dense structure with MO<sub>6</sub> octahedra [157]. The octahedra are linked by M-O-X-O-M bridges. Dealing with a strongly Jahn-Teller active cation like Cr<sup>2+</sup> should theoretically prevent the occurrence of the [Cr<sup>II</sup>O<sub>6</sub>] octahedra, i.e. avoid the modulation. We note the following ionic radii (Ni<sup>2+<sub>VI</sub></sup> : 0.69 Å, Fe<sup>2+<sub>VI</sub></sup> : 0.78 Å, Co<sup>2+<sub>VI</sub></sup> : 0.745 Å, Cu<sup>2+<sub>VI</sub></sup> : 0.73 Å, Cr<sup>2+<sub>VI</sub></sup> : 0.8 Å [73]) do not allow for a clear size effect. This rigid [M<sup>II</sup>O<sub>5+1</sub>] coordination is shared with BaCuP<sub>2</sub>O<sub>7</sub>, which doesn't show any modulation [156,164].

Similarly to the series BaMX<sub>2</sub>O<sub>7</sub> (M = Co, Fe; X = P, As) and BaCuP<sub>2</sub>O<sub>7</sub>, the crystal structure of BaCrP<sub>2</sub>O<sub>7</sub> consist of isolated infinite chains aligned along the a-axis, built from Cr<sub>2</sub>O<sub>8</sub> edge-sharing dimers of square pyramids interconnected by P<sub>2</sub>O<sub>7</sub> groups (see Figure II-9b, c). These chains are magnetically almost isolated, which should result in quasi 1D-antiferromagnetic chains. However, in contrast compounds BaMX<sub>2</sub>O<sub>7</sub> (M = Co, Fe; X = P, As), and similar to BaCuP<sub>2</sub>O<sub>7</sub>, the Cr<sup>2+</sup> ions adopt a square pyramidal coordination where the arrangement of the five oxygen atoms in the coordination sphere can be better described, as mentioned by Maaß et al [147], as CrO<sub>4+1</sub> coordination ( $d(\text{Cr}(1)\text{-O}(1)) = 2.031(14)$  Å,  $d(\text{Cr}(1)\text{-O}(2)) = 2.065(12)$  Å,  $d(\text{Cr}(1)\text{-O}(3)) = 2.032(12)$  Å and  $d(\text{Cr}(1)\text{-O}(4)) = 2.050(12)$  Å ). A sixth oxygen atom O(7), which is no longer included in the coordination sphere, is located at a distance  $d = 2.902(1)$  Å on the other side of the basal plane (see Figure II-9b, c). This rigid [Cr<sup>II</sup>O<sub>4</sub>] square-planar base emphasizes a major difference compared to previously mentioned compounds, which exhibit a distorted square base with the metal undergoing a coordination variation from one-unit cell to another, leading to a variation of  $d(\text{M-O})$  to the pyramid's tip, ranging from 2.27 Å to 3.71 Å in the case of Co, following a sinusoidal pattern (see Figure II-7c), hence the modulation. In

the case of Cr<sup>2+</sup>, the distance d(Cr(1)-O(2)), where O(2) denotes the oxygen at the pyramid's tip, remains constant (dCr1-O2 = 2.539(1) Å), hence the absence of modulation.

At first sight, although a dynamical aspect relating the lattice-phonon and the degenerate states is probably on the run, one can note that the two compounds which do not show the modulation (Cr<sup>2+</sup> and Cu<sup>2+</sup>) are strongly affected by JT effects in their metal coordination. As a simplistic and crystallographic-only scenario, one could argue that this distortion into CuO<sub>4+1</sub> and CrO<sub>4+1</sub> square-planar coordination is sufficiently stable to avoid the creation of octahedral-like polyhedra, through the static structural modulation. In fact, it is much probable, that the modulated undulation within the metal rows (in the modulated cases) reveal a mismatch between the Ba ions, the P<sub>2</sub>O<sub>7</sub> groups and the M polyhedral, which finally destabilize the stacking of the chains. In that sense, the shortest distances expected for JT active MO<sub>4+1</sub> plausibly locally relax the constraints.

### II.3.5. Magnetic Properties

#### II.3.5.1 Magnetic measurement

The magnetic measurements have been measured using polycrystalline samples. The magnetic susceptibility shows Curie-Weiss behaviour down to T ≈ 12K with μ<sub>eff</sub> = 4.47 μ<sub>B</sub>/F. U. and Θ<sub>CW</sub> = -18.48K (see Figure II-10), using the standard relation:

$$\chi = \frac{c}{(T - \theta)}$$

The μ<sub>eff</sub> value is smaller than the one calculated for a spin-only μ<sub>S.O.</sub> = 4.92 μ<sub>B</sub>/ F.U., which may suggest an orbital contribution, prone to decrease the effective moment for S = 2, J = 2, L = 0 spins. However, the small SOC parameter Zeta = 230 cm<sup>-1</sup> (in contrast to 830 cm<sup>-1</sup> for the JT-active Cu<sup>2+</sup>) plays against a SOC significant contribution. In addition, the ligand-field splitting for d<sup>4</sup> tends to be slightly larger than for d<sup>9</sup> ions. Thus, SOC becomes even less important and μ<sub>eff</sub> is expected to approach the spin-only value [165]. Experimental incertitude cannot be fully excluded as cause for the low μ<sub>eff</sub>.

Below 12 K, χ(T) shows a broadened maximum at T<sub>max</sub> = 9.3 K reminiscent of low-D magnetism with a very similar magnetic profile to the one observed for BaFeP<sub>2</sub>O<sub>7</sub> [160] (see Figure II-10a). However, we will see that the microscopic magnetic behaviour is very different. The 3D-Neel ordering occurs at T<sub>N</sub> = 5.7 K as was confirmed by the specific heat evolution with temperature

(see Figure II-10a), and by the Fisher heat capacity ( $d(\chi(T)) /dT$ ) (see Figure II-10a insert). BaCrP<sub>2</sub>O<sub>7</sub> shows a lower T<sub>N</sub> value in comparison to BaCoP<sub>2</sub>O<sub>7</sub> (T<sub>N</sub> = 10.4K), and BaFeP<sub>2</sub>O<sub>7</sub> (T<sub>N</sub> = 10.3K).

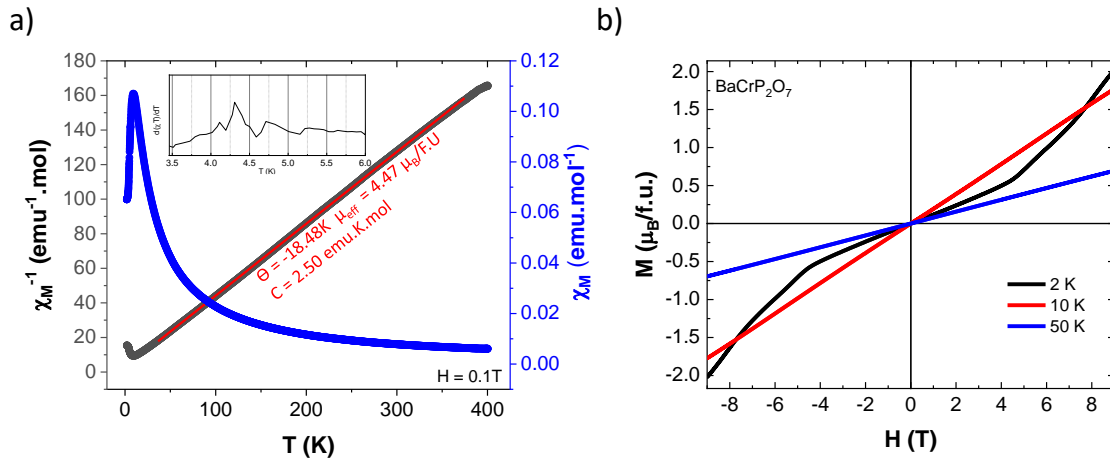


Figure II-10. BaCrP<sub>2</sub>O<sub>7</sub>. a) Magnetic susceptibility measurement  $\chi_M$  (in blue) and its inverse  $1/\chi_M$  (in black) and b) magnetization  $M$  versus field  $H$  at different temperature.

**Behavior above T<sub>N</sub>.** Due to time limits we have not been able to extract exchange values for this compound. However, one important point concerns the nature of the low-D magnetism above T<sub>N</sub>. The broad peak above T<sub>N</sub> suggests spin-gap features. Neglecting the effects of the inter-chain exchange, it could equally stem from S = 2 dimers (J), or the development of alternating (J/J') S = 2 antiferromagnetic chains scenario. At this point, in a rather “intuitive” manner, one could anticipate that both J and J' are significant for S = 2 Cr<sup>2+</sup> ions (see Figure II-15a), on the basis of our previous calculations of the coupling constants for other BaMX<sub>2</sub>O<sub>7</sub> (M = Co, Fe; X = P, As) compounds [155], including the Fe<sup>2+</sup> (S = 2) modulated case. The mean field determination of the J-J' average, according to the chain scenario is given by the relation  $\theta_{CW} = [z.S.(S+1).J]/3K_B$ . Here z = 2 corresponds to the number of Cr<sup>2+</sup> neighbours about each Cr<sup>2+</sup> centre, leading to  $J/K_B \approx 9$  K. Then the ordering on cooling is mediated by weaker interchain exchanges.

The comparison of the C<sub>p</sub>(T) plots under various fields and M(H) plots (see Figure II-11b) shows that:

i) the  $C_p$  anomaly at  $T_N$  is broad including a  $\lambda$ -peak and low-D effects up to 12 K. It progressively vanishes and shifts towards lower temperature, above  $H = 1T$ , where it transforms into a Schottky-like anomaly. This latter is reminiscent of gapped low-D systems, whatever the effect of the field is difficult to anticipate.

ii) Above  $T_N$ , the magnetization shows linear evolution of the  $M(H)$  plots, up to  $1.7 \mu_B/\text{Cr}$  at 10 K under 9T, in line with relatively weak AFM exchange couplings between Cr atoms (see Figure II-10b).

iii) Below  $T_N$ , in the ordered state, the spin alignment is more difficult as expected. It shows a metamagnetic transition at  $\mu_0 \cdot H_c = 4.7 \text{ T}$  (see Figure II-10b). The magnetization being rather smooth one should conclude the occurrence of a spin-flop like magnetic transition, associated to relatively weak magneto-crystalline anisotropy (see Figure II-12) [166]. In this scenario, dealing with powder sample, the majority of grains with the magnetic moments perpendicular to the magnetic field progressively align even at low-field. In contrast those parallel to  $H$  react after the critical field  $H_c$ , after which they deviate into an equilibrium canted situation, and then progressively align. The value of  $H_c$  corresponds to the result of the interplay between the AFM exchanges (which tend to stabilize the AFM order) and the magneto crystalline anisotropy (which favour the collinear spin situations FM or AFM).

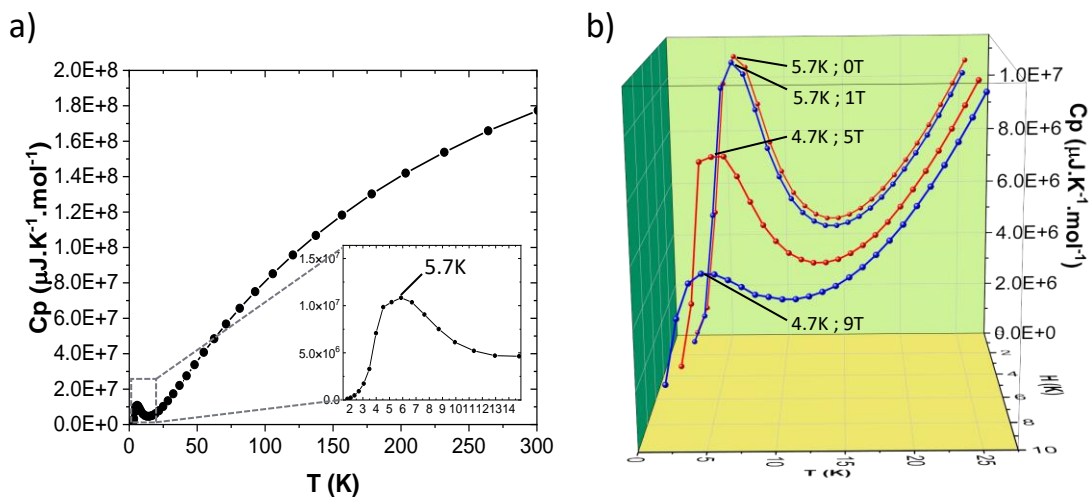
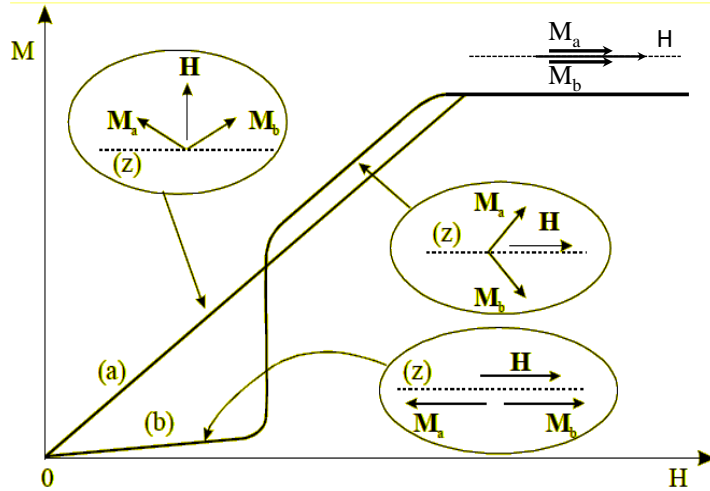


Figure II-11.  $\text{BaCrP}_2\text{O}_7$ . a) Specific heat measured at  $H = 0$ , from 300 K to 2 K. b) Specific heat measured from 25 K to 2 K under different fields from 0 to 9 T.

iv) At this point one can note the good agreement between the  $C_p$  data under field (Figure II-11b) which validate drastic changes of the  $\lambda$ -features at 5T. One can roughly estimate the spin energy at  $H_c$ , as given by  $E = g \cdot \mu_B \cdot H \cdot S$  with  $\mu_B = 0.672$  K/T. This calculation leads the  $E/K_B = 12.6$  K for the energy brought by the magnetic field above which the spin reversal is



enhanced.

Figure II-12. Schematic of spin-flop transition in a uniaxial antiferromagnet with two sublattices. At a critical magnetic field, the sublattice magnetizations rotate perpendicular to the easy axis (z) and applied field (b), indicating a spin-flop transition, followed by continuous rotation as H increases [166].

A spin flop transition was also observed for  $\text{BaFeP}_2\text{O}_7$  in which the spin-anisotropy is significantly small compared to the  $\text{Co}^{2+}$  isomorph, more prone to flip-like transitions [160].

### II.3.5.2 Magnetic structure

We resolved the magnetic structure using data collected at the D1b beamline ( $\lambda = 2.52$  Å) at the ILL (Institute Laue Langevin, Grenoble, France) in collaboration with Claire Colin. The appearance of the magnetic satellites below  $T_N$  is shown in Figure II-13a. Using the  $k_{\text{search}}$  tool in the FullProf software [78], magnetic satellites were indexed with a magnetic propagation vector  $k = [1/2, 0, 0]$ , similarly to other ordered compounds of the family. The Cr is located on the Wyckoff site 2i of the  $P$ -1 unit cell, which can be decomposed into positions  $\text{Cr}(1)$  ( $x, y, z$ ) and  $\text{Cr}(1)'$  ( $-x, -y, -z$ ). A symmetry analysis was performed using Baslreps; the magnetic representation can be decomposed into two irreducible representations of dimension 3, such as  $\Gamma: 3\Gamma_1 + 3\Gamma_2$ . Only the  $\Gamma_1$  representation leads to calculated intensities in good agreement with the experimental magnetic intensities, using the same representation for the two independent  $\text{Cr}(1)$  and  $\text{Cr}(2)$  ions listed above:

$$\Gamma_1 = \begin{matrix} S_1^x & - & S_2^x \\ S_1^y & - & S_2^y \\ S_1^z & - & S_2^z \end{matrix} \quad \text{Eq. II-6}$$

Where  $S_i^d$  is the component along the  $d$ -axis ( $d = a, b, c$ -axis) of the  $\text{Cr}_i$  atom. Using the difference patterns between 1.5 K (ordered) and 10 K (paramagnetic), the final refinement

results in  $R_{\text{Bragg}} = 2.17\%$  and  $R_{\text{magn}} = 4.4\%$  (1.5K) (see Figure II-13b). This led to a magnetic space group  $P-1'$  (No 2.6). The decomposition of the magnetic representation for all the six independent Cr is the following in Bilbao crystallographic server:  $\Gamma_{\text{mag,Cr}} = 3 \text{ mX}+(1) \oplus 3 \text{ mX}1-(1)$ . Were the  $\Gamma_1$  mentioned above corresponded to the  $\text{mX}+(1)$  founded Bilbao standard description.

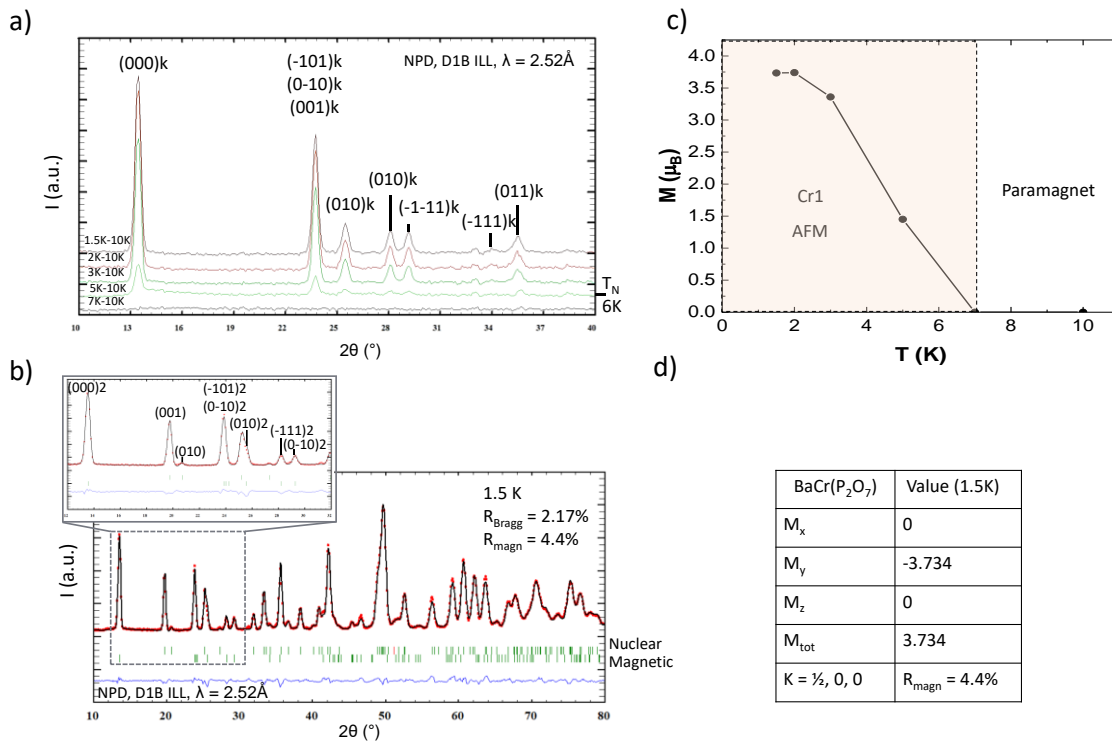


Figure II-13. *BaCrP<sub>2</sub>O<sub>7</sub>* a) NPD pattern of magnetic satellite show their appearance and evolution of magnetic at low T. b) NPD refinement at 1.5K of magnetic and nuclear structures. c) Magnetization Vs T. d) refined magnetic moment from NPD at 1.5 K.

The refined magnetic structure is represented in Figure II-14, and the evolution of the refined moment for different temperatures is shown in Figure II-13c. The spins show an antiferromagnetic (AFM) ordering along the chains (AFM in dimers, but FM in between two next dimers), and align perpendicular to the CrO<sub>4</sub> basale plan (see Figure II-14). The magnetic moment increases, reaching saturation with a value already evident at 2K, where  $M_{1.5\text{K}} = 3.73(4) \mu_B$  (see Figure II-13c).

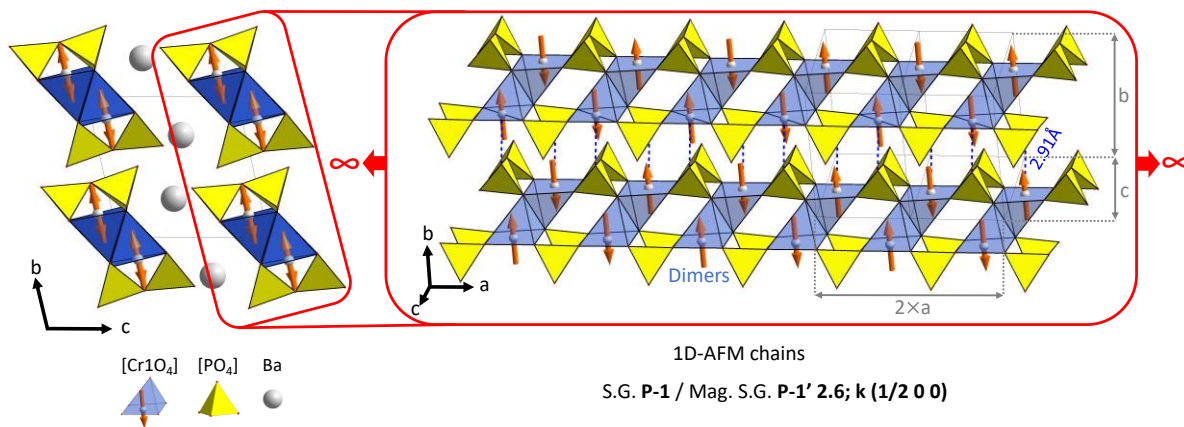


Figure II-14. BaCrP<sub>2</sub>O<sub>7</sub>. Projection on (001) of the magnetic structure showing the magnetic moments orientations within the Cr<sup>2+</sup> ions coordination.

Besides the modulated magnetic structure of the Fe<sup>2+</sup> pyrophosphate, one should keep in mind that in the Co<sup>2+</sup> and Fe<sup>2+</sup> case, FM dimers prevail in the magnetic structures. Therefore, BaCrP<sub>2</sub>O<sub>7</sub> stands out this family due to its AFM dimers. This is especially intriguing considering that both Cr<sup>2+</sup> and Fe<sup>2+</sup> have similar  $S = 2$  spins, but with different electronic configurations, i.e.  $d^4$  against  $d^6$ . The origin of such differences is most plausibly very complex in terms of overlap, but at least the Figure II-15c shows drastic differences in between the geometry of the dimers in the “average” crystal structure if the Fe case, against those refined for the Cr compound. According to the Kanamori-Goodenough rules,  $d^4$ -O- $d^4$  90° super-exchanges (Cr<sup>2+</sup> case) should return ferromagnetic coupling, opposite to what we observe, but in line with the Fe<sup>2+</sup> ( $d^6$ ,  $S = 2$ ) case. In the case of BaCrP<sub>2</sub>O<sub>7</sub>, one should note that the Cr-O-Cr path involves long Cr-O bonds (2.56 Å), which nest the  $d_{z^2}$  orbitals and its overlap with the empty  $d_{x^2-y^2}$  one of the next Cr ion (see Figure II-15c). In such a situation the electronic transfer is expected very weak. Oppositely, the direct exchange mediated by  $d_{yz}$ - $d_{yz}$  is active and expected AFM for half-filled orbitals. We assume that this sub-mechanism is mainly responsible of the AFM dimers in BaCrP<sub>2</sub>O<sub>7</sub>.

For comparison, in the case of the Cu<sup>2+</sup> ( $d^9$ ,  $S = 1/2$ ) compound, the main magnetic properties have been assigned to AFM chains running along the a-axis (between two dimers) and not interacting within the dimers [156]. It was confirmed by the estimation of the spin-exchanges [167]. To explain this situation, one should keep in mind that despite the aforementioned  $S = 2$  similarities, only the  $d_{x^2-y^2}$  magnetic orbital is magnetic for Cu<sup>2+</sup> (see Figure II-15c), which strongly reduce the dimeric interactions both through the filled- $d_{z^2}$  – half-filled  $d_{x^2-y^2}$ , and through direct exchanges (filled  $d_{yz}$ ).

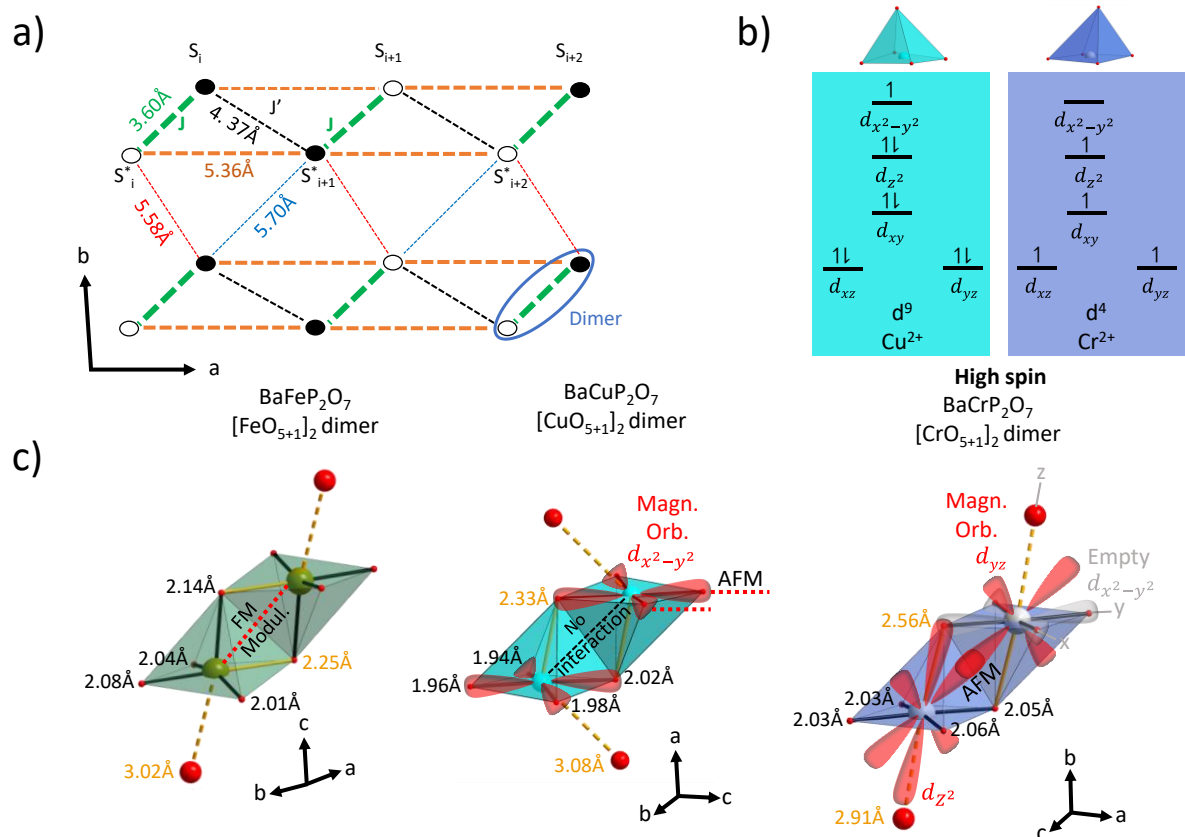


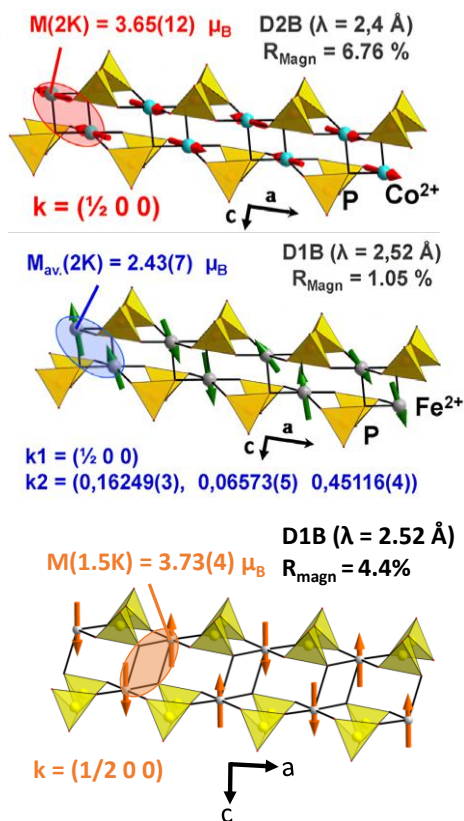
Figure II-15. a) Spin-interaction scheme for Chromium in BaCrP<sub>2</sub>O<sub>7</sub>. b) comparison of the filling of the *d*-orbital configuration in the pyramid square based coordination of Cu<sup>2+</sup> (*d*<sup>9</sup>, *S* = 1/2) and Cr<sup>2+</sup> (*d*<sup>4</sup>, *S* = 2). c) Comparison of Different [M<sub>2</sub>O<sub>8</sub>] Dimers (M: Fe, Cu, Cr) geometry and the *d*-orbitals Involved in the magnetic interactions for Cu<sup>2+</sup> (*d*<sup>9</sup>, *S* = 1/2) and Cr<sup>2+</sup> (*d*<sup>4</sup>, *S* = 2).

### II.3.6. Partial conclusion

In summary, our investigation of BaCrP<sub>2</sub>O<sub>7</sub> has provided valuable insights into its structural and magnetic properties. The refinement of the crystal structure, based on data from single-crystal diffraction, not only improved the quality of the refinement but also confirmed the absence of structural modulation, distinguishing it from similar compounds like BaMX<sub>2</sub>O<sub>7</sub> (M = Co, Fe; X = P, As) (see Figure II-16). Then, it turns out that such modulation vanishes for both the strongly JT-active Cr<sup>2+</sup> and Cu<sup>2+</sup> ions, which suggest that the anisotropic size of the MO<sub>4+1</sub> polyhedra could play against stacking mismatches.

The magnetic properties of BaCrP<sub>2</sub>O<sub>7</sub> were thoroughly examined, revealing paramagnetic behaviour down to *T* ≈ 14K, followed by a Neel ordering transition at *T*<sub>N</sub> = 6 K. The magnetic susceptibility, in the paramagnetic region, adhered to the Curie-Weiss law but shows a

reduced effective moment, difficult to explain, keeping in mind that  $\text{Cr}^{2+}$  is expected to show a low orbital contribution. The magnetic response to external fields at 2 K exhibited a spin-flop like metamagnetic transition at 5 T, followed a smooth alignment of the spins, reminiscent of the case [160]. The study also delved into the magnetic structure, revealing a 1D-AFM zig-zag spin chain configuration. In conclusion, the combined structural and magnetic characterization of  $\text{BaCrP}_2\text{O}_7$  enhances my knowledge of low-dimensional to 3D magnetic systems, offering valuable contributions to the broader field within these family of materials.



### $\text{BaCoX}_2\text{O}_7$ ( $X = \text{P, As}$ )

Modul. cryst. struct.  
+ colinear AFM spins + Ising spins + destabilizing MDD  
→ ME / Multiferroic

### $\text{BaFeP}_2\text{O}_7$

Modul. cryst. struct.  
+ modul. AFM spins + Heisenb. spins + stabilizing MDD  
→ ME inert

### $\text{BaCrP}_2\text{O}_7$

Non Modul. cryst. struct.  
+ colinear AFM spins + Heisenb. spins + stabilizing MDD  
→ ME inert

Figure II-16. Different  $\text{BaM}^{\text{II}}\text{P}_2\text{O}_7$  ( $M = \text{Co, Fe, Cr}$ ) structural and magnetic properties.

## II.4. Two-step 2D/3D magnetic ordering via idle spins and the optical signature of Jahn-Teller Cr<sup>2+</sup> ions in Sr<sub>2</sub>Cr(PO<sub>4</sub>)<sub>2</sub>

### II.4.1. Introduction

Here we report the crystal structure of the previously unknown phosphate Sr<sub>2</sub>Cr<sup>II</sup>(PO<sub>4</sub>)<sub>2</sub>, its magnetic behaviour and its optical spectra which respect the aforementioned aspects in the introduction of this chapter. Its crystal structure is unique by analogy to other A<sub>2</sub>M<sup>II</sup>(PO<sub>4</sub>)<sub>2</sub> (A = Sr, Ba) M = (Cu, Mn, Co, Ni) compounds of the literature (see Table II-2). It combines two crystallographically independent Cr<sup>II</sup>-containing layers, separated by Sr<sup>2+</sup> and (PO<sub>4</sub>)<sup>3-</sup>. The *JT* effect is pronounced returning CrO<sub>4</sub> and CrO<sub>4+1</sub> geometry with specific optical signatures and uncommon magnetic exchanges. These were analysed by DFT+U, magnetic measurements, neutron powder diffraction (NPD), optical spectroscopy, and ligand field analysis within the framework of the angular overlap model (AOM).

Table II-2. alkali earth-transition metal(II)-phosphate-compounds with similar structural formula to Sr<sub>2</sub>Cr(PO<sub>4</sub>)<sub>2</sub>

Compound	Space group	Cell parameters (Å, °), Z	Dimensionality of the main metal scaffold <sup>a)</sup>	Ref
Sr <sub>2</sub> Cu(PO <sub>4</sub> ) <sub>2</sub>	C2/m (12)	$a = 11.5155(1)$ , $b = 5.07543(6)$ $c = 6.57487(7)$ ; $\beta = 106.3563(6)^\circ$ ; 2	3D framework with 1D M-P-M chains	[168]
Ba <sub>2</sub> Cu(PO <sub>4</sub> ) <sub>2</sub>	C2/m (12)	$a = 12.160(4)$ , $b = 5.133(4)$ , $c = 6.885(4)$ , $\beta = 105.42(4)^\circ$ ; 2	3D framework with 1D M-P-M chains	[169]
Ba <sub>2</sub> Mn(PO <sub>4</sub> ) <sub>2</sub>	P2 <sub>1</sub> /n (14)	$a = 5.311(1)$ , $b = 8.968(1)$ , $c = 16.256(3)$ ; $\beta = 90.26(1)^\circ$ ; 4	3D framework with M-P-M dimers	[75]
Sr <sub>2</sub> Co(PO <sub>4</sub> ) <sub>2</sub>	P2 <sub>1</sub> /c (14)	$a = 11.6993(1)$ , $b = 9.99637(9)$ , $c = 9.06743(9)$ ; $\beta = 97.5144(8)^\circ$ ; 6	3D framework	[170]
Ba <sub>2</sub> Co(PO <sub>4</sub> ) <sub>2</sub>	P2 <sub>1</sub> /n (14)	$a = 5.298(1)$ , $b = 8.844(1)$ , $c = 16.144(3)$ ; $\beta = 90.68(2)^\circ$ ; 4	3D framework with M-P-M dimers	[75]
Ba <sub>2</sub> Ni(PO <sub>4</sub> ) <sub>2</sub>	P2 <sub>1</sub> /n (14)	$a = 5.32102(9)$ , $b = 8.80268(16)$ , $c = 16.0958(3)$ ; $\beta = 90.704(9)^\circ$ ; 4	3D framework with M-P-M dimers	[171]
Sr <sub>2</sub> Ni(PO <sub>4</sub> ) <sub>2</sub>	P2 <sub>1</sub> /c (14)	$a = 11.631(7)$ , $b = 9.929(2)$ , $c = 8.990(2)$ ; $\beta = 97.63(4)^\circ$ ; 6	3D framework	[172]

## II.4.2. Experimental

### I.1.3.2 *Materials and methods*

**XRD:** Powder diffraction pattern for phase identification and purity control were recorded at ambient temperature using an imaging plate Guinier camera (HUBER G670, CuK $\alpha_1$  radiation,  $\lambda = 1.54059 \text{ \AA}$ , 1h minutes exposure time in the angular range  $4^\circ \leq 2\theta < 100^\circ$ ). In addition, powders of polycrystalline samples were measured using a Bruker D8 Advance diffractometer with a Bragg-Brentano geometry using monochromated CuK $\alpha$  radiation. The collection of single crystal data was carried out on a Bruker X8 diffractometer using a fine-focus X-ray tube delivering AgK $\alpha$  radiation ( $\lambda = 0.56 \text{ \AA}$ ), a graphite monochromator and an APEX detector. The intensities were extracted and corrected from the Lorentz-polarization factor through the SAINT program [59]. The diffraction data were integrated and a multiscan absorption corrections was applied using Brukers APEX 2 [173] and SADABS programs [174], see in Table All-2a-e in the supporting Information for details.

**NPD:** Neutron powder diffraction data were collected on cooling in an orange cryostat at strategical temperatures, using the D1b diffractometer (HOPG monochromator,  $\lambda = 2.52 \text{ \AA}$ ) at the Institute Laue Langevin (ILL), Grenoble, France [175].

**Magnetic Properties:** Magnetic data and heat capacity were measured on a Dynacool (9T) Physical Property Measurement System (PPMS) from Quantum Design. Typical measurements using zero field cooling (ZFC) and field cooling (FC) procedures were performed at 0.1 T. Curie-Weiss fit was performed in the  $50 < T < 300 \text{ K}$  temperature range. Field dependence data of the magnetization was also collected at 2, 50, 100 and 300 K.

**Optical Spectroscopy:** Polarized optical absorption spectra of Sr<sub>2</sub>Cr(PO<sub>4</sub>)<sub>2</sub> single crystals were acquired using a modified CARY 17 single-beam micro-crystal spectrometer [176,177]. This spectrometer provides a resolution of up to 0.1 nm, equivalent to approximately  $0.35 \text{ cm}^{-1}$  in the NIR and  $12.5 \text{ cm}^{-1}$  in the UV range. A standard halogen lamp (Osram HLX64640, 150 W, 24 V) served as the light source. Measurements in the UV/vis range ( $12000 \text{ to } 36000 \text{ cm}^{-1}$ ) employed a photomultiplier as the detector, while a nitrogen-cooled germanium photodiode was used for measurements in the NIR range ( $6000 \text{ to } 16000 \text{ cm}^{-1}$ ). Additionally, a polarization filter was employed for orientation-dependent measurements. Diffuse powder reflectance spectra were measured at room temperature using modified CARY-14 (UV-region) and CARY-

17 (vis/NIR-region) spectrophotometers (OLIS Inc., Athens, GA, USA) equipped with Ulbricht spheres. Four different configurations (step width, bandwidth, scan rate, detector type) were applied to seize the range from 5000 cm<sup>-1</sup> to 40000 cm<sup>-1</sup>. In the UV range (200 nm to 600 nm) 800 data points (step width 0.5 nm, scan rate 1 nm · sec<sup>-1</sup>, band width 0.6 nm), in the visible range (300 nm to 900 nm) 600 data points (step width 1.0 nm, scan rate 1 nm · sec<sup>-1</sup>, band width 1.2 nm) and in the near infrared range (600 nm to 2200 nm) 500 data points (step width 4 nm, scan rate 2 nm · sec<sup>-1</sup>, band width 5 nm) were recorded. For detection in the UV/vis range a photomultiplier tube (PMT) was used, in case of the vis region with an aperture width of 0.06 nm. In the near-infrared region a semiconducting lead(II) sulfide detector with variant gap widths (1.4 nm to 2.2 nm) was utilized. The spectra are represented as *K/S* vs. wavenumber (Kubelka-Munk function [177,178]).

**DFT calculations:** DFT calculations were carried out by employing the projected-augmented-wave [179,180] method encoded in the Vienna ab initio simulation package (VASP) [181] and the generalized gradient approximation (GGA+U) of Perdew, Burke and Ernzerhof [64] for the exchange correlation functionals. Full geometry optimizations were carried out using a plane-wave energy cut-off of 550 eV and 32 k points in the irreducible Brillouin zone. The experimental model was used for calculations of the electronic structure. For the latter, a threshold of the self-consistent-field energy convergence of 10<sup>-6</sup> eV were used with U = 1.6 eV to match the experimental bandgap. For the calculations of the magnetic exchanges identified in the text, we mapped the total energies for a number of collinear spin-polarized configurations into a classical Heisenberg model to obtain individual exchange couplings using U = 3.2 eV, see section A.II.2, Figure A 0-3 and Table A 0-18 in the appendix.

#### *II.4.2.2 Synthesis*

First, the precursors Sr<sub>3</sub>(PO<sub>4</sub>)<sub>2</sub> and the CrPO<sub>4</sub> were prepared as single phases. The former was obtained by reaction between (NH<sub>4</sub>)<sub>2</sub>HPO<sub>4</sub> and BaCO<sub>3</sub> at 1273 K for 2 days. CrPO<sub>4</sub> was obtained by dissolving chromium metal in HCl before adding HNO<sub>3</sub> and heating until dryness. HNO<sub>3</sub> and then (NH<sub>4</sub>)<sub>2</sub>HPO<sub>4</sub> were re-added and heated up till dryness once again. The dried compound was fired at 1273 K for 2 days. Sr<sub>2</sub>Cr(PO<sub>4</sub>)<sub>2</sub> was then prepared from a stoichiometric mixture of Sr<sub>3</sub>(PO<sub>4</sub>)<sub>2</sub>, CrPO<sub>4</sub> and Cr (molar ratio 2:2:1), as described by the following equation:



This was ground and pressed into pellets under a uniaxial pressure. The pellets were placed in evacuated silica ampoules at 1273 K for 5 days, leading to single-phase material, as shown on Figure II-17a. Single crystals were grown by isothermal vapour phase moderated recrystallization after placing the microcrystalline  $\text{Sr}_2\text{Cr}(\text{PO}_4)_2$  in a seal silica tube at 1273 K for 15 days with a trace of iodine, and additional chromium. It allows the formation of  $\text{CrI}_2$  mineralizer and hampers the  $\text{Cr}^{2+}$  oxidation by  $\text{I}_2$ . Blue/turquoise platelet-shaped crystals where obtained with length up to 1 mm, see Figure II-17b.

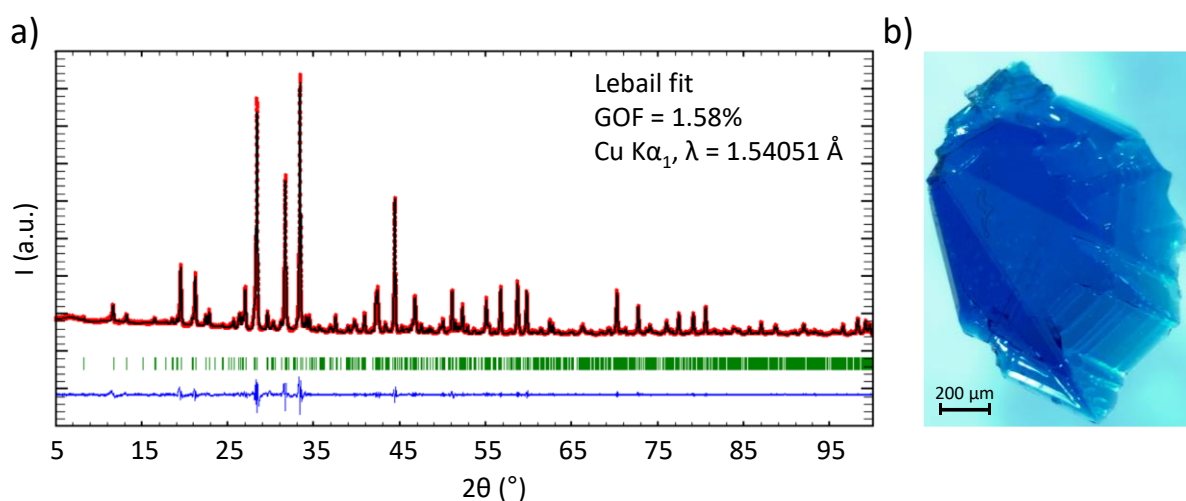


Figure II-17.  $\text{Sr}_2\text{Cr}(\text{PO}_4)_2$ . a) Le-Bail fit of the polycrystalline sample (Guinier recordings;  $\text{Cu K}\alpha_1$ ,  $\lambda = 1.54051 \text{ \AA}$ , quartz monochromator). b) Micro-photograph of an as-grown crystal.

### II.4.3. Crystal structure refinement and description

#### II.4.3.1 Structure refinement

All the tested crystals showed complicated diffraction patterns after reconstruction of the precession frames in the basal planes. Eventually, multiple, non-merohedral twinning (“trilling”) could be resolved, which lead initially to an erroneous large hexagonal unit cell ( $a = b = 21.4 \text{ \AA}$ ,  $c = 21.2 \text{ \AA}$ ,  $\gamma = 120^\circ$ ). From the diffraction data of such a multiple twin (three domains rotated by  $\pm 120^\circ$  around the  $c$ -axis) data for the real orthorhombic unit cell with  $a = 10.7064(18) \text{ \AA}$ ,  $b = 9.2730(14) \text{ \AA}$ ,  $c = 21.2899(7) \text{ \AA}$  were extracted using the Cell-Now routine [182]. As will be detailed later, this twinning originates from a hexagonal close-packing of  $\text{Sr}^{2+}$  ions and phosphate groups within the crystal structure, see Figure II-18. The best data were integrated using the orientation of the main domain only, with consideration of the twin overlap during the refinement stage. The crystal structure was solved (spin-flipping method) and refined using the Jana 2006 suite [61].  $\text{Sr}_2\text{Cr}(\text{PO}_4)_2$  crystallizes in space group  $Pbca$ . The

refinement with anisotropic thermal displacement parameters for all atoms in the last cycles converged at  $R_1 = 3.63\%$  ( $I > 2 \sigma(I)$ ), with respect to the three domain contributions refined to 42.3(7) %, 39.5(5) %, and 18.1(5) % respectively. Data collection, refinement parameters and detailed crystallographic information are listed in Table A 0-14. Fractional atomic coordinates, anisotropic atomic displacement parameters, and selected bond distances are listed in Table A 0-15-8.

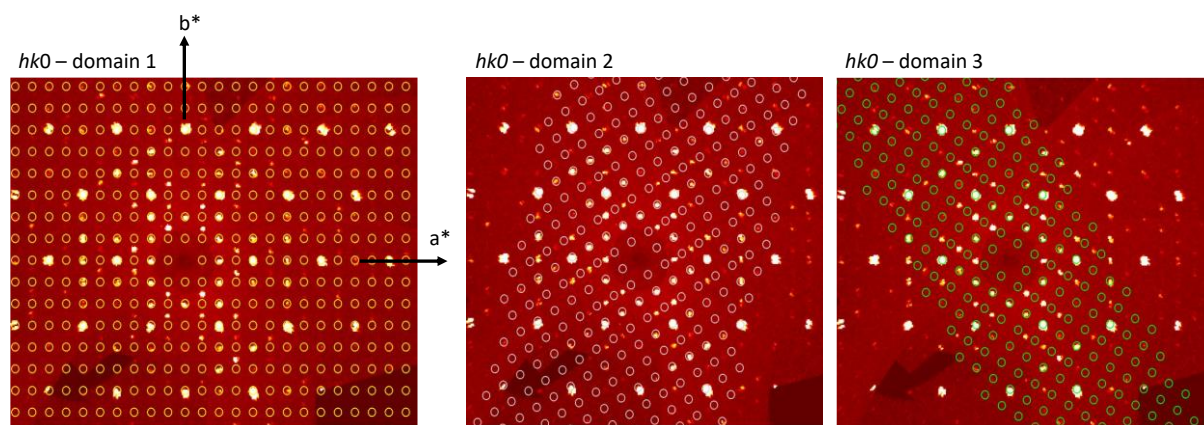


Figure II-18. Reconstructed  $hk0$  frames for  $Sr_2Cr(PO_4)_2$  single crystal at ambient conditions and the overlaid calculated positions in the three domains rotated by  $120^\circ$ .

#### II.4.3.2 Crystal Structure description

The crystal structure of the  $Sr_2Cr(PO_4)_2$  contains two independent  $Cr^{2+}$  ions with their coordination strongly influenced by the *JT* effect, *i.e.* square pyramidal [ $Cr^{II}O_{4+1}$ ] ( $1.983 \leq d(Cr(1)-O) \leq 2.388 \text{ \AA}$ ) and square planar [ $Cr^{II}O_4$ ] ( $1.994 \text{ \AA} \leq d(Cr(2)-O) \leq 1.995 \text{ \AA}$ ). Bond valence sums were calculated to 1.921(18) and 2.08(2) respectively (see Table A 0-16 in the supporting information for details). The projection of the crystal structure in the (*ac*) plane is shown in Figure II-19a. Cr(1) atoms are arranged into a pseudo-trigonal 2D-lattice and so do the surrounding atoms Sr(1) and Sr(3). This pseudo-trigonal symmetry is broken by the oxygen coordination around Cr(1), which finally creates a 2D lattice of corner sharing Cr(1)O<sub>5</sub> and three P(1)O<sub>4</sub> with 3/5<sup>th</sup> of the oxygen ligands in the layers, Figure II-19b. The pending corners are connected by the second set of phosphate groups, P(2)O<sub>4</sub> and P(3)O<sub>4</sub>, to the neighbouring layers containing the Cr(2). This second layer type consists of the Cr(2) ions in square-planar coordination by two P(2)O<sub>4</sub> and two P(3)O<sub>4</sub> as is shown in Figure II-19c. The three Sr atoms have distances between  $2.48 \text{ \AA} \leq d(Sr-O) \leq 2.96$  and coordination numbers between 8 and 10 (Table A 0-16). They are located in layers stacked along the *c*-axis. According to the *Pbca*

symmetry the two layers containing the Cr(1) (at  $z = 0.25$  and  $0.75$ ) as well as the two containing the Cr(2) (at  $z = 0$  and  $0.5$ ) are related by inversion symmetry.

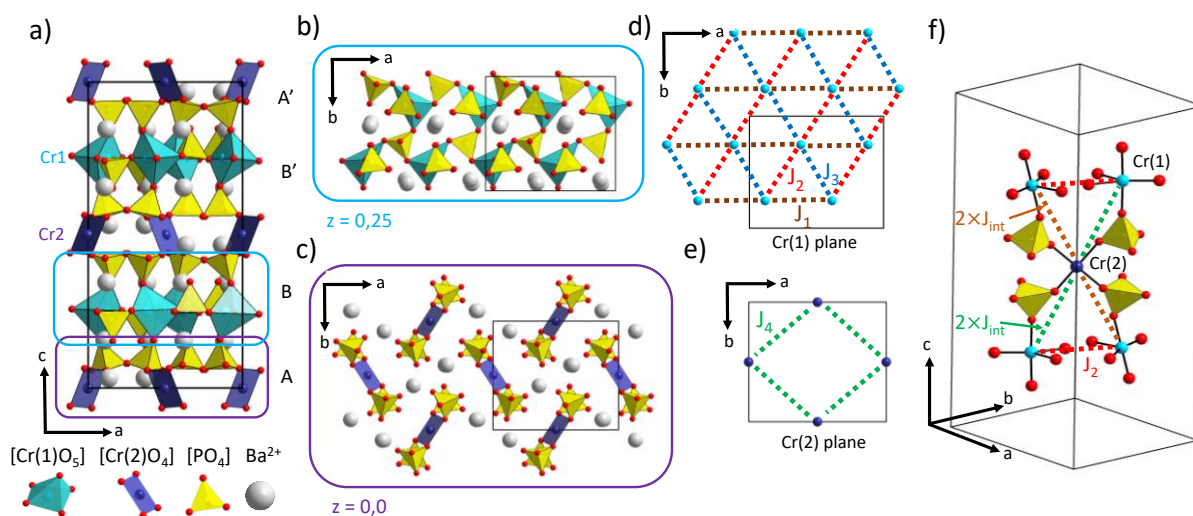


Figure II-19. a) Projections of the crystal structure of  $\text{Sr}_2\text{Cr}(\text{PO}_4)_2$  onto the  $ac$  plane. b-c) Individual Cr(1) and Cr(2) layers. d-f) Scheme of the main magnetic exchanges considered in the layers. g) Visualisation of the magnetic frustration within the Cr(2)-layers induced by the two neighbouring Cr(1)-layers.

#### II.4.4. Magnetic Properties

##### II.4.4.1 DFT+U investigation of magnetic exchanges in competition

Due to the high susceptibility of chromium(II) towards oxidation and the small number of surprisingly air stable anhydrous phosphates and silicates containing  $\text{Cr}^{2+}$  ions, little is known about their magnetic properties. To the best of our knowledge, only  $\alpha\text{-Cr}_2\text{P}_2\text{O}_7$  magnetic behaviour and magnetic structure are fully understood [19]. In view of the complex stacking of Cr(1)- and Cr(2)-layers within the crystal structure of  $\text{Sr}_2\text{Cr}(\text{PO}_4)_2$ , prior to the analysis of its experimentally characterized magnetic behaviour, an overview of the interplay between the various spin-exchanges seems appropriate. They were calculated by DFT+U in spin-polarized configuration. To that purpose, we mapped the total energies for a number of collinear spin configurations into a classical Heisenberg model (see section A.II.2, Figure A 0-3 and Table A 0-18 in the appendix.) to extract the individual  $J_{1-4}$  exchange couplings, see Figure II-19d-f and Table II-3. We used the scalar  $U = 3.2$  eV, estimated for  $\text{Cr}^{2+}$  ions [183]. The results of our calculations are listed in the Table II-3 together with the main geometrical paths.

**Exchanges in the Cr(1) slabs.** Within the pseudo-triangular lattice, the involved  $J_{1-3}$  exchanges develop antiferromagnetic (AFM)  $S = 2$  chains along the strongest  $J_1 (= 7.23 \text{ K})$  path, see Figure II-19d. Weaker interchain exchanges of  $0.91 \text{ K}$  ( $J_2$ , AFM) and  $-0.41 \text{ K}$  ( $J_3$ , FM) were calculated in the same slabs. Such AFM chains are known to open a Haldane-gap for  $S = 2$  integer spins. Similar chains occur in layered compounds, *i.e.*  $\alpha\text{-NaMnO}_2$  which orders due to anisotropic single ions and interlayer exchanges [184].

**Exchanges in the Cr(2) slabs.** The inner Cr(2)-Cr(2) exchanges were calculated weakly FM ( $J_4/K_b = -0.61 \text{ K}$ ) in spite of the long paths which involve four oxygen ions, with lack of significant orbital overlap between next  $\text{Cr}(\text{PO}_4)_4$  groups.

**Interlayer exchanges.** The two couplings between the Cr(1) and Cr(2) slabs labelled  $J_{\text{inter}}$  and  $J'_{\text{inter}}$  were assumed equal, see Table II-3. The average  $J_{\text{inter}}$  was calculated weak and FM,  $J_{\text{inter}}/K_b = -0.67 \text{ K}$ . It is expected so, due to the Cr(1)-O-P-O-Cr(2) paths, with long Cr(1)-Cr(2) distances ( $> 5.9 \text{ \AA}$ ) and unfavourable Cr-O-O-Cr dihedral angles of  $\sim 120^\circ$ . However, it is of preliminary importance that each Cr(2) interacts with two pairs of Cr(1) atoms, one pair in each of the adjacent layers via  $J_2$ . These interactions form planar  $\text{Cr}_5$  units, see Figure II-19f, where Cr(2) stand in a highly frustrated position via the corner-sharing triangles  $J_{\text{inter}}(\text{FM})$ - $J'_{\text{inter}}(\text{FM})$ - $J_2(\text{AFM})$ . We also checked that the exchange between two Cr(1) layers across a Cr(2) one is zero at the DFT accuracy level. Finally,  $\text{Sr}_2\text{Cr}(\text{PO}_4)_2$  consists of robust AFM low-D triangular Cr(1) layers, which are weakly coupled to the Cr(2) layers in a strongly frustrated situation.

Table II-3.  $J$  values from DFT+U calculations, Cr-Cr distances and Cr-O-O-Cr torsion angles.

Coupling	E(K)	d(Cr-Cr) (Å)	Torsion angle Cr-O-O-Cr (°)
$J_1$	7.23	5.3532(21)	Cr(1)-O(4)-O(6)-Cr(1) 166.1(5)
$J_2$	0.91	5.2609(21)	Cr(1)-O(8)-O(4)-Cr(1) 176.4(7)
$J_3$	-0.41	5.4514(21)	Cr(1)-O(6)-O(8)-Cr(1) 175.4(4)
$J_{\text{inter}}$	-0.67	5.9141(15)	Cr(2)-O(9)-O(2)-Cr(1) 116.6(6)
$J'_{\text{inter}}$		5.9523(15)	Cr(2)-O(3)-O(7)-Cr(1) 128.7(7)
$J_4$	-0.61	7.0819(3)	Cr(2)-O <sub>4</sub> -Cr(2) ---

#### II.4.4.2 Magnetic properties and ordering

**Magnetic properties.** The magnetic susceptibility of  $\text{Sr}_2\text{Cr}(\text{PO}_4)_2$  (assumed as  $M/H$ ) collected at  $\mu_0.H = 0.1$  T and its inverse are plotted on Figure II-20a. It is characterized by a two-step magnetic ordering occurring at  $T_{N1} = 11.5$  K and  $T_{N2} = 3.6$  K as i) suspected from the  $d\chi/dT$  plot (inset Figure II-20a) and attested by its heat capacity described below. It shows a concave downward slight deviation to the Curie-Weiss (CW) law below  $\sim 70$  K. Between 400 K and 70 K, our CW fit yields  $\mu_{\text{eff}} = 4.89(1) \mu_B/\text{Cr}$  and  $\vartheta_{\text{CW}} = -33.9(1)$  K, matching its spin-only moment ( $d^4, S = 2, \mu_{\text{eff}} = 4.89 \mu_B$ ). The magnetic data suggest no significant orbital contribution for the  $\text{Cr}^{2+}$  ions, which is confirmed by the ligand field analysis. Below the rounded bump between 25K and  $T_{N1} = 11.5$  K, a large  $\chi(T)$  paramagnetic-like tail persists.

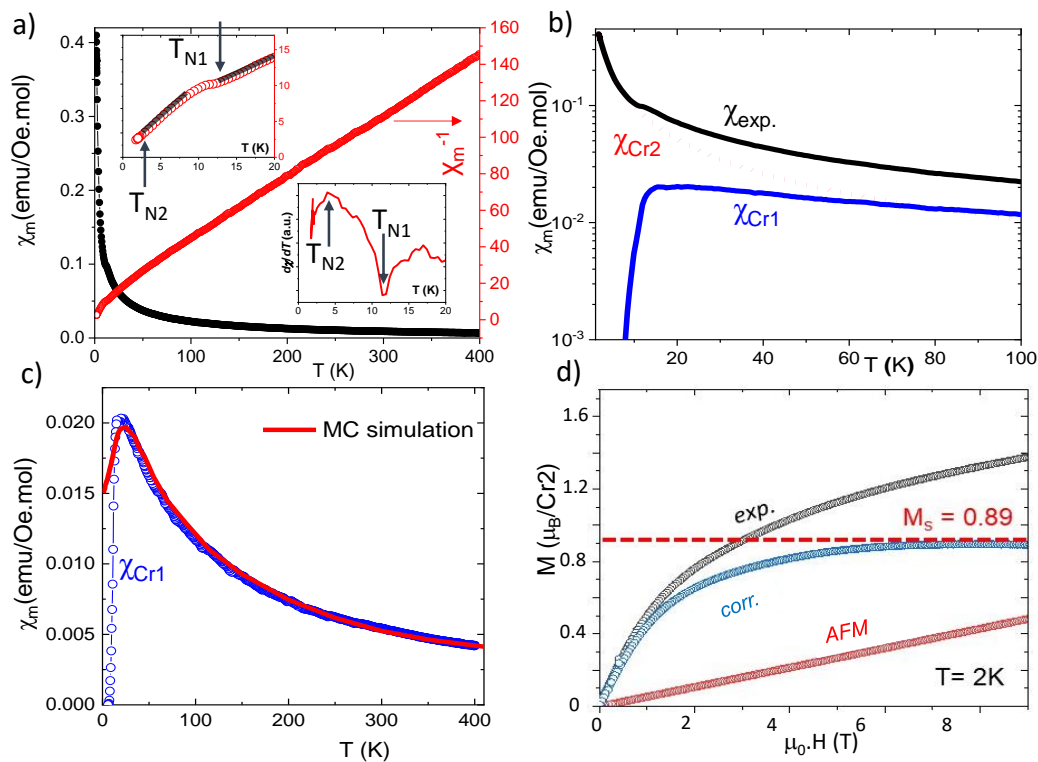


Figure II-20. a) Magnetic susceptibility ( $\chi$ ) and its inverse vs. temperature with zoom of the low-temperature shift for the later in the top inset and derivative  $d\chi/dT(T)$  in the bottom inset. b) the deconvolution of  $\chi(T)$  in a paramagnetic (Cr2)-like and gapped (Cr1)-like contributions. c) fit of the  $\chi(\text{Cr1})$  contribution obtained through Monte-Carlo simulation. d) field dependence of the Magnetization at 2K (before (black) and after (blue) removal of the AFM contribution (red).

In a first approximation, the low-temperature part ( $T_{N1}-T_{N2}$  K) was fitted using a second CW law with  $\mu_{\text{eff}2} = 2.95(2) \mu_B/\text{Cr}$ ,  $\vartheta_{\text{CW}2} = -1.1(1)$  K, this would correspond to the magnetic

contribution of  $\sim 0.36$   $\text{Cr}^{2+}$  spin-only ions per formula unit. This ratio is reminiscent of the 2:1 Cr(2):Cr(1) ratio such that the low-temperature paramagnetic-like may be assigned to  $\chi_{\text{Cr2}}$  while the Cr(1) ions are AFM ordered below  $T_{N1}$ .  $\chi_{\text{Cr1}}$  was estimated as  $\chi_{\text{total}} - \chi_{\text{Cr2}}$ , see Figure II-20b, and shows a typical spin-gapped behaviour with  $\chi_{\text{max}} \sim 23$  K.  $\chi_{\text{Cr1}}$  was properly reproduced using a Monte-Carlo simulation using the DFT values of  $J_{1,2,3}$  over a 2D lattice of Heisenberg spins [185], see Figure II-20c. The low-T divergence between  $\chi_{\text{Cr1}}$  and  $\chi_{\text{fit}}$  is due to the interactions at a lower energy scale between the Cr(1) and Cr(2) layers not taken into account here. At 2 K, below  $T_{N2}$  2 K, after removal of the linear  $M_{\text{Cr(1)}}(\text{H})$  AFM contribution, the saturated magnetization reaches  $M_s = 0.89 \mu_B/\text{FU}$ , *i.e.* 66% of the Cr(2) contribution,  $S = 2$ . see Figure II-20d. It is assigned to a partial fluctuation of Cr(2), as detailed later.

Two sharp  $\lambda$ -type peaks were observed for the specific heat  $C_p$  at  $T_{N1} = 11.3$  K (strong) and  $T_{N2} = 3.6$  K (weak), see Figure II-21a. It pictures the subsequent magnetic ordering of only the Cr(1) atoms at  $T_{N1}$  leaving Cr(2) mainly paramagnetic, and the further ordering of Cr(2) below  $T_{N2}$ . In this scenario, between  $T_{N1}$  and  $T_{N2}$  Cr(2) shows an idle spin situation due to its pivotal role as magnetic connector between the Cr(1)-layers, but its strong frustration due to the interplay between the Cr(2)-Cr(1) interactions. Assuming no electronic contribution in this insulating material, the magnetic contribution  $C_{\text{magn}}$  to the specific heat was obtained after subtracting the lattice contribution  $C_{\text{latt}}$  to total  $C_p$ .  $C_{\text{latt}}$  was fitted between 70 K and 320 K using two Debye contributions:

$$C_{\text{latt}} = 9R \sum_{i=1}^2 C_i (T/\theta_{Di})^3 \int_0^{\theta_{Di}/T} \frac{x^4 e^x}{(e^x - 1)^2} dx$$

Figure II-21b shows the  $C_{\text{magn}}/T(T)$  plot. Its integration returns a total entropy release of  $\sim 10.3$   $\text{J mol}^{-1} \cdot \text{K}^{-1}$  at 30 K which represents only 78% of the theoretical value  $S_{\text{theo}} = R \cdot \ln(2S + 1) = 13.37$   $\text{J mol}^{-1} \cdot \text{K}^{-1}$  expected for one  $S = 2$  spin per formula unit. A rough decomposition of the entropy released at  $T_{N2}$  and  $T_{N1}$  results in 2.9 ( $\sim 22\%$  of  $S_{\text{theo}}$ ) and 7.5 ( $\sim 56\%$  of  $S_{\text{theo}}$ )  $\text{J mol}^{-1} \cdot \text{K}^{-1}$  respectively. While the entropy contribution at  $T_{N1}$  is closed to the ideal Cr(1) ( $2/3^{\text{rd}}$ ) contribution, it is clear that both the low-temperature paramagnetic tail and ideal frustration of Cr(2) affects its degree of magnetic ordering. Moreover, as highlighted in Figure II-21c, we observe a prominent shift of the maximum of the magnetic contribution  $C_{\text{magn}}/T$  at  $T_{N2}$  towards higher temperature, under an increasing field, while, the maximum at  $T_{N1}$  rests nearly

unaffected. This indicates the relative fragility and high degree of spin fluctuation at  $T_{N2}$  compared to the robust ordering at  $T_{N1}$  in line with the relative  $J$  values.

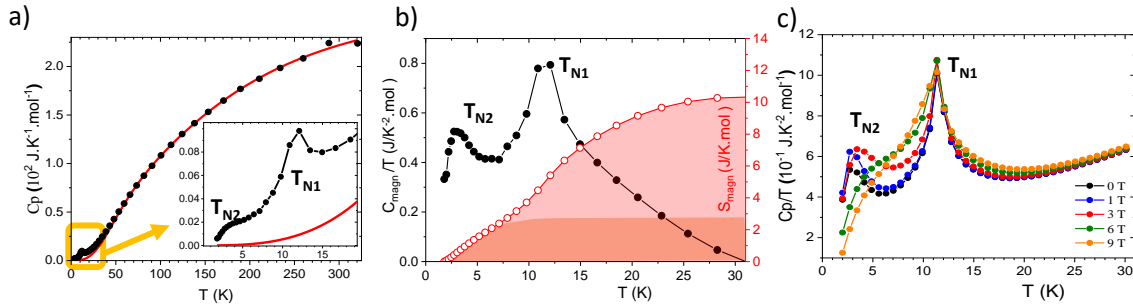


Figure II-21. a) Specific heat Measurement and the magnification at low  $T$  showing two sharp  $\lambda$ -type peaks. b)  $C_{magn}/T(T)$  plot and its integration. c)  $C_p/T(T)$  plot under different magnetic field.

**Magnetic ordering.** In  $\text{Sr}_2\text{Cr}(\text{PO}_4)_2$ , below the large thermal domain dominated by the Cr(1) 2D magnetic correlations, the effect of  $J_{inter}$  exchanges orders the system at  $T_{N1}$ . We checked that  $T_{N1} = 11.3$  K matches with the estimated value calculated using a modified random-phase approximation (RPA) for weakly coupled layers,  $T_{N1} = 4\pi \cdot n \cdot J_{intra} / [b - \ln(|J_{inter}/J_{intra}|)]$  where  $n$  and  $b$  parameters were adjusted from various materials [186] for  $S = 1/2$  and  $S = 1$  cases. For  $S = 5/2$   $\text{Fe}^{3+}$  ions, a good estimation of  $T_N$  was achieved using the  $S = 1$  parameter ( $n = 0.68$  and  $b = 3.12$ ) [187,188]. Here also in the  $S = 2$  case, using our DFT values for  $|J_{intra}| = 2.9$  K (averaged from  $J_{1-3}$ ) and  $|J_{inter}| = 0.7$  K, we calculate  $T_{N1} \sim 5.5$  K close to its experimental value. Hereafter, we use neutron-diffraction to unravel the specific role of Cr(2) on the two-stepped magnetic orderings. From our prior magnetic characterizations, Cr(2) appears in a frustrated idle spin situation, for which only a partial contribution is expected to be ordered. The antagonism between its key-role and mandatory connector between two Cr(1) layers, and its ideally frustrated state imposed by symmetry resembles the idle spin of the  $\text{Fe}_3\text{F}_8(\text{H}_2\text{O})_2$  case [189].

#### II.4.4.3 Magnetic Structures refinement

At 15 K, the crystal structure aligns well with the single-crystal model. Below the Néel temperature  $T_{N1}$ , new reflections emerge (see Figure II-22c), consistent with magnetic susceptibility and heat capacity measurements. The magnetic reflections are indexed to the same crystallographic cell, using a propagation vector  $\mathbf{k} = [0 \ 0 \ 0]$  (see Figure II-22a-c). Representation analysis performed with Basireps [151] indicates a decomposition of the  $\Gamma_{\text{Cr}(1)}$

magnetic representation into eight irreducible representations named below using the Bilbao Crystallographic Server standards:  $[3 \times mGM1+(1) \oplus 3 \times mGM1-(1) \oplus 3 \times mGM2+(1) \oplus 3 \times mGM2-(1) \oplus 3 \times mGM3+(1) \oplus 3 \times mGM3-(1) \oplus 3 \times mGM4+(1) \oplus 3 \times mGM4-(1)]$  of dimension one. The 4(b) Wyckoff position of Cr(2) yields the  $\Gamma_{Cr(2)}$  decomposition into four irreducible representations:  $[3 \times mGM1+(1) \oplus 3 \times mGM2+(1) \oplus 3 \times mGM3+(1) \oplus 3 \times mGM4+(1)]$  of dimension one.

Between  $T_{N1}$  and  $T_{N2}$ , only Cr(1) orders magnetically, adopting the  $mGM3-$  irreducible representation (details in in Table A 0-19 in the appendix section). Magnetic patterns were obtained by subtracting the paramagnetic pattern at 15 K, and the magnetic space group  $Pb'ca$  (61.435) was determined. At 5 K, Cr(1) moments of of 3.30(6)  $\mu B$  lie in the  $ab$  plane ( $M_z = 0$ ), forming collinear antiferromagnetic (AFM) chains along  $a$ , with a canting angle of  $\sim 32^\circ$  between adjacent chains and planes. Interlayer Cr(1) atoms also show AFM coupling with the same canting angle. Between two stacked layers along the  $c$ , two apical Cr(1) atoms are mostly AFM with this same canting angle. Constraining a colinear magnetic ( $M_y = 0$ ) structure failed, due to some non-calculated reflexions (see Figure II-22a and Figure A-II 2e, f in the Appendix II). In the  $ab$  planes, we note that the strongest  $J_1$  (AFM) relates two purely antiparallel sites, while both  $J_2$  (weak AFM) and  $J_3$  (weak FM) mediate pairs of non collinear canted spins, see Figure II-23a. The non-collinear order of Cr(1) indicates that single-ion anisotropy of  $Cr^{II}$  may be important and potentially exceeds weak interchain couplings  $J_2$  and  $J_3$ . The spin direction within each chain is then governed by the local anisotropy axis. The large ordered moment of 3.3  $\mu B$  (more than 80% of the theoretical value) and the not-too-low  $T_N$  of 11.3 K further indicate that this system is far away from the Haldane limit where no magnetic order would be expected. It is in echo with our previous MC results that proved the importance of both  $J_{2,3}$  inter-chain exchanges and the anisotropy to promote the magnetic order, away from the pure Haldane spin-liquid phase. The lack of magnetic ordering on “free” Cr(2) intermediate ions validates the ansatz of an idle spin for Cr(2) deduced from our magnetic and thermodynamic results. Alternatively, the simplest solution of the Cr(2) ideal frustration shown in Figure II-19f, would consist of either i) Cr(2) magnetic moments parallel to  $c$ , i.e. perpendicular to the Cr(1) moments, or ii) the breaking of the Cr(2) site  $-1$ -point symmetry of Cr(2).

Below  $T_{N2} = 3.6$  K, the system chooses the later (ii) scenario. Extra-magnetic satellites (re)start growing such as the (001), (100) and (101) magnetic peaks. We first explore systematically the possible combination of irreps keeping the mGM3- that was already present at  $T_{N1}$ . Only the addition of the mGM1+ irreps to the previous model, allows for an acceptable refinement, see Figure II-22b. Cr(1) is affected by mGM3- and mGM1+ and Cr(2) by MGM1+ only, see the Figure A II-2g, h in the Appendix II. However, the mixing of the mGM3- and mGM1+ returns a drastic effect on the Cr(1) moments, now split into two Cr(1)a and Cr(1)b magnetic orbits. A good fit ( $R_{\text{magn}} = 18.9\%$ , from magn. data only) was obtained by imposing  $M_{\text{Cr(1)a}} = M_{\text{Cr(1)b}}$  using MGM3- only for the  $M_x$  components and MGM1+ only for the  $M_y$  component ( $M_{y(\text{MGM3-})} = 0$ ,  $M_{x(\text{MGM1+})} = 0$ ,  $M_z = 0$ ). All Cr(1) orbits have colinear spins in-plane and Cr(2) ( $M_x, M_y, M_z \neq 0$ ) raises the frustration by an orientation nearly perpendicular to the planes. The group analysis indicates the magnetic space group P21ca.1 which highlights the necessity of an alternative fit with two individual Cr(1)a and Cr(1)b positions. It was performed using the magnetic space group approach. After transformation of the above space group to the standard setting by  $(-c, b + 1/4, a)$  the magnetic space group is Pca21 (29.99) and was used as such. Here, Cr(1)a and Cr(1)b are treated individually with respect to the loss of the inversion symmetry and their moments were restrained equal. Using the magnetic only contribution, the fit is equivalent to the previous one, see Figure II-22b ( $R_{\text{magn}} = 18.9\%$  from magn data only at 1.5 K) with  $M_{\text{Cr(1)a,b}} = 3.60(4) \mu\text{B}$  and  $M_{\text{Cr(2)}} = 2.06(7) \mu\text{B}$ . The Figure II-22c shows the result of the Rietveld fit of the full pattern at 1.5 K ( $R_{\text{Bragg}} = 1.9\%$  and  $R_{\text{magn}} = 4.9\%$ ) with similar local moments and orientations, using the crystallographic data listed in Table A II-11. The magnetic symmetry indicates a potential lowering of the crystal symmetry. When analyzing the full nuclear and magnetic pattern, the structural flexibility provided by the non-centrosymmetric  $Pca2_1$  space group is substantial. Consequently, only the Cr(1a) and Cr(1b) positions were refined, as they yielded the most significant improvement in the fit. However, the refined coordinates should be interpreted with caution due to parameter correlations during refinement. In practice, the loss of symmetry arises from spin-lattice interactions, i.e. the GM3- (nucl.) + mGM3- (magn.) + mGM1+ (magn.) trilinear coupling 60. From the symmetry viewpoint, the mGM3- mode contains the mGM1+ as second order parameter. Therefore, the activation of this mode below  $T_{N2}$  in the Cr(1) is endorsed by symmetry. The refined magnetic structure is shown in Figure II-23b. The thermal evolution of the refined moments is shown on Figure II-22e.

Examination of the lattice parameter evolution versus temperature shows that the expected cell contraction over the three orthorhombic axes on cooling, is inverted across  $T_{N1}$ , resulting in a positive magnetostrictive effect. This reverses again, leading to negative magnetostriction, see Figure II-22f. This comforts the plausible existence of crystal symmetry lowering in conjunction with magnetic ordering.

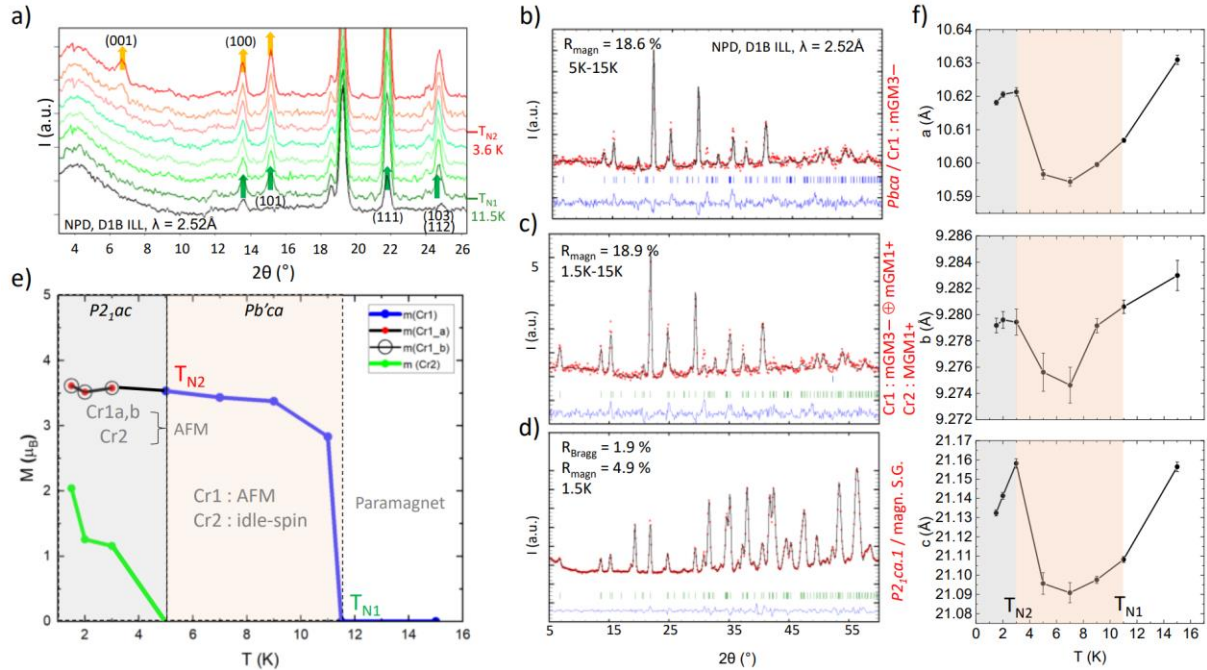


Figure II-22. a) NPD patterns on cooling. b) Refinement of the magnetic peaks at 1.5K using two Ireps and c) using the magnetic space group approach. d) Refinement of the full pattern at 1.5 K using the magnetic space group approach. e) Thermal evolution of the refined magnetic moments and f) cell parameters.

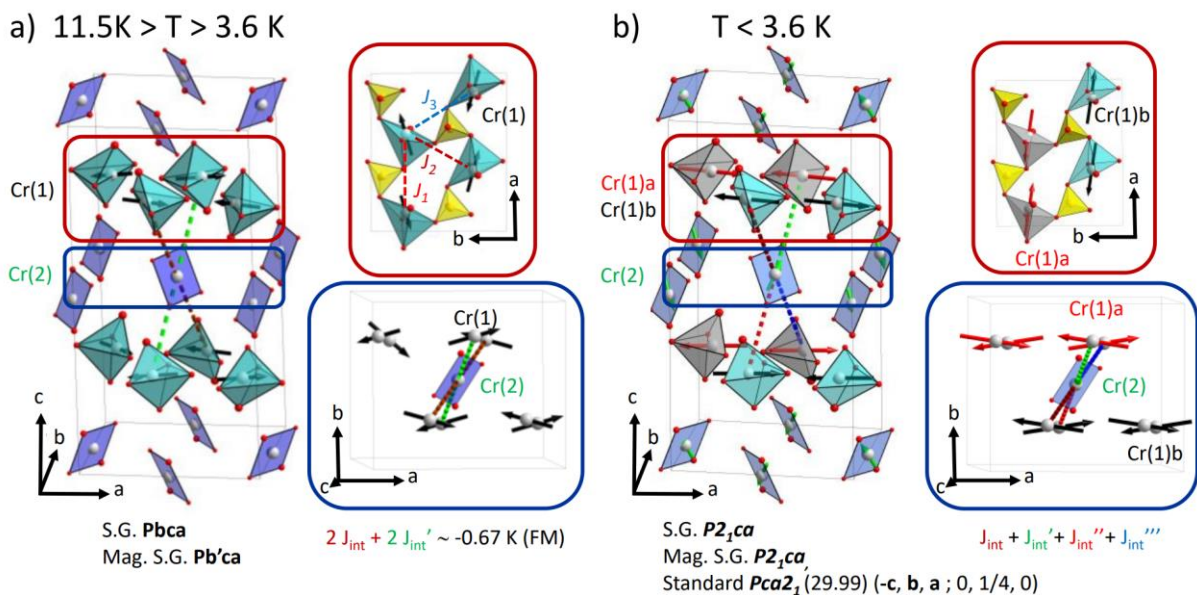


Figure II-23. Overlay of the nuclear structure and the magnetic structure at a) 5K and b) 1.5K with the various magnetic couplings and symmetries involved.

#### II.4.5. Combined spectroscopic and DFT analysis of ligand fields

**Optical spectra and ligand field analysis.** Plate-like crystals of  $\text{Sr}_2\text{Cr}(\text{PO}_4)_2$  with faces  $(0\ 0\ 1)$  and  $(0\ 0\ \bar{1})$  are weakly dichroic blue/blueish-green, whereas the powder shows dark turquoise colour. Figure II-24a show the diffuse powder reflectance spectrum (DRS) and polarized single-crystal spectra (all at ambient temperature). Band assignment is based on reference spectra in literature for square-pyramidal  $[\text{Cr}(\text{I})\text{O}_{4+1}]$  ( $\text{SrCrP}_2\text{O}_7$  [27, 28]) and square-planar  $[\text{Cr}(\text{II})\text{O}_4]$  ( $\text{ACrSi}_4\text{O}_{10}$ , A: Ca [135], Sr [134], Ba [134] ;  $\square$ - $\text{Ba}_2\text{Cr}(\text{PO}_4)_2$  [20]) chromophores and is also supported by AOM (see Appendix Section A.II.4.), these are in agreement with DFT calculations. According to Laporte rule the electronic transitions for the  $[\text{Cr}^{\text{II}}(\text{I})\text{O}_5]$  chromophore are parity-allowed for a static electric dipole mechanism. For the second chromophore,  $[\text{Cr}^{\text{II}}(\text{II})\text{O}_4]$ , electronic transitions can only occur via vibronic coupling. Thus, the absorption bands for the latter are expected to be much weaker (by a factor of  $10^{-2}$  [190]). In the polarized single crystal spectra the weak shoulder at  $\lambda = 11290\ \text{cm}^{-1}$  and the main absorption bands at  $\lambda = 13250\ \text{cm}^{-1}$  and  $16500\ \text{cm}^{-1}$  can readily be assigned to the electronic transitions on the  $[\text{Cr}^{\text{II}}(\text{I})\text{O}_5]$  chromophore:  $d(z^2) \rightarrow d(x^2-y^2)$ ,  $d(xy) \rightarrow d(x^2-y^2)$ ,  $d(xz, yz) \rightarrow d(x^2-y^2)$ , corresponding to the electronic states (for point group  $C_{4v}$ ):  ${}^5B_1 \rightarrow {}^5A_1$ ,  ${}^5B_1 \rightarrow {}^5B_2$ , and  ${}^5B_1 \rightarrow {}^5E$  (see Figure II-24b). This assignment is typical for  $\text{Cr}^{2+}$  ions in elongated octahedral coordination (with the square-pyramidal case being closely related). In contrast, the main absorption band of the centrosymmetric  $[\text{Cr}(\text{II})\text{O}_4]$  chromophore is discernible only in the powder reflectance spectrum of  $\text{Sr}_2\text{Cr}(\text{PO}_4)_2$ , where the intensity of weak transitions is generally overestimated. This band consists of three electronic transitions, which are (with increasing energy)  $d(xz, yz) \rightarrow d(x^2-y^2)$  and  $d(z^2) \rightarrow d(x^2-y^2)$ . The observed transition energies for the two chromophores are reasonably well matched by AOM using the Racah parameters  $B = 664\ \text{cm}^{-1}$ ,  $C = 2712\ \text{cm}^{-1}$  ( $B_{\text{fr. ion}} = 796\ \text{cm}^{-1}$ ,  $C_{\text{fr. ion}} = 3343.2\ \text{cm}^{-1}$ ,  $C/B = 4.2$ ) and the spin-orbit coupling constant  $\zeta = 184\ \text{cm}^{-1}$  ( $\zeta_{\text{fr. ion}} = 230\ \text{cm}^{-1}$ ). The free ion values [190] had been reduced in the AOM calculations (nephelauxetic ratio  $\beta = 0.80$ ). For both chromophores the AOM parameter  $e_{\sigma, \text{max}}(\text{Cr}^{\text{II}}-\text{O}) = 8000\ \text{cm}^{-1}$  for the oxygen ligand at  $d(\text{Cr}^{\text{II}}-\text{O})_{\text{min}}$  has been used. Longer distances  $d(\text{Cr}^{\text{II}}-\text{O})$  were accounted for by smaller  $e_{\sigma}(\text{Cr}^{\text{II}}-\text{O})$  according to the relation  $e_{\sigma}(\text{Cr}^{\text{II}}-\text{O}) \sim d(\text{Cr}^{\text{II}}-\text{O})^{-5.0}$ .

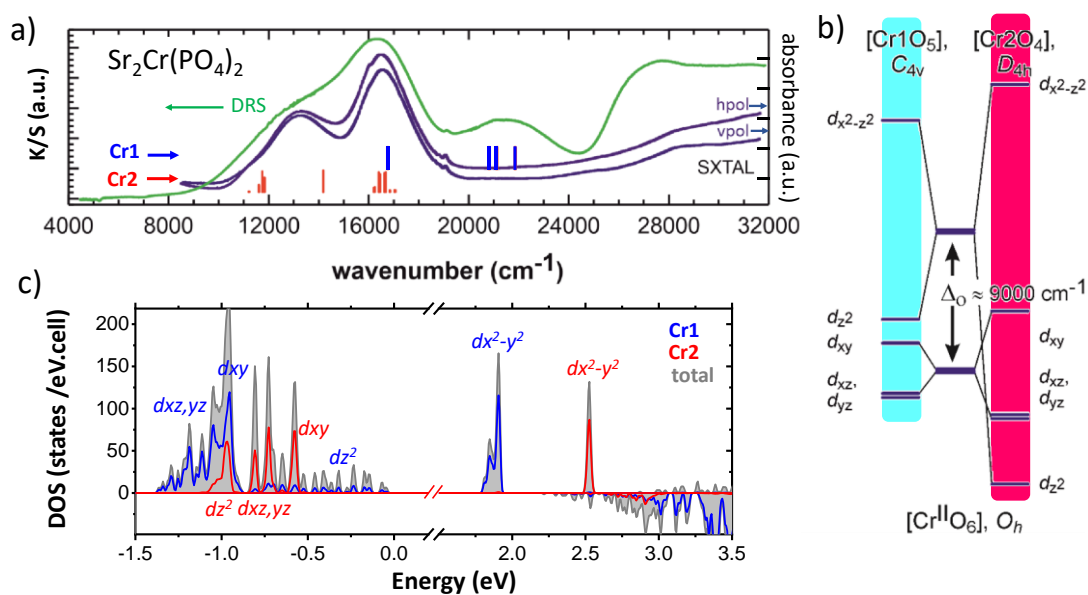


Figure II-24. Sr<sub>2</sub>Cr(PO<sub>4</sub>)<sub>2</sub>. a) Diffuse reflectance spectrum (DRS, greyish-green) and polarized single-crystal absorption spectra (incident light beam // crystallographic c-axis, hpol and vpol polarisation directions approximately bisecting the crystallographic a- and b-axis). b) d-orbital splitting for chromophores [Cr(1)O<sub>4+1</sub>] and [Cr(2)O<sub>4</sub>] from AOM (see A.II.4 in the appendix section). c) Total and Cr d-resolved density of states of Sr<sub>2</sub>Cr(PO<sub>4</sub>)<sub>2</sub>.

Table II-4. Sr<sub>2</sub>Cr<sup>II</sup>(PO<sub>4</sub>)<sub>2</sub>. Assignment of optical spectra.

Wavenumber (cm <sup>-1</sup> )	spectrum <sup>a)</sup>	comment	assignment
11290	DRS, hpol, vpol	weak shoulder	Cr(1): $d(z^2) \rightarrow d(x^2-y^2)$
13250	DRS, hpol, vpol	<b>main band</b>	Cr(1): $d(xy) \rightarrow d(x^2-y^2)$
16100	hpol	little kink	spin forbidden
16500	DRS, hpol, vpol	<b>main band</b>	Cr(1): $d(xz, yz) \rightarrow d(x^2-y^2)$
18700 to 19360	DRS, hpol, vpol	very weak, sharp lines	spin forbidden
21200 to 22300	DRS	<b>broad band</b>	Cr(2): $d(xz, yz) \rightarrow d(x^2-y^2)$ Cr(2): $d(z^2) \rightarrow d(x^2-y^2)$
24500	DRS, hpol, vpol	broad, weak band	spin forbidden
28300	DRS, hpol, vpol	broad, weak band	spin forbidden

a) Diffuse reflectance spectrum DRS, polarized single-crystal absorption spectra with incident light perpendicular to crystal face (0 0 1), polarisation directions hpol and vpol approximately bisecting the crystallographic a- and b-axis.

A brief account on the AOM and the fitting procedure using the computer program CAMMAG is given in supporting information. The weak, sharp absorption lines at 16100 cm<sup>-1</sup> and in the

range 18700 to 19360  $\text{cm}^{-1}$  are related to spin-forbidden transitions from the  ${}^5B_1$  ground state LF split levels of the free ions  ${}^3H$  and  ${}^3P$  states. The broader and very weak absorptions around 24500 and 28300 possibly stem from further spin-forbidden transitions to LF split levels of  ${}^3F$  and  ${}^3G$ .

The proposed band assignment (Table II-4) points to significantly different ligand field splitting of the  $d$  orbitals within the two chromophores, which is visualized in Figure II-24a.

**Cr crystal field from DFT.** The total and partial density of states (PDOS) of the  $d$  orbital of Cr(1) and Cr(2) are shown in grey, blue and red on Figure II-24c. Positive and negative values denote the majority and minority channels, respectively, from GGA+U ( $U = 1.6$  eV) in the ferromagnetic spin-polarized configuration. The energy of the Fermi level was set to zero. Although the  $U$  term did not allow reproducing perfectly the experimental bandgap of  $\sim 1.9$  eV (calculated  $E_g = 1.78$  eV), qualitatively the DOS is expected reliable and agrees well with the results from ligand field analysis based on the UV/vis spectra. Here, we focus only on the Cr- $d$  orbital levels of Cr(1) and Cr(2) which stand at the top of the valence band (VB) between  $-1.3$  eV and  $E_F$ . As usual in transition metal phosphates the Cr- $d$  — O- $p$  hybridization is weaker than in simpler oxides, because phosphorus competes with the transition metal for bonding with the oxygen, which is the well-known “inductive effect” [42]. This effect is responsible for stabilizing the Cr<sup>II</sup> low oxidation state in phosphates compared to the binary oxides. Therefore, a strong contribution of P and O levels is found in the deep VB, below  $-2$  eV. For Cr(2), centring nearly perfect square-planar  $\text{CrO}_4$ , the ligand field effect calculated by DFT reproduces reasonably well the one obtained from the analysis of the optical spectra, with  $d(z^2)$ ,  $d(xz)/d(yz)$ , and  $d(xy)$  being separated by approximately  $0.25$  eV ( $2000$   $\text{cm}^{-1}$ ). Most importantly, the DFT calculations confirm for the  $[\text{Cr}(2)\text{O}_4]$  chromophore  $d(z^2)$  as the lowest lying  $d$  orbital, in contrast to the “more spherical” five-fold coordination of the  $[\text{Cr}(1)\text{O}_{4+1}]$  chromophore, see Figure II-24c. This low-lying level is hybridized with  $4s$  states not shown here. The lifting of the  $d(xz)/d(yz)$  degeneracy is probably related to differences in the second coordination sphere, small angular distortion of the square-planar ligand arrangement, and minor differences between  $d(\text{Cr}(2)\text{-O}(3))$  and  $d(\text{Cr}(2)\text{-O}(9))$ . As expected for high-spin  $d^4$  ions,  $d(x^2-y^2)$  is found as a sharp empty level in the conduction band (CB) at  $2.5$  eV. For Cr(1) the states related to the  $t_{2g}$  orbitals are found between  $-1.4$  and  $-0.8$  eV, while the  $d(z^2)$ -related

level is split into a broad series of higher weak discrete levels at the top of VB. The empty  $d(x^2-y^2)$ -related state appears as a sharp doublet at the bottom of the CB, *i.e.* around 1.8 eV.

#### II.4.6. Partial conclusion

Strontium chromium(II) orthophosphate,  $\text{Sr}_2\text{Cr}^{\text{II}}(\text{PO}_4)_2$ , shows unexpected stability against oxidation in moist air, in contrast to many other chromium(II) compounds. Its crystal structure is unique among the extended series of compounds  $\text{A}_2\text{M}(\text{XO}_4)_2$  with A: alkali or alkali earth element, M: transition metal, X: tetrahedrally coordinated main group or transition metal, e.g.  $\text{S}^{6+}$ ,  $\text{P}^{5+}$ ,  $\text{As}^{5+}$ ,  $\text{V}^{5+}$ ,  $\text{Si}^{4+}$ , ... . The two independent  $\text{Cr}^{2+}$  ions show a highly distorted  $[\text{Cr}(1)\text{O}_{4+1}]$  five-fold square-pyramidal and  $[\text{Cr}(2)\text{O}_4]$  four-fold square-planar coordination. Ligand field analysis based on the optical spectra show significantly different  $d$ -orbital splitting for these two. We relate the  $[\text{Cr}(2)\text{O}_4]$  units to the huge splitting of the  $e$  orbital set of approximately  $22000\text{ cm}^{-1}$ , leading to  $d(z^2) < d(xz)$ ,  $d(yz) < d(xy) \lll d(x^2-y^2)$ , with significant  $d$ - and  $s$ -orbital mixing. Layers containing either Cr(1) or Cr(2) are stacked along the crystallographic  $c$ -axis. Detailed magnetic susceptibility, specific heat and neutron powder diffraction data together with DFT calculations revealed several competing magnetic exchange pathways. These lead to strong AF coupling within the Cr(1)-layers and weak inter-layer exchange, giving rise to 2D magnetic ordering between 11.5 and 2 K in these layers along with Cr(2) idle spins. The difference between intra- and inter-layer exchange, as well as the stark difference in the cooperative magnetic behaviour within the Cr(1)- and Cr(2)-layers can be retraced to the peculiar 3D crystal structure of  $\text{Sr}_2\text{Cr}(\text{PO}_4)_2$  and the unusual chemical bonding of the  $JT$ -active  $\text{Cr}^{2+}$  ions.

## General Conclusion

In Conclusion, this thesis has explored the synthesis, structural investigation, characterization of physical properties, complemented by theoretical investigations through computational methods. The focus has been on unravelling structure-property relationships within the group 6 transition metal phosphates (Cr, Mo, W).

Our research into the quasi-ternary system  $\text{BaO}/\text{WO}_x/\text{P}_2\text{O}_5$ , an area extensively studied, has led to the discovery of a new family of compounds within the phosphate tungsten bronzes (PTB) following the general formula  $[\text{Ba}(\text{PO}_4)_2]\text{W}_m\text{O}_{3m-3}$ , with  $2 \leq m \leq 5$ . We refer to them as layered monophosphate tungsten bronzes (L-MPTB) to highlight their enhanced two-dimensional (2D) nature compared to other MPTBs, which are more three-dimensional. This distinction arises from the central role of the  $[\text{Ba}(\text{PO}_4)_2]^{4-}$  spacer in this new family of compounds, which separates the  $\text{WO}_6$  octahedral layers arranged in a  $\text{ReO}_3$ -type structure of varying thickness, determined by the number of  $\text{WO}_6$  octahedra in each layer, conferring enhanced 2D metallicity compared to the MPTBs, trigonal symmetry, robust structural stability over a wider temperature range, in contrast to the commonly observed (in)commensurate modulations associated with CDW instabilities in their parent tungsten bronzes, where W-shifts are observed in monoclinic and orthorhombic structures. Such in-plane atomic displacements are hindered by the trigonal symmetry and rigid  $[\text{Ba}(\text{PO}_4)_2]$  interfacial spacers, allowing these compounds to maintain their metallic properties without exhibiting any CDW signatures in terms of structure, resistivity, or thermopower. Additionally, the influence of the inductive effect of the phosphate spacer results in the antipolar displacement of the tungsten atoms along with their concomitant induced polarity, achieving the equivalent of charged domain walls in ferroelectrics. This effect significantly increases the carrier concentration towards the centre of the  $\text{WO}_3$  blocks and thus preserves the 2D metallic character across the entire series. Attempts to substitute W with Mo within this compound family suggest a potential extension to the more general formula  $[\text{Ba}(\text{PO}_4)_2]\text{W}_{m-x}\text{Mo}_x\text{O}_{3m-3}$ , with a solid solution limit observed at  $x = 1.5$ . This section has been the subject of two publications [83,202].

In unsuccessful attempts to achieve mixed-metal substitution in this new L-MPTB family, akin to what was achieved for mm-MPTBs, the substitution of hexavalent tungsten ( $\text{W}^{\text{VI}}$ ) by  $\text{W}^{5+}$

along with  $M^{2+}/W^{6+}$  and  $M^{3+}/W^{6+}$  in the L-MPTB series led to the discovery of the new "fully-oxidized" tungsten phosphate  $A(PO_4)_2(W^{VI}O_2)_2$  ( $A = Ba, Sr, Pb$ ). Surprisingly, this compound exhibits a much more symmetrical structure (P-31m) compared to its iso-formula analogue  $A(PO_4)_2(MoO_2)_2$  ( $A = Ba, Pb, Sr, (Li, K)$ ) (P2<sub>1</sub>/c). Despite their close crystallochemistry (with almost identical cationic radii in octahedral coordination, IR (WVI) = 0.6 Å and IR (Mo<sup>VI</sup>) = 0.59 Å), both compounds consist of building units comprising isolated [WO<sub>6</sub>] octahedra interconnected through [PO<sub>4</sub>] tetrahedra. Each [WO<sub>6</sub>] octahedron shares four corners with PO<sub>4</sub> groups and leaves two free corners bonded to oxygen, resulting in  $A(PO_4)_2(MoO_2)_2$  ( $A = Ba, Pb, Sr, (Li, K)$ ) forming an interconnected 3D framework with channels housing a single independent A atom, while  $A(PO_4)_2(W^{VI}O_2)_2$  ( $A = Ba, Sr, Pb$ ) forms isolated 1D tunnels containing a primary independent cation A(1) positioned at the junction between channels containing A(2). The distribution of A(2) differs: for Ba and Sr, it is positioned at (0 0 1/2), whereas for Pb, Pb(1) is positioned at (0 0 0), maintaining the same symmetry but resulting in two polymorphs. To understand these structural differences, various calculations were conducted using evolutionary crystallographic algorithms with USPEX, alongside phonon calculations, to elucidate the dynamic and thermodynamic driving forces behind their existence. From these computational analyses, it was found that the existence of  $A(PO_4)_2(W^{VI}O_2)_2$  ( $A = Ba, Sr, Pb$ ) in its P-31m symmetry is driven by dynamic stability, whereas  $A(PO_4)_2(W^{VI}O_2)_2$  ( $A = Ba, Sr, Pb$ ) shows dynamic instability in the same symmetry. USPEX calculations indicate that the P2<sub>1</sub>/c symmetry is thermodynamically more stable across all compositions studied. This underscores the importance of dynamic stability and emphasizes the necessity for combined USPEX and phonon calculations to improve predictive accuracy. This step does not allow us to differentiate the stability of the  $Ba(PO_4)_2(W^{VI}O_2)_2$  or  $Pb(PO_4)_2(W^{VI}O_2)_2$  structure types. Only precise DFT calculations indicate that the compactness of the structural model plays a crucial role, with energy per volume unit consistently favouring the experimental cell, thus distinguishing the stability of  $Ba(PO_4)_2(W^{VI}O_2)_2$  or  $Pb(PO_4)_2(W^{VI}O_2)_2$  structures in their respective compositions.

Chromium(II) phosphates were another significant focus, highlighting the stabilizing effect of phosphates through their inductive influence on Cr<sup>2+</sup> ions and the pivotal role they play in creating a variety of chemical coordination environments. This gives rise to complex exchange pathways, as observed in studies like alpha-beta Cr<sub>3</sub>(PO<sub>4</sub>)<sub>2</sub>, which exhibit intricate magnetic

structures influenced by strong competition between multiple exchange interactions, driven by the Jahn-Teller effect of  $\text{Cr}^{2+}$ .

In the case of  $\text{BaCrP}_2\text{O}_7$  and  $\text{Sr}_2\text{Cr}(\text{PO}_4)_2$ , the crystal structures are significantly influenced by the Jahn-Teller effect of  $\text{Cr}^{2+}$  ions and the redox behaviour of the  $[\text{PO}_4]^{3-}$  group. When paired with large iono-covalent cations such as  $\text{Ba}^{2+}$  and  $\text{Sr}^{2+}$ , these compounds adopt low-dimensional (Low-D) crystal structures, resulting in distinct magnetic properties. For  $\text{BaCrP}_2\text{O}_7$ , this manifests as a 1D antiferromagnetic (AFM) zig-zag spin chain behaviour with a Néel ordering transition occurring at 6 K, accompanied by a spin-flop-like metamagnetic transition at 2 K.

In  $\text{Sr}_2\text{Cr}(\text{PO}_4)_2$ , the distinct magnetic behaviour is attributed to its unique crystal structure featuring layered arrangements along the c-axis and the presence of Jahn-Teller-active  $\text{Cr}^{2+}$  ions. These ions exhibit two distinct coordination environments as Cr(1) and Cr(2), leading to significantly different d-orbital splitting. Magnetic studies including susceptibility measurements, specific heat analysis, neutron powder diffraction, and DFT calculations revealed strong antiferromagnetic (AFM) coupling within the Cr(1) layers and weak inter-layer exchange. This results in 2D magnetic ordering observed between 11.5 and 2 K, facilitated by the presence of Cr(2) idle spins. The contrasting magnetic behaviours within the Cr(1) and Cr(2) layers are intricately linked to the unique 3D crystal structure and the unconventional chemical bonding characteristics of the Jahn-Teller active  $\text{Cr}^{2+}$  ions. This section has been also the subject of a publication [203].

The discoveries made underscore the importance of precise structural characterization, computational modelling, and theoretical insights in advancing our knowledge of 6 group transition metal phosphates and their unique properties.

## Appendix I

### A.I.1 Crystallographic data

Table A 0-1. Data collection and refinement details.

Data collection	Crystal data			
Formula	<b>Ba(PO<sub>4</sub>)<sub>2</sub>W<sub>2</sub>O<sub>3</sub></b>	<b>Ba(PO<sub>4</sub>)<sub>2</sub>W<sub>3</sub>O<sub>6</sub></b>	<b>Ba(PO<sub>4</sub>)<sub>2</sub>W<sub>4</sub>O<sub>9</sub></b>	<b>Ba(PO<sub>4</sub>)<sub>2</sub>W<sub>5</sub>O<sub>12</sub></b>
Molecular weight (g. mol <sup>-1</sup> )	830.8	974.8	1206.67	1438.5
Symmetry	<i>trigonal</i>	<i>trigonal</i>	<i>trigonal</i>	<i>trigonal</i>
Space group	<i>R-3m (166)</i>	<i>R-3m (166)</i>	<i>P-3c1 (165)</i>	<i>R-3m</i>
Unit cell dimensions (Å)	<i>a</i> = 5.2308(2) <i>c</i> = 29.0237(11)	<i>a</i> = 5.2380(2) <i>c</i> = 35.464(3)	<i>a</i> = 5.2092(2) <i>c</i> = 28.1625(13)	<i>a</i> = 5.2292(6) <i>c</i> = 48.740(6)
Volume (Å <sup>3</sup> )	687.73(5)	842.64(9)	661.83(5)	1154.2(2)
Z	3	3	2	3

#### Data Collection

Equipment	Bruker Quazar SMART APEXII	Bruker D8 XRK900	Bruker Quazar SMART APEXII	Bruker Quazar SMART APEXII
λ (Å)	0.71073 [Mo Kα]	0.56087 [Ag Kα]	0.71073 [Mo Kα]	0.71073 [Mo Kα]
Temperature collection (K)	293	293	270	293
Calculated density (g cm <sup>-3</sup> )	5.3780	5.7631	6.0551	6.2087
Crystal shape	Platelet	Platelet	Parallelepiped	Parallelepiped
Crystal dimensions (μm)	80 80 25	80 80 25	30 40 20	40 30 20
Color	Copper-coloured	Copper-coloured	Black	Black
Absorption correction	Sadabs (Multiscan)	Sadabs (Multiscan)	Sadabs (Multiscan)	Sadabs (Multiscan)
Scan mode	ω, φ	ω, φ	ω, φ	ω, φ
θ (min–max) (°)	2.11–29.77	1.36–25.54	2.9–33.54	2.51 – 27.48
μ (mm <sup>-1</sup> )	504.785	18.505	37.902	40.058
F(000)	966	1260	1036	1848
Reciprocal space recording	–13 ≤ h ≤ 13 –13 ≤ k ≤ 13 –77 ≤ l ≤ 76	–7 ≤ h ≤ 8 –7 ≤ k ≤ 7 –54 ≤ l ≤ 54	–8 ≤ h ≤ 7 –5 ≤ k ≤ 7 –42 ≤ l ≤ 42	–6 ≤ h ≤ 6 –6 ≤ k ≤ 6 –63 ≤ l ≤ 63
No. of measured reflections	60216	9880	10411	20832
No. of independent reflections	294	291	518	400
I > 3σ(I) (total)	279	223	378	335

#### Refinement

Number of refined parameters	22	19	26	23
Refinement method	L.S. on F <sub>hkl</sub>			
Weighting scheme	Sigma	Sigma	Unity	Sigma
R1(F) [I > 3σ(I)]/R1(F <sup>2</sup> ) (all data, %)	0.0190/0.0204	0.0239/0.0416	0.0294/0.0424	0.0529/0.0616
wR2(F <sup>2</sup> ) [I > 3σ(I)]/wR2(F <sup>2</sup> ) (all data, %)	0.04370/0.0441	0.0249/0.0493	0.0185/0.0185	0.0724/0.0731
Goodness of Fit	1.75	2.31	0.91	4.46
Max/Min residual electronic density (e <sup>-</sup> /Å <sup>3</sup> )	0.61/-5.45	2.36/-2.71	2.57/-2.47	6.31/-3.99
T <sub>min</sub> / T <sub>max</sub>	0.4953/0.7535	0.5891/0.7452	0.4561/0.6478	0.5511/0.7456

Table A 0-2. Interatomic distances (Å).

Central atom	Neighb. atoms	Distance (Å)	BVS	Central atom	Neighb. atoms	Distance (Å)	BVS
<b>Ba(PO<sub>4</sub>)<sub>2</sub>W<sub>2</sub>O<sub>3</sub> (m = 2)</b>							
W(1)	O(1)	1.8459(2) × 3	5.164(9)	P(1)	O(2)	1.540(4) × 3	5.23(3)
	O(2)	2.031(4) × 3			O(3)	1.505(7)	
Ba(1)	O(2)	2.934(4) × 6	1.811(4)	W(1)	W(1)	5.2308(6)	
	O(3)	3.0563(10) × 6					
<b>Ba(PO<sub>4</sub>)<sub>2</sub>W<sub>3</sub>O<sub>6</sub> (m = 3)</b>							
W(1)	O(2)	1.805(14) × 3	5.7(1)	W(2)	O(2)	1.905(14) × 6	5.77(9)
	O(3)	2.052(14) × 3		W(1)	W(1)	5.2380(6)	
Ba(1)	O(1)	3.058(3) × 6			W(2)	3.7073(9)	
	O(3)	2.926(14) × 6		W(2)	W(2)	5.2380(6)	
P(1)	O(1)	1.461(2)					
	O(3)	1.541(14) × 3					
<b>Ba(PO<sub>4</sub>)<sub>2</sub>W<sub>4</sub>O<sub>9</sub> (m = 4)</b>							
W(1)	O(2)	1.806(7) × 3	5.70(6)	W(2)	O(1)	1.865(2) × 3	5.76(6)
	O(3)	2.052(6) × 3			O(2)	1.950(7) × 3	
Ba(1)	O(3)	2.939(5) × 6		W(1)	W(1)	5.2292(12)	
	O(4)	3.0481(14) × 6			W(2)	3.7124(8)	
P(1)	O(3)	1.550(6)*3		W(2)	W(2)	5.2292(12)	
	O(4)	1.495(9)					
<b>Ba(PO<sub>4</sub>)<sub>2</sub>W<sub>5</sub>O<sub>12</sub> (m = 5)</b>							
W(1)	O(2)	2.049(17) × 3	6.1(1)	W(2)	O(3)	1.978(19) × 3	6.2(1)
	O(3)	1.763(19) × 3			O(4)	1.801(17) × 3	
W(3)	O(4)	1.895(17) × 6	5.9(1)	W(1)	W(1)	5.2292(12)	
Ba(1)	O(1)	3.060(6) × 6			W(2)	3.7124(8)	
	O(2)	2.915(16) × 6			W(3)	5.2705(16)	
P(1)	O(1)	1.495(4)		W(2)	W(2)	5.2292(12)	
	O(2)	1.570(18) × 3		W(2)	W(3)	3.6949(12)	
				W(3)	W(3)	5.2292(12)	

Table A 0-3. Atomic coordinates and isotropic displacement parameters

Atom	Wyckoff site	x	y	z	SOF	U <sub>eq</sub> [Å <sup>2</sup> ]
<b>Ba(PO<sub>4</sub>)<sub>2</sub>W<sub>2</sub>O<sub>3</sub> (m = 2)</b>						
W(1)	6c	0	0	0.13008(1)	1	0.00318(11)
Ba(1)	3a	0	0	0	1	0.01199(18)
P(1)	6c	0.3333	0.6667	0.06804(7)	1	0.0046(4)
O(1)	9d	0.3333	0.1667	0.1667	1	0.0121(15)
O(2)	18h	0.1729(4)	0.3457(8)	0.08550(14)	1	0.0136(11)
O(3)	6c	0.3333	0.6667	0.0162(2)	1	0.0131(16)
<b>Ba(PO<sub>4</sub>)<sub>2</sub>W<sub>3</sub>O<sub>6</sub> (m = 3)</b>						
W(1)	6c	0	0	0.39380(4)	1	0.0107(18)
W(2)	3a	0.6667	0.3333	0.3333	1	0.011(2)
Ba(1)	3b	0	0	0.5	1	0.062(4)
P(1)	6c	0.3333	0.6667	0.4460(2)	1	0.0035(17)
O(1)	6c	0.3333	0.6667	0.4872(6)	1	0.009(5)
O(2)	18h	0.333(3)	0.1667(16)	0.3660(4)	1	0.013(3)
O(3)	18h	0.1745(16)	0.349(3)	0.4306(4)	1	0.013(3)
<b>Ba(PO<sub>4</sub>)<sub>2</sub>W<sub>4</sub>O<sub>9</sub> (m = 4)</b>						
Ba(1)	2b	0	0	0	1	0.0130(3)
W(1)	4c	0	0	0.13500(2)	1	0.0047(18)
W(2)	4d	0.6667	0.3333	0.21227(3)	1	0.0051(3)
P(1)	4d	0.3333	0.6667	0.06963(14)	1	0.0049(9)
O1	6f	0.443(3)	0	0.25	1	0.009(3)
O2	12g	0.3316(18)	0.218(2)	0.1696(2)	1	0.009(2)
O3	12g	0.136(2)	0.3459(14)	0.08818(17)	1	0.0103(18)
O4	4d	0.3333	0.6667	0.0176(3)	1	0.006(2)
<b>Ba(PO<sub>4</sub>)<sub>2</sub>W<sub>5</sub>O<sub>12</sub> (m = 5)</b>						
W1	6c	0	0	0.07818(13)	1	0.0067(5)
W2	6c	0	0	0.78957(13)	1	0.0050(5)
W3	3b	0	0	0,5	1	0.0041(6)
Ba1	3a	0	0	0	1	0.0223(12)
P1	6c	0	0	0.3724(2)	1	0.0032(4)
O1	6c	0	0	0.3403(11)	1	0.040(10)
O2	18h	0.172(5)	0.344(9)	0.0486(11)	1	0.017(4)
O3	18h	0.328(9)	0.164(5)	0.0993(10)	1	0.039(6)
O4	18h	0.002(11)	0.501(6)	0.1439(12)	1	0.038(6)

Table A 0-4. Data collection and refinement details for  $Ba(PO_4)_2Fe_{0.22}W_{3.78}O_9$  ( $m = 4$ ).

Data collection	Crystal data
Formula	$Ba(PO_4)_2Fe_{0.22}W_{3.78}O_9$
Molecular weight (g. mol <sup>-1</sup> )	1179.8
Symmetry	<i>trigonal</i>
Space group	<i>P-3 (166)</i>
Unit cell dimensions (Å)	<i>a</i> = 5.2049(5) <i>c</i> = 14.0870(15) × 2
Volume (Å <sup>3</sup> )	330.50(6)
Z	1
Equipment	Bruker Quazar SMART APEXII
λ (Å)	0.71073 [Mo Kα]
Temperature collection (K)	293
Calculated density (g cm <sup>-3</sup> )	5.9276
Crystal shape	Parallelepiped
Crystal dimensions (μm)	30 40 20
Color	Black
Absorption correction	Sadabs (Multiscan)
Scan mode	ω, φ
θ (min–max) (°)	2.17– 42.56
μ (mm <sup>-1</sup> )	36.354
F(000)	508
Reciprocal space recording	-9 ≤ <i>h</i> ≤ 9 -9 ≤ <i>k</i> ≤ 9 -22 ≤ <i>l</i> ≤ 26
No. of measured reflections	21336
No. of independent reflections	734
I > 3σ(I) (total)	254
Number of refined parameters	22
Refinement method	L.S. on F <sub>hkl</sub>
Weighting scheme	Sigma
R1(F) [I > 3σ(I)]/R1(F <sup>2</sup> ) (all data, %)	0.0385/0.1379
wR2(F <sup>2</sup> ) [I > 3σ(I)]/wR2(F <sup>2</sup> ) (all data, %)	0.0911/0.0982
Goodness of Fit	1.43
Max/Min residual electronic density (e <sup>-</sup> /Å <sup>3</sup> )	6.80/-7.23
Tmin / Tmax	0.4551/0.6378

Table A 0-5. Interatomic distances (Å) for  $Ba(PO_4)_2Fe_{0.22}W_{3.78}O_9$  ( $m = 4$ ).

Central atom	Neighb. atoms	Distance (Å)	BVS	Central atom	Neighb. atoms	Distance (Å)	BVS
<b>Ba(PO<sub>4</sub>)<sub>2</sub>W<sub>2</sub>O<sub>3</sub> (<math>m = 4</math>)</b>							
W1	O(2)	1.80(2) × 3	5.472(11)	W2	O(2)	1.95(2) × 3	5.405(13)
	O(3)	2.06(2) × 3			O(1)	1.86(3) × 3	
Fe1	O(2)	1.80(2) × 3	3.871(18)	Fe2	O(2)	1.95(2) × 3	3.49(10)
	O(2)	2.06(2) × 3			O3	1.86(3) × 3	
Ba1	O(3)	2.93(2) × 6	1.7927(7)	P1	O2a	1.53(2) × 3	5.25(3)
	O(4)	3.050(3) × 6			O2b	1.53(2) × 3	
					O4	1.452(18)	

Table A 0-6. Data collection and refinement details for  $A(PO_4)_2(WO_2)_2$  ( $A = Ba, Pb$ ).

Data collection	Crystal data	
Formula	<b>Ba(PO<sub>4</sub>)<sub>2</sub>(WO<sub>2</sub>)<sub>2</sub></b>	<b>Pb(PO<sub>4</sub>)<sub>2</sub>(WO<sub>2</sub>)<sub>2</sub></b>
Molecular weight (g. mol <sup>-1</sup> )	830.8	1206.67
Symmetry	<i>trigonal</i>	<i>trigonal</i>
Space group	<i>P-31m (162)</i>	<i>P-31m (162)</i>
Unit cell dimensions (Å)	<i>a</i> = 11.52109(8) <i>c</i> = 6.34628(5)	<i>a</i> = 5.2092(2) <i>c</i> = 28.1625(13)
Volume (Å <sup>3</sup> )	729.520(9)	661.83(5)
Z	1	2
Equipment	ALBA Synchrotron	ALBA Synchrotron
λ (Å)	0.41288	0.41288
Temperature collection (K)	293	293
Calculated density (g cm <sup>-3</sup> )	5.0324	5.6928
Color	Light green powder	Light green powder
θ (min–max) (°)	0.300–49.002	0.500– 81.200
μ (mm <sup>-1</sup> )	6.811	10.511
F(000)	784	784
Step size (°)	0.003	0.003
No. of points	16235	1036
Number of refined parameters	78	26
Refinement method	L.S.	L.S.
Weighting scheme	Sigma	Sigma
R1(F) [ <i>I</i> > 3σ( <i>I</i> )]/R1(F <sup>2</sup> ) (all data, %)	0.0170/0.0171	0.0209/0.0210
wR2(F <sup>2</sup> ) [ <i>I</i> > 3σ( <i>I</i> )]/wR2(F <sup>2</sup> ) (all data, %)	0.0238/0.0238	0.0390/0.0391
Goodness of Fit (%)	1.23	12.84
Profile function	Pseudo-Voigt	Pseudo-Voigt
Background function	35 Legendre polynoms	35 Legendre polynoms
Max/Min residual electronic density (e <sup>-</sup> /Å <sup>3</sup> )	2.00/--1.49	2.57/-2.47

Table A 0-7. Interatomic distances (Å) for  $A(\text{PO}_4)_2(\text{WO}_2)_2$  ( $A = \text{Ba}, \text{Pb}$ ).

Central atom	Neighb. atoms	Distance (Å)	BVS	Central atom	Neighb. atoms	Distance (Å)	BVS
<b>Ba(PO<sub>4</sub>)<sub>2</sub>(WO<sub>2</sub>)<sub>2</sub></b>							
W(1)	O(1)	2.155(10) × 2	5.72(4)	P(1)	O(1)	1.505(7) × 2	5.26(5)
	O(2)	1.822(6)			O(2)	1.500(9)	
	O(3)	2.177(5)			O(3)	1.500(7)	
	O(4)	1.782(4) × 2					
Ba(1)	O(1)	3.069(7) × 12	1.495(8)				
Ba(2)	O(4)	2.514(4) × 6	2.928(16)				
<b>Pb(PO<sub>4</sub>)<sub>2</sub>(WO<sub>2</sub>)<sub>2</sub></b>							
W(1)	O(1)	2.079(19) × 2	5.42(9)	P(1)	O(1)	1.473(13) × 2	5.07(9)
	O(2)	2.034(11)			O(2)	1.591(12)	
	O(3)	1.795(11)			O(3)	1.545(13)	
	O(4)	1.889(11) × 2					
Pb(1)	O(1)	3.007(11) × 12	1.323(11)				
Pb(2)	O(4)	2.472(10) × 6	2.22(3)				

Table A 0-8. Atomic coordinates and isotropic displacement parameters Interatomic distances (Å) for  $A(\text{PO}_4)_2(\text{WO}_2)_2$  ( $A = \text{Ba}, \text{Pb}$ ).

Atom	Wyckoff site	x	y	z	SOF	U <sub>eq</sub> [Å <sup>2</sup> ]
<b>Ba(PO<sub>4</sub>)<sub>2</sub>(WO<sub>2</sub>)<sub>2</sub></b>						
Ba(1)	1b	0	0	0.5	1	0.0021(12)
Ba(2)	2b	0.3333	0.6667	0.5	1	0.0121(8)
W(1)	6k	0	0.33489(9)	0.25010(10)	1	0.00487(8)
P(1)	6k	0.7240(3)	0	0.2529(8)	1	0.0239(11)
O(1)	12l	0.7240(3)		0 0.2529(8)	1	0.035(2)
O(2)	6k	0.7394(6)	-0.1221(5)	0.2436(15)	1	0.0185(19)
O(3)	6k	0.6711(10)		0 0.0369(10)	1	-0.0049(18)
O(4)	12l	0.6284(5)		0 0.4134(8)	1	0.0010(15)
<b>Pb(PO<sub>4</sub>)<sub>2</sub>(WO<sub>2</sub>)<sub>2</sub></b>						
Pb(1)	1a	0	0	0	1	0.0074(3)
Pb(2)	2b	0.3333	0.6667	0.5	1	0.0272(5)
W(1)	6k	0	0.33566(13)	0.2532(2)	1	0.00711(12)
P(1)	6k	0.7330(4)	0	0.2464(10)	1	0.0107(10)
O(1)	12l	0.7369(12)	-0.1276(10)	0.2421(15)	1	0.065(4)
O(2)	6k	0.6360(9)	0	0.0647(17)	1	0.002(2)
O(3)	6k	0.6697(13)	0	0.4628(17)	1	0.030(4)
O(4)	12l	0.1454(12)	0.5169(13)	0.2604(17)	1	0.063(4)

### A.1.2. Diffraction experiments

The temperature-dependent tracking of diffractograms from 19 to 299K was carried out on the Rigaku SmartLabXE using monochromated CuK $\alpha$ 1 radiation in the range  $2\theta = (5-90)^\circ$  with  $0.02^\circ$  steps and  $10^\circ$  per minute. The peaks corresponding to the Bragg position numbers (0 0 3) (see Figure A 0-1a) and (4 -2 0) (see Figure A 0-1b) show an evolution of the (0 0 3) peak, indicating a decrease in the c-parameter as the temperature decreases. Meanwhile, the evolution of the (4 -2 0) peak corresponds to an increase in the a and b parameters as the temperature decreases.

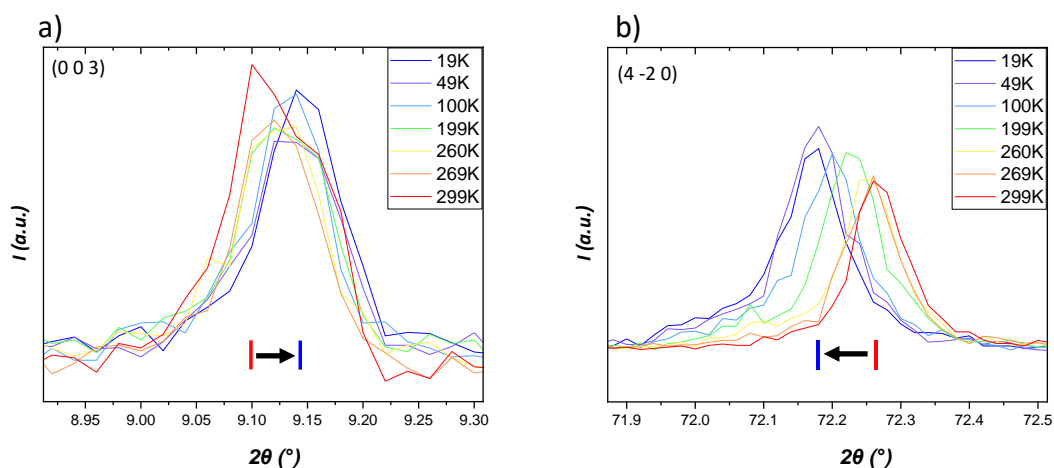


Figure A 0-1. Evolution of a) (0 0 3) and b) (4 -2 0) peaks for different temperatures

### A.1.3. Physical properties and fit functions

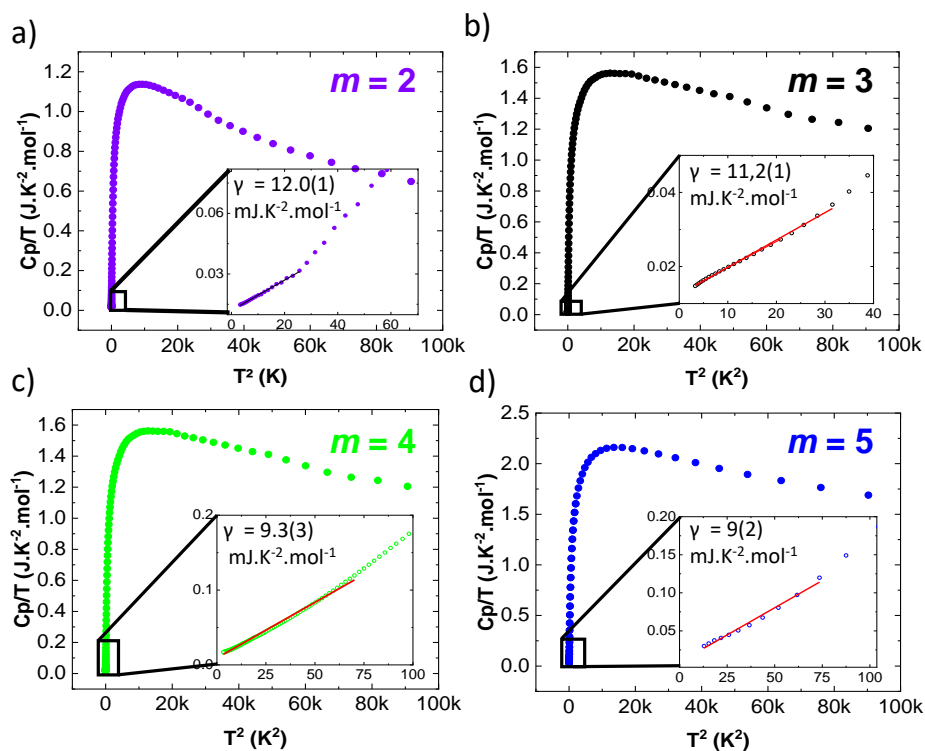


Figure A 0-2.  $C_p/T$  as a function of  $T^2$  lower temperature a)  $m = 2$ , b)  $m = 3$ , c)  $m = 4$  and d)  $m = 5$ .

Table A 0-9. Fit functions coefficients for Cp and Seebeck measurements.

	<b>Ba(PO<sub>4</sub>)<sub>2</sub>W<sub>2</sub>O<sub>3</sub></b> <b>(m = 2)</b>	<b>Ba(PO<sub>4</sub>)<sub>2</sub>W<sub>3</sub>O<sub>6</sub></b> <b>(m = 3)</b>	<b>Ba(PO<sub>4</sub>)<sub>2</sub>W<sub>4</sub>O<sub>9</sub></b> <b>(m = 4)</b>	<b>Ba(PO<sub>4</sub>)<sub>2</sub>W<sub>5</sub>O<sub>12</sub></b> <b>(m = 5)</b>
Molecular weight (g, mol <sup>-1</sup> )	830.8	974.8	1206.67	2413.33
Z	3	3	2	1
<b>Resistivity measurement <math>\rho = f(T)</math></b>				
$\rho$ ( $\Omega$ ,cm) at 2K	4.01E-02	5.71E-04	1.31E-03	1.19E-03
Applied current (mA)	5E-3	1	1	1
<b>Heat capacity Electronic and lattice contribution <math>H_c/T = f(T)</math></b>				
$\gamma$ (J.K <sup>-2</sup> .mol <sup>-1</sup> )	12.0(1)E-03	11.2(1)E-03	9.3(3)E-03	9(2)E-03
A (J.K <sup>-4</sup> .mol <sup>-1</sup> )	1.46(6)E-03	8.52(9)E-04	14.8(1)E-03	1.43(5)E-03
<b>Heat capacity for lattice fitting coefficient (<math>H_c</math> lattice = f(T))</b>				
C <sub>1</sub> (J.K <sup>-1</sup> .mol <sup>-1</sup> )	6.69 (5)	12.8(8)	14.6(1)	17.9(1)
$\Theta_{D1}$ (K)	451(3)	711(8)	848(9)	733(11)
C <sub>2</sub> (J.K <sup>-1</sup> .mol <sup>-1</sup> )	1.85(6)	4.4(1)	7.4(1)	6.5(2)
$\Theta_{D2}$ (K)	138(3)	195(3)	248(3)	208(4)
<b>Seebeck fitting coefficient <math>S = f(T)</math></b>				
$\Theta_D$ (K)	147(26)	208(2)	208(8)	170(2)
F <sub>diff</sub> ( $\mu$ V.K <sup>-1</sup> )	0.6(1)	-5.4(6)	-1.8(3)	-5.05(6)
F <sub>diff</sub> / $\Theta_D$ ( $\mu$ V.K <sup>-2</sup> )	0.004	-0.026	-0.0087	-0.0296
F <sub>ph</sub> ( $\mu$ V.K <sup>-1</sup> )	-8.1(5)	-16.1(8)	-13.9(2)	-90.0(3)
F <sub><math>\tau</math></sub> ( $\mu$ V.K <sup>-2</sup> )	0.09(3)	2(1) E-03	3(1)E-03	-5(2)E-03

## Appendix II

### A.II.1. Crystallographic data

Table A 0-10. Data collection and refinement details for BaCrP<sub>2</sub>O<sub>7</sub>.

Formula	BaCrP <sub>2</sub> O <sub>7</sub>
Molecular weight (g. mol <sup>-1</sup> )	363.3
Symmetry	<i>triclinic</i>
Space group	<i>P</i> -1 (2)
Unit cell dimensions (Å)	a = 1 5.359(2)
	b = 7.259(3)
	c = 7.568(3)
	α = 103.156(13) β = 90.004(14) γ = 93.527(14)
Volume (Å <sup>3</sup> )	286.1(2)
Z	2
Data Collection	
Equipment	Bruker Quazar SMART APEXII
λ [Mo Kα; Å]	0.71073
Calculated density (g cm <sup>-3</sup> )	3.7593
Crystal shape	Platelet
Crystal dimensions (μm)	50×50×20
Color	Turquoise
Absorption correction	Sadabs (Multiscan)
Tmin / Tmax	0.5012/0.7567
Scan mode	ω, φ
θ (min-max) (°)	2.76-31.39
μ (mm <sup>-1</sup> ; for λ Kα = 0.56087Å)	9.282
F(000)	332
Reciprocal space recording	-5 ≤ h ≤ 7
	-10 ≤ k ≤ 10
	-10 ≤ l ≤ 10
No. of measured reflections	8949
No. of independent reflections	603
I > 3σ(I) (total)	475
Refinement	
Number of refined parameters	103
Refinement method	L.S. on F <sub>hkl</sub>
Weighting scheme	(1/σ <sup>2</sup> (F)+0.0001F <sup>2</sup> )
R1(F) [I > 3σ(I)]/R1(F <sup>2</sup> ) (all data, %)	0.0516/0.0670
wR2(F <sup>2</sup> ) [I > 3σ(I)]/wR2(F <sup>2</sup> ) (all data, %)	0.0891/0.0912
Max/Min residual electronic density (e <sup>-</sup> /Å <sup>3</sup> )	3.82/-2.92

Table A 0-11. BaCrP<sub>2</sub>O<sub>7</sub> atomic coordinates and isotropic displacement parameters (P-1, Z = 2, a = 5.359(2) Å, b = 7.259(3) Å, c = 7.568(3) Å, α = 103.156(13)°, β = 90.004(14)°, γ = 93.527(14)°)

Atom	Wyckoff site	x	y	z	SOF	U <sub>eq</sub> [Å <sup>2</sup> ]
Ba(1)	2i	0.2273(3)	0.26976(19)	0.42645(18)	1	0.0096(6)
Cr(1)	2i	0.2095(7)	0.1493(5)	-0.1008(4)	1	0.0135(14)
P(1)	2i	0.2801(12)	0.7649(8)	0.2924(7)	1	0.009(2)
P(2)	2i	-0.2723(12)	0.3245(8)	0.0971(7)	1	0.010(2)
O(1)	2i	0.471(3)	0.2190(18)	0.1015(15)	1	0.011(6)
O(2)	2i	-0.064(2)	0.1917(19)	0.0939(17)	1	0.011(6)
O(3)	2i	0.473(2)	0.1154(17)	0.7033(15)	1	0.006(6)
O(4)	2i	0.060(2)	-0.1125(18)	0.3002(16)	1	0.012(6)
O(5)	2i	0.269(3)	0.6523(17)	0.4358(16)	1	0.012(6)
O(6)	2i	0.260(3)	0.6185(17)	0.0978(16)	1	0.010(5)
O(7)	2i	0.239(3)	0.4948(17)	0.7638(17)	1	0.016(6)

Table A 0-12. ADP harmonic parameters U<sub>ij</sub> (Å<sup>2</sup>) for BaCrP<sub>2</sub>O<sub>7</sub>.

Atom	U <sub>11</sub>	U <sub>22</sub>	U <sub>33</sub>	U <sub>12</sub>	U <sub>13</sub>	U <sub>23</sub>
Ba(1)	0.0135(11)	0.0120(9)	0.0037(9)	-0.0011(6)	0.0005(6)	0.0030(6)
Cr(1)	0.011(3)	0.021(2)	0.009(2)	0.0004(19)	0.0016(19)	0.0044(18)
P(1)	0.008(4)	0.019(4)	0.000(4)	0.000(3)	-0.004(3)	0.003(3)
P(2)	0.008(4)	0.018(4)	0.006(4)	-0.007(3)	0.000(3)	0.006(3)
O(1)	0.025(11)	0.019(9)	-0.011(8)	0.001(8)	0.000(7)	0.000(6)
O(2)	-0.022(9)	0.036(10)	0.019(9)	0.007(8)	-0.004(7)	0.003(8)
O(3)	0.002(10)	0.014(9)	0.006(8)	0.006(7)	0.001(7)	0.007(7)
O(4)	-0.002(10)	0.020(9)	0.016(9)	0.001(7)	0.008(7)	-0.001(7)
O(5)	0.028(11)	0.007(8)	0.002(8)	-0.010(8)	-0.010(7)	0.007(7)
O(6)	0.020(10)	0.002(8)	0.013(8)	0.002(7)	0.006(7)	0.011(7)
O(7)	0.026(11)	0.012(8)	0.003(8)	-0.010(8)	0.005(7)	-0.010(7)

Table A 0-13. Selected interatomic distances (Å), bond valences and valence sums for BaCrP<sub>2</sub>O<sub>7</sub>.

Central atom	Neighbour atoms	Distance (Å)	BVS	Central atom	Neighbour atoms	Distance (Å)	BVS
Ba(1)	O(1)	2.745(13)	2.09(2)	Cr(1)	O(1)	2.031(14)	1.98(3)
	O(2)	2.887(12)			O(2)	2.065(12)	
	O(3)	2.938(13)			O(2)	2.561(14)	
	O(3)	3.266(12)			O(3)	2.032(12)	
	O(4)	2.811(12)			O(4)	2.050(12)	
	O(4)	2.969(13)			O(7)	2.913(14)	
	O(5)	2.898(16)					
	O(5)	2.757(13)					
	O(7)	2.698(12)					
P(1)	O(3)	1.534(13)	5.05(8)	P(2)	O(1)	1.983(7)	5.04(9)
	O(4)	1.514(14)			O(2)	2.389(7)	
	O(5)	1.499(15)			O(6)	2.988(7)	
	O(6)	1.607(12)			O(7)	2.114(7)	

Table A 0-14. Data collection and refinement details for Sr<sub>2</sub>Cr(PO<sub>4</sub>)<sub>2</sub>.

<b>Formula</b>	<b>Sr<sub>2</sub>Cr(PO<sub>4</sub>)<sub>2</sub></b>
Molecular weight (g. mol <sup>-1</sup> )	417.18
Symmetry	<i>orthorhombic</i>
Space group	<i>Pbca (61)</i>
Unit cell dimensions (Å)	a = 10.7064(18) b = 9.2730(14) c = 21.272(3)
Volume (Å <sup>3</sup> )	2111.9(6)
Z	12
Data Collection	
Equipment	Bruker D8 XRK900
λ [Ag Kα; Å]	0.56087
Calculated density (g cm <sup>-3</sup> )	3.9362
Crystal shape	Platelet
Crystal dimensions (mm)	50×50×20
Color	Light blue
Absorption correction	Sadabs (Multiscan)
Tmin / Tmax	0.4912/0.7447
Scan mode	ω, φ
θ (min–max) (°)	1.51–23.66
μ (mm <sup>-1</sup> ; for λ Kα = 0.56087Å)	9.198
F(000)	2328
	–14 ≤ h ≤ 15
Reciprocal space recording	–13 ≤ k ≤ 12
	–30 ≤ l ≤ 30
No. of measured reflections	54862
No. of independent reflections	2314
I > 3σ(I) (total)	1812
Refinement	
Number of refined parameters	181
Refinement method	L.S. on F <sub>hkl</sub>
Weighting scheme	(1/σ <sup>2</sup> (F)+0.0001F <sup>2</sup> )
R1(F) [I > 3σ(I)]/R1(F <sup>2</sup> ) (all data, %)	0.0363/0.0525
wR2(F <sup>2</sup> ) [I > 3σ(I)]/wR2(F <sup>2</sup> ) (all data, %)	0.0585/0.0783
Max/Min residual electronic density (e <sup>-</sup> /Å <sup>3</sup> )	0.99/–1.02

Table A 0-15. Atomic coordinates and isotropic displacement parameters (Pbca, Z = 4, a = 10.7064(18) , b = 9.2730(14) Å, c = 21.272(3) Å).

Atom	Wyckoff site	x	y	z	SOF	U <sub>eq</sub> [Å <sup>2</sup> ]
Sr(1)	8c	0.61862(8)	0.40414(11)	0.15477(4)	1	0.0114(3)
Sr(2)	8c	0.13338(8)	0.09390(9)	0.03289(4)	1	0.0111(3)
Sr(3)	8c	0.10633(9)	0.43581(10)	0.15618(4)	1	0.0107(3)
Cr(1)	8c	0.38388(13)	0.25529(16)	0.24996(6)	1	0.0093(5)
Cr(2)	4b	0.5	0	0	1	0.0105(7)
P(1)	8c	0.6491(2)	0.0850(3)	0.27650(11)	1	0.0081(8)
P(2)	8c	0.3814(2)	0.2516(2)	0.08799(10)	1	0.0082(8)
P(3)	8c	0.3631(2)	0.2572(3)	0.41170(11)	1	0.0090(8)
O(1)	8c	0.3906(6)	0.1005(7)	0.4244(4)	1	0.019(3)
O(2)	8c	0.3527(6)	0.2892(8)	0.3406(3)	1	0.025(3)
O(3)	8c	0.3822(5)	0.0978(6)	0.0586(3)	1	0.007(2)
O(4)	8c	0.6058(6)	0.2372(7)	0.2584(3)	1	0.012(2)
O(5)	8c	0.6592(6)	0.0663(8)	0.3473(3)	1	0.021(3)
O(6)	8c	0.7814(6)	0.0609(7)	0.2470(3)	1	0.010(2)
O(7)	8c	0.4226(6)	0.2260(7)	0.1574(3)	1	0.011(2)
O(8)	8c	0.5575(7)	-0.0271(7)	0.2500(3)	1	0.011(2)
O(9)	8c	0.4772(6)	0.3468(7)	0.4353(3)	1	0.016(2)
O(10)	8c	0.4787(6)	0.3482(7)	0.0583(3)	1	0.011(2)
O(11)	8c	0.2429(6)	0.3097(8)	0.4392(3)	1	0.017(2)
O(12)	8c	0.2521(5)	0.3145(7)	0.0809(3)	1	0.014(2)

Table A 0-16.  $Sr_2Cr(PO_4)_2$ . Selected interatomic distances (Å), bond valences and valence sums.

Central atom	Neighbour atoms	Distance (Å)	BVS	Central atom	Neighbour atoms	Distance (Å)	BVS
Sr(1)	O(1)	2.481(8)	1.957(15)	Sr(2)	O(1)	2.754(8)	2.027(14)
	O(2)	2.725(8)			O(3)	2.720(7)	
	O(4)	2.697(8)			O(5)	2.576(7)	
	O(6)	2.664(7)			O(9)	2.961(7)	
	O(7)	2.670(7)			O(10)	2.608(7)	
	O(8)	2.840(7)			O(10)	2.631(7)	
	O(10)	2.593(7)			O(11)	2.481(7)	
	O(11)	2.556(7)			O(12)	2.616(7)	
Sr(3)	O(1)	2.941(9)	2.084(15)	Cr(1)	O(2)	1.983(7)	1.921(18)
	O(3)	2.565(7)			O(4)	2.389(7)	
	O(4)	2.587(7)			O(4)	2.988(7)	
	O(5)	2.788(8)			O(6)	2.114(7)	
	O(6)	2.652(7)			O(7)	2.032(7)	
	O(7)	2.710(7)			O(8)	2.112(7)	
	O(8)	2.678(7)					
	O(9)	2.528(7)					
	O(12)	2.504(7)					
Cr(2)	O(3)	1.989(7)	2.08(2)	P(1)	O(4)	1.536(7)	4.76(5)
	O(3)	1.989(7)			O(5)	1.520(7)	
	O(9)	1.991(7)			O(6)	1.566(8)	
	O(9)	1.991(7)			O(8)	1.537(8)	
P(2)	O(3)	1.560(7)	4.84(5)	P(3)	O(1)	1.508(8)	4.95(5)
	O(7)	1.558(7)			O(2)	1.545(7)	
	O(10)	1.510(7)			O(9)	1.559(8)	
	O(12)	1.509(7)			O(11)	1.493(7)	

Table A 0-17. ADP harmonic parameters  $U_{ij}$  ( $\text{\AA}^2$ ) for  $\text{Sr}_2\text{Cr}(\text{PO}_4)_2$ .

Atom	$U_{11}$	$U_{22}$	$U_{33}$	$U_{12}$	$U_{13}$	$U_{23}$
Sr(1)	0.0113(5)	0.0186(6)	0.0045(5)	-0.0011(4)	-0.0005(3)	-0.0004(3)
Sr(2)	0.0108(5)	0.0192(5)	0.0032(5)	-0.0040(4)	-0.0010(3)	0.0016(4)
Sr(3)	0.0119(5)	0.0159(5)	0.0044(5)	-0.0004(4)	0.0000(3)	0.0003(3)
Cr(1)	0.0122(10)	0.0129(10)	0.0027(8)	-0.0018(7)	0.0003(6)	0.0000(6)
Cr(2)	0.0145(12)	0.0142(13)	0.0028(11)	0.0033(10)	0.0030(9)	0.0018(9)
P(1)	0.0062(13)	0.0122(14)	0.0059(13)	0.0002(9)	0.0011(10)	0.0003(10)
P(2)	0.0101(14)	0.0105(16)	0.0039(12)	0.0003(10)	-0.0004(9)	-0.0004(10)
P(3)	0.0105(14)	0.0121(16)	0.0043(12)	0.0002(10)	0.0011(10)	-0.0014(10)
O(1)	0.017(4)	0.017(4)	0.023(5)	0.003(3)	-0.006(3)	0.000(3)
O(2)	0.029(4)	0.042(6)	0.005(4)	0.003(4)	0.002(3)	-0.002(3)
O(3)	0.009(4)	0.010(4)	0.001(4)	0.002(3)	0.003(3)	0.001(2)
O(4)	0.008(4)	0.018(4)	0.010(4)	0.000(3)	-0.002(3)	0.002(3)
O(5)	0.023(4)	0.039(5)	0.003(4)	-0.006(4)	-0.004(3)	0.002(3)
O(6)	0.004(3)	0.018(4)	0.009(4)	-0.006(3)	0.001(2)	-0.003(3)
O(7)	0.012(3)	0.017(4)	0.003(3)	0.000(3)	-0.001(3)	0.001(3)
O(8)	0.012(4)	0.011(4)	0.011(4)	0.000(3)	-0.003(3)	0.000(3)
O(9)	0.020(4)	0.020(4)	0.007(4)	-0.008(3)	0.003(3)	-0.007(3)
O(10)	0.014(4)	0.017(4)	0.003(3)	-0.002(3)	-0.004(3)	0.002(3)
O(11)	0.015(4)	0.033(5)	0.003(4)	0.011(3)	0.004(3)	0.000(3)
O(12)	0.017(4)	0.019(4)	0.007(4)	0.007(4)	0.001(3)	0.000(3)

## A.II.2. DFT Calculations and Magnetic Exchanges

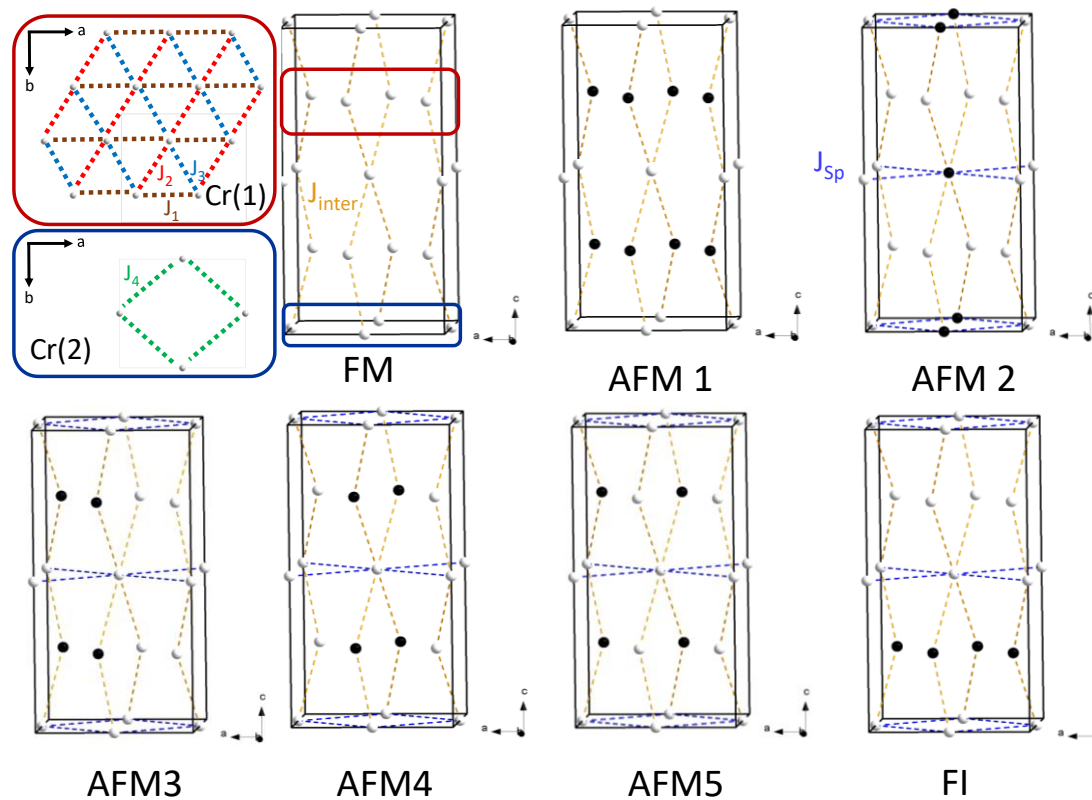


Figure A 0-3. Different spin configurations of Cr onto a classical Heisenberg model, spin up (white) spin down (black) for the DFT.

Table A 0-18. Energy value for different configuration from DFT+U calculations

Configurations	E(eV)	$E_1-E_n$	E(K)
AFM3	-1.14430840E+03	0.00000000	-1.32791555E+07
AFM5	-1.14430110E+03	0.00730000	-1.32790708E+07
AFM1	-1.14426720E+03	0.04120000	-1.32786774E+07
FI	-1.14426630E+03	0.04210000	-1.32786670E+07
AFM2	-1.14426360E+03	0.04480000	-1.32786357E+07
AFM4	-1.14426350E+03	0.04490000	-1.32786345E+07
FM	-1.14425980E+03	0.04130000	-1.32785916E+07
FI2	-1.14426350E+03	0.04490000	-1.32786345E+07
FI3	-1.14426350E+03	0.04490000	-1.32786345E+07

GGA+U (U = 3.2 eV)

Detailed calculation process to determine the values of different magnetic couplings:

$$FI - AFM3 = 64 \times J_1 + 64 \times J_2 \quad \text{Eq. A 0-1}$$

$$FI - AFM4 = 64 \times J_1 + 64 \times J_3 \quad \text{Eq. A 0-2}$$

$$FI - AFM5 = 64 \times J_2 + 64 \times J_3 \quad \text{Eq. A 0-3}$$

$$FM = 64 \times J_{inter} \quad \text{Eq. A 0-4}$$

$$J_1 = [(FI - AFM4) - (FI - AFM5) + (FI - AFM3)]/128 \quad \text{Eq. A 0-5}$$

$$J_2 = [(FI - AFM3) - (64 \times J_1)]/64 \quad \text{Eq. A 0-6}$$

$$J_3 = (FI - AFM5) - (64 \times J_2)/64 \quad \text{Eq. A 0-7}$$

$$J_{inter} = (FI - FM)/128 \quad \text{Eq. A 0-8}$$

$$J_{sp} = [(FM - AFM2) - (64 \times J_{inter})]/64 \quad \text{Eq. A 0-9}$$

### A.II.3. Magnetic structure detail

Table A 0-19. Magnetic Space Group (MSG) description of the commensurate magnetic structure of  $\text{Sr}_2\text{Cr}(\text{PO}_4)_2$  at 5K.

MSG symbol	<i>Pb'ca</i>
MSG number	61.435
Transformation to the standard setting of MSG	( <b>a,b,c</b> ;0,0,0)
Unit cell parameters (Å)	a = 10.62006 $\alpha = 90^\circ$ b = 9.28517 $\beta = 90^\circ$ c = 21.18998 $\gamma = 90^\circ$
MSG symmetry operations	x,y,z,+1 -x,-y,-z,-1 -x+1/2,-y,z+1/2,-1 x+1/2,y,-z+1/2,+1 -x,y+1/2,-z+1/2,-1 x+1/2,-y+1/2,-z,+1 x,-y+1/2,z+1/2,+1 -x+1/2,y+1/2,z,-1
MSG symmetry centering operations	x,y,z,+1
Position of magnetic atoms	Cr(1) Cr 0.35791 0.23161 0.24713 Cr(2) Cr 0.5 0.0 0.0
Magnetic moments components ( $\mu_B$ ) of magnetic atoms, their symmetry constraints and moment magnitudes	Cr(1) -3.12(4) 1.02(5) 0.0 (mx,my,mz) 3.29(4) Cr(2) 0.0 0.0 0.0 (0,0,0) 0.0
Position of non-magnetic atoms	Sr(1) Sr 0.62450 0.40790 0.15128 Sr(2) Sr 0.12762 0.10064 0.03638 Sr(3) Sr 0.09964 0.44053 0.16034 P(1) P 0.65394 0.10169 0.27863 P(2) P 0.37776 0.26000 0.08620 P(3) P 0.38398 0.26317 0.41131 O(1) O 0.40962 0.09094 0.41917 O(2) O 0.34755 0.27847 0.33891 O(3) O 0.37577 0.09393 0.05841 O(4) O 0.58453 0.24693 0.26430 O(5) O 0.67399 0.05906 0.34346 O(6) O 0.78428 0.04835 0.24313 O(7) O 0.42388 0.22492 0.15532 O(8) O 0.57133 -0.02128 0.24041 O(9) O 0.48146 0.36023 0.44053 O(10) O 0.48313 0.34202 0.05784 O(11) O 0.24035 0.29339 0.43341 O(12) O 0.25066 0.31934 0.08056

Table A 0-20. Magnetic Space Group (MSG) description of the commensurate magnetic structure of  $Sr_2Cr(PO_4)_2$  at 1.5K.

MSG symbol	$Pca2_1$
MSG number	29.99
Transformation to the standard setting of MSG	$(-c, \mathbf{b}, \mathbf{a}; 0, 1/4, 0)$
Unit cell parameters (Å)	$a = 10.60289 \quad \alpha = 90^\circ$ $b = 9.28982 \quad \beta = 90^\circ$ $c = 21.18187 \quad \gamma = 90^\circ$
MSG symmetry operations	$x, y, z, +1$ $x+1/2, -y+1/2, -z, +1$ $x+1/2, y, -z+1/2, +1$ $x, -y+1/2, z+1/2, +1$
MSG symmetry centering operations	$x, y, z, +1$
Position of magnetic atoms	Cr(1_1) Cr 0.35791 0.23161 0.24713 Cr(1_2) Cr 0.14209 0.76839 0.74713 Cr(1)(15K) 0.36047 0.24720 0.24800 Cr(2) Cr 0.0 0.0 0.5
Magnetic moments components ( $\mu_B$ ) of magnetic atoms, their symmetry constraints and moment magnitudes	Cr(1_1) -3.07(3) 0.55(6) 0.0 ( $m_x, m_y, m_z$ ) 3.12(3) Cr(1_2) -3.26(6) 0.40(20) 0.0 ( $m_x, m_y, m_z$ ) 3.12(3) Cr(2) 0.95(5) -1.35(8) 1.13(9) ( $m_x, m_y, m_z$ ) 1.99(7)
Position of non-magnetic atoms	Sr(1_1) Sr 0.62450 0.40790 0.15128 Sr(1_2) Sr 0.87550 0.59210 0.65128 Sr(2_1) Sr 0.12762 0.10064 0.03638 Sr(2_2) Sr 0.37238 0.89936 0.53638 Sr(3_1) Sr 0.09964 0.44053 0.16034 Sr(3_2) Sr 0.40036 0.55947 0.66034 P(1_1) P 0.65394 0.10169 0.27863 P(1_2) P 0.84606 0.89831 0.77863 P(2_1) P 0.37776 0.26000 0.08620 P(2_2) P 0.12224 0.74000 0.58620 P(3_1) P 0.38398 0.26317 0.41131 P(3_2) P 0.11602 0.73683 0.91131 O(1_1) O 0.40962 0.09094 0.41917 O(1_2) O 0.09038 0.90906 0.91917 O(2_1) O 0.34755 0.27847 0.33891 O(2_2) O 0.15245 0.72153 0.83891 O(3_1) O 0.37577 0.09393 0.05841 O(3_2) O 0.12423 0.90607 0.55841 O(4_1) O 0.58453 0.24693 0.26430 O(4_2) O 0.91547 0.75307 0.76430 O(5_1) O 0.67399 0.05906 0.34346 O(5_2) O 0.82601 0.94094 0.84346 O(6_1) O 0.78428 0.04835 0.24313 O(6_2) O 0.71572 0.95165 0.74313 O(7_1) O 0.42388 0.22492 0.15532 O(7_2) O 0.07612 0.77508 0.65532 O(8_1) O 0.57133 0.97870 0.24041 O(8_2) O 0.92867 0.02130 0.74041 O(9_1) O 0.48146 0.36023 0.44053 O(9_2) O 0.01854 0.63977 0.94053 O(10_1) O 0.48313 0.34202 0.05784 O(10_2) O 0.01687 0.65798 0.55784 O(11_1) O 0.24035 0.29339 0.43341

O(11\_2) O 0.25965 0.70661 0.93341  
O(12\_1) O 0.25066 0.31934 0.08056  
O(12\_2) O 0.24934 0.68066 0.58056

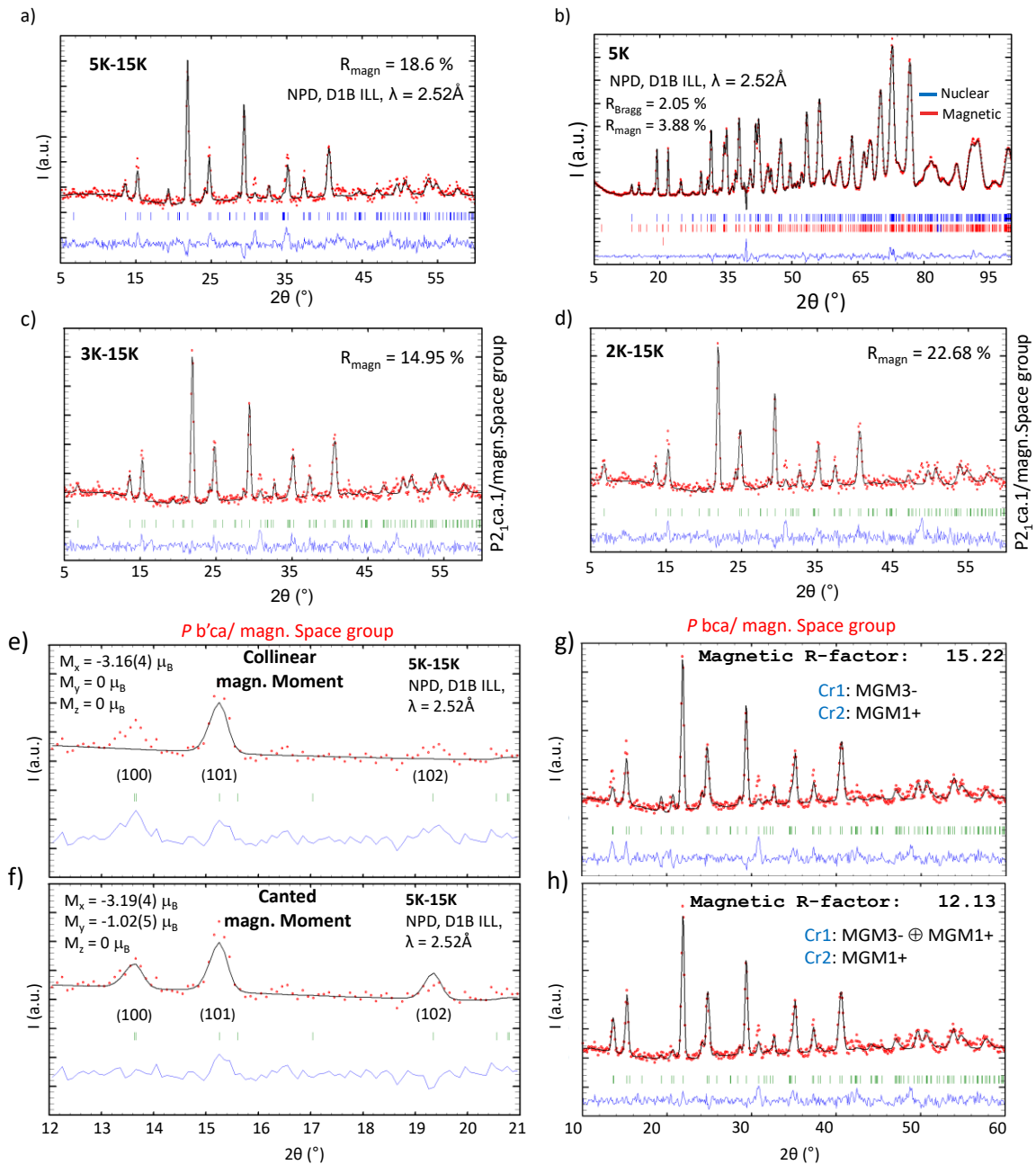


Figure A 0-4.  $Sr_2Cr(PO_4)_2$  NPD refinement at 5K of a) the magnetic structure only and b) magnetic and nuclear structures at 5K, NPD refinement of the magnetic structure at c)3K and d) 2K. NPD refinement of the magnetic structure at 5 K with: e) the magnetic component refined only along the x-axis and f) refined along both the x and y axes. NPD refinement of the magnetic structure at 1.5 K with the magnetic component refined for Cr(1): g) using only the  $mGM3-$  Irrep, compared to h) using  $mGM3- \oplus mGM1+$  Irreps and Cr(2) both refinement have  $MGM1+$  only as Irreps

#### A.II.4. AOM for Sr<sub>2</sub>Cr<sup>II</sup>(PO<sub>4</sub>)<sub>2</sub> and selected reference compounds

Synthesis and spectroscopic characterization of Sr<sub>2</sub>Cr<sup>II</sup>(PO<sub>4</sub>)<sub>2</sub> are described in the main text. Optical spectra for the reference compounds have been taken from the literature (SrCr<sup>II</sup>P<sub>2</sub>O<sub>7</sub> [147,148], SrCr<sup>II</sup>Si<sub>4</sub>O<sub>10</sub> [134], α-Ba<sub>2</sub>Cr<sup>II</sup>(PO<sub>4</sub>)<sub>2</sub> [20]). The diffuse powder reflectance spectra (10000 ≤  $\tilde{\nu}$  ≤ 35000 cm<sup>-1</sup>) were recorded at ambient temperature using two modified CARY 14 and CARY 17 spectrophotometers (OLIS, Inc., USA), which were equipped with integrating spheres. For the whole spectral range three different experimental setups (detectors, slits, scan range, step width) were used. From 280 to 600 nm (UV range) a total of 640 data points were collected by a photomultiplier detector (PMT) system with a scan rate of 1.0 nm·s<sup>-1</sup>, step width 0.5 nm, and the slit width of 0.1 mm. From 300 to 900 nm (vis range) and 600 to 2600 nm (NIR range) the total of collected data points was 600 and 500 respectively, with scan rates of 1.0 nm·s<sup>-1</sup> and 4.0 nm·s<sup>-1</sup> accordingly. For the Vis region a PMT detector (slit width of 0.06 mm) was used. In the NIR region the data were collected by a PbS detector at a variable slit width (1.4–2.2 mm). In every case the intensity of BaSO<sub>4</sub> was measured as standard. The diffuse reflectance (K/S) was calculated using the Kubelka-Munk function [177,178],

$$K / S = \frac{(1 - R_{diff})^2}{2R_{diff}} \quad \text{Eq. A 0-10}$$

Polarized optical absorption spectra of single crystals were acquired using a modified CARY 17 single-beam micro-crystal spectrometer [176,191]. This spectrometer provides a resolution of up to 0.1 nm, equivalent to approximately 0.35 cm<sup>-1</sup> in the NIR and 12.5 cm<sup>-1</sup> in the UV range. A standard halogen lamp (Osram HLX64640, 150 W, 24 V) served as the light source. Measurements in the UV/vis range (12000 to 36000 cm<sup>-1</sup>) employed a photomultiplier as the detector, while a nitrogen-cooled germanium photodiode was used for measurements in the NIR range (6000 to 16000 cm<sup>-1</sup>). Additionally, a polarization filter was employed for orientation-dependent measurements.

In the AOM approach to ligand field analysis (for details on AOM we refer the reader to literature [192,193]) the global ligand field, frequently described by the physically strictly correct but chemically meaningless Wybourne parameters  $\hat{B}_q^k$  [194,195], is decomposed into individual contributions from the various metal-ligand interactions. These are described by the AOM parameters  $e_{\sigma}$  and  $e_{\pi}$ . In accordance with literature, these parameters are assumed to depend on the metal-ligand distance, eq. (S2) [196–198], with  $d(\text{Cr}-\text{O})_{\min}$  being the shortest distance Cr–O in each compound. Detailed accounts for the dependence of  $e_{\sigma}(\text{M}-\text{L})$  on  $d(\text{M}-\text{L})^{-5.0}$  have been given in literature [196–198].

$$e_m(d(\text{Cr}-\text{O})) = e_m(d(\text{Cr}-\text{O})_{\min}) \cdot \left( \frac{d(\text{Cr}-\text{O})_{\min}^{-5.0}}{d(\text{Cr}-\text{O})^{-5.0}} \right) \quad \text{Eq. A 0-11}$$

For all chromophores  $[\text{Cr}^{\text{II}}\text{O}_n]$  in  $\text{Sr}_2\text{Cr}^{\text{II}}(\text{SO}_4)_3$ ,  $\text{SrCr}^{\text{II}}\text{P}_2\text{O}_7$ ,  $\text{SrCr}^{\text{II}}\text{Si}_4\text{O}_{10}$ , and  $\alpha\text{-Ba}_2\text{Cr}^{\text{II}}\text{Cr}(\text{PO}_4)_2$  isotropic  $e_{\pi}$ -interactions ( $e_{\pi,x} = e_{\pi,y}$ ) with  $e_{\pi,\text{iso}} = \frac{1}{4} e_{\pi}$  are assumed. In effect, these assumptions leave just one parameter,  $e_{\pi,\text{max}}(\text{Cr}^{2+}\text{-O}^{2-})$  which relates to the shortest distance  $d(\text{Cr-O})_{\text{min}}$  in each compound for matching calculated against observed excited state energies (see Table AII-5). For the square-planar chromophores  $e_{ds}$  was included as additional parameter to account for  $ds$  mixing [192]. Thus, for the three reference compounds similar  $e_{\pi,\text{max}}(\text{Cr-O})_{\text{max}} \approx 8000 \text{ cm}^{-1}$  were obtained at  $d_{\text{min}}(\text{Cr-O}) \approx 2.0 \text{ \AA}$ .

The energies of the free ion electronic states were introduced into the AOM calculations via the Racah parameters  $B$ ,  $C$ , and the spin-orbit coupling constant  $\zeta$  [190]. For the free  $\text{Cr}^{2+}$  ion ( $B_{\text{fr.ion}} = 796 \text{ cm}^{-1}$ ,  $C_{\text{fr.ion}} = 3343 \text{ cm}^{-1}$ ,  $C/B = 4.2$  and the spin-orbit coupling constant  $\zeta = 230 \text{ cm}^{-1}$ ) is suggested in literature [178]. These numbers were reduced in the AOM calculations for each compound according to an anticipated nephelauxetic ratio  $\beta = B/B_{\text{fr.ion}} = 0.80$ . In the same way, the Stevens orbital reduction factor  $k$  [199] was reduced (see Table A 0-21). For the AOM calculations, the computer program *CAMMAG* in a modified PC version was used [196,200,201].

The results of AOM for  $\text{Sr}_2\text{Cr}^{\text{II}}(\text{SO}_4)_3$ ,  $\text{SrCr}^{\text{II}}\text{P}_2\text{O}_7$ , and  $\alpha\text{-Ba}_2\text{Cr}^{\text{II}}\text{Cr}(\text{PO}_4)_2$  are graphically compared to the observed spectra in Figure AII-3. A summary of the AOM parameters is contained in Table AII-5.

*Table A 0-21. Chromophores and observed transition energies as well as AOM parameters derived thereof for  $\text{Sr}_2\text{Cr}^{\text{II}}(\text{PO}_4)_2$ ,  $\text{SrCr}^{\text{II}}\text{P}_2\text{O}_7$ ,  $\text{SrCr}^{\text{II}}\text{Si}_4\text{O}_{10}$ , and  $\alpha\text{-Ba}_2\text{Cr}^{\text{II}}(\text{PO}_4)_2$ .*

	$\text{Sr}_2\text{Cr}^{\text{II}}(\text{PO}_4)_2$	$\text{SrCr}^{\text{II}}\text{P}_2\text{O}_7$	$\text{SrCr}^{\text{II}}\text{Si}_4\text{O}_{10}$	$\alpha\text{-Ba}_2\text{Cr}^{\text{II}}(\text{PO}_4)_2$
<b>references</b>	[20], this work	[147]	[134]	[20]
<b>chromophores</b>	[Cr(1)O <sub>4+1</sub> ] [Cr(2)O <sub>4</sub> ]	[CrO <sub>4+1</sub> ]	[CrO <sub>4</sub> ]	[CrO <sub>4</sub> ]
$d(\text{Cr}^{\text{II}}\text{O}) / \text{\AA}$	Cr(1): 1.983, 2.033 2.111, 2.113 2.388 Cr(2): 1.994 (2x) 1.995 (2x)	1.995, 2.056 2.058, 2.109 2.362	1.997 (4x)	2.003 (4x)
<b>electronic transitions</b>				
observed	Cr(1) 11440	9500	-----	-----
spin-allowed	Cr(1) 13340	12300	15090	14070
transitions / $\text{cm}^{-1}$	Cr1(1/2) 16570	14700	19520	18920
	Cr(2) 21000	-----	22850	21000
	Cr(2) 22000	-----		
observed	16100	-----	-----	-----
spin-forbidden	18600 - 18900	18660 - 18980	(18000 - 18600)	18000 - 19000
transitions / $\text{cm}^{-1}$	19072	19341		

AOM parameters				
$B, C / \text{cm}^{-1\text{f}}$	664, 2712	664, 2712	664, 2712	664, 2712
$C/B$	4.1	4.1	4.1	4.1
$\theta^{\text{h}}$	0.8	0.8	0.8	0.8
$\zeta / \text{cm}^{-1\text{h}}$	184	184	184	184
$e_{\sigma, \text{max}}(\text{Cr}^{\text{II}}\text{-O}) / \text{cm}^{-1}$	Cr(1): 8400 Cr(2): 8400	7400	7800	7500
$e_{\pi, \text{iso}}(\text{Cr}^{\text{II}}\text{-O})$	$1/4e_{\sigma}$	$1/4e_{\sigma}$	$1/4e_{\sigma}$	$1/4e_{\sigma}$
$e_{\text{ds}}(\text{Cr}^{\text{II}}\text{-O})$	Cr(1): no $e_{\text{ds}}$ Cr(2): $0.15e_{\sigma}$	no $e_{\text{ds}}$	$0.23e_{\sigma}$	$0.20e_{\sigma}$

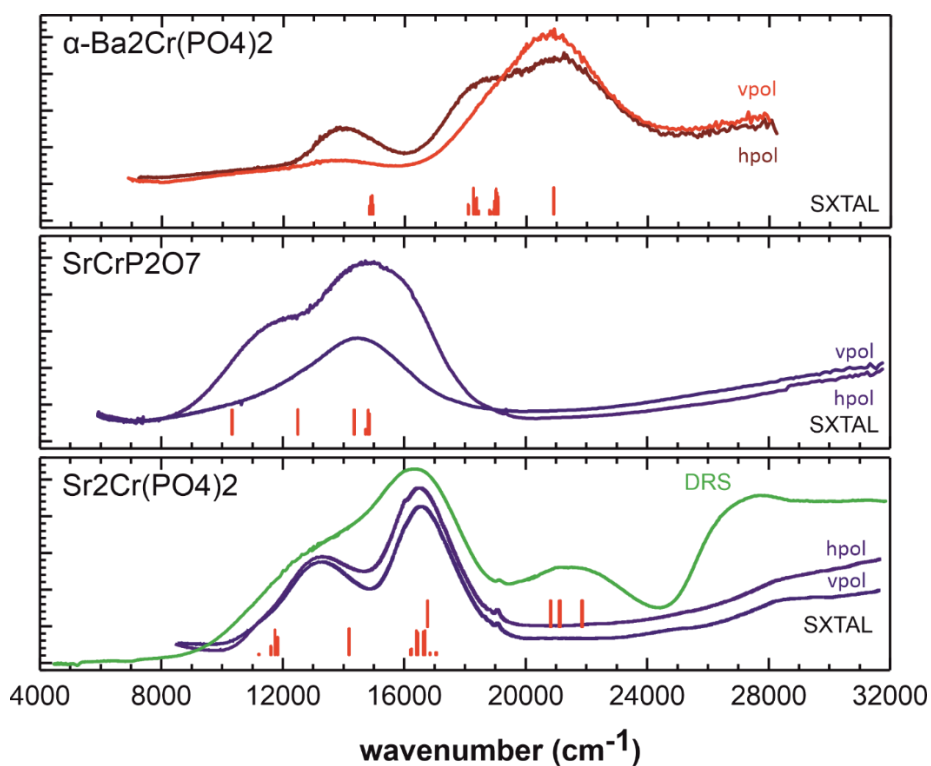


Figure A 0-5. Comparison of observed optical spectra and energy levels from AOM for the  $[\text{Cr}^{\text{II}}\text{O}_n]$  chromophores in  $\text{Sr}_2\text{Cr}^{\text{II}}(\text{PO}_4)_2$ ,  $\text{SrCr}^{\text{II}}\text{P}_2\text{O}_7$ , and  $\alpha\text{-Ba}_2\text{Cr}^{\text{II}}(\text{PO}_4)_2$ . Single-crystal (SXTAL) spectra for all compounds, diffuse powder reflectance spectrum (DRS) at ambient temperature is given for  $\text{Sr}_2\text{Cr}^{\text{II}}(\text{PO}_4)_2$ . Quintet levels from AOM are given as red ticks at the bottom of each spectrum.

## References

- [1] B.C.H. Steele, A. Heinzl, Materials for fuel-cell technologies, *Nature* 414 (2001) 345–352. <https://doi.org/10.1038/35104620>.
- [2] G.J. Snyder, E.S. Toberer, Complex thermoelectric materials, *Nat. Mater.* 7 (2008) 105–114. <https://doi.org/10.1038/nmat2090>.
- [3] M.A. Green, K. Emery, Y. Hishikawa, W. Warta, E.D. Dunlop, Solar cell efficiency tables (version 44), *Prog. Photovolt. Res. Appl.* 22 (2014) 701–710. <https://doi.org/10.1002/pip.2525>.
- [4] M. Wuttig, N. Yamada, Phase-change materials for rewriteable data storage, *Nat. Mater.* 6 (2007) 824–832. <https://doi.org/10.1038/nmat2009>.
- [5] P.K. Mehta, P.J.M. Monteiro, *Concrete: Microstructure, Properties, and Materials*, 4th Edition, McGraw-Hill Education, 2014. <https://www.accessengineeringlibrary.com/content/book/9780071797870> (accessed January 6, 2025).
- [6] C.G. Granqvist, Oxide electrochromics: An introduction to devices and materials, *Sol. Energy Mater. Sol. Cells* 99 (2012) 1–13. <https://doi.org/10.1016/j.solmat.2011.08.021>.
- [7] A. Corma, From Microporous to Mesoporous Molecular Sieve Materials and Their Use in Catalysis, *Chem. Rev.* 97 (1997) 2373–2420. <https://doi.org/10.1021/cr960406n>.
- [8] A.R. Oganov, C.W. Glass, Crystal structure prediction using ab initio evolutionary techniques: Principles and applications, *J. Chem. Phys.* 124 (2006) 244704. <https://doi.org/10.1063/1.2210932>.
- [9] J. Schmidt, M.R.G. Marques, S. Botti, M.A.L. Marques, Recent advances and applications of machine learning in solid-state materials science, *Npj Comput. Mater.* 5 (2019) 1–36. <https://doi.org/10.1038/s41524-019-0221-0>.
- [10] F. REINAUER, R. GLAUM, R. GRUEHN, Preparation and chemical vapour transport of mixed valent titanium (III, IV)-phosphates. With a note on the crystal structure of titanium (IV)-orthophosphate Ti5P4O20, *Prep. Chem. Vap. Transp. Mix. Val. Titan. III IV-Phosphates Note Cryst. Struct. Titan. IV-Orthophosphate Ti5P4O20* 31 (1994) 779–791.
- [11] E. Benser, R. Glaum, T. Dross, H. Hibst, V(III)V(IV)3O3(PO4)3: A Novel Vanadium Phosphate for Selective Oxidation of Light Hydrocarbons, *Chem. Mater.* 19 (2007) 4341–4348. <https://doi.org/10.1021/cm071036u>.
- [12] R. Glaum, Beiträge zum thermischen Verhalten wasserfreier Phosphate. IX. Darstellung und Kristallstruktur von  $\text{Cr}_6(\text{P}_2\text{O}_7)_4$ . Ein gemischtvalentes Pyrophosphat mit zwei- und dreiwertigem Chrom, *Z. Für Anorg. Allg. Chem.* 616 (1992) 46–52. <https://doi.org/10.1002/zaac.19926161008>.
- [13] P. Roussel, O. Pérez, P. Labbé, Phosphate tungsten bronze series: crystallographic and structural properties of low-dimensional conductors, *Acta Crystallogr. B* 57 (2001) 603–632. <https://doi.org/10.1107/S0108768101009685>.

- [14] S.C. Roy, W. Assenmacher, T. Linden, L. Esser, W. Mader, R. Glaum, Substitution of W<sup>5+</sup> in monophosphate tungsten bronzes by combinations Mn<sup>+</sup>/W<sup>6+</sup>, *Z. Für Naturforschung B* 71 (2016) 543–552. <https://doi.org/10.1515/znb-2016-0036>.
- [15] A. Karbstein, M. Weber, D. Lahr, J. Daniels, W. Assenmacher, W. Mader, F. Rosowski, S.A. Schunk, R. Glaum, Mixed-Metal Monophosphate Tungsten Bronzes Containing Rhodium and Iridium, *Eur. J. Inorg. Chem.* 2021 (2021) 1459–1469. <https://doi.org/10.1002/ejic.202100047>.
- [16] R. Masse, M.T. Averbuch-Pouchot, A. Durif, Crystal structures of phosphomolybdenyl salts: Pb(MoO<sub>2</sub>)<sub>2</sub>(PO<sub>4</sub>)<sub>2</sub> and Ba(MoO<sub>2</sub>)<sub>2</sub>(PO<sub>4</sub>)<sub>2</sub>, *J. Solid State Chem.* 58 (1985) 157–163. [https://doi.org/10.1016/0022-4596\(85\)90229-4](https://doi.org/10.1016/0022-4596(85)90229-4).
- [17] A. Jain, S.P. Ong, G. Hautier, W. Chen, W.D. Richards, S. Dacek, S. Cholia, D. Gunter, D. Skinner, G. Ceder, K.A. Persson, Commentary: The Materials Project: A materials genome approach to accelerating materials innovation, *APL Mater.* 1 (2013) 011002. <https://doi.org/10.1063/1.4812323>.
- [18] F.A. Cotton, J.B. Goodenough, *Magnetism and the chemical bond*, Vol Interscience—John Wiley N. Y. (1963).
- [19] R. Glaum, *Neue Untersuchungen an wasserfreien Phosphaten der Übergangsmetalle*, 1999.
- [20] E.-M. Hammer, *Neue polynäre Phosphate des zweiwertigen Chroms und eine neue Modifikation von Chrom(ii)-Orthophosphat*, Thesis, Universitäts- und Landesbibliothek Bonn, 2012. <https://bonndoc.ulb.uni-bonn.de/xmlui/handle/20.500.11811/5277> (accessed May 13, 2024).
- [21] F. Wöhler, XXXVIII. On tungsten, *Philos. Mag.* (1825). <https://doi.org/10.1080/14786442508673961>.
- [22] P.G. Dickens, M.S. Whittingham, The tungsten bronzes and related compounds, *Q. Rev. Chem. Soc.* 22 (1968) 30. <https://doi.org/10.1039/qr9682200030>.
- [23] R. The tungsten bronzes and related compounds, P. Bordet, J. Bossy, H. Schober, S. Eibl, Superconductivity in the tungsten bronze RbxWO<sub>3</sub> (0.20 ≤ x ≤ 0.33) in connection with its structure, electronic density of states, and phonon density of states, *Phys. Rev. B* 76 (2007) 174511. <https://doi.org/10.1103/PhysRevB.76.174511>.
- [24] P. Labbé, M. Goreaud, B. Raveau, J.C. Monier, Etude comparative des structures MxWO<sub>3</sub> de type bronze hexagonal. I. Analyse structurale des bronzes de composition MO<sub>30</sub>WO<sub>3</sub>. Stéréochimie des éléments M = RbI, TlI et InI, *Acta Crystallogr.* 34 (1978) 1433–1438.
- [25] J.P. Giroult, M. Goreaud, Ph. Labbé, B. Raveau, RbxP<sub>8</sub>W<sub>32</sub>O<sub>112</sub>: a tunnel structure built up from ReO<sub>3</sub>-type blocks and P<sub>2</sub>O<sub>7</sub> groups, *Acta Crystallogr. Sect. B* 36 (1980) 2570–2575. <https://doi.org/10.1107/S0567740880009466>.
- [26] J.P. Giroult, M. Goreaud, P. Labbé, B. Raveau, P<sub>4</sub>W<sub>8</sub>O<sub>32</sub>: a mixed-valence tunnel structure built up of ReO<sub>3</sub>-type slabs connected through PO<sub>4</sub> tetrahedra, *Acta Crystallogr. Sect. B* 37 (1981) 2139–2142. <https://doi.org/10.1107/S0567740881008248>.
- [27] E. Wang, M. Greenblatt, I.E.-I. Rachidi, E. Canadell, M.-H. Whangbo, S. Vadlamannati, Electronic instabilities of the quasi-two-dimensional monophosphate tungsten bronze P<sub>4</sub>W<sub>12</sub>O<sub>44</sub>, *Phys. Rev. B* 40 (1989) 11964–11964. <https://doi.org/10.1103/PhysRevB.40.11964.2>.

- [28] D. Feinberg, J. Friedel, Imperfections of Charge Density Waves in Blue Bronzes, in: C. Schlenker (Ed.), *Low-Dimens. Electron. Prop. Molybdenum Bronzes Oxides*, Springer Netherlands, Dordrecht, 1989: pp. 407–448. [https://doi.org/10.1007/978-94-009-0447-7\\_7](https://doi.org/10.1007/978-94-009-0447-7_7).
- [29] M.-H. Whangbo, E. Canadell, P. Foury, J.-P. Pouget, Hidden Fermi Surface Nesting and Charge Density Wave Instability in Low-Dimensional Metals, *Science* 252 (1991) 96–98. <https://doi.org/10.1126/science.252.5002.96>.
- [30] C. Schlenker, J. Dumas, M. Greenblatt, S. Van Smaalen, eds., *Physics and Chemistry of Low-Dimensional Inorganic Conductors*, Springer US, Boston, MA, 1996. <https://doi.org/10.1007/978-1-4613-1149-2>.
- [31] E. Duverger-Nédellec, Transitions vers des états électroniques complexes et des structures super périodiques dans les bronzes mono phosphates de tungstènes, Thèse de doctorat, Normandie, 2017. <https://www.theses.fr/2017NORMC239> (accessed March 6, 2024).
- [32] A. Minelli, Monophosphate tungsten bronzes and antimony: the interplay of framework instability and electron-phonon coupling, PhD thesis, Université Grenoble Alpes, 2018. <https://theses.hal.science/tel-02271297> (accessed March 6, 2024).
- [33] M. Ghedira, H. Vincent, M. Marezio, J. Marcus, G. Furcaudot, Structure cristalline du conducteur métallique bidimensionnel Mo<sub>4</sub>O<sub>11</sub>- $\gamma$ , *J. Solid State Chem. Fr.* 56 (1985) 66–73. [https://doi.org/10.1016/0022-4596\(85\)90253-1](https://doi.org/10.1016/0022-4596(85)90253-1).
- [34] A. Magnéli, B. Barfod, P. Gjertsen, The Crystal Structure of Mo<sub>4</sub>O<sub>11</sub> ( $\gamma$ -Molybdenum Oxide), *Acta Chem. Scand.* 2 (1948) 861–871. <https://doi.org/10.3891/acta.chem.scand.02-0861>.
- [35] M. Hervieu, B. Domengès, B. Raveau, Formation of pentagonal tunnels bordered with P<sub>2</sub>O<sub>7</sub> groups in diphosphate tungsten bronzes (P<sub>2</sub>O<sub>4</sub>)<sub>2</sub>(WO<sub>3</sub>)<sub>2m</sub>: A HREM investigation, *J. Solid State Chem.* 58 (1985) 233–242. [https://doi.org/10.1016/0022-4596\(85\)90240-3](https://doi.org/10.1016/0022-4596(85)90240-3).
- [36] H. Miao, G. Fabbris, R.J. Koch, D.G. Mazzone, C.S. Nelson, R. Acevedo-Esteves, G.D. Gu, Y. Li, T. Yilimaz, K. Kaznatcheev, E. Vescovo, M. Oda, T. Kurosawa, N. Momono, T. Assefa, I.K. Robinson, E.S. Bozin, J.M. Tranquada, P.D. Johnson, M.P.M. Dean, Charge density waves in cuprate superconductors beyond the critical doping, *Npj Quantum Mater.* 6 (2021) 1–6. <https://doi.org/10.1038/s41535-021-00327-4>.
- [37] W. Fogle, J.H. Perlstein, Semiconductor-to-Metal Transition in the Blue Potassium Molybdenum Bronze, K<sub>0.30</sub>MoO<sub>3</sub> Example of a Possible Excitonic Insulator, *Phys. Rev. B* 6 (1972) 1402–1412. <https://doi.org/10.1103/PhysRevB.6.1402>.
- [38] W.L. McMillan, Landau theory of charge-density waves in transition-metal dichalcogenides, *Phys. Rev. B* 12 (1975) 1187–1196. <https://doi.org/10.1103/PhysRevB.12.1187>.
- [39] K. Takita, K. Masuda, Charge density wave transition and superconductivity in 2H-NbSe<sub>2</sub>. Direct measurement of the penetration depth in a layered superconductor, *J. Low Temp. Phys.* 58 (1985) 127–142. <https://doi.org/10.1007/BF00682569>.
- [40] S. Aubry, Bipolaronic charge density waves and polaronic spin density waves in the Holstein-Hubbard model, *J. Phys. IV* 03 (1993) C2-349-C2-355. <https://doi.org/10.1051/jp4:1993270>.

- [41] W. Wen, C. Dang, L. Xie, Photoinduced phase transitions in two-dimensional charge-density-wave 1T-TaS<sub>2</sub>, *Chin. Phys. B* 28 (2019) 058504. <https://doi.org/10.1088/1674-1056/28/5/058504>.
- [42] M.H. Whangbo, E. Canadell, C. Schlenker, Band electronic structure of the purple potassium molybdenum bronze K<sub>0.9</sub>Mo<sub>6</sub>O<sub>17</sub>, *J. Am. Chem. Soc.* 109 (1987) 6308–6313. <https://doi.org/10.1021/ja00255a013>.
- [43] S. Paul, A. Ghosh, T. Sato, D.D. Sarma, T. Takahashi, E. Wang, M. Greenblatt, S. Raj, Electronic band structure and Fermi surfaces of the quasi-two-dimensional monophosphate tungsten bronze, P4W<sub>12</sub>O<sub>44</sub>, *Europhys. Lett.* 105 (2014) 47003. <https://doi.org/10.1209/0295-5075/105/47003>.
- [44] E. Canadell, M.-H. Whangbo, Structural and electronic origin of the hidden nesting and charge density waves in transition metal oxides and bronzes, *Int. J. Mod. Phys. B* 07 (1993) 4005–4043. <https://doi.org/10.1142/S0217979293003577>.
- [45] S. Paul, S. Kumari, S. Raj, Vacancy-induced in-gap states in sodium tungsten bronzes: Density functional investigations, *Europhys. Lett.* 114 (2016) 37011. <https://doi.org/10.1209/0295-5075/114/37011>.
- [46] S.L. Wang, C.C. Wang, K.H. Lii, Crystal structure of WPO<sub>5</sub>, the second member of the monophosphate tungsten bronze series (WO<sub>3</sub>)<sub>2m</sub>(PO<sub>2</sub>)<sub>4</sub>, *J. Solid State Chem.* 82 (1989) 298–302. [https://doi.org/10.1016/0022-4596\(89\)90295-8](https://doi.org/10.1016/0022-4596(89)90295-8).
- [47] J. Dumas, C. Hess, C. Schlenker, G. Bonfait, E. Gomez Marin, D. Groult, J. Marcus, Localization effects in the charge density wave state of the quasi-two-dimensional monophosphate tungsten bronzes, *Eur. Phys. J. B* 14 (2000) 73–82. <https://doi.org/10.1007/s100510050108>.
- [48] J. Dumas, U. Beierlein, S. Drouard, C. Hess, D. Groult, Ph. Labbé, P. Roussel, G. Bonfait, E.G. Marin, C. Schlenker, Electronic Instabilities and Localization Effects in the Quasi-Two-Dimensional Monophosphate Tungsten Bronzes (PO<sub>2</sub>)<sub>4</sub>(WO<sub>3</sub>)<sub>2m</sub> and K<sub>x</sub>P<sub>4</sub>W<sub>8</sub>O<sub>32</sub>, *J. Solid State Chem.* 147 (1999) 320–327. <https://doi.org/10.1006/jssc.1999.8289>.
- [49] C.L. Touze, G. Bonfait, C. Schlenker, J. Dumas, M. Almeida, M. Greenblatt, Shubnikov-de Haas effect in the quasi-two-dimensional bronze P<sub>4</sub>W<sub>8</sub>O<sub>32</sub>, *Czechoslov. J. Phys.* 46 (1996) 2617–2618. <https://doi.org/10.1007/BF02570295>.
- [50] C. Hess, C. Schlenker, G. Bonfait, J. Marcus, T. Ohm, C. Paulsen, J. Dumas, J.L. Tholence, M. Greenblatt, M. Almeida, Superconductivity in the charge density wave state of the quasi-two-dimensional monophosphate tungsten bronze P<sub>4</sub>W<sub>14</sub>O<sub>50</sub>, *Phys. C Supercond. Its Appl.* 282–287 (1997) 955–956. [https://doi.org/10.1016/S0921-4534\(97\)00589-3](https://doi.org/10.1016/S0921-4534(97)00589-3).
- [51] C. Hess, C. Schlenker, J. Dumas, M. Greenblatt, Z.S. Teweldemedhin, Magnetotransport and thermopower properties of the quasi-two-dimensional charge-density-wave compounds (PO<sub>2</sub>)<sub>4</sub>(WO<sub>3</sub>)<sub>2m</sub> (m = 4,6), *Phys. Rev. B* 54 (1996) 4581–4588. <https://doi.org/10.1103/PhysRevB.54.4581>.
- [52] A. Rötger, J. Lehmann, C. Schlenker, J. Dumas, J. Marcus, Z.S. Teweldemedhin, M. Greenblatt, Magnetotransport Properties in the Charge Density Wave State of the Quasi-Two-Dimensional Compounds (PO<sub>2</sub>)<sub>4</sub>(WO<sub>3</sub>)<sub>2m</sub>, *Europhys. Lett.* 25 (1994) 23. <https://doi.org/10.1209/0295-5075/25/1/005>.

- [53] K.K. Kolincio, Study of thermal and electronic transport properties in low dimensional oxides, 2013.
- [54] C. Schlenker, C. Hess, C.L. Touze, J. Dumas, Charge Density Wave Properties of Quasi Low-Dimensional Transition Metal Oxide Bronzes, *J. Phys. I* 6 (1996) 2061–2078. <https://doi.org/10.1051/jp1:1996205>.
- [55] M. Chung, Y.-K. Kuo, G. Mozurkewich, E. Figueroa, Z. Teweldemedhin, D. a. D. Carlo, M. Greenblatt, J.W. Brill, Specific heat at CDW transitions in bronzes, *J. Phys. IV* 03 (1993) C2-250. <https://doi.org/10.1051/jp4:1993249>.
- [56] V. Bondarenko, J.W. Brill, J. Dumas, C. Schlenker, Specific heat anomalies in the quasi two-dimensional monophosphate tungsten bronzes  $K_xP_4W_8O_{32}$ , *Solid State Commun.* 129 (2004) 211–215. <https://doi.org/10.1016/j.ssc.2003.10.014>.
- [57] G. Reményi, S. Sähling, K. Biljaković, D. Starešinić, L. Lasjaunias, J.-E. Lorenzo, P. Monceau, A. Cano, Incommensurate systems as model compounds for disorder revealing low-temperature glasslike behavior, *Phys Rev Lett* 114 (2015) 195502. <https://doi.org/doi:10.1103/PhysRevLett.114.195502>.
- [58] J. Wang, R. Xiong, D. Yin, C. Li, Z. Tang, Q. Wang, J. Shi, Y. Wang, H. Wen, Low-temperature specific heat of the quasi-two-dimensional charge-density wave compound  $KMo_6O_{17}$ , *Phys. Rev. B* 73 (2006) 193102. <https://doi.org/10.1103/PhysRevB.73.193102>.
- [59] Bruker (2005) SAINT, (2005).
- [60] L. Palatinus, Ab initio determination of incommensurately modulated structures by charge flipping in superspace, *Acta Crystallogr. A* 60 (2004) 604–610. <https://doi.org/10.1107/S0108767304022433>.
- [61] V. Petříček, M. Dušek, L. Palatinus, Crystallographic Computing System JANA2006: General features, *Z. Für Krist. - Cryst. Mater.* 229 (2014) 345–352. <https://doi.org/10.1515/zkri-2014-1737>.
- [62] P. Giannozzi, S. Baroni, N. Bonini, M. Calandra, R. Car, C. Cavazzoni, D. Ceresoli, G.L. Chiarotti, M. Cococcioni, I. Dabo, A.D. Corso, S. de Gironcoli, S. Fabris, G. Fratesi, R. Gebauer, U. Gerstmann, C. Gougoussis, A. Kokalj, M. Lazzeri, L. Martin-Samos, N. Marzari, F. Mauri, R. Mazzarello, S. Paolini, A. Pasquarello, L. Paulatto, C. Sbraccia, S. Scandolo, G. Sclauzero, A.P. Seitsonen, A. Smogunov, P. Umari, R.M. Wentzcovitch, QUANTUM ESPRESSO: a modular and open-source software project for quantum simulations of materials, *J. Phys. Condens. Matter* 21 (2009) 395502. <https://doi.org/10.1088/0953-8984/21/39/395502>.
- [63] M.J. van Setten, M. Giantomassi, E. Bousquet, M.J. Verstraete, D.R. Hamann, X. Gonze, G.-M. Rignanese, The PseudoDojo: Training and grading a 85 element optimized norm-conserving pseudopotential table, *Comput. Phys. Commun.* 226 (2018) 39–54. <https://doi.org/10.1016/j.cpc.2018.01.012>.
- [64] J.P. Perdew, K. Burke, M. Ernzerhof, Generalized Gradient Approximation Made Simple, *Phys. Rev. Lett.* 77 (1996) 3865–3868. <https://doi.org/10.1103/PhysRevLett.77.3865>.
- [65] Y. Hinuma, G. Pizzi, Y. Kumagai, F. Oba, I. Tanaka, Band structure diagram paths based on crystallography, *Comput. Mater. Sci.* 128 (2017) 140–184. <https://doi.org/10.1016/j.commatsci.2016.10.015>.

- [66] L.-J. Jongh, *Magnetic Properties of Layered Transition Metal Compounds*, in: *Magn. Prop. Layer. Transit. Met. Compd.*, 1st ed., Springer Dordrecht, 1990. <https://link.springer.com/book/10.1007/978-94-009-1860-3> (accessed March 26, 2024).
- [67] R. David, A. Pautrat, D. Filimonov, H. Kabbour, H. Vezin, M.-H. Whangbo, O. Mentré, *Across the Structural Re-Entrant Transition in BaFe<sub>2</sub>(PO<sub>4</sub>)<sub>2</sub>: Influence of the Two-Dimensional Ferromagnetism*, *J. Am. Chem. Soc.* 135 (2013) 13023–13029. <https://doi.org/10.1021/ja404697b>.
- [68] A. Magneli, *Crystal structure studies on gamma-tungsten oxide*, *Ark. Foer Kemi* 1 (1949) 223–230.
- [69] M. Binnewies, R. Glaum, M. Schmidt, P. Schmidt, *Chemical Vapor Transport Reactions*, Walter de Gruyter, 2012.
- [70] V.P. Nikolaev, G.G. Sadikov, A.V. Lavrov, M.A. Poraj-Koshits, *Crystal structure of CsTa(PO<sub>4</sub>)<sub>2</sub> and TaH(PO<sub>4</sub>)<sub>2</sub>*, *Izv Akad Nauk SSSR Neorg Mater* 19 (1983) 972–977.
- [71] D. Bregiroux, K. Popa, R. Jardin, P.E. Raison, G. Wallez, M. Quarton, M. Brunelli, C. Ferrero, R. Caciuffo, *Crystal structure and thermal expansion of the low- and high-temperature forms of BaMIV(PO<sub>4</sub>)<sub>2</sub> compounds (M=Ti, Zr, Hf and Sn)*, *J. Solid State Chem.* 182 (2009) 1115–1120. <https://doi.org/10.1016/j.jssc.2009.02.012>.
- [72] A. Leclaire, M.M. Barel, J. Chardon, B. Raveau, *A Mo(IV) Monophosphate, BaMo(PO<sub>4</sub>)<sub>2</sub>, with the Yavapaiite Layer Structure*, *J. Solid State Chem.* 116 (1995) 364–368. <https://doi.org/10.1006/jssc.1995.1227>.
- [73] R.D. Shannon, *Revised effective ionic radii and systematic studies of interatomic distances in halides and chalcogenides*, *Acta Crystallogr. A* 32 (1976) 751–767. <https://doi.org/10.1107/S0567739476001551>.
- [74] H. Kabbour, R. David, A. Pautrat, H.-J. Koo, M.-H. Whangbo, G. André, O. Mentré, *A Genuine Two-Dimensional Ising Ferromagnet with Magnetically Driven Re-entrant Transition*, *Angew. Chem. Int. Ed.* 51 (2012) 11745–11749. <https://doi.org/10.1002/anie.201205843>.
- [75] N. Faza, W. Treutmann, D. Babel, *Struktur- und magnetochemische Untersuchungen an den ternären Phosphaten Ba<sub>2</sub>MII(PO<sub>4</sub>)<sub>2</sub> (MII = Mn, Co) und Strukturverfeinerung von BaNi<sub>2</sub>(PO<sub>4</sub>)<sub>2</sub>*, *Z. Für Anorg. Allg. Chem.* 627 (2001) 687–692. [https://doi.org/10.1002/1521-3749\(200104\)627:4<687::AID-ZAAC687>3.0.CO;2-5](https://doi.org/10.1002/1521-3749(200104)627:4<687::AID-ZAAC687>3.0.CO;2-5).
- [76] H. Vincent, M. Ghedira, J. Marcus, J. Mercier, C. Schlenker, *Structure cristalline d'un conducteur métallique bidimensionnel: Le bronze violet de potassium et molybdene K<sub>0.9</sub>Mo<sub>6</sub>O<sub>17</sub>*, *J. Solid State Chem.* 47 (1983) 113–121. [https://doi.org/10.1016/0022-4596\(83\)90050-6](https://doi.org/10.1016/0022-4596(83)90050-6).
- [77] M. Onoda, Y. Matsuda, M. Sato, *Structure determination of low-dimensional conductor sodium molybdenum purple bronze Na<sub>0.9</sub>Mo<sub>6</sub>O<sub>17</sub>*, *J. Solid State Chem.* 69 (1987) 67–75. [https://doi.org/10.1016/0022-4596\(87\)90011-9](https://doi.org/10.1016/0022-4596(87)90011-9).
- [78] J. Rodriguez-Carvajal, FullProf, (n.d.).
- [79] M. Kockert, R. Mitdank, A. Zykov, S. Kowarik, S.F. Fischer, *Absolute Seebeck coefficient of thin platinum films*, *J Appl Phys* 126 (2019) 105106. <https://doi.org/10.1063/1.5101028>.

- [80] D.K.C. MacDonald, *Thermoelectricity: An Introduction to the Principles*, Courier Corporation, 2013.
- [81] A. Cano, A.P. Levanyuk, Explanation of the Glasslike Anomaly in the Low-Temperature Specific Heat of Incommensurate Phases, *Phys Rev Lett* 93 (4AD) 245902.
- [82] L.S. Palatnik, O.A. Obol'yaninova, M.N. Naboka, N.T. Gladkikh, New modifications of tungsten oxides, *Inorg Mater USSR Engl Transl* V 9 No 5 Pp 718-720 (1973). <https://www.osti.gov/biblio/4370613> (accessed March 27, 2024).
- [83] H. Nimoh, A.M. Arévalo-López, M. Huvé, C. Minaud, A. Cano, R. Glaum, O. Mentré, Layered Monophosphate Tungsten Bronzes [Ba(PO<sub>4</sub>)<sub>2</sub>]<sub>2</sub>W<sub>m</sub>O<sub>3m-3</sub>: 2D Metals with Locked Charge-Density-Wave Instabilities, *Angew Chem Int Ed Int.* 62 (2023) e202302049. <https://doi.org/10.1002/anie.202302049>.
- [84] P. Sharma, S. Singh, K. Kuga, T. Takeuchi, R. Bindu, Synthesis and structural link to the electronic and magneto-transport properties of spin-orbit Mott insulator Sr<sub>2</sub>IrO<sub>4</sub>, *J. Phys. Condens. Matter* 34 (2022) 435402. <https://doi.org/10.1088/1361-648X/ac8961>.
- [85] Y. Liu, Z. Wang, M. Wu, Q. Sun, M. Chao, Y. Jia, Negative thermal expansion in isostructural cubic ReO<sub>3</sub> and ScF<sub>3</sub>: A comparative study, *Comput Mater Sci* 107 (2015) 157–162. <https://doi.org/10.1016/j.commatsci.2015.05.019>.
- [86] H. Hamdi, E.K.H. Salje, P. Ghosez, E. Bousquet, First-principles reinvestigation of bulk WO<sub>3</sub>, *Phys Rev B* 94 (2016) 245124.
- [87] N. Mascello, N.A. Spaldin, A. Narayan, Q.N. Meier, Theoretical investigation of twin boundaries in WO<sub>3</sub>: Structure, properties, and implications for superconductivity, *Phys. Rev. Res.* 2 (2020) 033460. <https://doi.org/10.1103/PhysRevResearch.2.033460>.
- [88] D. Meier, J. Seidel, A. Cano, K. Delaney, Y. Kumagai, M. Mostovoy, N.A. Spaldin, R. Ramesh, M. Fiebig, Anisotropic conductance at improper ferroelectric domain walls, *Nat Mater* 11 (2012) 284–288. <https://doi.org/10.1038/nmat3249>.
- [89] P. Botella, B. Solsona, J.M. López Nieto, P. Concepción, J.L. Jordá, M.T. Doménech-Carbó, Mo–W-containing tetragonal tungsten bronzes through isomorphic substitution of molybdenum by tungsten, *Catal. Today* 158 (2010) 162–169. <https://doi.org/10.1016/j.cattod.2010.05.024>.
- [90] I.J. McColm, R.J.D. Tilley, C.P.M. Barton, N.N. Greenwood, Evidence for the existence of iron tungsten bronzes, *J. Solid State Chem.* 16 (1976) 265–270. [https://doi.org/10.1016/0022-4596\(76\)90041-4](https://doi.org/10.1016/0022-4596(76)90041-4).
- [91] M.F. Zid, A. Driss, T. Jouini, K<sub>2</sub>MoO<sub>2</sub>P<sub>2</sub>O<sub>7</sub>, *Acta Crystallogr. Sect. E Struct. Rep. Online* 59 (2003) i65–i67. <https://doi.org/10.1107/S1600536803007001>.
- [92] M. Abudourehman, J. Zheng, P. Wang, B. Wei, Z. Guo, Z. Chen, Y. Chen, A<sub>6</sub>Mo<sub>2</sub>P<sub>4</sub>O<sub>19</sub> (A = Rb, Cs) and Rb<sub>2</sub>MoP<sub>2</sub>O<sub>9</sub>: new molybdophosphates with distinct polyanionic configurations, *Dalton Trans.* 51 (2022) 1481–1488. <https://doi.org/10.1039/D1DT03756K>.
- [93] M.T. Averbuch-Pouchot, Structure of an ammonium molybdenyl diphosphate: (NH<sub>4</sub>)<sub>2</sub>MoO<sub>2</sub>P<sub>2</sub>O<sub>7</sub>, *Acta Crystallogr. C* 44 (1988) 2046–2048. <https://doi.org/10.1107/S0108270188008509>.

- [94] P. Kierkegaard, Crystal structure of NaWO<sub>2</sub>PO<sub>4</sub> and NaMoO<sub>2</sub>PO<sub>4</sub>, *Ark. KEMI* 18 (1962) 553.
- [95] P. Kierkegaard, S. Holmen, The crystal Structure of AgMoO<sub>2</sub>PO<sub>4</sub>, *Ark. Foer Kemi* 23 (1965) 213–221.
- [96] R. Peascoe, A. Clearfield, Synthesis and structural characterization of K(MoO<sub>2</sub>)(PO<sub>4</sub>) · H<sub>2</sub>O, and its topotatic reaction to form KMoO<sub>2</sub>PO<sub>4</sub>, *J. Solid State Chem.* 95 (1991) 83–93. [https://doi.org/10.1016/0022-4596\(91\)90378-U](https://doi.org/10.1016/0022-4596(91)90378-U).
- [97] A. Leclaire, A. Guesdon, M.M. Borel, F. Berrah, B. Raveau, Two molybdenum (VI) monophosphates with a tunnel structure: AMoO<sub>2</sub>PO<sub>4</sub> (A=Cs, Tl) and structural relationships in the series, *Solid State Sci.* 3 (2001) 877–882. [https://doi.org/10.1016/S1293-2558\(01\)01191-8](https://doi.org/10.1016/S1293-2558(01)01191-8).
- [98] P. Gong, X. Jiang, Y. Yang, S. Luo, R. Huang, L. Li, C. Chen, Z. Lin, Cs<sub>3</sub>W<sub>3</sub>PO<sub>13</sub>: A Tungsten Phosphate with One-Dimensional Zigzag Tunnels Exhibiting Strongly Anisotropic Thermal Expansion, *Inorg. Chem.* 55 (2016) 5113–5115. <https://doi.org/10.1021/acs.inorgchem.6b00926>.
- [99] M. Tsuboi, M. Hibino, N. Mizuno, S. Uchida, Crystalline polyoxometalate (POM)–polyethylene glycol (PEG) composites aimed as non-humidified intermediate-temperature proton conductors, *J. Solid State Chem.* 234 (2016) 9–14. <https://doi.org/10.1016/j.jssc.2015.11.030>.
- [100] F. Goubin, L. Guénée, P. Deniard, H.-J. Koo, M.-H. Whangbo, Y. Montardi, S. Jovic, Synthesis, optical properties and electronic structures of polyoxometalates K<sub>3</sub>P(Mo<sub>1-x</sub>W<sub>x</sub>)<sub>12</sub>O<sub>40</sub> (0 ≤ x ≤ 1), *J. Solid State Chem.* 177 (2004) 4528–4534. <https://doi.org/10.1016/j.jssc.2004.08.046>.
- [101] P. Armand, D. Granier, A. van der Lee, Rb<sub>3</sub>[PMo<sub>12</sub>O<sub>40</sub>], a compound containing Keggin anions, *Acta Crystallogr. Sect. E Struct. Rep. Online* 63 (2007) i191–i191. <https://doi.org/10.1107/S1600536807052506>.
- [102] H. Liu, H. Wu, H. Yu, Z. Hu, J. Wang, Y. Wu, Effect of Mo/P Ratios on Dimensions: Syntheses, Structures, and Properties of Three New Molybdophosphates, *Inorg. Chem.* 59 (2020) 5742–5750. <https://doi.org/10.1021/acs.inorgchem.0c00511>.
- [103] M.F. Hazenkamp, E.H. Voogt, G. Blasse, Luminescence of two dioxo<sup>0</sup> transition-metal complexes: K<sub>2</sub>MoO<sub>2</sub>F<sub>4</sub> · H<sub>2</sub>O and NaWO<sub>2</sub>PO<sub>4</sub>, *J. Solid State Chem.* 101 (1992) 26–31. [https://doi.org/10.1016/0022-4596\(92\)90196-3](https://doi.org/10.1016/0022-4596(92)90196-3).
- [104] E. Bordes-Richard, P. Courtine, Optical Basicity: A Scale of Acidity/Basicity of Solids and Its Application to Oxidation Catalysis, in: J. Fierro (Ed.), *Met. Oxides*, CRC Press, 2005: pp. 319–352. <https://doi.org/10.1201/9781420028126.ch10>.
- [105] M. Cifre-Herrando, G. Roselló-Márquez, P.J. Navarro-Gázquez, M.J. Muñoz-Portero, E. Blasco-Tamarit, J. García-Antón, Characterization and Comparison of WO<sub>3</sub>/WO<sub>3</sub>-MoO<sub>3</sub> and TiO<sub>2</sub>/TiO<sub>2</sub>-ZnO Nanostructures for Photoelectrocatalytic Degradation of the Pesticide Imazalil, *Nanomaterials* 13 (2023) 2584. <https://doi.org/10.3390/nano13182584>.
- [106] C. Prameela, M. Anjaiah, K. Murthy, K. Srinivasarao, Optical and IR studies on (MoO<sub>3</sub>)<sub>1-x</sub>-(WO<sub>3</sub>)<sub>x</sub> mixed oxide thin films, *Phys. Chem. Glas. Eur. J. Glass Sci. Technol. Part B* 57 (2016) 139–145. <https://doi.org/10.13036/17533562.57.3.014>.

- [107] G. Andersson, B. Bak, A. Hillebert, H. Westermark, I. Steensgaard, Th. Rosenberg, On the Crystal Structure of Tungsten Trioxide., *Acta Chem. Scand.* 7 (1953) 154–158. <https://doi.org/10.3891/acta.chem.scand.07-0154>.
- [108] N. Wooster, The crystal structure of Molybdenum Trioxide, MoO<sub>3</sub>, *Z. Für Krist. - Cryst. Mater.* 80 (1931) 504–512. <https://doi.org/10.1524/zkri.1931.80.1.504>.
- [109] P. Kierkegaard, S. Åsbrink, T. Reistad, D.R. Sparrow, The Crystal Structure of W<sub>2</sub>O<sub>3</sub>(PO<sub>4</sub>)<sub>2</sub>. Determination of a Superstructure by Means of Least-Squares Calculations., *Acta Chem. Scand.* 18 (1964) 2329–2338. <https://doi.org/10.3891/acta.chem.scand.18-2329>.
- [110] M. Hanawa, H. Imoto, Structures of Two New Polymorphic Forms of Hexavalent Tungsten Oxide Phosphates, *J. Solid State Chem.* 144 (1999) 325–329. <https://doi.org/10.1006/jssc.1999.8153>.
- [111] P. Kierkegaard, On the crystal structure of (MoO<sub>2</sub>)<sub>2</sub>P<sub>2</sub>O<sub>7</sub>, *Ark. Foer Kemi* 19 (1962) 1–14.
- [112] H.F. Barry, P.C.H. Mitchell, Chemistry and uses of molybdenum, in: *Climax Molybdenum Company, Ann Arbor, MI, 1979*. <https://www.osti.gov/biblio/5051400> (accessed July 7, 2024).
- [113] A. Boultif, D. Louër, Indexing of powder diffraction patterns for low-symmetry lattices by the successive dichotomy method, *Appl. Crystallogr.* 24 (1991) 987–993.
- [114] V. Favre-Nicolin, R. Černý, FOX, free objects for crystallography': a modular approach to ab initio structure determination from powder diffraction, *J. Appl. Crystallogr.* 35 (2002) 734–743.
- [115] C.W. Glass, A.R. Oganov, N. Hansen, USPEX—Evolutionary crystal structure prediction, *Comput. Phys. Commun.* 175 (2006) 713–720. <https://doi.org/10.1016/j.cpc.2006.07.020>.
- [116] A. Togo, L. Chaput, T. Tadano, I. Tanaka, Implementation strategies in phonopy and phono3py, *J. Phys. Condens. Matter* 35 (2023) 353001. <https://doi.org/10.1088/1361-648X/acd831>.
- [117] Y. Ma, M. Eremets, A.R. Oganov, Y. Xie, I. Trojan, S. Medvedev, A.O. Lyakhov, M. Valle, V. Prakapenka, Transparent dense sodium, *Nature* 458 (2009) 182–185. <https://doi.org/10.1038/nature07786>.
- [118] T. Yu, O.O. Kurakevych, V.L. Solozhenko, Ionic high-pressure form of elemental boron, (2009). <https://uspex-team.org/static/file/Boron-Nature-2009.pdf> (accessed July 5, 2024).
- [119] A. Togo, I. Tanaka, First principles phonon calculations in materials science, *Scr. Mater.* 108 (2015) 1–5.
- [120] I. Pallikara, P. Kayastha, J.M. Skelton, L.D. Whalley, The physical significance of imaginary phonon modes in crystals, *Electron. Struct.* 4 (2022) 033002. <https://doi.org/10.1088/2516-1075/ac78b3>.
- [121] H. Lux, G. Illmann, Zur Kenntnis der Chrom(II)-Salze und des Chrom(II)-oxyds, I, *Chem. Ber.* 91 (1958) 2143–2150. <https://doi.org/10.1002/cber.19580911021>.
- [122] H. Lux, G. Illmann, Zur Kenntnis der Chrom(II)-Salze und des Chrom(II)-oxyds, II, *Chem. Ber.* 92 (1959) 2364–2371. <https://doi.org/10.1002/cber.19590920953>.

- [123] Zur Kenntnis der Chrom(II)-Salze und des Chrom(II)-oxids, III - Lux - 1961 - Chemische Berichte - Wiley Online Library, (n.d.). <https://chemistry-europe.onlinelibrary.wiley.com/doi/abs/10.1002/cber.19610940621> (accessed June 15, 2024).
- [124] Zur Kenntnis der Chrom(II)-Salze und des Chrom(II)-oxids, IV - Lux - 1964 - Chemische Berichte - Wiley Online Library, (n.d.). <https://chemistry-europe.onlinelibrary.wiley.com/doi/abs/10.1002/cber.19640970228> (accessed June 15, 2024).
- [125] V. Dufek, F. Petrů, V. Brožek, Über Sauerstoff-haltige Verbindungen vom Strukturtyp B1 der ersten vier Übergangsmetalle, Monatshefte Für Chem. Verwandte Teile Anderer Wiss. 98 (1967) 2424–2430. <https://doi.org/10.1007/BF00902443>.
- [126] Data retrieved from the Materials Project for CrO (mp-1283577, mp-1302566, mp-755073) from database version v2023.11.1, (n.d.). <https://next-gen.materialsproject.org/>.
- [127] D.D. Wagman, W.H. Evans, V.B. Parker, R.H. Schumm, I. Halow, S.M. Bailey, K.L. Churney, R.L. Nuttall, The NBS tables of chemical thermodynamic properties. Selected values for inorganic and C1 and C2 organic substances in SI units, J. Phys. Chem. Ref. Data 18 (1989) 1807–1812.
- [128] R.J. Nelmes, F.R. Thornley, Structural studies of boracites. The cubic phase of chromium chlorine boracite, Cr<sub>3</sub>B<sub>7</sub>O<sub>13</sub>Cl, J. Phys. C Solid State Phys. 7 (1974) 3855. <https://doi.org/10.1088/0022-3719/7/21/009>.
- [129] F. Kubel, S.Y. Mao, H. Schmid, K. Yvon, Tetragonal ferroelastic/antiferroelectric chromium–chlorine boracite, Cr<sub>3</sub>B<sub>7</sub>O<sub>13</sub>Cl, from X-ray diffraction on a single-domain crystal at 230 K, Acta Crystallogr. B 47 (1991) 692–696. <https://doi.org/10.1107/S0108768191003920>.
- [130] F. Kubel, H. Schmid, M. Yoshida, K. Yvon, Cubic structure of chromium-bromine boracite at 298 and 113 K, Acta Crystallogr. B 48 (1992) 30–32. <https://doi.org/10.1107/S0108768191011965>.
- [131] G. Berset, A. Monnier, H. Schmid, K. Yvon, Cubic structure of chromium iodine boracite, Acta Crystallogr. C 43 (1987) 1243–1245. <https://doi.org/10.1107/S0108270187092291>.
- [132] R. Miletich, M. Nowak, F. Seifert, R.J. Angel, G. Brandstätter, High-pressure crystal chemistry of chromous orthosilicate, Cr<sub>2</sub>SiO<sub>4</sub>. A single-crystal X-ray diffraction and electronic absorption spectroscopy study, Phys. Chem. Miner. 26 (1999) 446–459. <https://doi.org/10.1007/s002690050207>.
- [133] W.A. Dollase, F. Seifert, H.St.C. O'Neill, Structure of Cr<sub>2</sub>SiO<sub>4</sub> and possible metal-metal interactions in crystal and melt, Phys. Chem. Miner. 21 (1994) 104–109. <https://doi.org/10.1007/BF00205221>.
- [134] R. Miletich, D.R. Allan, R.J. Angel, The synthetic Cr<sup>2+</sup> silicates BaCrSi<sub>4</sub>O<sub>10</sub> and SrCrSi<sub>4</sub>O<sub>10</sub>: The missing links in the gillespite-type AB<sub>2</sub>Si<sub>4</sub>O<sub>10</sub> series, Am. Mineral. 82 (1997) 697–707. <https://doi.org/10.2138/am-1997-7-807>.
- [135] H.L. Belsky, G.R. Rossman, C.T. Prewitt, T. Gasparik, Crystal structure and optical spectroscopy (300 to 2200 nm) of CaCrSi<sub>4</sub>O<sub>10</sub>, Am. Mineral. 69 (1984) 771–776.
- [136] A. Schmidt, R. Glaum, J. Beck, Preparation and Crystal Structure of Cr<sub>4</sub>(Si<sub>2</sub>O<sub>7</sub>)X<sub>2</sub>(X = Cl, Br): The First Chromous Halide-Disilicates, J. Solid State Chem. 127 (1996) 331–340. <https://doi.org/10.1006/jssc.1996.0391>.

- [137] A. Schmidt, R. Glaum, Cr<sub>3</sub>Si<sub>2</sub>O<sub>7</sub>·1/4MX (MX = NaCl, NaBr, KCl, KBr): A Cage Structure Built from [CrIIIO<sub>4</sub>] and [Si<sub>2</sub>O<sub>7</sub>] Units<sup>1</sup>, *Inorg. Chem.* 36 (1997) 4883–4887. <https://doi.org/10.1021/ic9700718>.
- [138] M. Dušek, B. El Bali, R. Glaum, L. Palatinus, The incommensurately and commensurately modulated crystal structures of chromium(II) diphosphate, *Acta Crystallogr. B* 62 (2006) 556–566. <https://doi.org/10.1107/S0108768106010238>.
- [139] R. Glaum, A. Schmidt, Contributions on thermal behaviour and crystal chemistry of anhydrous phosphates. XIX. Tri-chromium(II)-bis-phosphate Cr<sub>3</sub>(PO<sub>4</sub>)<sub>2</sub> (≅ Cr<sub>6</sub>(PO<sub>4</sub>)<sub>4</sub>) – A transition metal(II)-orthophosphate with new structure type, *Z. Für Anorg. Allg. Chem.* 623 (1997) 1672–1678. <https://doi.org/10.1002/zaac.19976231032>.
- [140] A.N. Vasiliev, O.S. Volkova, E. Hammer, R. Glaum, J.-M. Broto, M. Millot, G. Nénert, Y.T. Liu, J.-Y. Lin, R. Klingeler, M. Abdel-Hafiez, Y. Krupskaya, A.U.B. Wolter, B. Büchner, Weak ferrimagnetism and multiple magnetization reversal in alpha-Cr<sub>3</sub>(PO<sub>4</sub>)<sub>2</sub>, *Phys. Rev. B* 85 (2012) 014415. <https://doi.org/10.1103/PhysRevB.85.014415>.
- [141] E. Mosymow, R. Glaum, R.K. Kremer, Searching for “LiCrIIPO<sub>4</sub>,” *J. Solid State Chem.* 218 (2014) 131–140. <https://doi.org/10.1016/j.jssc.2014.06.020>.
- [142] M. Ben Amara, R. Olazcuaga, G. Le Flem, M. Vlasse, The crystal structure of cadmium sodium orthophosphate Cd<sub>4</sub>Na(PO<sub>4</sub>)<sub>3</sub>, *Acta Crystallogr. B* 35 (1979) 1567–1569. <https://doi.org/10.1107/S0567740879007147>.
- [143] B. Dickens, W.E. Brown, The crystal structure of Ca<sub>5</sub>(PO<sub>4</sub>)<sub>2</sub>SiO<sub>4</sub> (Silico-Carnotite), *Tschermaks Mineral. Petrogr. Mitteilungen* 16 (1971) 1–27. <https://doi.org/10.1007/BF01099075>.
- [144] D. Colignon, E. Kartheuser, S. Rodriguez, M. Villeret, Optical and magnetic properties of Fe<sup>2+</sup> and Cr<sup>2+</sup> in II–VI semiconductors: the Jahn-Teller effect, *J. Cryst. Growth* 159 (1996) 875–878. [https://doi.org/10.1016/0022-0248\(95\)00685-0](https://doi.org/10.1016/0022-0248(95)00685-0).
- [145] R. Glaum, E. Hammer, W. Hermes, R. Pöttgen, Synthese und Charakterisierung von β-Chrom(II)-orthophosphat, *Z. Für Anorg. Allg. Chem.* 637 (2011) 1052–1061. <https://doi.org/10.1002/zaac.201100089>.
- [146] K. Maaß, R. Glaum, R. Gruehn, Beiträge zum thermischen Verhalten und zur Kristallchemie von wasserfreien Phosphaten XXXII [1] Neue Orthophosphate des zweiwertigen Chroms – Mg<sub>3</sub>Cr<sub>3</sub>(PO<sub>4</sub>)<sub>4</sub>, Mg<sub>3</sub>, 75Cr<sub>2</sub>, 25(PO<sub>4</sub>)<sub>4</sub>, Ca<sub>3</sub>Cr<sub>3</sub>(PO<sub>4</sub>)<sub>4</sub> und Ca<sub>2,00</sub>Cr<sub>4,00</sub>(PO<sub>4</sub>)<sub>4</sub>, *Z. Für Anorg. Allg. Chem.* 628 (2002) 1663–1672. [https://doi.org/10.1002/1521-3749\(200207\)628:7<1663::AID-ZAAC1663>3.0.CO;2-Y](https://doi.org/10.1002/1521-3749(200207)628:7<1663::AID-ZAAC1663>3.0.CO;2-Y).
- [147] K. Maaß, R. Glaum, R. Gruehn, (Mg<sub>1-x</sub>Cr<sub>x</sub>)<sub>2</sub>P<sub>2</sub>O<sub>7</sub>, CaCrP<sub>2</sub>O<sub>7</sub>, SrCrP<sub>2</sub>O<sub>7</sub> und BaCrP<sub>2</sub>O<sub>7</sub> – Neue Diphosphate des zweiwertigen Chroms, *Z. Für Anorg. Allg. Chem.* 627 (2001) 2081–2090. [https://doi.org/10.1002/1521-3749\(200109\)627:9<2081::AID-ZAAC2081>3.0.CO;2-0](https://doi.org/10.1002/1521-3749(200109)627:9<2081::AID-ZAAC2081>3.0.CO;2-0).
- [148] R. Glaum, K. Maaß, Strontium chromium(II) diphosphate, SrCrP<sub>2</sub>O<sub>7</sub>, *Acta Crystallogr. C* 56 (2000) 404–406. <https://doi.org/10.1107/S0108270100000226>.
- [149] A.G. Nord, P. Kierkegaard, M. Von Glehn, O. Tolboe, J. Paasivirta, The Crystal Structure of Mg<sub>3</sub>(PO<sub>4</sub>)<sub>2</sub>, *Acta Chem. Scand.* 22 (1968) 1466–1474. <https://doi.org/10.3891/acta.chem.scand.22-1466>.

- [150] A.N. Vasiliev, O.S. Volkova, E. Hammer, R. Glaum, J.-M. Broto, M. Millot, G. Nénert, Y.T. Liu, J.-Y. Lin, R. Klingeler, M. Abdel-Hafiez, Y. Krupskaya, A.U.B. Wolter, B. Büchner, Weak ferrimagnetism and multiple magnetization reversal in  $\alpha$ -Cr<sub>3</sub>(PO<sub>4</sub>)<sub>2</sub>, *Phys. Rev. B* 85 (2012) 014415. <https://doi.org/10.1103/PhysRevB.85.014415>.
- [151] J. Rodríguez-Carvajal, Recent advances in magnetic structure determination by neutron powder diffraction, *Phys. B Condens. Matter* 192 (1993) 55–69. [https://doi.org/10.1016/0921-4526\(93\)90108-I](https://doi.org/10.1016/0921-4526(93)90108-I).
- [152] B.J. Campbell, H.T. Stokes, D.E. Tanner, D.M. Hatch, ISODISPLACE: a web-based tool for exploring structural distortions, *J. Appl. Crystallogr.* 39 (2006) 607–614. <https://doi.org/10.1107/S0021889806014075>.
- [153] D.G. Mazzone, Y. Shen, H. Suwa, G. Fabbris, J. Yang, S.-S. Zhang, H. Miao, J. Sears, K. Jia, Y.G. Shi, M.H. Upton, D.M. Casa, X. Liu, J. Liu, C.D. Batista, M.P.M. Dean, Antiferromagnetic excitonic insulator state in Sr<sub>3</sub>Ir<sub>2</sub>O<sub>7</sub>, *Nat. Commun.* 13 (2022) 913. <https://doi.org/10.1038/s41467-022-28207-w>.
- [154] R. David, H. Kabbour, D. Filimonov, M. Huvé, A. Pautrat, O. Mentré, Reversible Topochemical Exsolution of Iron in BaFe<sub>2</sub>+2(PO<sub>4</sub>)<sub>2</sub>, *Angew. Chem.* 126 (2014) 13583–13588. <https://doi.org/10.1002/ange.201404476>.
- [155] B. Leclercq, A.M. Arévalo-López, H. Kabbour, S. Daviero-Minaud, A. Pautrat, T. Basu, C.V. Colin, R.-R. Das, R. David, O. Mentré, Multiferroic BaCoX<sub>2</sub>O<sub>7</sub> (X = P, As) Compounds with Incommensurate Structural Waves but Collinear Spin Ingredients, *Adv. Quantum Technol.* 4 (2021) 2000064. <https://doi.org/10.1002/qute.202000064>.
- [156] A.A. Belik, M. Azuma, M. Takano, Magnetic Properties of Isostructural BaCoP<sub>2</sub>O<sub>7</sub>, BaNiP<sub>2</sub>O<sub>7</sub>, and BaCuP<sub>2</sub>O<sub>7</sub> Studied with dc and ac Magnetization and Specific Heat, *Inorg. Chem.* 44 (2005) 7523–7529. <https://doi.org/10.1021/ic050938z>.
- [157] R.R. Das, B. Leclercq, P. Bouvier, A.M. Arévalo-López, C. Goujon, J.-P. Itié, A. Polian, O. Mentré, C.V. Colin, Compressibility of structural modulation waves in the chain compounds BaCoX<sub>2</sub>O<sub>7</sub> (X = As, P): a powder study, *Acta Crystallogr. Sect. B Struct. Sci. Cryst. Eng. Mater.* 78 (2022) 162–171. <https://doi.org/10.1107/S2052520622001159>.
- [158] D. Riou, P.H. Labbe, M. Goreaud, Les pyrophosphates A(II)<sub>x</sub>MP<sub>2</sub>O<sub>7</sub>: Synthèse et étude structurale de BaCoP<sub>2</sub>O<sub>7</sub> et BaNiP<sub>2</sub>O<sub>7</sub>, *Comptes Rendus Seances Acad. Sci. Ser. C Sci. Chim.* 307 (1988) 903–907.
- [159] R. David, Oxydes et ferromagnétisme de basse-dimensionnalité : nouvelles topologies à propriétés remarquables, These de doctorat, Lille 1, 2014. <https://theses.fr/2014LIL10006> (accessed May 13, 2024).
- [160] B. Leclercq, Unités ferromagnétiques « basse D » : frustration et transitions méta-magnétiques pour la mise en place de couplages magnétoélectriques, These de doctorat, Université de Lille (2018-2021), 2019. <https://theses.fr/2019LILUR078> (accessed May 13, 2024).
- [161] J.P. Attfield, P.D. Battle, A.K. Cheetham, The spiral magnetic structure of  $\beta$ -chromium(III) orthophosphate ( $\beta$ -CrPO<sub>4</sub>), *J. Solid State Chem.* 57 (1985) 357–361. [https://doi.org/10.1016/0022-4596\(85\)90199-9](https://doi.org/10.1016/0022-4596(85)90199-9).

- [162] N. Schönberg, W.G. Overend, A. Munthe-Kaas, N.A. Sørensen, An X-Ray Investigation of Transition Metal Phosphides., *Acta Chem. Scand.* 8 (1954) 226–239. <https://doi.org/10.3891/acta.chem.scand.08-0226>.
- [163] A.A. ElBelghitti, A. Elmarzouki, A. Boukhari, E.M. Holt,  $\sigma$ -Dibarium Pyrophosphate, *Acta Crystallogr. C* 51 (1995) 1478–1480. <https://doi.org/10.1107/S0108270195001739>.
- [164] A. Moqine, A. Boukhari, E.M. Holt, Structure of BaCuP<sub>2</sub>O<sub>7</sub>, *Acta Crystallogr. C* 47 (1991) 2294–2297. <https://doi.org/10.1107/S0108270191004419>.
- [165] J. Bendix, M. Brorson, C.E. Schaffer, Accurate empirical spin-orbit coupling parameters  $\zeta$  for gaseous transition metal ions. The parametrical multiplet term model, *Inorg. Chem.* 32 (1993) 2838–2849. <https://doi.org/10.1021/ic00065a010>.
- [166] O. Isnard, Questions, (2013). <https://magnetism.eu/esm/2013/questions/isnard-af.pdf>.
- [167] H.-J. Koo, M.-H. Whangbo, P.D. VerNooy, C.C. Torardi, W.J. Marshall, Flux Growth of Vanadyl Pyrophosphate, (VO)<sub>2</sub>P<sub>2</sub>O<sub>7</sub>, and Spin Dimer Analysis of the Spin Exchange Interactions of (VO)<sub>2</sub>P<sub>2</sub>O<sub>7</sub> and Vanadyl Hydrogen Phosphate, VO(HPO<sub>4</sub>)·0.5H<sub>2</sub>O, *Inorg. Chem.* 41 (2002) 4664–4672. <https://doi.org/10.1021/ic020249c>.
- [168] A.A. Belik, A.P. Malakho, B.I. Lazoryak, S.S. Khasanov, Synthesis and X-ray Powder Diffraction Study of New Phosphates in the Cu<sub>3</sub>(PO<sub>4</sub>)<sub>2</sub>–Sr<sub>3</sub>(PO<sub>4</sub>)<sub>2</sub> System: Sr<sub>1.9</sub>Cu<sub>4.1</sub>(PO<sub>4</sub>)<sub>4</sub>, Sr<sub>3</sub>Cu<sub>3</sub>(PO<sub>4</sub>)<sub>4</sub>, Sr<sub>2</sub>Cu(PO<sub>4</sub>)<sub>2</sub>, and Sr<sub>9.1</sub>Cu<sub>1.4</sub>(PO<sub>4</sub>)<sub>7</sub>, *J. Solid State Chem.* 163 (2002) 121–131. <https://doi.org/10.1006/jssc.2001.9380>.
- [169] K.M.S. Etheredge, S.-J. Hwu, Synthesis and Characterization of a New Quasi-One-Dimensional Copper(II) Phosphate, Ba<sub>2</sub>Cu(PO<sub>4</sub>)<sub>2</sub>, *Inorg. Chem.* 35 (1996) 1474–1477. <https://doi.org/10.1021/ic9511783>.
- [170] A.A. Belik, B.I. Lazoryak, T.P. Terekhina, S.N. Polyakov, Synthesis and structure of Sr<sub>2</sub>Co(PO<sub>4</sub>)<sub>2</sub>, *Zhurnal Neorganicheskoy Khimii* 46 (2001) 1453–1459.
- [171] B. ELBALI, A. BOUKHARI, J. ARIDE, M. BELAICHE, F. ABRAHAM, M. DRILLON, Crystal structure and magnetic properties of Ba<sub>2</sub>Ni(PO<sub>4</sub>)<sub>2</sub>, *Cryst. Struct. Magn. Prop.* Ba<sub>2</sub>NiPO<sub>4</sub> 31 (1994) 61–73.
- [172] J. Aride, A. Boukhari, B. Elbali, E.M. Holt, Distrontium nickel orthophosphate, *Acta Crystallogr. C* 49 (1993) 1131–1133. <https://doi.org/10.1107/S0108270192012599>.
- [173] Bruker (2006) APEX 2, (n.d.).
- [174] S. G. M., SADABS, (n.d.).
- [175] O. MENTRE, A. AREVALO LOPEZ, C.V. Colin, H. NIMOH, Magnetic structure in exotic magnetic-topologies, formed by rare Cr<sup>2+</sup> S = 2 ions, Institut Laue-Langevin (ILL), n.d. <https://doi.ill.fr/10.5291/ILL-DATA.CRG-2972> (accessed May 29, 2024).
- [176] E. Krausz, A Single-Beam Approach to the Absorption Spectroscopy of Microcrystals, *Aust. J. Chem.* 46 (1993) 1041–1054. <https://doi.org/10.1071/ch9931041>.
- [177] K. P., M. F., Ein Beitrag zur Optik der Farbanstriche, *Z Techn Phys.* 12 (1931) 593–601.

- [178] Reflectance Spectroscopy: Principles, Methods, Applications | SpringerLink, (n.d.). <https://link.springer.com/book/10.1007/978-3-642-88071-1> (accessed May 29, 2024).
- [179] P.E. Blöchl, Projector augmented-wave method, *Phys. Rev. B* 50 (1994) 17953–17979. <https://doi.org/10.1103/PhysRevB.50.17953>.
- [180] G. Kresse, D. Joubert, From ultrasoft pseudopotentials to the projector augmented-wave method, *Phys. Rev. B* 59 (1999) 1758–1775. <https://doi.org/10.1103/PhysRevB.59.1758>.
- [181] G. Kresse, J. Hafner, Ab initio molecular dynamics for liquid metals, *Phys. Rev. B* 47 (1993) 558–561. <https://doi.org/10.1103/PhysRevB.47.558>.
- [182] G.M. Sheldrick, *CELL\_NOW*, (2008).
- [183] E.B. Linscott, D.J. Cole, M.C. Payne, D.D. O’Regan, The role of spin in the calculation of Hubbard U and Hund’s J parameters from first principles, *Phys. Rev. B* 98 (2018) 235157. <https://doi.org/10.1103/PhysRevB.98.235157>.
- [184] A. Zorko, S. El Shawish, D. Arčon, Z. Jagličić, A. Lappas, H. van Tol, L.C. Brunel, Magnetic interactions in alpha-NaMnO<sub>2</sub>: Quantum spin-2 system on a spatially anisotropic two-dimensional triangular lattice, *Phys. Rev. B* 77 (2008) 024412. <https://doi.org/10.1103/PhysRevB.77.024412>.
- [185] A. Gaenko, A.E. Antipov, G. Carcassi, T. Chen, X. Chen, Q. Dong, L. Gamper, J. Gukelberger, R. Igarashi, S. Isakov, M. Könz, J.P.F. LeBlanc, R. Levy, P.N. Ma, J.E. Paki, H. Shinaoka, S. Todo, M. Troyer, E. Gull, Updated core libraries of the ALPS project, *Comput. Phys. Commun.* 213 (2017) 235–251. <https://doi.org/10.1016/j.cpc.2016.12.009>.
- [186] C. Yasuda, K. Hukushima, F. Alet, M. Keller, M. Troyer, H. Takayama, Neel Temperature of Quasi-Low-Dimensional Heisenberg Antiferromagnets, *Phys. Rev. Lett.* 94 (2005) 217201. <https://doi.org/10.1103/PhysRevLett.94.217201>.
- [187] H. Yang, O. Mentré, T. Zhu, C. Minaud, C. Ritter, X. Zhang, Y. Jin, M. Lü, Fragile magnetic ordering between robust 2D-ferrimagnets in the AFe<sub>3</sub>(SeO<sub>3</sub>)<sub>2</sub>F<sub>6</sub> (A = K, Rb, Cs) series, *J. Mater. Chem. C* 10 (2022) 2139–2148. <https://doi.org/10.1039/D1TC05650F>.
- [188] O. Mentré, M.A. Juárez-Rosete, M. Colmont, C. Ritter, F. Fauth, M. Duttine, M. Huvé, C. Terryn, V. Duffort, Á.M. Arévalo-López, All-Magnetic Slabs and Multiferroism in (Bi<sub>2-x</sub>O<sub>2</sub>)(MF<sub>4</sub>) Aurivillius Oxyfluorides (M = Fe and Ni), *Chem. Mater.* 34 (2022) 5706–5716. <https://doi.org/10.1021/acs.chemmater.2c01213>.
- [189] M. Leblanc, G. Ferey, P. Lacorre, J. Pannetier, Fe<sub>3</sub>F<sub>8</sub>(H<sub>2</sub>O)<sub>2</sub>: Magnetic structures at 40 and 2 K and Monte Carlo simulation, *Phys. B Condens. Matter* 156–157 (1989) 327–328. [https://doi.org/10.1016/0921-4526\(89\)90668-6](https://doi.org/10.1016/0921-4526(89)90668-6).
- [190] Ligand field theory and its applications, B. N. Figgis and M. A. Hitchman, Wiley–VCH, New York, 2000, xviii + 354 pages. £51.95, ISBN 0.471-31776-4 - Wade - 2000 - Applied Organometallic Chemistry - Wiley Online Library, (n.d.). [https://onlinelibrary.wiley.com/doi/10.1002/1099-0739\(200008\)14:8%3C449::AID-AOC14%3E3.0.CO;2-6](https://onlinelibrary.wiley.com/doi/10.1002/1099-0739(200008)14:8%3C449::AID-AOC14%3E3.0.CO;2-6) (accessed May 29, 2024).
- [191] E. Krausz, AOS News 1998, 12, 21.(b) Krausz, E, Aust J Chem 46 (1993) 1041.

- [192] M.J. Riley, The effects of ds mixing in low symmetry transition metal complexes, *Inorganica Chim. Acta* 268 (1998) 55–62.
- [193] M. Suta, F. Cimpoesu, W. Urland, The angular overlap model of ligand field theory for f elements: An intuitive approach building bridges between theory and experiment, *Coord. Chem. Rev.* 441 (2021) 213981.
- [194] B.G. Wybourne, Effective Operators and Spectroscopic Properties, *J. Chem. Phys.* 48 (1968) 2596–2611. <https://doi.org/10.1063/1.1669488>.
- [195] D.J. Newman, B. Ng, *Crystal field handbook*, Cambridge University Press Cambridge, 2000. <http://www2.phys.canterbury.ac.nz/~mfr24/crystalfield/bibliography/cfhbibliography.pdf> (accessed May 30, 2024).
- [196] D.A. Cruse, J.E. Davies, J.H. Harding, M. Gerloch, R.F. Mackey, R.F. McMeeking, *CAMMAG: A FORTRAN Program for Ligand Field Analysis*, Cambridge UK, 1980.
- [197] A.B.P. Lever, *Inorganic Electronic Spectroscopy*, Elsevier, 1984.
- [198] M. Bermejo, L. Pueyo, On the RML dependence of 10Dq, *J. Chem. Phys.* 78 (1983) 854–857. <https://doi.org/10.1063/1.444786>.
- [199] K.W.H. Stevens, M.H.L. Pryce, On the magnetic properties of covalent XY<sub>6</sub> complexes, *Proc. R. Soc. Lond. Ser. Math. Phys. Sci.* 219 (1997) 542–555. <https://doi.org/10.1098/rspa.1953.0166>.
- [200] M. Riley, *CAMMAG 95: PC version v. 4.0*, (1997).
- [201] M. Gerloch, *Magnetism and ligand-field analysis*, CUP Archive, 1983. [https://books.google.com/books?hl=fr&lr=&id=Ovo8AAAAIAAJ&oi=fnd&pg=PR11&dq=Magnetism+and+ligand-field+analysis&ots=P-JN3zjTBi&sig=ux5WhGrDjTh9ygA\\_o2eoBYrtPtg](https://books.google.com/books?hl=fr&lr=&id=Ovo8AAAAIAAJ&oi=fnd&pg=PR11&dq=Magnetism+and+ligand-field+analysis&ots=P-JN3zjTBi&sig=ux5WhGrDjTh9ygA_o2eoBYrtPtg) (accessed May 30, 2024).
- [202] H. Nimoh, A.M. Arévalo-López, Q.N. Meier, C. Minaud, M. Huvé, F. Capet, A. Cano, R. Glaum, O. Mentré, Antipolar 2D Metallicity with Tunable Valence W<sub>x</sub><sup>+</sup> (5 ≤ x ≤ 5.6) in the Layered Monophosphate Tungsten Bronzes [Ba(PO<sub>4</sub>)<sub>2</sub>]<sub>W</sub>mO<sub>3m-3</sub>, *J. Am. Chem. Soc.* 146 (2024) 23955–23962. <https://doi.org/10.1021/jacs.4c07022>.
- [203] H. Nimoh, O. Mentré, E.-M. Hammer, M. Jähnig, V. Dittrich, C. Minaud, C.V. Colin, A. Arevalo-López, R. Glaum, Layer-By-Layer Magnetic Ordering via Idle Spins and the Optical Signature of Jahn–Teller Cr<sup>2+</sup> Ions in Sr<sub>2</sub> Cr(PO<sub>4</sub>)<sub>2</sub>, *Inorg. Chem.* 63 (2024) 21000–21011. <https://doi.org/10.1021/acs.inorgchem.4c02544>.